UNIVERSITE DE PROVENCE - AIX-MARSEILLE I

Institut Universitaire des Systèmes Thermiques Industriels
CNRS UMR 6595

Ecole Polytechnique Universitaire de Marseille
Département Mécanique Energétique

THESE

pour obtenir le grade de
DOCTEUR de l'UNIVERSITE de PROVENCE

discipline : **MECANIQUE ENERGETIQUE**

Ecole Doctorale PHYSIQUE, MODELISATION et SCIENCES POUR L'INGENIEUR

présentée et soutenue publiquement par
Marc COATANEA-GOUACHET
le 15 février 2012

QUENCH DETECTION AND BEHAVIOUR IN CASE OF QUENCH IN THE ITER MAGNET SYSTEMS

DETECTION DE QUENCH ET COMPORTEMENT EN CAS DE QUENCH DANS LES SYSTEMES MAGNETIQUES D'ITER

JURY

Dr. C. MEURIS	CEA Saclay	Rapporteur
Pr. P. TIXADOR	Grenoble INP	Rapporteur
Dr. F. TOPIN	IUSTI Marseille	Directeur de thèse
Dr. J.L. DUCHATEAU	CEA Cadarache	Responsable CEA
Pr. L. TADRIST	IUSTI Marseille	Examinateur
Dr. L. BOTTURA	CERN	Examinateur
Pr. J. LEVEQUE	Univ. Lorraine	Examinateur
Dr. A. DEVRED	ITER Organization	Examinateur

Quench detection and quench behaviour in case of quench in the ITER magnet systems

Abstract

The quench of one of the ITER magnet system is an irreversible transition from superconducting to normal resistive state, of a conductor. This normal zone propagates along the cable in conduit conductor dissipating a large power. The detection has to be fast enough to dump out the magnetic energy and avoid irreversible damage of the systems.

The primary quench detection in ITER is based on voltage detection, which is the most rapid detection. The very magnetically disturbed environment during the plasma scenario makes the voltage detection particularly difficult, inducing large inductive components in the coils and voltage compensations have to be designed to discriminate the resistive voltage associated with the quench.

A conceptual design of the quench detection based on voltage measurements is proposed for the three majors magnet systems of ITER. For this, a clear methodology was developed. It includes the classical hot spot criterion, the quench propagation study using the commercial code Gandalf and the careful estimation of the inductive disturbances by developing the TrapsAV code.

Specific solutions have been proposed for the compensation in the three ITER magnet systems and for the quench detection parameters, which are the voltage threshold (in the range of 0.1 V- 0.55 V) and the holding time (in the range of 1 -1.4 s).

The selected values, in particular the holding time, are sufficiently high to ensure the reliability of the system and avoid fast safety discharges not induced by a quench, which is a classical problem.

Keywords: cable in conduit conductors, superconducting magnets, fusion, ITER, quench detection, quench propagation

Acknowledgments

First of all, I wish to greatly thank my supervisors, Dr. Duchateau and Pr. Topin, for having framed my work as much as they could. They provided me with very experienced advice, always had an open ear for me, and gave me everything I could catch from their experience with CICCs and thermo hydraulics.

I take this opportunity to thank Jean-Luc again, for all these memories of him singing George Brasses (in particular, “le mauvais sujet repenti”), or telling me the history of syndicalism in CEA, also these moments where he believed that an electrical engineer could teach a mechanical engineer how to read a blueprint… (come on…), or for his poetry... He shared with me much more than part of his professional experience, and this has a great value to my eyes. It is a pleasure to work with him, no doubt! Oh, also, I see now that he has been incredibly … patient!

Of course, I thank the rest of the ‘quench team’ without whom I could not have done anything., They taught me everything, from best jokes of the week to the finest manipulations of Gandalf/Excel… so many good moments, with people I had the chance to work with. The quench team: Sylvie, Benoit, and Jean-Luc. Many many thanks; it was a pleasure to share these years with you!

Of course, many other people at CEA contributed to this work, or supported me during these three years… all the GCRY section, actually, but in particular, Daniel, Patrick Hertout, Christophe, Alex, Patrick, Jean-Vincent, Denis, Sylvain… I cannot list all of them, but all were a good reason to have a big smile while coming to the office.

Many thanks to Félix, Denis, Sébastien, Nello (Iter Organization), for their contribution, their availability, and their will to do their best to ease my task.

I thank specially Dr. Devred, who was one of the first people I contacted when I was looking for a PhD subject opportunity. Without his intervention, everything would have been far much harder! He trusted me, and I hope the results of the studies satisfy him.

Thank you to Céline, my Doudoue, who supported me, and, when difficulties appeared, answered with love, psychology and comprehension… Priceless help… thank you so much, Doue! I want also to thank my parents, for their support, and for they wish to be informed of the evolution of the things here … with so many details, I am sure they also followed these studies with great interest and patience.

I also thank Florent, Julien, Nicoko, Gael, Romain, Marie, Miguel, Remi, Vivien, David, and all the others, who followed my work, gave help and/or conscientious advice from time to time, or just for their friendship and the great moments we had along these three years.

Thank you all, this manuscript is somehow, a little bit made thanks to each of you!

Finally, congratulations to all the people who read this manuscript until the end, some said it is “touffu”…

Table of contents

1. Introduction

This chapter presents the thermonuclear fusion, and the tokamak ITER.
It also helps understanding the choice of superconductivity for Iter,
and presents the magnet systems and the role they play on the plasma.

1.1. Nuclear fusion, from the need of a new source of energy.

In the beginning, mankind just used the energy of the sun. Then fire was discovered, introducing the use of fossil energy. World's energy consumption has not stopped growing since that time. Two major steps can be identified: the first is the industrial revolution in the 19th century, the second is the waking up of the emergent countries, in the 90's. According to the International Energy Agency (IEA), if the energy consumption does not stop growing, the world will face an oil and gas shortage within 80~100 years, and coal shortage before 200 years from now [1].

Moreover, considering the growth of large newly industrialized and highly populated countries such as China, the demand for energy production will tremendously increase (world primary energy demand would increase by 36% between 2008 and 2035) [3]. This justifies the need to develop new sources of energy. Several alternatives to fossil energies have been promoted, including renewable energy (solar, wind, hydraulic dams …). Nuclear fusion is one of the possible ways to new energy source [2], [3], [5].

Nuclear fusion is the process by which two or more atomic nuclei join together, or "fuse", to form a single heavier nucleus. This is usually accompanied by the release or absorption of large quantities of energy, depending on the atomic mass of the atoms entering in collision. In order to produce energy, only light atoms will be involved in fusion reactions.

The energetic products of the fusion reactions are deposited on the walls of the fusion reactor, and their high energy is transferred to the coolant of the walls.

In literature one can find plenty of more or less realistic devices supposed to be able to produce electricity from the fusion of atoms. Among the most studied ways of producing electricity from thermonuclear fusion, there is fusion by magnetic confinement.

1.1.1. Principle of thermonuclear fusion magnetically confined

As explained in the former paragraph, thermonuclear fusion consists in fusing two atoms, the reaction of which releases energy. Although there are many reactions possible in theory, one of the most promising reaction regarding energy release and probability, is the deuterium-tritium reaction (see Figure 1 and Figure 2).

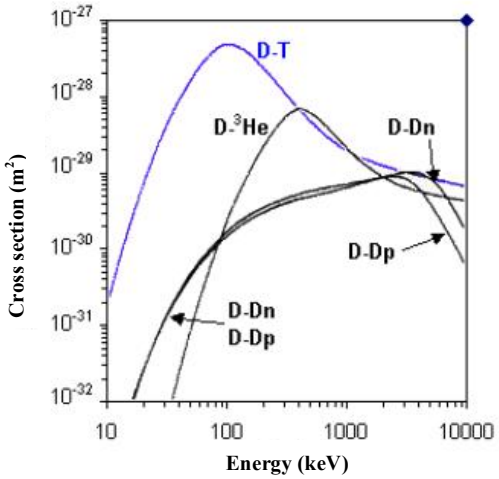

Figure 1: Effective cross-section with respect to the kinetic energy of the incident particle

This reaction produces a helium atom (α particle), and a high-energized neutron, which transmit its energy to the coolant of the walls of the reactor.

$$D^+ + T^+ \rightarrow \alpha^{2+} + n + 17.6 \quad MeV$$

This reaction has been produced at JET and TFTR [20], but also at a larger scale in the atomic bombs. In this fusion reaction, 20% of the energy is transferred to the α particle, whereas the other 80% is kept by the neutron (14 MeV).

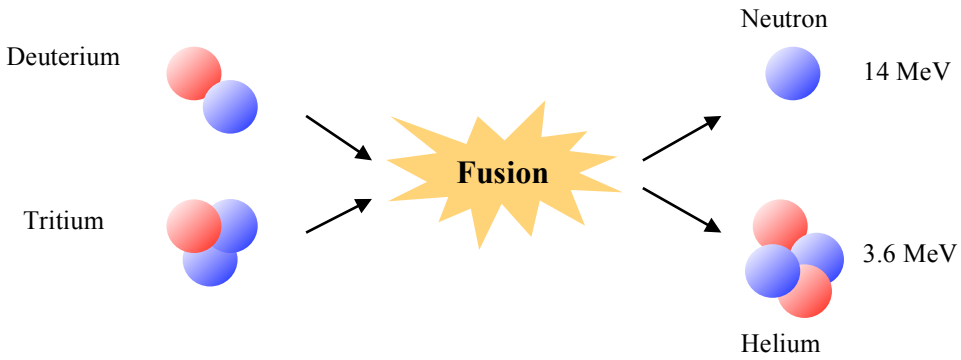

Figure 2: Deuterium-Tritium fusion reaction

Among the mechanisms which rule atoms physics, there are two major and opposite phenomena playing against each other in a fusion reaction between two atoms or ions.

On one hand, there is the Coulomb interaction, which makes two particles charged either negatively or positively repulsing. The nuclei involved in fusion reactions are positively charged, they repulse each other (D^+ and T^+).

On the other hand, at short range only, there is the nuclear force, which tends to bind the nuclei.

It results in the creation of a barrier of potential, illustrated in Figure 3, which has to be crossed such that by increasing the particle energy a fusion reaction becomes possible. It means that Deuterium (D) and Tritium (T) nuclei must be close enough so that the nuclear

force outweighs the Coulomb repulsive force. Actually, thanks to the tunnel effect, it is not necessary to give them the energy required to cross the barrier, just enough to increase the probability of crossing the barrier.

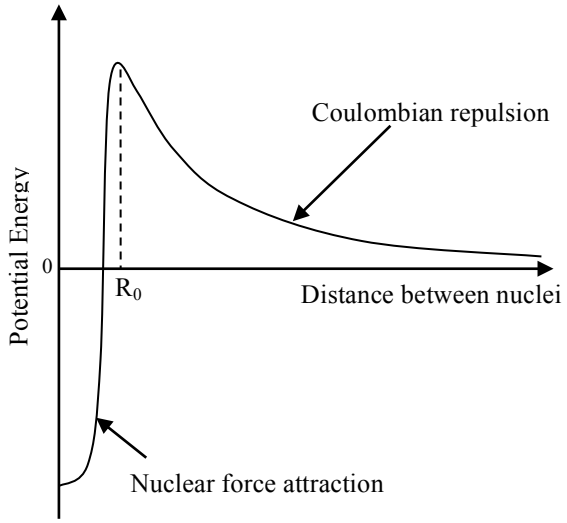

Figure 3: Barrier of potential repulsion/attraction

The energy of the particles is obtained by increasing their global velocity v_t, and the Boltzmann equation shows that this energy can be transferred to the particles by increasing the temperature of the mixture:

$$v_t = \sqrt{\frac{2k_B T}{m}}$$

With T the temperature of the mixture, k_B the Boltzmann constant, and m the mass of the considered particle.

Consequently, it has been deduced that at atmospheric pressure, a temperature of 150 million kelvins [13], 100 times more than the temperature in the centre of the sun, is required to ensure significant amount of fusion reactions. At this temperature, the gas is fully ionized, and is called plasma. No material on earth can sustain such temperature and a simple contact with the mixture would cool it down rapidly. In order to limit the thermal losses, the plasma should not be in contact with any material [4], [6].

1.1.2. Improving plasma performances, the tokamak.

Believing they were solving the problem of the heating and confinement of the D-T mixture, the Russian physicists Igor Tamm and Andrei Sakharov invented the first Tokamak, in the early 50's, and experimental researches started in 1956. In 1968, thanks to the principle of tokamak, they reached an electronic temperature of 1000 eV, which was a great progress at that time. British scientists confirmed the principle and the results they gave in 1969 [11].

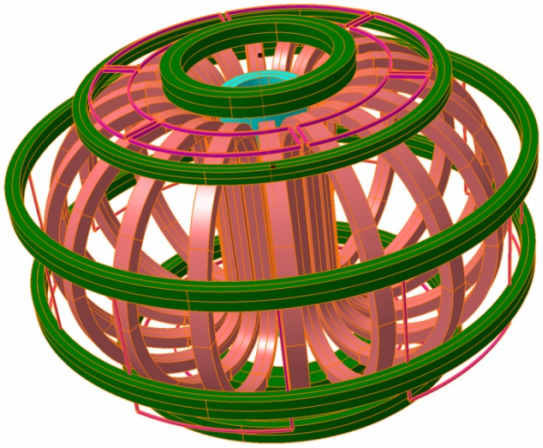

Figure 4: Tokamak and its plasma

A tokamak is a device, which uses magnetic fields to confine an ionized gas (plasma) to achieve fusion in a doughnut-shaped vacuum chamber. The D-T plasma burns, forming helium ashes and highly energized neutrons, which are not magnetically confined. Helium atoms are immediately ionized and confined, they participate to the thermal equilibrium of the plasma.

Due to the Lorentz force, the ionized particles of deuterium and tritium gyrate around closed magnetic lines, and consequently, can be confined and stay away from the tokamak walls.

$$\vec{F} = q(\vec{v} \wedge \vec{B})$$

The magnetic system of a tokamak is rather complex and needs further description, given in the following sections. The tokamak and all the physics that rule the plasma are largely described in [4].

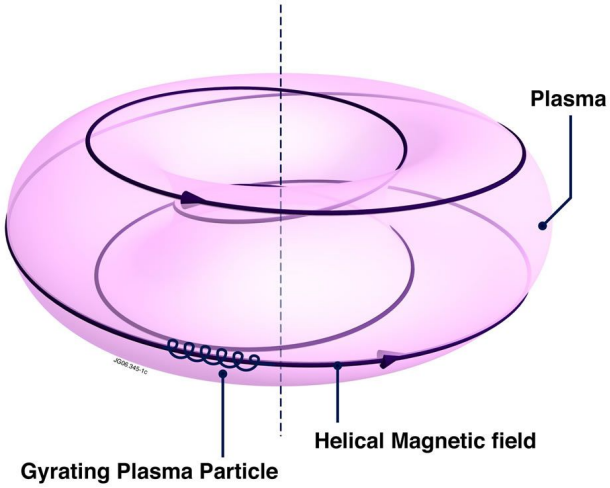

Figure 5: Closed magnetic lines inside the tokamak

The plasma must be heated up, to give its particles enough energy such that they have good chances to cross the barrier of potential due to tunnel effect, and interact to produce a fusion reaction. The main source of heating power is brought by the α particles, but this power is not sufficient to reach ignition in the existing tokamaks. In the mind of the inventors of the tokamak, this heating complement would be provided by joule effect. If there were a current in the plasma, the internal resistance of the plasma would cause heat dissipation by joule effect inside it.

A plasma scenario, or plasma discharge, is a sequence of events which is punctuated by the following events:

- Plasma initiation
- Plasma current ramp-up
- Start of current flat-top
- Plasma current ramp-down
- Plasma termination

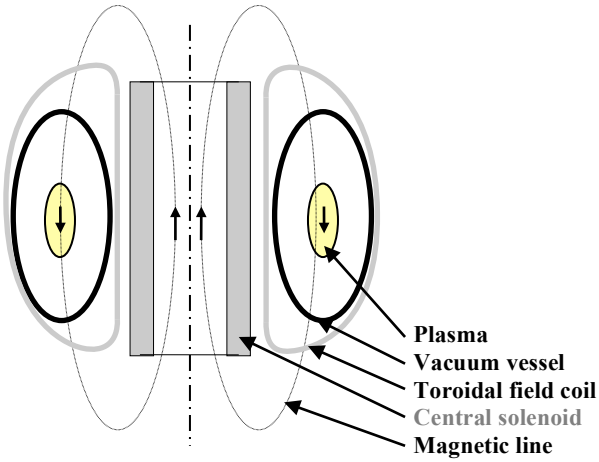

Figure 6: Tokamak cross section, with the central solenoid along the main axis

Inducing a current in the plasma is the role of the central solenoid (CS), located in the middle of the torus, as shown in Figure 6. This CS basically induces a current in the plasma in the toroidal direction, like the primary of a transformer, the secondary of which is the plasma.

The heating caused by the induced current is called Ohmic (or resistive) heating. The heat generated depends on the resistance of the plasma and the current intensity. But as the temperature of heated plasma rises, the resistivity of the plasma decreases and Ohmic heating becomes less effective. To obtain temperatures required for fusion, additional heating methods must be used [7].

This additional heating is provided by radiofrequencies (RF) waves, and neutral beam injections (NBI).

Nevertheless, Ohmic heating plays a great role in the early times of the plasma discharge.

The main confinement magnetic field is the toroidal field. However it can be shown that this field alone does not allow plasma confinement. The total confinement of the plasma is made by three distinct influences.

- The toroidal field $\overrightarrow{B_T}$ creates quasi-circular magnetic lines around the primary axis of the torus.
- Intrinsically, there is a hoop stress in the plasma, which tends to enlarge its major radius. A vertical field $\overrightarrow{B_V}$ compensates for this hoop stress, thanks to the Lorentz force
- The varying magnetic field produced by the CS induces a current in the plasma. This current causes a contraction of the plasma around its centre due to the plasma current and associated generated field $\overrightarrow{B_\theta}$. This contraction force finalizes the magnetic equilibrium, inward Lorentz force is balanced by the explosion force.

An illustration of these magnetic field components is presented in Figure 7.

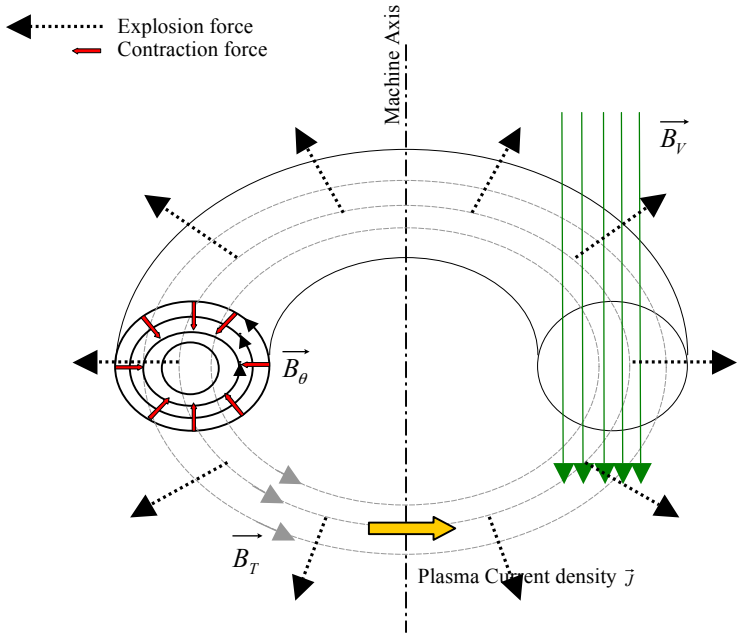

Figure 7: Magnetic fields involved in the plasma confinement

The combination of the fields created by the plasma current and the toroidal field coils, gives the helical closed magnetic lines of Figure 5.

The tokamak principle met a great success. Many of them were constructed over the world, improving their performances. Today it is possible to name the most important of them:

- Joint European Torus (JET) in the United Kingdom
- DIII-D in the United States of America
- Axially Symmetric Divertor Experiment (ASDEX) in Germany
- Experimental Advanced Superconducting Tokamak (EAST) in China
- Korea Superconducting Tokamak Advanced Research (KSTAR) in South Korea
- Tore Supra (TS) in France, Figure 8.
- Two of these machines are particular regarding their plasma performances:
- JET creates the largest plasma volume, 100 m^3, associated with a world record of 16 MW of controlled D-T fusion. During this plasma discharge, 24 MW of heating power was injected in the plasma. Fusion reactions gave back 66 % of the power given to the plasma.

- Tore Supra can create plasmas with a duration up to 6 min and 30 s, among the longest plasma discharge ever produced in a tokamak [86]. It is also demonstrating the feasibility to make the required large magnets in superconducting materials. It has been now in operation for more than 20 years.

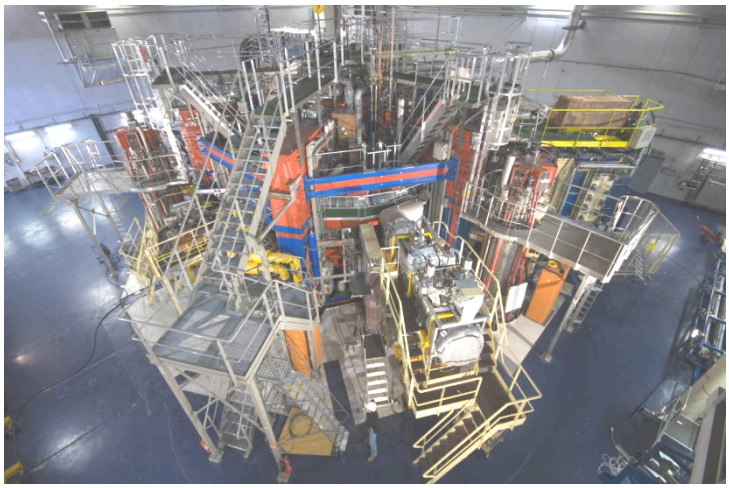

Figure 8: Tore Supra, the first tokamak using superconducting magnets

Since the first plasma discharge inside a tokamak, the techniques and knowledge related to such state of the matter and its control have made much progress. Consequently, plasma performances aiming at creating thermonuclear fusion have much improved. Taking experience from the existing machines, (tens all around the world), several empirical laws can be found. Deriving these laws, it becomes possible to dimension a tokamak according to the requirements in terms of fusion power and Q, ratio of the fusion power and external power (RF power, neutral beam injection …). The following calculation aims at highlighting the importance of the tokamak toroidal field on its performance and cost-effectiveness. This work and associated code is presented in [14].

For a plasma in thermal equilibrium, the power balance must be reached, as follows:

$$P_\alpha + P_{ext} = P_{los}$$

P_α is the power in the alpha particles

P_{ext} is the additional heating by external means (NBI, RF antennas, Ohmic heating…)

P_{los} is the power transferred from the plasma to the tokamak (thermal losses).

Starting simply by deriving the Lawson Criterion [12], the previous relationship can be expressed as follows, in terms of energy per volume unit.

The thermal energy contained in the plasma:

$$W_{th} \propto nTR^3$$

Where n is the plasma electronic density (in m^{-3}), R the major radius of the plasma (in meters), and $T = T_i = T_e$ the electronic temperature, expressed in electron-volt (eV). Introducing confinement time constant τ_E:

$$P_{los} = W_{th} / \tau_E$$

The temperature of species like ions and electrons are proportional to the kinetic energy of the particles, with a factor k_B, the Boltzmann constant.

It comes to express thermal equilibrium:

$$P_\alpha + P_{ext} = W_{th} / \tau_E$$

Introducing the amplification factor Q between the power generated by fusion reaction and the power brought to heat the plasma:

$$Q = \frac{P_{fus}}{P_{ext}}$$

The power P_{fus} released by the fusion reactions can be expressed as follow in the case of ITER:

$$P_{fus} \propto n^2 T^2 R^3$$

for 10 keV < T < 18 keV

And finally, recalling that

$$P_\alpha \approx \frac{1}{5} P_{fus}$$

The first equation can be written

$$\frac{1}{5} P_{fus} + \frac{P_{fus}}{Q} = \frac{W_{th}}{\tau_E}$$

$$nT\tau_E \propto \frac{3.10^{21}}{1 + \frac{5}{Q}}$$

This approximation is valid for $T_e = T_i = T$, Temperature considered uniform, and low gradients in terms of particle density and current density. The previous relationship can be translated using the engineering parameters (R, B_t) which are the magnetic field on the plasma axis and the major radius:

$$R^{1.98} B_t^{2.98} \propto C \frac{P_{fus}^{0.38}}{\left(1 + 5/Q\right)^{0.62}}$$

Where C is a constant describing the tokamak geometries and plasma expected characteristics. The values of Q and P_{fus} are key values regarding a tokamak performance for industrial electricity production purpose. For a tokamak whose requirements specify the fusion power to be produced, and the efficiency of the plasma represented by Q, (with appropriate aspect ratio), it is possible to define a factor of merit ξ proportional to the fusion power :

$$\xi \approx R^2 B_t^3$$

This factor of merit is very important regarding the engineering aspect of the machine. According to the work of J. Johner presented in [14], for a given tokamak project involving an amplification factor Q and a fusion power P_{fus}, a couple (R,B_t) can be found, which drives the dimensioning of the tokamak. The optimization of the choice regarding the couple (R,B_t) has to be done, taking into account economics, and other constraints like the space required to install a central solenoid with enough flux to initiate the plasma current. As a function of the magnetic field, the choice of the superconducting material (Nb_3Sn or NbTi) is a very important issue, as it will be presented later.

1.1.3. ITER

The International Thermonuclear Experimental Reactor, ITER (in Latin: “the path”), presented in Figure 9, is the next step in the direction of mastering fusion energy. Exceeding the power and volume of JET (the largest tokamak around the world in 2011), with more than the plasma duration of Tore Supra, ITER is being built with the goal of demonstrating the scientific and technical feasibility of fusion power. The requirements are summed up in Table 1. The first plasma discharges are scheduled in 2019.

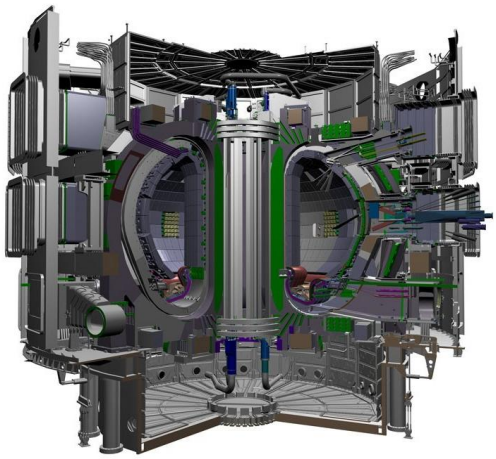

Figure 9: ITER Tokamak

Table 1: JET, Tore Supra and ITER plasma characteristics

Tokamak	Plasma Volume	Duration	Major Radius	Q	Fusion Power
JET	100 m^3	10 to 30 s	2.96 m	0.7	16.1 MW
Tore Supra	24 m^3	Up to 400 s	2.25 m	0	0 MW
ITER	835 m^3	> 300 s*	6.21 m	10*	500MW*

*** These values are not reached simultaneously**

ITER is not meant to produce electricity on the power grid. Achieving Q=10 for a plasma discharge of 400 s is very representative of future reactors. The political aspect of ITER is

also a great achievement: this peaceful and environment-friendly project involves the efforts of half the population of the planet, by the economic and/or scientific support to the project.

1.1.4. Magnets, key components for tokamak design

As said before, huge and strong magnets (partly represented in Figure 10) are required to control the plasma, and confine it in order to maintain a high temperature in his core. In addition, strength of the magnetic field has also a direct impact of the performances of the tokamak [14].

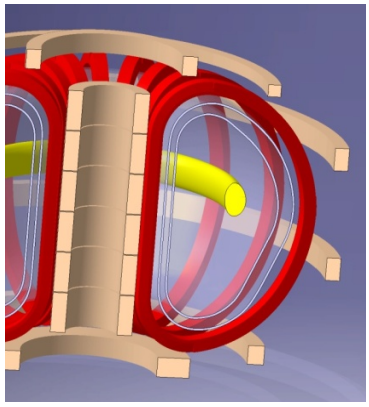

Figure 10: Simplified view of ITER magnetic system

ITER magnets are commonly divided into four subsystems, involved in one or more functions, and all contributing to the control of the magnetic lines guiding the particles. The four subsystems are:

- Toroidal Field coils (TF coils), in Figure 10, establish the main confinement field. The strength of this field has a strong impact on the tokamak expected performances.
- Central Solenoid (CS). In light brown in Figure 10, induces a current in the plasma, helps shaping of the plasma, and participates to the Ohmic heating.
- Poloidal Field coils (PF). In light brown in Figure 10, used for vertical field establishment, plasma vertical stabilization and shaping.
- Correction Coils (CC). For error field correction.

Additionally to these systems, two other elements contribute significantly to the magnetic field in a tokamak.

- Plasma in yellow in Figure 10. Its effect will be shown in section 8.4.3.
- Passive structures (PS), due to eddy currents in transient (demonstration in 5.3.3).

Each of the four subsystems will be described in the next paragraphs.

a. Toroidal Field coils (TF coils)

18 Toroidal Field coils generate the main toroidal magnetic field aiming at confining the plasma. In 1.1.2, the importance of the strength of the toroidal magnetic field $\overrightarrow{B_t}$ has been pointed out. The field they generate reaches at maximum 11.8 T on the conductor. 15 m high, more than 350 tons each, they store more than 40 GJ of magnetic energy. The strands composing the cables of these coils have a total length of more than 80 000 km. One TF coil is shown in Figure 11. Further details can be found in [15] and [80], in the ITER Design Description Document.

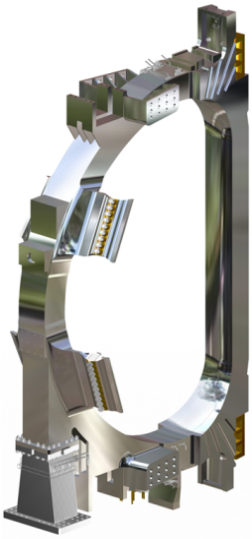

Figure 11: One of the ITER 18 TF coils

They are bound together, and form a discontinued torus. They are surrounded by the PF coils, and inside the torus formed by the TF coils, there is the chamber where plasma burns, the vacuum vessel (refer to Figure 10 and Figure 16).

In normal operation, the cables forming the coils carry a current of 68 kA. Such high current is required to create a magnetic field of 5.3 T at the centre of the plasma (6.2 m from the torus main axis).

The magnetic lines created by the TF coils are quasi circular; they are the main contributors to the path of the final magnetic lines around which the charged particles would wind. The value of the TF coils magnetic field is also greatly responsible for the expected performance of ITER, as showed in 1.1.2.

b. Central Solenoid (CS)[94]

ITER Central Solenoid is a stack of six independently powered modules. The assembly of the ITER CS forms a solenoid of 13 m high. This stack has several roles inherent to the use of a tokamak.

- The primary role of the CS has been defined since the early times of the tokamaks. It consists in driving a current in the plasma. This current will be involved in the Ohmic heating of the plasma, and involved in the self confinement as well, as explained in 1.1.1.
- The CS flux is responsible for the plasma initiation: with its 120 Wb when fully loaded, it creates inductively the electric field needed to initiate the electron cascade, which starts the plasma. This electric field is created toroidally.
- After the plasma initiation phase, the CS flux is used to ramp up the plasma current. In ITER, the reference scenario specifies that the plasma current ramp up from 0 to 15 MA should last 70 s. During this scenario, the current in the CS central modules (CS1U and L) cables decreases from 40 kA to -40 kA, as shown in Figure 12.
- During the whole discharge, it also helps stabilizing the plasma, subject to numerous instabilities.

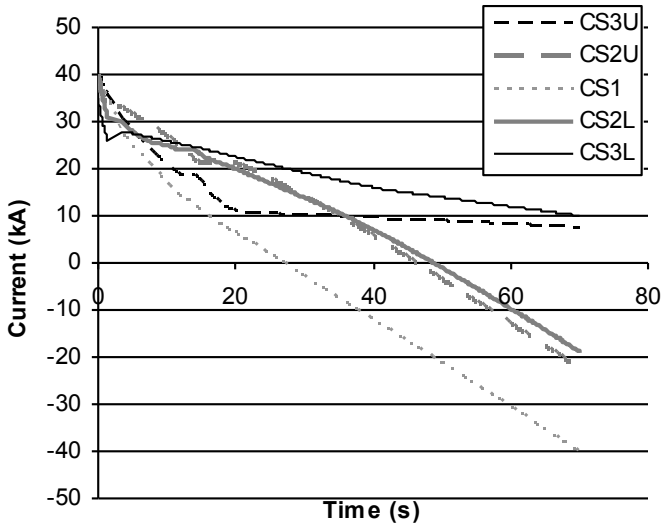

Figure 12: Current in the CS modules during plasma current ramp-up

The general shape of the ITER Central Solenoid is presented in Figure 13, and its localization in the tokamak, Figure 14.

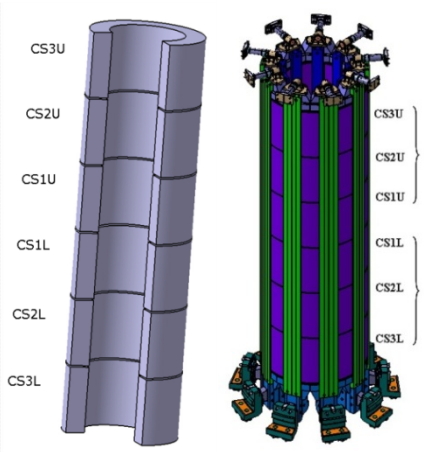

Figure 13: ITER Central Solenoid with and without its mechanical structure

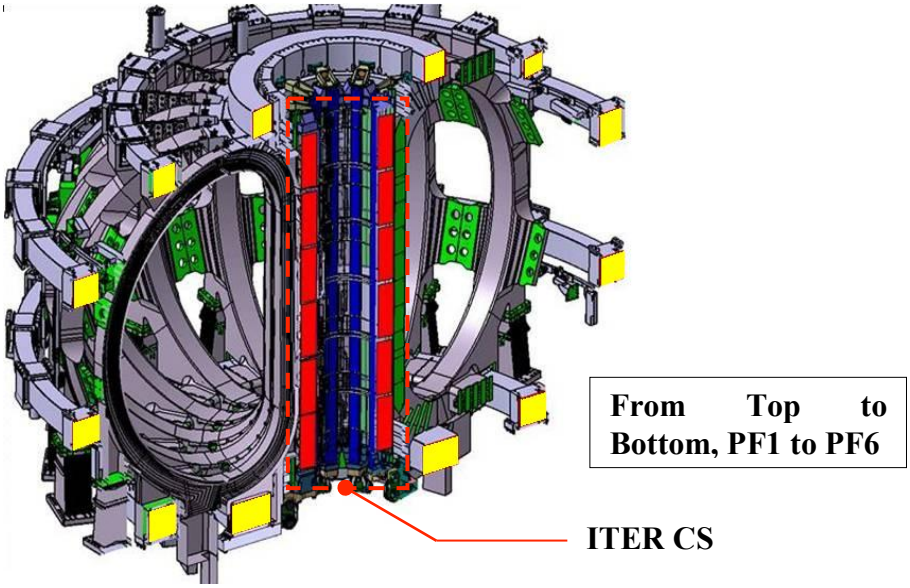

Figure 14: ITER magnet systems. CS cross-section in red and PF coils in yellow

The CS will be described in details in chapter 6.

c. Poloidal field coils (PF coils)

Six Poloidal Field coils compose the tokamak poloidal system (yellow cross-section in Figure 14). They are all different and their radii vary between 3.95 m and 12 m. They will be described in details in 6. The primary role of the PF system is to act on the plasma geometry and position in the vacuum vessel. By creating a vertical magnetic field, and coupled with the action of the CS, they can adjust the ellipticity of the plasma, and stabilize its position.

The CS and PF coils are represented in Figure 15

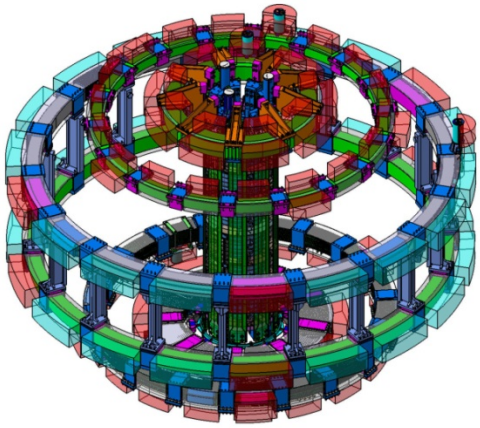

Figure 15: CS and PF coils with clamps and supports

d. Correction Coils (CC coils)

Smaller in size than the previously mentioned coils, the correction coils are designed to correct the field errors than could exist due to tolerances in the positioning of the other coils. They also have a role of stabilizing the plasma, and prevent rapid movements of it. There are three types of correction coils, represented in Figure 16.

Six Side Correction Coils (SCC), arranged between the TF coils and the PF coils around a cylinder.

Six Top Correction Coils (TCC), located between the top PF coil and the second one.

Six Bottom Correction Coils (BCC), located between the lower PF coil, and the PF coil before.

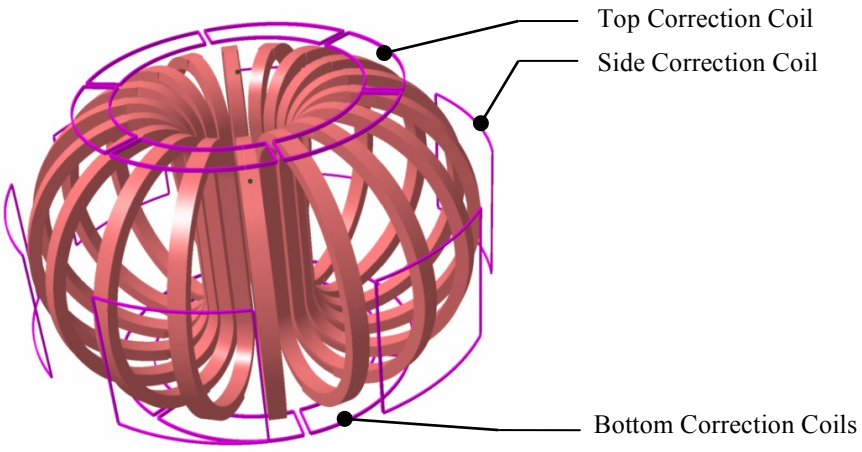

Figure 16: TF coils torus, and correction coils

1.2. ITER and superconductivity

ITER will be the largest tokamak over the world, and is equipped with the largest magnets ever built. One of the main requirements of ITER is to produce a burning plasma of 500 s, as mentioned in Table 1. Consequently, the magnets must produce high field during several minutes. The examination of the power needed to energize such magnets if copper had been selected (2 GW during 500 s) suggested that it was not realistic to take this power from the electrical grid.

It is recalled that:

$$\xi = R^{1.98} B_t^{2.98} \propto C \frac{P_{fus}^{0.38}}{\left(1 + 5/Q\right)^{0.62}}$$

The existence of the factor of merit ξ highlights that, for a given fusion project, several solutions are possible characterized by the couples (R, B).

The final selected solution can be based on a cost optimization, which is not straightforward.

This point can be illustrated with ITER. For ITER a possible choice could have been to select a solution with NbTi cooled at 1.8 K (like in Tore Supra) with a maximum field of 11 T on the conductor and a major radius of about 7 m.

A solution with Nb_3Sn at 5 K has been preferred corresponding to a maximum field of 11.8 T and a smaller machine with a major radius of 6.2 m.

The maximum magnetic field on the ITER TF conductor, B_{TFMax} can be deduced easily from B_t. Assuming the tokamak axisymmetric regarding its vertical axis, and symmetric with respect to the horizontal plan located between CS1U and CS1L (two middle modules of the CS), it is possible to apply the Ampere theorem:

$$\oint_C \overrightarrow{B(r)}.\overrightarrow{dl} = \iint_S \vec{j}.\overrightarrow{dS}$$

$$B(r) = \frac{18.N_t.I}{2.\pi.r}$$

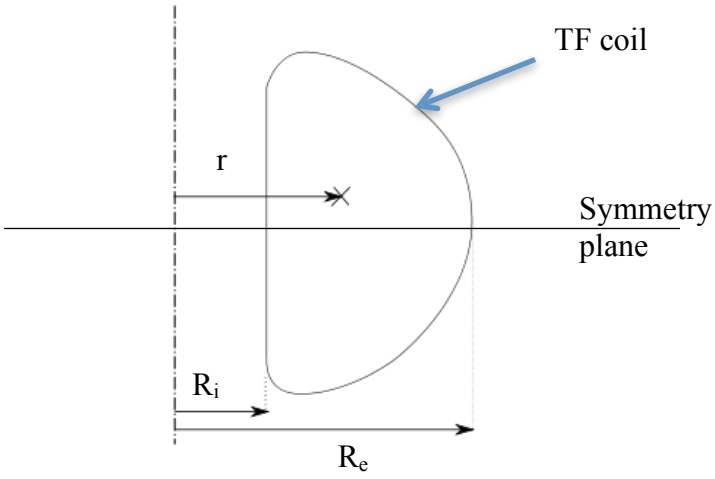

The plasma centre is located at radius R_0=5.3 m, and the field at this point is B_t. It can be easily deduced that $B(r)=R_0.B_t/r$

With I the current carried by the conductor of one TF coil, N_t the number of turns of one TF coil, and r, the radius.

Using the above equation, it is possible to estimate the dependency of Q as a function of $B_{TFMax}=B(R_i)$ the maximum magnetic field on the TF conductor, such as it is expressed in Figure 17.

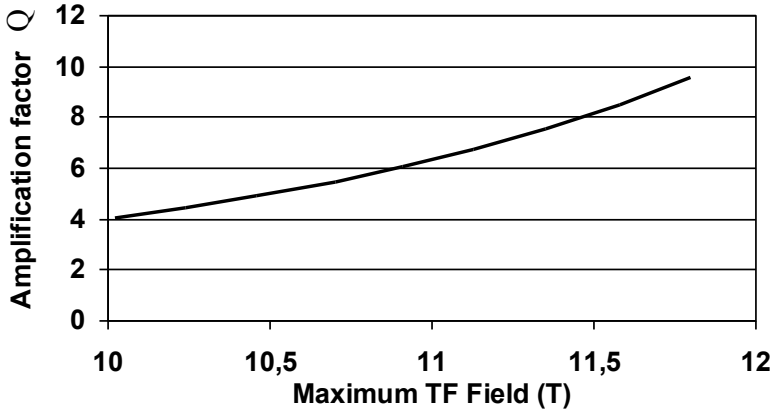

Figure 17: With ITER dimensions, dependance of the amplification factor on the maximum field

To obtain the amplification factor Q of 10, B_{TFMax} should be 11.8 T. Considering the space available for the implementation of the TF coils, and the CS systems, very high current densities will be required. It can be seen that a reduction by 10 % of the magnetic field cause a reduction of Q by 2. This shows how the performance of the TF coil conductor is crucial for the machine: if I is not as high as expected, $B(R_i)$ is decreased as well, and finally, $B_{t.}$, which affects the tokamak performance.

ITER using superconducting magnets can in addition prove the feasibility of the magnets technology for future fusion reactors, with very long plasma discharges, for which superconductivity is compulsory.

Superconductivity and ITER:

- Power consumption reduction from 2 GW (copper) to 20 MW [84](superconductors)
- High field of 11.8 T for the TF system

1.3. Thesis outline

This thesis, deals with issues regarding the application of superconductivity to ITER magnets, and in particular the problem of quench detection. The following chapter will be dedicated to the presentation of superconductivity, its application to ITER, and to the technological aspects of the conductors.

As it will be explained in details in chapter 3, under certain circumstances ITER magnets can loose superconductivity, which could permanently damage the magnets. This phenomenon, called a quench, will be described in chapter 3: a description of its signatures, the chronology of a quench initiation, its potential known consequences, and the different phases of quench detection.

Chapter 4 will introduce the complex mechanism of the quench propagation, as well as the codes, which are used, for investigating quench propagation in the ITER conductors. In particular, the code Gandalf, which has been used for the studies, will be introduced.

As the electromagnetic perturbations are responsible for the appearance of disturbances in the measurement circuits, they must be estimated, in order to know how to compensate them. The 5th chapter introduces TrapsAV, a code especially developed during this thesis. This code aims at calculating these perturbations.

Finally, as ITER magnets are subject to electromagnetic perturbations rather uncommon for superconducting magnets, a special methodology to circumvent the problem of magnet protection has been developed. This methodology is explained and applied in chapters 6, 7, and 8, concluding by several proposals of quench detection for the three main ITER magnet systems.

It is recalled that the views and opinions expressed herein do not necessarily reflect those of the ITER Organization.

2. Superconductivity and Cable-In-Conduit Conductors

Iter magnets will be made up with superconducting materials.
Chapter 2 describes this special feature of some materials, and its limitations.
Finally, it also presents the Cable in Conduit Conductors, used in Iter.

Superconductivity is a property of certain materials, presenting a zero electrical resistance under a critical temperature, which depends on magnetic field. Above this temperature the material is said "normal", or "resistive". It means that under certain conditions, a superconducting material can carry a direct current with a quasi-null resistivity (below 10^{-25} Ωm). This very special feature was discovered in solid mercury by H. Kamerlingh Onnes in 1911. Along with the development of applied superconductivity during the last fifty years in particular, the progress on materials has enabled the design and construction of, among other applications, high field magnets such as those used in tokamaks.

2.1. Some words about superconductivity

Since the Kamerlingh Onnes discovery, many researches have been led all over the world to understand the origin of superconductivity from its bases (such as the BCS theory presented in [26]). At the same time, since the sixties, researches dedicated to applications aimed at developing superconducting materials and processes, associated with proper refrigeration making of superconductivity, something that could be used in projects requiring low energy consumption and/or large currents densities.

Superconductivity represents one of the most striking manifestations of quantum physics at human scale. Superconductivity is however not totally understood now, especially as regards the Cooper pairs and phonon mechanisms. It did not prevent the development of applications and especially the development of a very dynamic commercial application: imaging by NMR with more than 2000 systems produced per year.

2.1.1. Limits of superconductivity

The discovery of the superconducting state is strongly linked to the development of the first helium liquefactor, since Kamerlingh Onnes was looking for the electrical behaviour of metals at very low temperature.

One main feature of a superconductor is its special behaviour when surrounded by a magnetic field. Historically, the superconductors have been sorted in two types with respect to their reaction to the magnetic field.

a. Type-I superconductor

These superconductors have been discovered first, and show two major characteristics. The first consists obviously in carrying a constant current without electrical resistance, up to a certain critical field B_{c1} which is very low. The second one is more curious, and lies in its reaction to the magnetic field: when superconducting, the matter expels the magnetic lines, as showed in Figure 18. This apparent perfect diamagnetism is due to the creation of screening currents near the surface of the superconducting object (London penetration depth), which exactly cancel the magnetic field inside the conductor. This phenomenon is called the "Meissner effect", discovered in 1933. Among others, aluminium, lead, and mercury are type-I superconductors. Unfortunately, such superconductors are not very useful for practical applications because of the low value of B_{c1}.

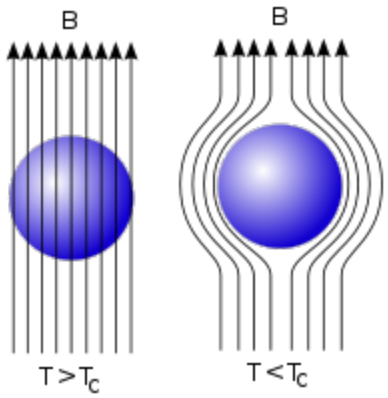

Figure 18: Field expulsion in type-I superconductor

b. Type-II superconductors

The Ginzburg-Landau theory is a phenomenological theory of superconductivity proposed in 1950 by two physicists L. D. Landau and V. L. Ginzburg [22]. In theory the Ginzburg-Landau equation allows to predict the existence of two types of Superconductivity, from the relationship between two important parameters of the equations, which are the coherence length, and the penetration length. In practice type II Superconductivity was identified only later by A. Abrikosov based on the Ginzburg-Landau equation, by drawing all the consequences of a negative surface energy for a category of superconducting material [21].

Type II Superconductivity is characterized by a particular magnetism, appearing above B_{c1}, based on a vortex network, allowing magnetic field penetration in the material and associated with high critical magnetic field. This state is called "superconducting mixed state" (see Figure 19). In the vortex regions, the material is in normal state, and the current to be transported circulates in the superconducting material, around the vortices.

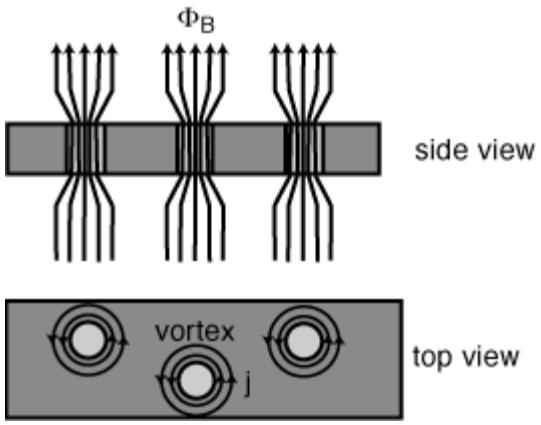

Figure 19: Magnetic flux penetrating locally the material

The higher the surrounding field is, the more numerous the fluxoids are. The limit is reached when the material is full of fluxoids. The field associated with this limit is called B_{C2}. What is important is that B_{c2} can be very high (more than 10 teslas), opening the way to superconducting magnets and applied superconductivity.

It has been showed very early that the existence of the superconducting state is depending on three parameters, the temperature, the magnetic field, and the current density. These limits depend on the material and context, and many superconducting compounds (metallic and

ceramic) have been studied to define these limits. Basically, it can be showed that there is a space the critical boundary of which, is delimited by a function of T, B, and J, as showed in Figure 20.

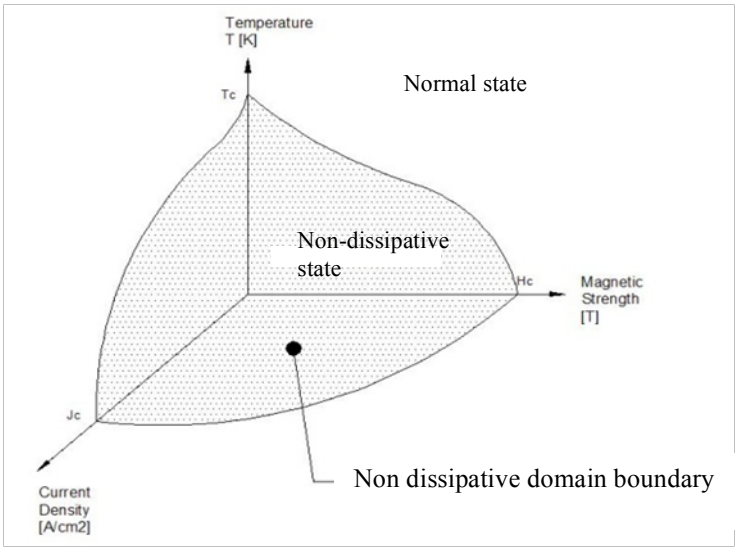

Figure 20: Superconductivity of a material is limited to a domain whose boundaries are function of the triplet B, T, and J

Despite the fact that the levels of these limits are depending on the material, they received common names, which are given below.

- T_{C0} is the critical temperature at B=0 T
- $T_C(B)$ is the critical temperature
- B_{C0} is the critical magnetic field at T=0 K
- J_{C0} is the critical current density at T=0 K and B=0 T
- $B_{C1}(T)$ is the critical magnetic field of type-I, and the start of fluxoids penetration of type-II (mixed state)
- $B_{C2}(T)$ is the critical magnetic field for type-II materials

Other quantities and key values for the properties of applied superconductivity (tapes, wires …) have been defined; they will be explained in the next sections, in particular, the current-sharing temperature, page 33.

c. High critical Temperature Superconductors (HTS)

The High critical Temperature Superconductors are the latest discovered materials, with much higher critical temperatures than classical superconductors previously described, called therefore LTS standing for Low critical Temperature Superconductors. These materials, which are of type II, were discovered in 1986 by Johannes Georg Bednorz and Karl Alexander Müller. Before their discovery, the highest critical temperature was around 23 K. They pointed out that in cuprates compounds such as BaLaCuO, superconductivity still exists around 35 K. Since their discovery, new superconducting materials like bismuth strontium calcium copper oxide (BSCCO: 110 K) and yttrium barium copper oxide (YBCO: 90 K) with much higher T_c have been identified. Some of these new materials have a T_c higher than the boiling point of liquid nitrogen (much cheaper than liquid helium), which is important

regarding applications of superconductivity. Nevertheless, most of the existing superconducting applications are still making use of LTS, as discussed in the next paragraph.

2.1.2. Applied superconductivity

Since the discovery of applied superconductivity, many usages of these extraordinary properties have been made. The areas driving the development of applied superconductivity are Magnetic Resonance Imagery (MRI) [93], magnets for Particle Physics and fusion [85], magnets for NMR. Other applications are being explored such as power cables, current limiters, energy transformers motors, levitating trains, or energy storage (SMES). Every two years a dedicated international conference is held on magnet technology, and in 2011, 99% of the contributions in this conference dealt with applied superconductivity or necessary subsystems (cooling, protection, …). This demonstrates the important part played by superconductivity in the generation of magnetic fields.

As explained before, superconductivity enables transportation of DC current without losses, provided that the superconducting material can be shaped in wires, so that cables can be manufactured. It is obviously extremely interesting for the production of large magnetic field in large volumes and potentially interesting for power transportation.

The emergence of materials with practical mechanical characteristics enabled to manufacture such cables, the architecture of which can be extremely varying from one technology to another. As an example, in Figure 21 is presented the cable of the Large Hadron Collider (LHC) magnets composed of 26 niobium titanium (NbTi) wires. When plunged into liquid helium at about 2 K, this cable can carry current densities up to 10^3 A.mm^{-2} (The domestic copper usually carries only 10 A.mm^{-2}). The shape of this conductor is very different from the fusion conductors, as it will be shown later.

The application, which requires the most advanced performance, is certainly the generation of large magnetic fields. Indeed, in order to sustain very high fields of more than 10 T during long time periods, magnets must carry very high currents, and have to be constantly cooled. Copper cables would require far more power, to achieve such magnetic fields. ITER is one significant example of the advantages brought by superconducting cables, as it allows to divide by 100 the power (20 MW, in the ITER cryoplant) which would be required if the magnets were made in copper (estimated at 2 GW in the ITER copper version).

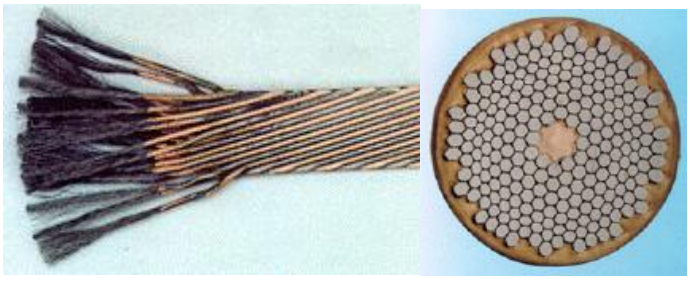

Figure 21: LHC Rutherford type superconducting cable, and the NbTi wire (strand), with grey superconducting filaments

Finally, the most striking example of applied superconductivity remains the MRI technologies. Indeed, every year, more than 2000 MRI superconducting magnets are sold all over the world. In hospitals, with a minimum maintenance, they help research and medication of the human body at a worldwide scale.

Despite the fact that the discovery of superconducting materials at high critical temperature enables an easier use of superconductivity with liquid nitrogen at 1 atm, LTS are still the corner stone of applied superconductivity. Nevertheless, it must be noticed that HTS materials have found applications in power transportation projects like the Long Island Power Authority superconducting cables (version 1 and 2), current fault limiters, magnetic bearings for motors, and in particular, the current leads of several fusion machines (EAST, ITER, JT-60SA, W7-X) [90].

The two main materials used in superconducting magnets are still NbTi and Nb_3Sn. NbTi is a ductile and cheap material, easy to manufacture, used in MRI magnets, in the LHC, in Tore Supra, for instance. Nevertheless, its critical temperature (T_c=9 K) and its B_{c2} (14 T at 0 K) can be too low for some applications. The operation of Tore Supra TF coil at 1.8 K was really a breakthrough allowing the use of NbTi at higher magnetic field. This was later used for LHC.

The increasing need of higher fields, in Nuclear Magnetic Resonance (NMR) studies or in fusion for instance, requires the development of Nb_3Sn-based (first material to be used) wires, which can sustain superconductivity at higher fields. Unfortunately, Nb_3Sn is very brittle. Basically, to manufacture a Nb_3Sn based wire, one has first to extrude a billet either with Nb and Sn separately ("Internal Tin"), or with a compound of tin bronze plus Niobium separately ("Bronze" method). The materials are still ductile (despite the fact that bronze requires a special high temperature treatment), since the Nb_3Sn compound is not formed which allows processing the wire until its final size. Then the operation of cabling and winding can be done. A thermal process is then applied to the object (a coil for instance). In this operation Nb_3Sn can be obtained by diffusion of the Nb into the copper matrix to form bronze which reacts with Sn ("Internal Tin"), or dissociation of the bronze to release Sn atoms, which can diffuse and react with Niobium to form Nb_3Sn ("bronze") see Figure 22. Such process is very sensitive and many parameters have to be tuned such that the expected performances can be reached.

2.2. ITER Dual channel conductors

Stabilizing magnets against local mechanical disturbances appear possible without any contribution from helium, the price being a strict mechanical maintaining. In this case it is considered that the heat generated by the transition of a zone can be conducted by the ends of this zone. There is a limit for the extension of the zone, which is the minimum propagating length, beyond which the quench propagates. This is the concept of indirectly cooled magnets such as MRI magnets.

This is hardly possible for large magnets subject in addition to large external disturbances such as nuclear heating or disruption in fusion. Cryogenic stabilization can in this case provide effective cooling bringing the He coolant with high volumetric heat capacity in tight contact with the conductor by means of channels (ex: TORE SUPRA) in Cable-In-Conduits (fusion). The concept of cryogenic stabilization has been considered in the sixties as the only solution for large magnets, opening the way to practical realisations, which were not possible before this concept [84].

2.2.1. The strands

The elementary brick of a cable is the wire, or strand. ITER cables are made of copper strands and superconducting composite strands. The superconducting strands are chosen

regarding the considered system (ITER PF and CC use NbTi while ITER TF and CS use Nb_3Sn because of their higher magnetic field) [17], [95]. Furthermore, for each ITER magnet system (especially for CS and TF), there are several options in terms of manufacturing processes, as explained in the former paragraph.

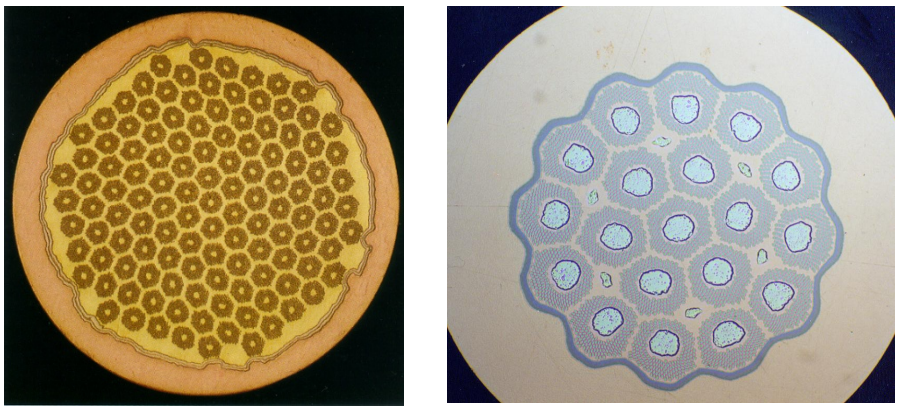

Figure 22: Strand with bronze (left) process and internal tin process (right)

2.2.2. Thermal loads in the winding

As explained in 1.1.2 and 1.1.3, ITER is a tokamak, the performances of which are strongly linked to the performances of its magnet system. Moreover, regarding the next steps to be made in order to produce electricity at industrial scale, it has been demonstrated that fusion by magnetic confinement could not be possible without superconductivity, because of power consumption.

However the ITER coils are submitted to thermal loads, which are detailed below. They are expressed in average supposing one plasma discharge every 1800 s. The presented values are only indicative.

Figure 23: Two ITER CICCs, on the left, the CS model coil CICC, on the right the ITER TF model coil conductor

- Pulsed losses

The ITER TF system is a steady state system but part of the magnets, at the exact opposite of MRI magnets, is pulsed. This is particularly the case for the PF and CS systems the current

of which varies according to the different phases of the plasma discharge scenario. It is recalled that due to magnetohydrodynamics (MHD) perturbations, plasma is fundamentally highly instable, and its position and shape in the torus must be constantly adapted to the most efficient configuration thanks to feedback loops. In addition, the role of the CS system is to induce the plasma current, by creating a large magnetic flux variation. Consequently, power losses appear in the magnet winding due to eddy currents produced in the large magnet structures. Moreover, hysteretic losses and coupling losses are produced within the superconducting cables and these losses will cause temperature increase. These losses are not described in details in this thesis, but additional documentation can be found in [10]. They are expected to be 14.8 kW in average on one 1800 s cycle [84].

- Nuclear heating.

As ITER is a nuclear machine, there will be a neutron production from the plasma during plasma discharges. The shielding thickness is not sufficient to completely shield the winding from the resulting neutrons and gamma fluxes. The magnets and especially the TF system are therefore subject to these fluxes. This will be translated into heat deposition during the plasma burn, as well as in a temperature margin reduction, which has to be estimated. They are evaluated at around 3.1 kW in average on one 1800 s cycle.

- static and resistive loads

Heat by radiation and by conduction is falling on the winding pack constituting the so called static losses. In addition losses due to TF joints are permanent resistive losses. They are evaluated at around 12 kW.

All these thermal loads have to be constantly removed by the cooling system in order to maintain the temperature. The refrigeration mode, which is chosen for ITER, is forced flow refrigeration based on CICCs. This is a complex system involving helium distribution in Double-Pancakes through many pipes, which can be taken at high voltage during operation. A simpler bath cooled system such as in Tore Supra would not have been possible because of the high level of these thermal loads.

The following Table 2 summarizes the losses, and specifies the duration of the energy deposition. Nevertheless, it has to be noticed that these losses repartition are not uniform, they are the average over the specified duration.

Table 2: Thermal loads in ITER

Loss type	Power / Energy	Duration
Pulsed losses	53.3 kW	During plasma : ~ 500 s
Nuclear heating	11.2 kW	During plasma : ~ 500 s
Static and resistive	12 kW	When powered
Disruption	15 MJ over 18 TF coils	~ 0.1 s

2.2.3. CICC, conductors adapted to tokamaks in pulsed operation

As described in the previous paragraph, the ITER cables experience from high thermal loads some of them being pulsed and the other being permanent. These heat depositions can decrease the performances of the superconductor. Because of the low thermal capacity of metallic materials at low temperature, any heat deposition is susceptible to increase the temperature, which leads to decrease the critical current density. Consequently, one has to

keep the material cold, and the heat must be removed from the conductor, otherwise it would lose its superconductivity.

The technology used for the conductors is the Cable-In-Conduit Conductor (CICC), showed in Figure 23, which is imposed as the consequence of the required high current, high voltage and also the capability to absorb quickly heat depositions as a function of time [25], [30]. This capability is linked to the presence of helium, which has a very large volumetric heat capacity. The strands are in contact with helium through a large wetted perimeter.

The ITER CICC used in the PF, CS, and TF systems, is a cable made up with copper and superconducting strands, twisted in five stages (Figure 24). The last step in the twist process consists in the twisting of six bundles of strands, called “petals”, around a central stainless steel spiral. The petals are individually wrapped in a stainless steel tape designed to mitigate the AC losses. The cable is then compacted and inserted in a stainless steel jacket, the external shape of which can be round (TF) or square (PF and CS).

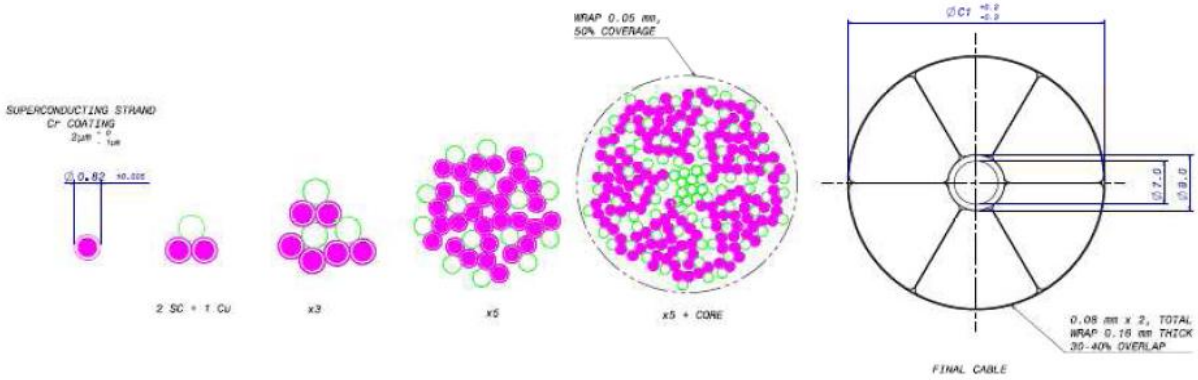

Figure 24: ITER TF coils CICC twist pattern

The CICC used for the CCs has only 4 stages. The petal is inserted in a tube, then compacted to have a square shape. This conductor has no central spiral.

With this configuration, the cold helium is in contact with the strands, hence, can absorb very quickly the heat in case of local temperature increase. It is recalled that at 4.5 K, the thermal capacity of helium is about one hundred time higher than the copper one. The energy needed to increase the temperature of the helium from 4.5 K to 6.5 K is presented compared to the other components involved in the construction of TF and CS conductors in Table **3**.

Table 3: Energy needed to increase the temperature of conductor materials by 2 K from 4.5 K

Material	Enthalpy for a temperature excursion of 2 K starting from 4.5 K
Copper	2700 J/m^3
Nb_3Sn	7400 J/m^3
A316 (steel)	46 kJ/m^3
Helium (constant volume)	640 kJ/m^3
Helium (local enthalpy)	1660 kJ/m^3
Helium (enthalpy at constant pressure)	2270 kJ/m^3

The CICC has the advantages required in ITER, such as:

- high capability to limit AC losses thanks to the “petals” wrapping
- enhanced electrical insulation versus turn-to-turn high voltage thanks to the turn-to-turn insulation
- low sensitivity to external and internal heat deposition compared to MRI cables (for instance), due to the large wetted perimeter which exists between the strands and the helium. Therefore, in such cables, the evacuation of a given heat can be done directly to the helium and not only through the resin or by conduction, as presented in [24].

The details of the cable are given in and [17], and an overview of the twisting process is presented in Figure 24.

2.3. Cooling of the CICC

The CICC is designed to be able to maintain superconductivity in spite of rapid heat depositions, or continuous heat losses during long periods. In order to evacuate the heat from the strands, the convection between the superconducting strands and helium plays the major role. The supercritical helium is continuously extracted from the cable thanks to a circulating pump.

Dual channel CICC has been chosen for the TF, PF and CS systems of ITER. In this concept, two zones can be distinguished such as presented in Figure 25.

- The strand region presenting typically 30 % of helium in the cross section, where thermal loads are heating the strands. This region is also called “bundle” and “annular region”, depending on the context in this thesis.
- The central hole

The interface between the two regions is ensured by a central spiral allowing a good thermalization between the two regions, such that the temperature difference between the two regions is less than 0.04 K [87].

The helium mass flow in the range of 8-10 g/s allows the elimination of the thermal loads by convection with an acceptable pressure drop along the hydraulic length (typically 400 meters) thanks to the central hole. The circulating pump power is proportional to the pressure drop and it is in the range of 10 kW for ITER.

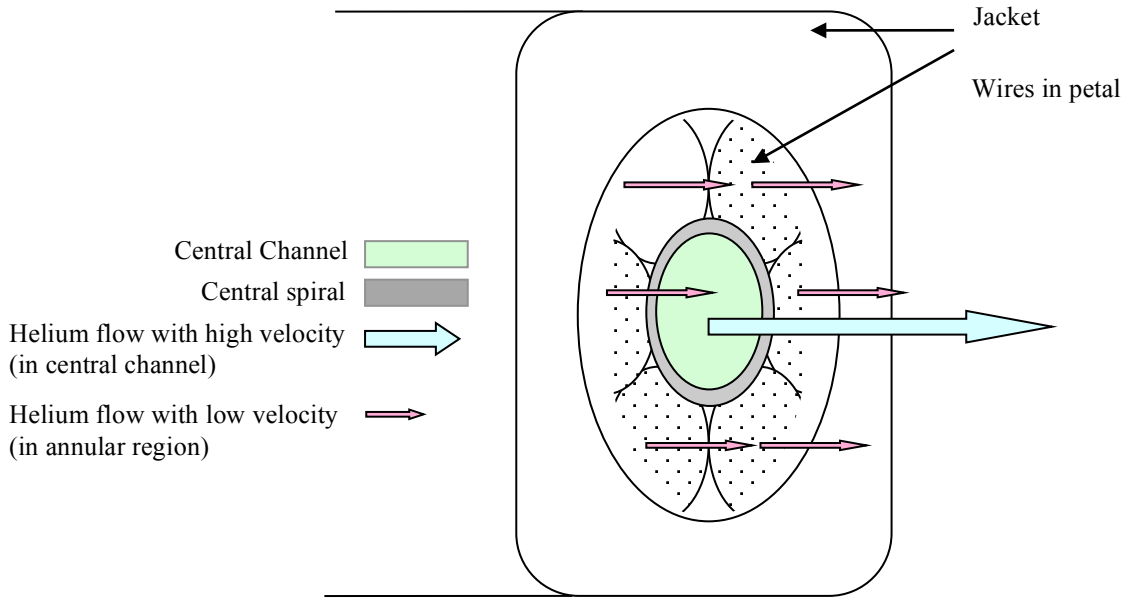

Figure 25: Dual Channel CICC, with central channel, bundle of wires (petals), and jacket

Quench initiation and quench propagation are very different in a CICC and in dry magnets such as the one used for MRI for instance. This is due to the leading role of helium in case of the CICC.

In dry magnets the quench initiation and quench propagation are dominated by thermal conduction and heat generation in the normal zone. A Minimum Propagating Zone (MPZ) can be defined as discussed in [10], [27] and [28], and the Minimum Quenching Energy (MQE) is the energy to establish the MPZ.

The MPZ can be high (~ 1 m) in case of the LHC detectors Atlas and CMS due to the large section of stabilizing aluminium. These magnets are subject to low energy deposition, and consequently, they can afford a low MQE (The enthalpy margin for the Atlas detector is 2 kJ/m^3 while for the ITER CS it is in the range of 300 kJ/m^3 [88]), and their favourable environment does not require presence of helium to absorb it. It can be seen that the quench propagates at constant velocity.

In forced flow magnets with CICC the concept of MPZ is not used due to the leading role of the heat exchange with helium for the MQE. There is no longer a unique MPZ associated with a unique MQE. In a CICC the MQE is a function of the length on which the energy is deposited and of the power function as a function of space and time P(x,t). Note that the length can be several meters long in case of a disruption, the time constant of the heat deposition being in the range 50 ms – 100 ms [89], as shown in Table 2.

The problem can be solved using codes like Gandalf [76] or Vincenta [69]. Analytical solutions can be found in simple cases such as infinite length and constant power. The MQE is generally two orders of magnitude larger than the one for dry magnets.

Regarding quench propagation in CICC, no simple analytical solution can be found.

Nevertheless, the concept of MPZ is totally adequate for MRI cables, since they are embedded in a resin, which induces a low thermal conductivity in the radial direction, and a zone at T_c is coherent with a simulation of a crack in the resin.

3. Quench detection in superconducting magnets

Chapter 3 introduces the quench,
an event which should be avoided in a superconducting magnet.
Its mechanisms, its potential consequences, and its signatures will be described.

As presented in section 2.1, superconductivity in direct current (DC) mode, constant current, generates no resistive losses. As mentioned before, superconductivity can be obtained only within a range of temperature, current density and magnetic field. This chapter answers the following question: what if locally or globally, superconductivity is lost in the coils conductors during tokamak operation?

3.1. Introduction to the quench

Quench is the word used here to designate an irreversible transition from superconducting to normal, resistive state, of a conductor. This normal zone, most of the time in CICC, propagates along the conductor with a certain velocity called here "quench propagation velocity".

In the quenched zone ($T > T_c$), the superconducting material does not have a null resistance anymore. Actually, for the NbTi as well as for the Nb_3Sn, the electrical resistivity in the normal state becomes far higher than the resistivity of copper, which is used (Oxygen-Free High Conductivity Copper, OFHC) at equivalent temperature, as shown in Table 4.

Table 4: Resistivities of the OFHC copper used for ITER, and NbTi and Nb_3Sn in normal state

Material	Resistivity at 4 K and 3 T	Resistivity at 293 K
Nb_3Sn	Superconducting	4.10^{-7} Ω.m
NbTi	Superconducting	$7.3.10^{-7}$ Ω.m
OFHC, RRR=100	3.10^{-10} Ω.m	$1.7.10^{-8}$ Ω.m

At the scale of the cable, the current does not circulate in the superconducting section anymore, the superconducting (in normal state) is bypassed by the copper (refer to Figure 24, page 33).

The appearing resistance causes a heat release in the cable, due to the joule effect produced by the current in the copper:

$$P_{joule} = \rho j^2$$

P_{joule} volumetric power in a coil cell
J average current density in a coil cell
ρ equivalent resistivity of the cell → $\rho=\rho_{cu}/\eta_{cu}$
η_{cu} ratio of copper on total material in the cell

If the heat cannot be removed by the helium or by conduction to allow recovery under the current sharing temperature T_{CS}, the resistive zone extends, and the whole coil is facing a quench.

For a superconducting material a limit in current density can be defined which is J_{noncu}, it is a function of the magnetic field B_{op} of the temperature and of the strain ε in case of Nb_3Sn. This limit is defined when an electric field of 10 $\mu V.m^{-1}$ is measured in the conductor.

The current-sharing temperature T_{cs} , a key parameter of the superconducting conductor, is defined such as:

$$J_{noncu}(B_{op}, T_{cs}, \varepsilon) = {}^{I}/_{S_{noncu}}$$

With I the current in the superconductor, and S_{noncu} the cross section of non copper, B_{op} the magnetic field

If the magnet is operating at a temperature T_{op}, the temperature margin T_{margin} can be deduced:

$$T_{margin} = T_{cs} - T_{op}$$

When the margin becomes null, the conductors starts losing its superconductivity, and dissipates a power P due to Joule effect, as shown in the Figure 26

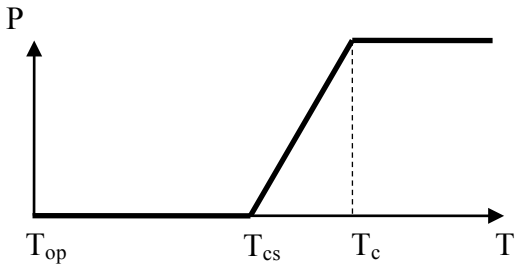

Figure 26: Power dissipated, when reaching Tcs

The current sharing temperature depends on many parameters, linked to the material, the fabrication method, the strain, the magnetic field, the cable assembly, etc… Above this temperature, part of the current uses the copper, since the superconductor becomes resistive. The more this temperature is exceeded, the more the current is carried by the copper. To the end, the conductor becomes fully resistive, and all the currents circulate through the copper.

The consequences of a quench are multiple, and can be more or less severe regarding the cable integrity, depending on the detection and protection. In the worst case, an undetected quench can lead to the destruction of the magnet. In this document, only the case of a quench in ITER CICCs will be treated, since the behaviour of the cables with a different design is very different, and the approach used here cannot be directly applied to them.

Among the signatures of a quench appearing in a CICC, there is the helium release which sometimes happens in laboratories or during tests, as shown in Figure 27.

Figure 27: Helium release in the test lab

Apart this impressive consequence of a (correctly managed) quench, there are additional signatures of a quench. In Figure 28, is shown the temperature in the conductor at the initial quench location, as well as the voltage appearing across it after a quench initiation. The values given are arbitrary, but illustrate the phenomenology linked to the appearance of a quench.

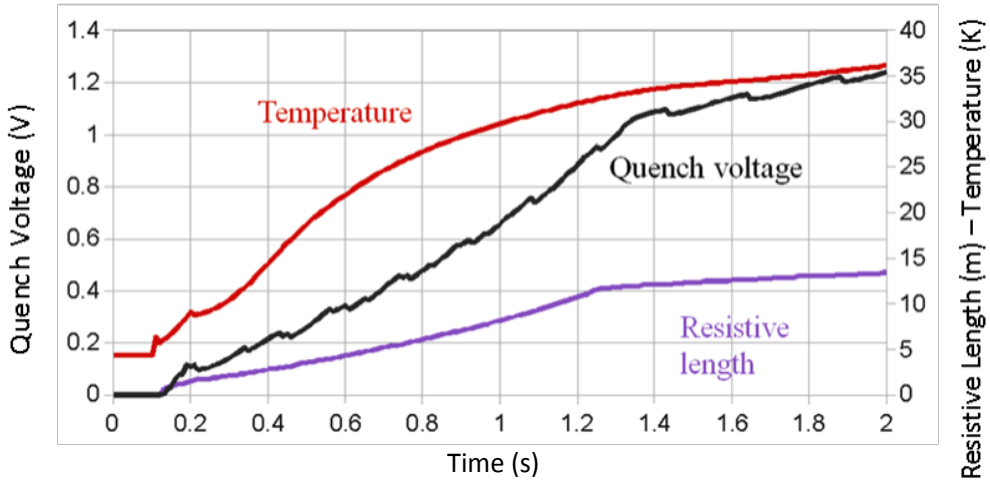

Figure 28: Increase of voltage and temperature after a quench initiation

Two major categories of signatures of a quench can be observed. They are presented in the next two sections.

3.1.1. Thermal signature

Heat is released in the copper section due to Joule effect. At low temperature (5 - 6 K maximum in ITER), the copper at this temperature has a very low thermal capacity. Consequently, its temperature will increase soon after the quench initiation. The heat will be collected by convection to helium causing temperature increase, as well as pressurization and

expansion of helium. This factor, with heat conduction in copper, is the main vector of the quench propagation in CICCs.

The temperature of jacket and electrical insulation of the CICC will increase as well, with a delay to accommodate heat diffusion from the cable and from the helium.

As the normal zone expands, thermal gradients will appear, between jacket and insulation, which could finally cause an electrical failure with risks of arcing, when coupled to a fast discharge. The concept of fast discharge will be described later.

The quench initiation can take place possibly deep in the winding of the coil. The variations of physical parameters of the helium flow such as temperature, pressure or mass flow) can be observed only at the outlets of the magnet, which can be very far from the quench initiation. The quench signal in this case, due to the sound velocity, can be observed only several seconds after the quench initiation. This is too long to activate the fast safety discharge and keep the hottest temperature in the magnet at an acceptable level. For this reason this type of detection can be considered only as a secondary detection [70].

3.1.2. Electrical signature

The appearance of the resistive zone in the conductor will result, apart from any variation of current, in a variation in terms of voltage across the conductor. Moreover along time, this voltage will inevitably increase, because of to two factors:

- The increase of the copper resistivity. The quenched zone resistance per meter is proportional to the copper resistivity. Consequently at constant current, the rise of the temperature will increase a given quenched zone resistance, and finally, the voltage across this zone.

$$\rho_{cu}(t) \uparrow \Rightarrow V(t) \uparrow$$

- The increase of the quenched zone length. Rapidly after the quench initiation, on the same transversal cross section, all the strands will be affected by the loss of superconductivity. Then, the quenched zone will possibly propagate thanks to conduction in the copper and helium expansion both sides along the longitudinal direction, increasing the resistive length, and finally the voltage will increase as well

It is useful to note, that wherever the quench initiation is, the quench will be sensed the same way across the conductor length. In Figure 29, a quench initiated in the CS conductor has been simulated (Current 40 kA, magnetic field 12.17 T). The resistive voltage across this conductor is represented. In this figure, it can be seen that the electrical signature evolves along time.

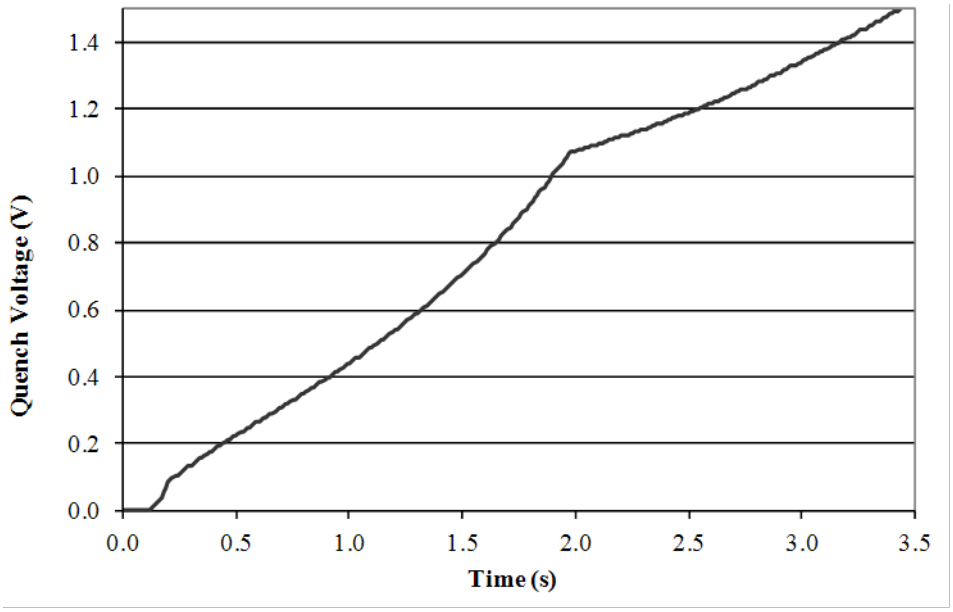

Figure 29: Quench initiated in the ITER CS conductor.

In the present study, only the electrical signature will be detailed. In ITER, as specified in the Design Description Document (DDD), the protection relying on electrical survey of the magnet is meant to be the primary protection system.

The electrical signature is used for quench detection, with the aim of preserving the magnets from degradation, and the thermohydraulic signals will be used for quench detection in order to protect the people and the environment, satisfying the safety conditions inherent to a nuclear project like ITER.

3.2. Possible causes of a quench

Quenches do not occur simply by chance, they can be triggered by events internal or external to the superconducting coil. Hereafter, several events likely to trigger a quench are listed and explained:

- Heat deposition, due to external events. In tokamaks, this can be coming from plasma events (disruptions, neutron beams, electron beams, …). Such events can also make the operating conditions of the conductor vary, leading to a decrease of T_{margin}

- Insulation weakness: in ITER at each plasma discharge, the PF and CS coil systems are submitted to very large voltage to the ground (10 kV) which can result in arcing especially in the bus bars regions. A large voltage is present in the TF coil system only during the fast safety discharge. It can happen that insulation fails (possibly because of the aging, or under an excessive applied voltage), then a short circuit current circulates to the ground carbonising the insulation, and eventually an arc forms.

- Conductor quench: A conductor can quench due to a non-predicted weakness or overestimation of the critical properties at the design stage. Under aging and cycling some degradation can also take place causing the conductor to quench, this can be the case for Nb_3Sn due to strain [74]. The quench can be initiated also in a joint due to some defect or design imperfection causing excessive heating.

- Loss of coolant: a breakdown of the cryoplant, resulting in the injection of “hot” helium in the coil will certainly lead to quench if not detected.

- Loss of vacuum: the magnets as well as the cryoplant power, are designed taking into account the thermal insulation provided by the vacuum in the cryostat. This vacuum between the coil and the 80 K thermal shield reduces strongly the heat losses by suppressing the convection process. If this vacuum is lost, the magnets will experience a breath of hot gas, and convective exchange with the gas will start. It will result in a heat deposition in the range of 2000 W/m [73] on the conductor. If not immediate, it will shortly lead to temperature increase in the magnet. A Paschen [36] breakdown associated with an arc can happen if the surface exposed to vacuum is taken to high voltage simultaneously to vacuum degradation.

- Conductor movements or local crack in insulating resin. This is possible especially for impregnated magnets. For some conductors (embedded in resin for instance), just small heat depositions can trigger a quench because heat evacuation is slow, typically in persistent magnets. In such magnets, tensions are released during the training of the magnets. The current is ramped up until a crack in the resin due to increasing Lorentz forces occurs. The current is decreased, then re-ramped up, until the nominal current is reached. At this moment all the cracks in the resin are developed and no further movements should occur. Nevertheless, there can be remaining stresses, which could cause a crack later on, triggering a quench.

- External causes: Beam losses in particle physics, or plasma disruption in tokamaks like ITER.

In ITER and in fusion magnets in general, the main defaults, which can be envisaged, are related to leaks, high voltages, and weak points in the conductor or insulation.

3.3. Consequences of a quench and principle of protection against quench in case of ITER.

As showed in the preceding paragraph, superconducting magnets can quench and it is very important to detect the quench.

As mentioned in paragraph 3.1, the main characteristic of a quench is the increase of the conductor temperature and resistance.

If not detected, a quench can therefore lead very rapidly to local overheating of the conductor at the hot spot (see 3.5). This overheating can burn the conductor leading ultimately to a rupture and an arc between the two conductors ends or to the ground, leading to irreversible damage of the magnet.

Without reaching this stage, late quench detection is likely to cause dilatations and differential dilatations due to thermal gradients and increasing temperature. A thermal gradient can be sensed mechanically; it creates internal constraints in the materials, hence, can lead to a permanent degradation of the electrical insulation at worst, and at least, a decrease in terms of magnet performance

All these points motivate the aim to effectively detect quenches and protect magnets against quenches.

The study presented in this thesis is focused on the protection of ITER, and the need to preserve their capability to produce their nominal magnetic field, hence, carry large currents. As they use CICCs, the first two protection methods described below do not meet the requirements of ITER magnets, but illustrate well the difficulty related to those magnets, and the principle of a superconducting magnet protection.

- Energy dissipation in the magnet itself

  In NMR magnets, and commonly in steady state impregnated magnets, the magnetic stored energy is absorbed by the magnet itself during the protection phase. It means, once the quench is detected, small resistors are activated all around the magnet, and heat up the conductor in several locations in order to accelerate the quench propagation. Once the magnet is fully quenched, the power and consequently the temperatures and dilatations are uniform, and the magnet can dissipate its magnetic energy in itself.

- The quenching coil is bypassed by a diode

  In other magnets, like in LHC multipoles, if the magnet becomes resistive, the current goes through a diode mounted in parallel, bypassing very rapidly the magnet. The opening of a current breaker simultaneously discharges the stored energy of the considered unit, with a time constant of about 100 s. In addition, in the case of the LHC, the propagation of the quench is accelerated by heaters, the small resistors described in the previous paragraph.

- Energy dissipation into external resistors

  This method is the one which will be used in ITER. The magnetic energy stored in the magnets is too high to be absorbed in the magnets in a way such that any prejudicial differential dilatation, and the voltage across the magnets is variable (varying current), so bypassing the magnet through a diode is not a reliable solution.
  In this case, the protection requires the use of external resistors to dump the magnets energy and dissipate it away from the magnet. This protection system has been used in Tore Supra for 20 years, and has been activated a hundred of times, always due to false quench detection, which highlights the difficulty of quench detection in such a complex system [33]. The only quench which occurred in Tore Supra during operation followed a very severe plasma disruption (1989) causing excessive neutron irradiation into one of the magnet. The quench was correctly detected and the system was discharged and could be reenergized without showing any degradation.

For the three methods described above, the quench must be detected in order to trigger the quench management system, activation of the heating systems to propagate the quench (for MRI and LHC), and opening of the current breakers (LHC and ITER).

In the following, only the last protection system described above will be detailed. In Figure 30, the manifestation of the quench is visible thanks to the increase of the resistive voltage along the conductor.

3.4. The different phases of a quench detection during a plateau

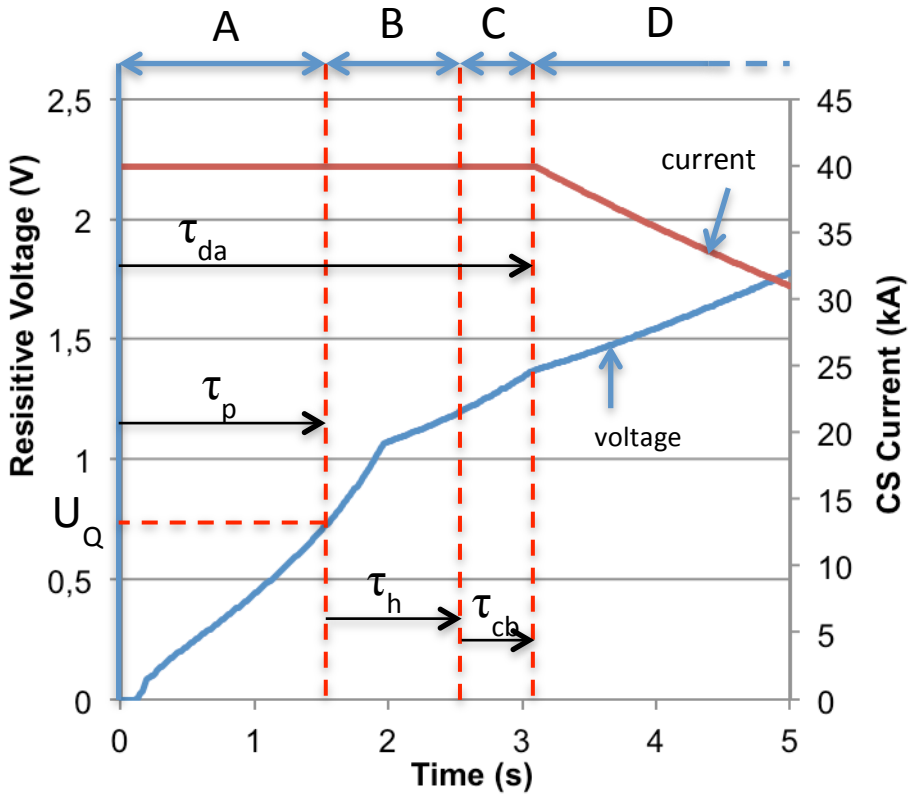

Figure 30: Principle of quench management applied to the CS conductor of ITER.

In Figure 30, the following notations can be found, and are explained in the following paragraphs. The case which is presented is corresponding to a situation where no inductive voltage is considered. The different characteristics of the detection phase are:

- U_Q is the resistive voltage detection threshold
- τ_p is the propagation time, needed for the quench to produce a voltage equal to U_Q
- τ_h is the holding time, a period dedicated to the identification of a quench, for differentiating it from an electromagnetic perturbation.
- τ_{da} is the detection and action time
- τ_{cb} is the maximum time needed for the current breakers to open

The protection can be easily described as follows, in four distinct phases, as shown in Figure 30:

- Phase A (hidden): quench propagation. This phase starts with the appearance of the normal zone, and ends (but the propagation continues!) when the voltage across the conductor reaches a voltage U_Q. The higher U_Q the longer τ_p.

- Phase B: discrimination. This phase starts when U_Q is reached, and can end with one of the two following events:
    - The voltage keeps on exceeding U_Q for a duration defined by the designer of the protection system, called τ_h. h stands for 'holding'
    - The voltage decreases below U_Q before τ_h.

  In ITER and in tokamaks in general, numerous electromagnetic perturbations are expected. Some of them are predictable like the inductive response to coils currents scenario due to the set of mutual and self-inductances, but others will come randomly from plasma instabilities or from reaction of the feedback loop to a plasma movement for instance. It has been observed in tokamaks in operation that other perturbations can come from auxiliary systems, like RF heating devices. These events occurrence can be predicted, but the amplitude of the perturbation cannot be known in advance.
  In the real system, the resistive voltage may be overwhelmed by electromagnetic perturbations, and even in absence of resistive voltage, the quench detectors could misread the signals, and react to perturbations as if it was a real quench.
  These perturbations could make the voltage across the conductor exceeding the voltage threshold during a certain time. The unpredictable perturbations related to plasma or other devices, although they are not perfectly known, will rapidly fade out.
  In order not to trigger the quench protection system due to electromagnetic perturbations not related to a real quench, this holding time τ_h, longer than a perturbation, is implemented. It will be explained in chapter 5 that compensation methods must be used to mitigate these inductive perturbations.

- Phase C: current breaker opening time, τ_{cb}. The role of the current breakers is to redirect the current into a resistor such that the current in the coil decreases. In the protection system they are crucial components, which have to be fully redundant. In order to secure the magnet, the "worst" credible scenarios have to be envisaged. Therefore, the maximum time for opening the current breakers, even in case of failure of one of them, has been calculated and estimated at maximum 0.5 s [52]. This phase is the only one the maximum duration of which is perfectly known.

- Phase D: Fast Discharge, or Fast Safety Discharge (FSD). This phase starts by the opening of the current breakers, and ends with the complete decrease of current to zero. Hypotheses can be taken to estimate its duration. Typically, for each magnet, an exponential discharge is assumed, with a time constant τ_{fsd} such that at the end of the FSD, the energy released is the same as in the real discharge. This will be described in more details in the next paragraph. Therefore, it is assumed that the current decays according to the relationship presented hereafter:

$$I(t) = I_0 e^{-t/\tau_{fsd}}$$

  In the equation above, I_0 is the current in the magnet at the initiation of the FSD. The time t=0 s refers to the time of the opening of the current breakers. The time constant of the discharge is in relation with the voltage, which will appear across the coil to be protected. This voltage plays a very import part in the design of the magnet. It can be expressed as follow in case of exponential discharge:

$$U_{\max} = \frac{2W}{I_0 \tau_{fsd}}$$

with W the stored magnetic energy:

$$W = \frac{1}{2} L I_0^2$$

The following Eq. 1, states that the sum of the duration of phases A, B, and C (the duration of which, are respectively τ_p, τ_h, and τ_{cb}), must not exceed the maximum available detection and action time, τ_{da}, which is calculated for each magnet, and which depends on the scenario.

$$\tau_p + \tau_h + \tau_{cb} \leq \tau_{da} \qquad \textbf{Eq. 1}$$

It should be kept in mind while reading chapters 6 - 8 that, unless specified, the values given to the parameters reported in the Table 5 below refer only to the magnet system studied in the section.

Symbol	Name	Unit
τ_p	Propagation time	s
τ_h	Holding time	s
τ_{cb}	Current breakers opening time	s
τ_{da}	Detection and action time	s
τ_{fsd}	Fast Safety Discharge time constant	s
U_Q	Resistive voltage threshold	V
Ut	Compensated voltage threshold	V

Table 5: Characteristic parameters involved in quench detection

3.5. Hot spot criterion

The existence of thermal gradients and sudden high temperature elevations, as well as the various studies on CICCs behaviour, has led conductor designers to envisage a limit in terms of temperature, which should not be exceeded in any case during the whole protection phase. This requirement is called the “hot spot criterion”. It stipulates that in any case, the temperature of the conductor should not exceed 250 K see [91] in particular, and [55] for ITER. There are several versions of this criterion, but the only one used in the present study refers to the adiabatic hypotheses. Methods using this criterion are also used in [10] and [23].

Below 150 K, the various materials used in the conductors have low difference in terms of differential dilatation. Hence, it is considered that the ITER coils will not be damaged if the temperature on the conductor jacket remains below 150 K. Finally, it leads to consider a strand temperature of 250 K.

The hot spot criterion aims at evaluating the maximum total detection and action time τ_{da} introduced in 3.3, available such that the temperature, reached at the end of the fast safety discharge, is 250 K.

It is supposed that the starting point of the quench is the hottest point of the magnet in case of a quench. This hypothesis is supported by the fact that this point is the one being subject to joule heating for the longest timespan.

For a given conductor, a cell representing the initial point of the quench is described in terms of section contents (fraction of copper and superconducting material). Then, the following adiabatic heat equation, Eq. 2., is applied to the cell:

$$C_p(T)dT = \rho(T).j(t)^2 dt \qquad \text{Eq. 2}$$

with

$$j(t) = \frac{I(t)}{A}$$

In this equation:

- C_p is the average thermal capacity of the cell in [$J.K^{-1}.m^{-3}$]
- ρ is the average resistivity of the cell, which depends on the copper content.
- I(t) is the current of the cell, equal to the current carried by the CICC, in [A]
- A is the area of the cell in [m^2]
- T is the temperature in [K]
- t is the time in [s]

In Eq. 2, the left-hand side is the storage of heat, resulting in the increase of the temperature. The right-hand side is the heat generation due to joule effect. In addition, it must be clarified that all the components, copper and superconducting material, are considered isothermal, as they are in contact. Then this equation is integrated as follows:

$$\int_{T=T_{op}}^{T=250K} \frac{C_p(T)}{\rho(T)} dT = \int_{t=0}^{t=\infty} j(t)^2 dt$$

$$\int_{T=T_{op}}^{T=250K} \frac{C_p(T)}{\rho(T)} dT = \int_{t=0}^{t=\tau_{da}} j_0^2 .dt + \int_{t=\tau_{da}}^{t=\infty} j_0^2 .e^{-\frac{2(t-\tau_{da})}{\tau_{fsd}}} dt$$

$$\int_{T=T_{op}}^{T=250K} \frac{C_p(T)}{\rho(T)} dT = \tau_{da} j_0^2 + \frac{1}{2}\tau_{fsd} j_0^2$$

Nevertheless, especially at low temperature, the magneto-resistance plays a great role, hence must be included in the calculation.

The integration is done numerically, first by evaluating the left-hand member, and τ_{da} is determined. There can be variations of this calculation, especially when the current in the conductor varies rapidly, as it is the case for the CS. This special formulation will be presented in details in 6.4.

4. Considerations on quench propagation in Cable-In-Conduit

The quench is not instantaneous, and its propagation velocity is a key value which plays a crucial role in quench detection issues.
Chapter 4 presents the studies of the quench at early times, and puts the lights on the parameters which influence the propagation velocity.

Examining the literature, there are not so many experimental studies regarding quench propagation in CICC. We will concentrate here on dual channel CICCs as the central channel is playing a role in the propagation.

One can mention the article of Anghel regarding the Quell experiment [47], and the studies conducted during the CS model coil experiment [48] and [49]. The analysis developed by Shajii and Freidberg [92] in 1995 is an important tentative to model the quench propagation in a cable in conduit, and can also be mentioned. In this model the inertia forces of helium are neglected and the temperatures of the jacket, the strands and helium are supposed equal. There is no central channel.

Four different propagation regimes are identified according to the length of the coil and the pressure increase. Starting with a simplified numerical model, it is important to point out that analytical formula are given for these four regimes, to predict the quench propagation velocity and the pressure increase which are the two most important parameters of the quench propagation.

Starting after a certain time, a quench back regime is also identified in the model corresponding to a drastic acceleration in quench velocity and pressure increase.

The development of numerical codes during the last ten years has allowed identifying the limits of this model.

In the four regimes apart the influence of the starting operating helium conditions (P_{op} and T_{op}), mainly the influence of the overall current cable current density and of the initial quench length is pointed out. By the way, this influence can express differently according to the regimes. Using the numerical codes, it will be seen however that the temperature margin is in addition playing a leading role. It is also clear that the central channel influences the quench velocity. Moreover the onset of the quench back is a complex phenomenon, which is not predicted correctly by the model.

It is of course not possible in the framework of this thesis to completely cover this vast subject. By the way quench detection is mainly concerned by the early times of the quench propagation, which turns out to be very specific in comparison with later times.

However the first calculations with Gandalf (further details are given in section 4.3) regarding the CS coil and the observations of behaviour were an invitation to perform a kind of academic study to assess the results. This study has been performed on the CS conductor, which is presented in

Table 6, but the conclusions have been very useful also for the other ITER coils.

Table 6: Salient parameters of CS conductor

	CS conductor	
Type of strand	Nb_3Sn	
ITER cycle phase	SOD	EOB
Maximum operation current (kA)	40.	46
Peak field (T)	13	12.7
Operating temperature (K)	@ peak field 4.5	
Non copper (mm^2) untwisted [twisted]	154.3 [160.8]	
Total copper (mm^2) untwisted [twisted]	308.6 [321.5]	

Inner hole internal diameter (mm)	7

4.1. Adiabatic quench propagation velocity and influence of Helium cooling

It is unfortunately not possible to give an analytical formula for the quench propagation in a CICC, however such an analytical approach is possible for dry magnets such as MRI magnets. This approach is very useful and helpful even for magnets made of CICCs.

To simplify the model, the current sharing zone is not detailed, the conductor is considered as not quenched under T_s (defined by the following formula) and quenched above T_s. In reality the quenching zone is not peaked at T_s but lays on a temperature range between T_{cs} and T_c which is about 3.3 K (see Table 7). Note that, for a given conductor, a variation in J impacts not only J in Eq. 3 but also T_s is affected. In addition, the magnetic field is generally proportional to J, which further impacts T_s.

$$T_S = \frac{1}{2}\left(T_C + T_{CS}\right)$$

In [10], M. Wilson gives an analytical expression of the propagation velocity of the quench, when adiabatic conditions are assumed, as in dry magnets, the winding of which is embedded in epoxy resin:

$$v_{ad} = \frac{J}{\gamma C(T_s)}\sqrt{\frac{L_0 T_s}{T_s - T_{op}}} = \frac{J}{\gamma C(T_s)}\sqrt{\frac{\rho\lambda}{T_s - T_{op}}} \qquad \text{Eq. 3}$$

v_{ad} is the velocity of one of the boundaries of the normal zone ($m.s^{-1}$)

J is the average current density carried by the conductor (A/mm^2)

γ is the density of copper (8900 $kg.m^{-3}$)

C is the average thermal capacity of the conductor ($J.kg^{-1}.K^{-1}$)

L_0 is the Lorentz number (2.45×10^{-8} $W.\Omega.K^{-2}$)

T_{op} is the operating temperature

ρ is the resistivity and λ is the conductivity

To calculate the normal length and the associated resistive voltage from Eq. 3 a factor of 2 has to be introduced to account for the propagation of the normal front in two opposite directions. The average thermal capacity is taken equal to the copper thermal capacity as copper and bronze are dominating in the CS conductor.

Eq 3. is applied to the case of the inner turn of the ITER Central solenoid during plateau.

Table 7: Main parameters of Eq. 3.

Operating current	38046 A
Magnetic field (T)	12.18 T
J	82.2 A.mm^{-2}
γC	3400 J.m^{-3}K^{-1}
T_{op}	4.3 K
T_c	9 K
T_{cs}	5.7 K
T_s	7.35 K
T_{cs}- T_{op}	1.38 K
T_s- T_{op}	3.05 K
v_{ad}	5.85 m/s

In [10], Eq 3. is corrected to take into account the effect of a bath at constant temperature T_{op} with a convection heat transfer coefficient h to the bath.

P is the strand wetted perimeter, A is the conductor section with an average resistivity ρ.

$$v_h = v_{ad}\frac{(1-2y)}{\sqrt{1-y}} = \alpha v_{ad} \quad \text{with} \quad y = \frac{h.P(T_s - T_{op})}{\rho J^2 A} \qquad \text{(Eq. 4 and Eq. 5)}$$

Applying the correction due to heat transfer [10] of Eq. 4, which slows down the propagation, a value of y of 0.91 and a negative value of α of -2.75 is found for a typical value of h of 1000 W.m^{-2}K^{-1} (see Table 8), which means that the normal zone does not propagate. This result is not surprising as y is the inverse of the Stekly parameter [24]. It is well known that the conductor is infinitely stable as soon as y is larger than 0.5 (Maddock criterion) and the conductor has been designed according to the Stekly criterion.

However the model implicitly supposes that the temperature of the surrounding helium is constant and equal to T_{op}, which is true for a bath, but certainly not for a CICC. On another hand the velocity and the heat transfer coefficient are certainly different from their values in the situation suggested by the model, in the vicinity of the quenching zone. Some light can be put on this point using a dedicated code Gandalf associated with a conductor model. This will be presented in the next sections.

The application of Eq. 5. is illustrated in Table 8, on the left column by assuming a bath at constant temperature and on the right by taking account the values of temperature from Gandalf (see section 4.3).

Table 8: Main parameters of equation applying Eq. 5

	$T_{He} = T_{op}$	T_{He}-T_{op} from Figure 32
J	82.2 A/mm^2	82.2 A/mm^2
P	1.5 m	1.5 m
A	462.9 mm^2	462.9 mm^2
ρ	1.08 10^{-9} Ω m	1.08 10^{-9} Ω m
$T_s - T_{He}$	3.07 K	---
hΔT	3070 W/m^{2}K	~300 W/m^{2}K (Figure 33)
y	0.91	0.13

α	-2.75	0.8

4.2. The virtual 150 m long conductor model

To eliminate end effects and spatial magnetic field variations, which complicate the analysis from Eq. 5, it has been decided to build a virtual model, for use with Gandalf. This virtual model is a conductor 150 m long, at the same current, strain and magnetic field as those used for PC101 (101st pancake of the CS, starting by the bottom) of the ITER CS [51]. With its constant field and current, it can be considered that the simulated turn is 150 m long. The quench has been initiated with the deposition of power over 1 m during 0.1 s between 74.5 m and 75.5 m (the middle of the conductor), with 2 times the energy needed to initiate a propagating quench, this value being determined by successive trials. With this model, the whole conductor is quenched within 5.47 s (5.67 s minus the duration of the energy deposition) for the first turn. The propagation, after heat deposition, can be divided into 3 parts as indicated in Figure 31:

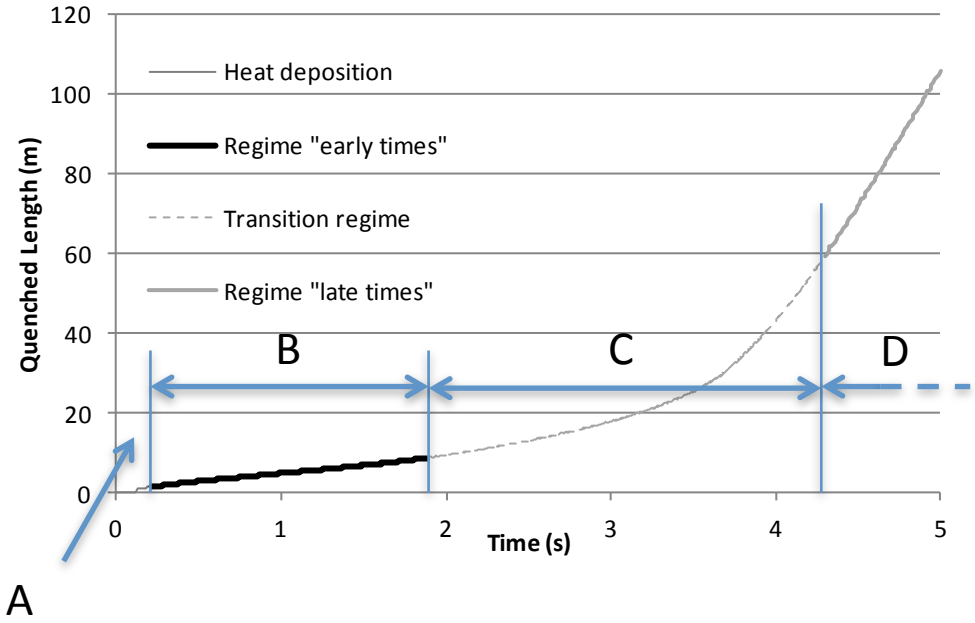

Figure 31: Normal zone as a function of time, simulated with Gandalf2.1+Flower

After the heat deposition (A: from 0.0 s to 0.2 s), there are 3 regimes in the propagation:

B: The first regime is from 0.2 s to 1.9 s, the “early times propagation”

C: The second is the transition regime

D: The third part is from 4.3 s to 5.67 s, the “late times propagation”

For other turns, the same phases can be extracted.

The present study focuses on the first seconds (first regime), which is relevant regarding quench detection issues, as explained in [51].

It can be noticed that the propagation of the normal length can be simply approximated with a linear evolution as a function of time between 0.2 s and 1.9 s. The coefficients used in

the next developments are the coefficients of the linear regression deduced from the signals presented above.

4.3. Gandalf Code – Flower subroutines

A simple analytical simulation of quench initiation and quench propagation in CICCs is not possible. The experimental database is in addition very poor.

The only solution for these studies is to rely on existing commercial or semi-commercial codes. There are in practice only two codes commercially available: Gandalf (presented in [76] and [75]) and Vincenta, developed at the Efremov institute, and presented in [69].

Gandalf, has been chosen. It is used by many laboratories around the world, and this makes possible crosschecking. The first version of the code was made available more than 15 years ago.

Gandalf is a 1-D code especially developed for dual channel CICC, allowing quench initiation and quench propagation simulations. It solves Navier-Stokes equations coupled with the laws, which define superconducting properties. This software is completed by a set of subroutines and Flower, aiming at simulating the cooling network.

The 1-D presentation makes the implementation of data very simple, and was sufficient for this study.

Gandalf is not able to model several thermally coupled hydraulic circuits or to take into account heat conduction between the turns of a given hydraulic circuit such as it is the case in a pancake of an ITER coil.

In the thesis the model used for Gandalf is a pancake without any heat exchange between parts of the pancakes. This model is realistic only for the early times of the quench (useful for quench detection) due to the large insulation thickness, which surrounds the conductor (1.6 mm). At larger time scale (> 30 s), adjacent turns (upper and lower pancakes) should be taken into account, which is not possible in Gandalf 2.1.

It is possible to estimate the helium temperature in the quenching zone using Gandalf. In Figure 32 the result of a quench simulation on the ITER CS conductor, which is presented in

Table 6, is shown. The temperatures are presented at t = 0.7 s (chosen arbitrarily) in a 150 m long conductor at uniform magnetic field after the quench initiation, the quench has been initiated at the abscissa 75 m, in the centre of the conductor length, as illustrated by the conductor temperature which is maximum at this abscissa. It is propagating in the two directions.

It can be seen in Figure 32 that the helium temperature does not stay at T = 4.3 K in the quenching zone, the limits of which are T_{cs} = 5.7 K and T_c = 9 K. The maximum temperature difference between helium bundle and cable in this zone is about 0.2 K. Higher temperature difference up to 0.5 K can be found in a zone where the conductor is fully quenched. It can be seen that the temperature of the helium hole is larger than the conductor temperature, which is a driver of the propagation.

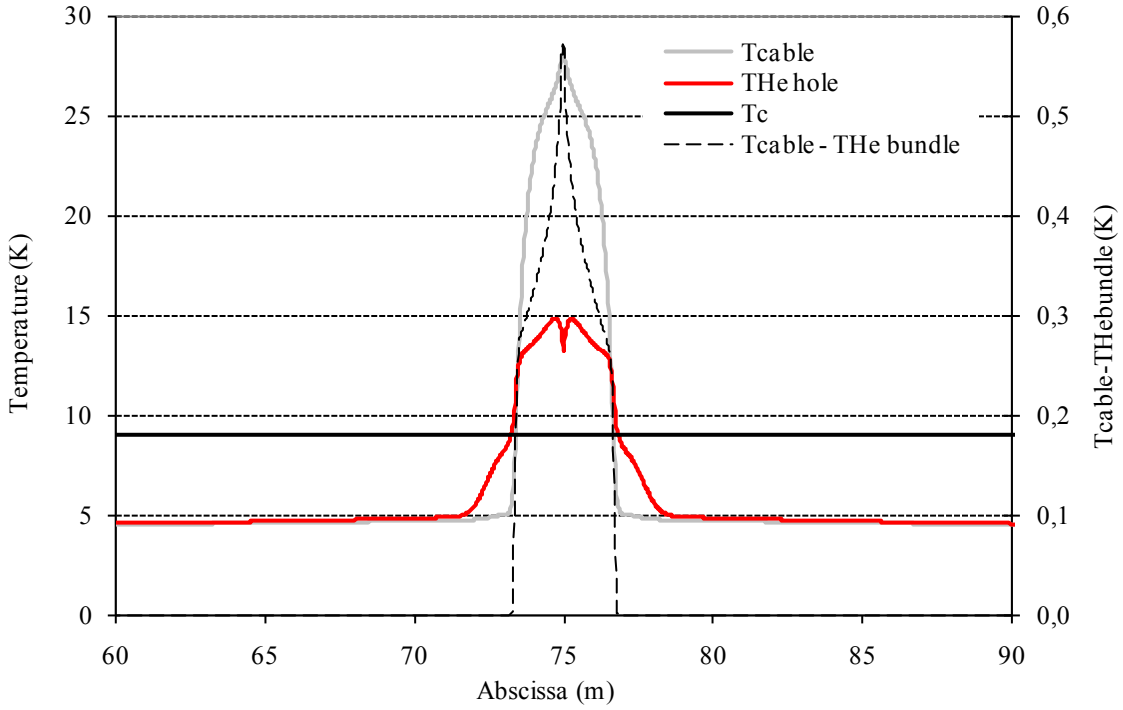

Figure 32: Illustration of thermalization between conductor and He bundle

Moreover the heat flux, which can be considered zero far from the quenched zone, is presenting an important depression in the central region down to 300 $W.m^{-2}$ due to the modification of the helium velocity, which is nearly 0 in the centre of the quenched zone (see Figure 33).

It is therefore possible to recalculate y and α of Eq 4. and Eq 5. using $h(T_s - T_{He})$ of 300 $W.m^{-2}$ and an adjusted h. Doing this, it is possible to see that the quench velocity is less affected by the presence of helium in comparison with the adiabatic propagation (see Table 8).

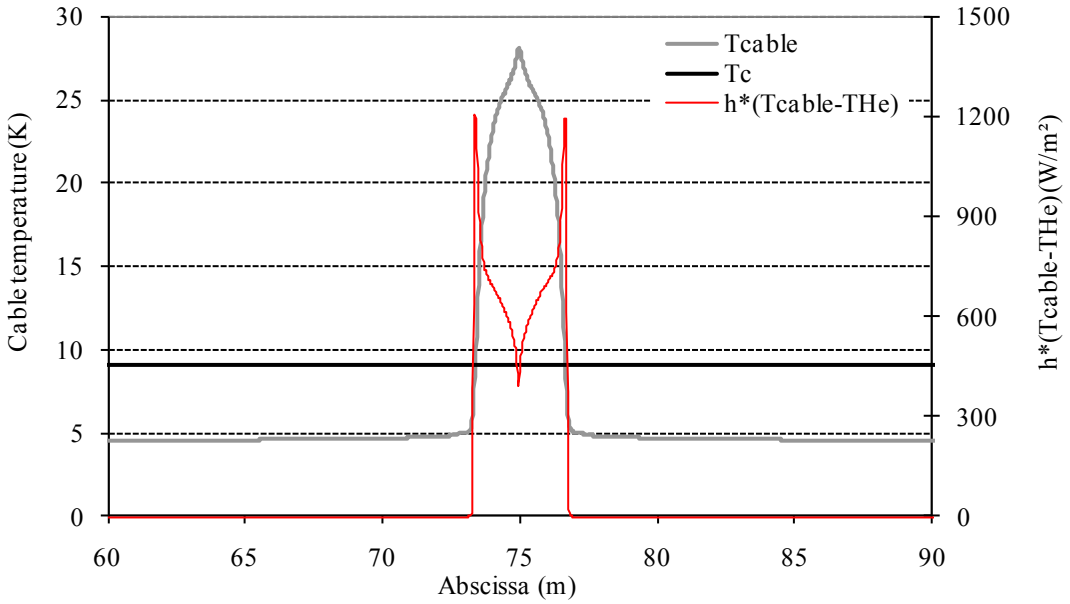

Figure 33: Heat flux depression in vicinity of quenching zone. Here, T_{HE} stands for He_Bundle

4.4. Simulations with the virtual model using Gandalf.

Three simulations have been performed with the 150 m model. The conductor has been discretized with 4000 elements the length of which is 0.0375 m. The inlet pressure is set up at 3 bars and the helium velocity is relevant of the CS conductor (0.1 m/s in the annular region, and 0.9 m/s in the central hole. These values result from thermohydraulic calculation, starting from the CS conductor properties, and a total mass flow of 8 g/s in the pancake).

The conductor is an ITER CS-like conductor, and the power deposition is made on a centred 1 m length (between 74.5 m and 75.5), in 0.1 second. The power injected to initiate the quench is equal to two times the power required to initiate a quench, which does not recover.

The first simulation aims at exploring the influence of the magnetic field, simulating the propagation when the quench is initiated in various turns of the CS.

The second simulation aims at exploring the influence of the current density.

The third aims at investigating the influence of the heat deposition length at quench initiation.

4.4.1. Influence of the magnetic field on the propagation

The cable properties (B, I, strain) are set up in order to simulate the behaviour of a quench happening during the initial current plateau, just before the start of a plasma discharge. The results are shown in Figure 34 and Table 9 for turns 1 to 4, and 13 in terms of normal length, highlighting that the quench velocity is maximum for the maximum magnetic field corresponding to the minimum temperature margin. This trend is similar of course to the one observed for dry magnet (see Eq 3.).

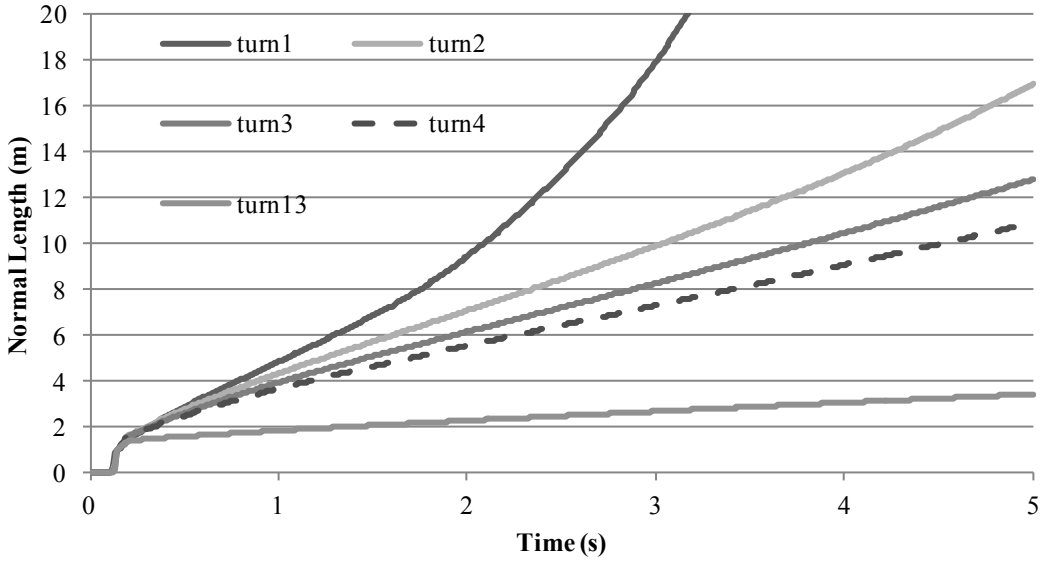

Figure 34: Normal zone as a function of time for different turns of the CS ITER coil (150 m virtual model).

Table 9: Parameters of 5 simulations of the CS ITER coil corresponding to different turns at J=84.5 A./mm2

	1turn	2turn	3turn	4turn	13turn
Injected Power (W/m)	4820	8920	12000	14200	28000
Field (T)	12.17	11.26	10.34	9.43	1.20
T_{ma} (K)	1.34	2.19	2.99	3.76	10.29
T_{c0} (K)	9.05	9.65	10.24	10.83	15.94
T_{cs} (K)	5.64	6.48	7.29	8.06	14.59
Gandalf (m/s)	3.98	3.33	2.57	2.10	0.63

In the table above, T_{ma} is the temperature margin, defined such as:

$$T_{ma} = T_{cs} - T_{op}$$

For comparison, the propagation velocity in case of adiabatic conditions has been plotted in Figure 35. It can be seen that there is a linear dependency between Gandalf velocity and the adiabatic velocity. Due to formula Eq. 3, the adiabatic velocity is tending to a limit when the magnetic field is decreased to zero. In Figure 35, the proportionality coefficient is coming from the automatic fit.

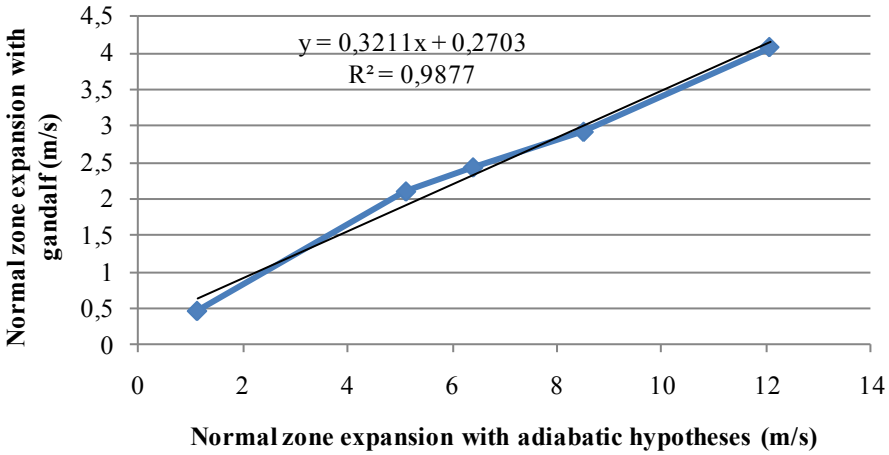

Figure 35: Comparison of simulated velocity with Gandalf and adiabatic velocity for different turns of the CS ITER coil (150 m virtual model)

4.4.2. Influence of the current on the propagation

The same procedure has been applied to estimate the influence of the current at constant magnetic field, as summarized up in the following Table 10 and Figure 36. In Table 10, in "Gandalf" row, the time derivative of the normal zone expansion is given. In "adiabatic" row, the velocity is given by Eq. 3. The current variation impacts T_{cs} and J in formula Eq 3.

Table 10: Parameters of 6 simulations corresponding to different currents at constant magnetic field 12.18 T

Current % of nominal	100%	90%	80%	60%	50%	30%
Current Value (A)	38046	34241	30437	22827	19023	11413
Injected power (W/m)	6000	7200	8600	10900	11900	15400
Tcs (K)	5.63	5.85	6.07	6.53	6.78	7.34
Tma (K)	1.34	1.55	1.77	2.23	2.48	3.04
Gandalf (m/s)	3.98	3.09	2.50	1.66	1.27	0.56
Adiabatic (m/s)	11.89	9.44	7.39	4.55	3.50	1.82

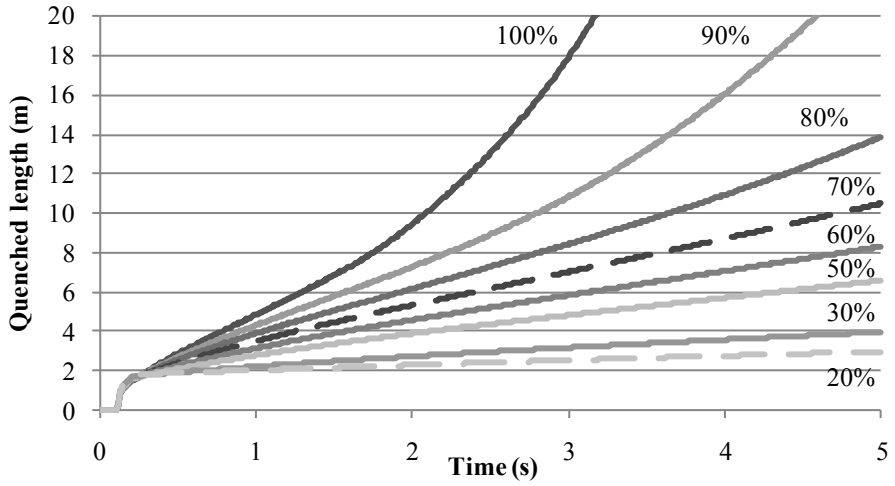

Figure 36: Normal zone as a function of time for different Ratios of the nominal current, at constant magnetic field (150 m virtual model)

It can be noticed again that the simulated velocity is almost proportional to the adiabatic velocity (Figure 37).

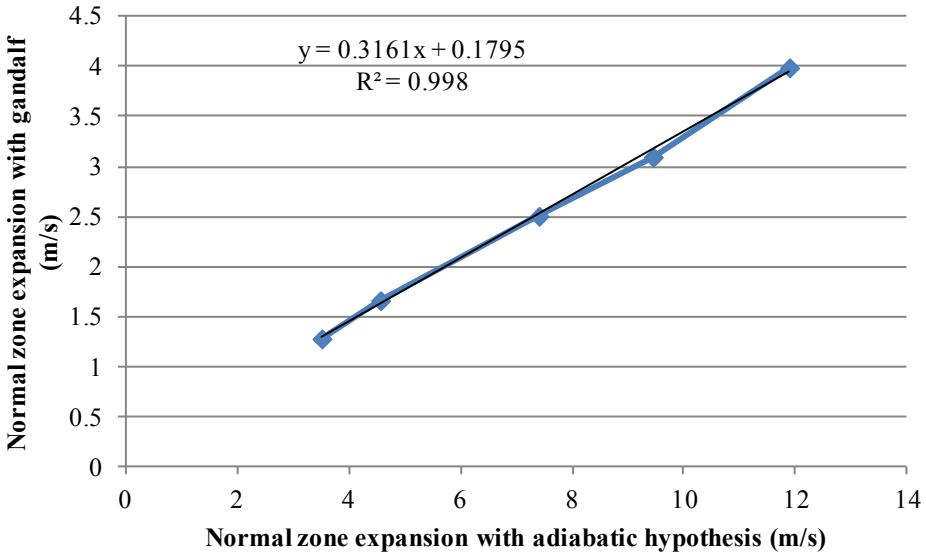

Figure 37: Comparison of simulated velocity with Gandalf and adiabatic velocity for different currents of the CS ITER coil (150 m virtual model)

4.4.3. Influence of the power deposition length for quench initiation

For the simulations the results, which are shown above, a power deposition length of 1m was used, which has been arbitrarily selected as the "standard" quenched initial region. In Figure 38, both the magnetic field and the current are maintained at the same value (100%), while the deposition length varies from 1 m to 10 m. It can be seen from Gandalf that the initial quenched length has a strong influence on the velocity of the quench propagation.

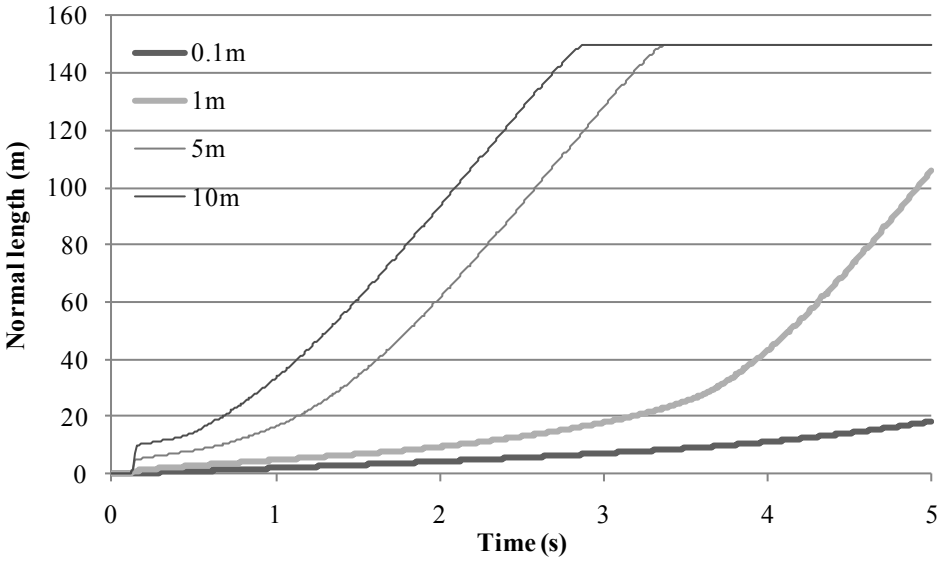

Figure 38: Normal length as a function of time according to the initial quenched length

4.5. Comments on some experimental studies on quench propagation in CICCs

It is not possible here to come back on all the results regarding Quell. This is practically the only paper entering in details about quench propagation in CICCs. One of the most important results regarding Quell is presented in [47] and illustrated in Figure 39.

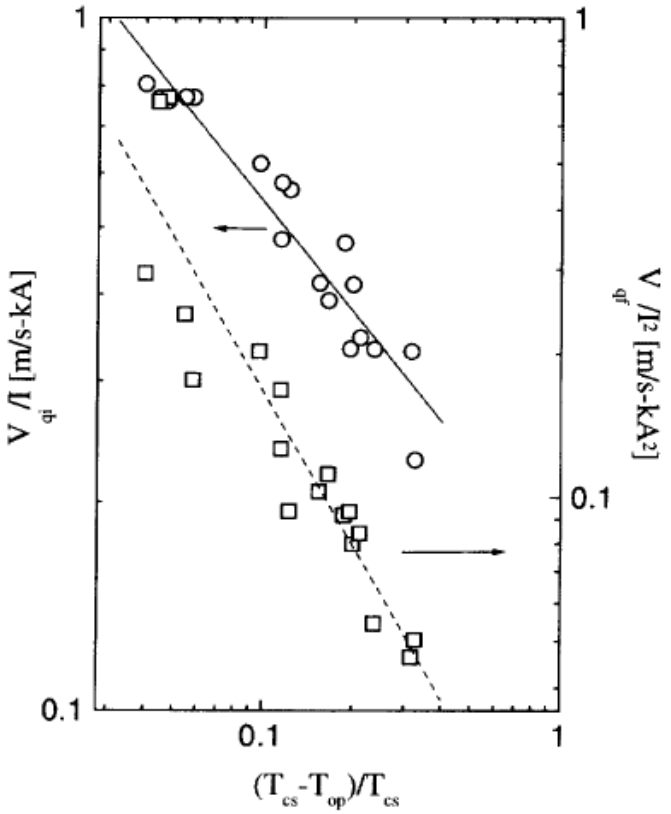

Figure 39: The initial and final values of the quench propagation velocity: ○, early times; □, late times. Continuous and dashed lines represent the fit with Eq 6.

Compared to the ITER CS conductor, the Quell conductor is scaled down by a factor 1/5 with a typical current of 12 kA. The porosity of the central channel is 14.5 %. The total length exposed to the Sultan magnetic field is about 100 m. The initial quenched zone in case of Fig. 10 is about 1.2 m, triggered by a resistive heater wound on the conductor jacket. The following equations are the fit of the velocities observed respectively at early and late times in the quell Experiment. One should notice the dependency, which exists between the quench propagation velocity and the temperature margin.

$$v = I.a\left[\frac{T_{cs}}{T_{cs}-T_{op}}\right]^{0.5} \qquad v = I^2.a\left[\frac{T_{cs}}{T_{cs}-T_{op}}\right]^{1} \qquad \text{Eq. 6}$$

The main conclusion of the study is that there are two regimes: a first one where the velocity is very close to the dry adiabatic velocity, and a second one with a velocity proportional to I^2, observed in the late times, according to the Eq. 6.

The velocities observed from the Gandalf simulations presented above do not match the results of Quell, the velocities at early times are slower than the adiabatic one.

In the CS insert coil, velocities comparable with the Gandalf simulations have been obtained. The quenches were triggered by an inductive heater on a very short length of 109 mm [82]. The corresponding quench propagation in this case is slower than the adiabatic case. The results which are shown in this thesis are coherent with the results of the CS insert, despite the fact that the CS insert conductor is at a reduced scale.

4.6. Conclusion on quench propagation in the ITER CS conductor

The Cable-In-Conduit cannot be considered as a dry conductor as the helium section represents a third of the total section of the conductor. In case of an initial quenched zone of 1 meter, the simulations made with Gandalf 2.1 coupled to Flower 2.1 converge however to quench velocities approximately three times less than the adiabatic velocity, as visible in Figure 40, when the magnetic field is varied to simulate turns.

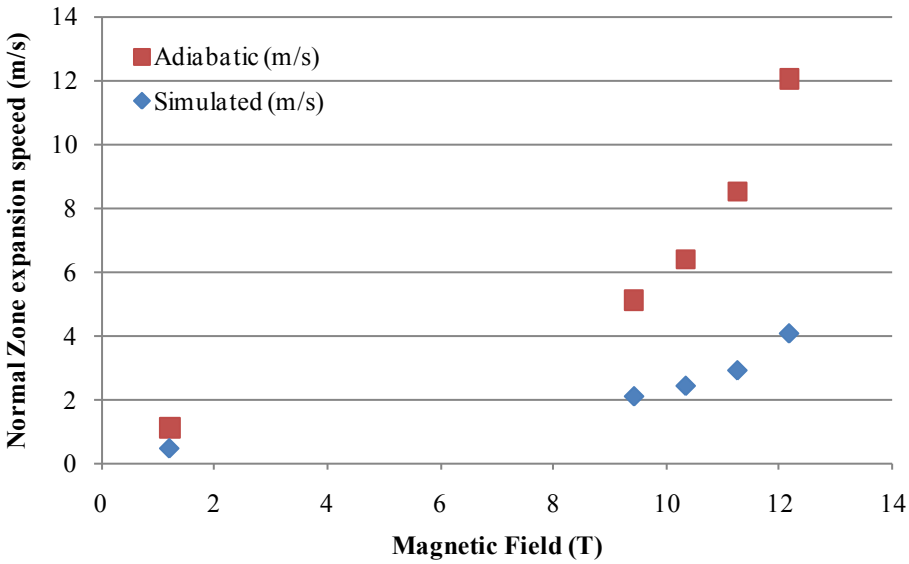

Figure 40: Influence of magnetic field on quench velocity, given by Gandalf model and from adiabatic model

It has been also shown that the quench propagation is in reality very depending on the length of the initial quenched zone as it is visible in Figure 41.

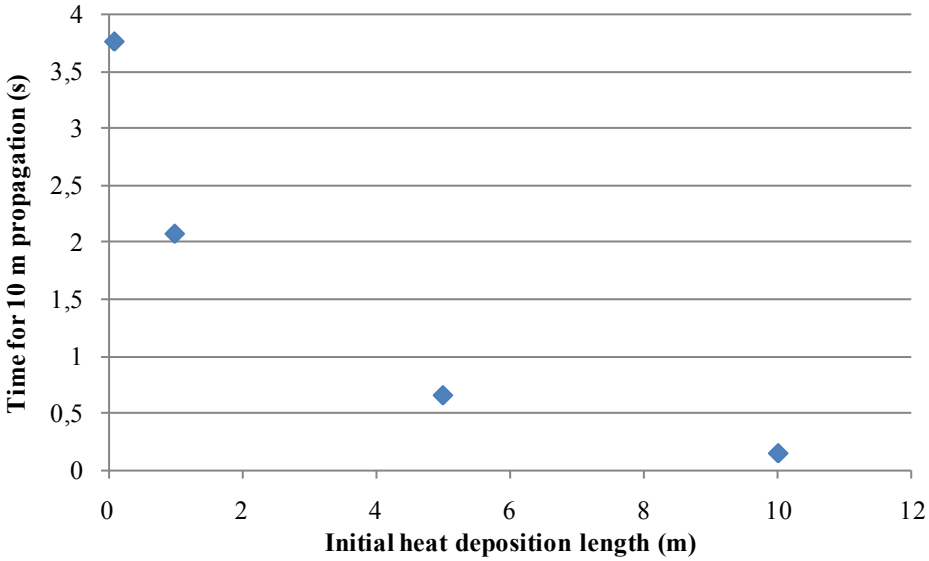

Figure 41: Influence of the initial heated length on quench velocity

The quench velocity at early time of the quench is determining for the quench propagation time τ_p to reach a given value of detection voltage difference U_t.

It has been seen, in case of the CS conductor, that the quench velocity is around the third of the adiabatic velocity, which is favourable to quench detection. This value is found for maximum current and magnetic field (minimum temperature margin, highest probability for the appearance of a quench).

However it has to be pointed out that this result is not universal, the quench propagation velocity in a CICC is certainly linked to the size of the central hole in particular.

It is probably difficult to establish analytical correlations for the quench velocity and Gandalf is therefore a very useful tool.

Thanks to the virtual model it was also possible to see that there is not a unique quench propagation velocity within a coil. There can be an “adiabatic” velocity which is certainly correlated to a power deposition length larger than 1 m.

It is therefore necessary for the quench detection designer to select the reference configuration for the quench, which is the most likely to happen during the quench detection study.

For all the ITER coils a quench at high field was selected because it is at this point that the temperature margin is the lowest.

It has been considered that the energy of the quench initiation is deposited at constant power during 0.1 s, which is the typical time constant of plasma disruption. The plasma disruption is linked to a very fast decrease of the plasma current in a time lower than 10 ms, resulting in magnetic field variations and corresponding ac losses in the coil conductors. This magnetic field is however “filtered” by the time constant of the vacuum vessel, which is in the range of 100 ms.

The reference initial quenched length for the selection of the detection is depending on the length of the conductor at high field, which can be affected by the disruption. In general (but not for the CCs) this length is larger than 10 meters. Conservatively a length of one meter has been considered for the heat deposition initiating the quench.

5. TrapsAV and inductive disturbances in tokamaks

The quench has to be detected fast enough to avoid permanent damage of the transiting magnet. The electrical signature of the quench has good chances to give this indication in time. Chapter 5 explains how perturbations inherent to the use of a tokamak can be estimated, and their origin. TrapsAV is the code which has been used to select the detection threshold.

As presented in the first chapters of this thesis, especially in 1.1.4, the magnetic configuration of a tokamak is complex and varying along time. In consequence of the varying magnetic fluxes collected by the various magnets, appearance of electromotive forces can be observed. The estimation of such electromotive forces is crucial to define a detection threshold for the quench.

5.1. Introduction to the inductive electromotive forces in the tokamak magnets

Moreover, the magnets are strongly coupled to each other, coupled to passive structures like the vacuum vessel, and coupled to the plasma. Basically, the voltage U_{PSi} appearing across a magnet power supply PSi can be expressed as follows:

$$U_{PSi}(t) = \left(R_{cl} + R_{joints-i} + R_i(t)\right) I_i(t) + L_i \frac{dI_i(t)}{dt} + \sum_{j=1, j\neq i}^{j=N_{magnets}} M_{ij} \frac{dI_j(t)}{dt} + I_{plasma}(t) \frac{dM_{i-plas}(t)}{dt} + M_{i-plas}(t) \frac{dI_{plasma}(t)}{dt} + \sum_{j_{vv}} M_{ij_{vv}} \frac{dI_{j_{vv}}(t)}{dt}$$

In this equation, the resistances, expressed in ohms [Ω]:

- $R_{joints-i}$ corresponds to the sum of the joints resistances of the magnet.
- R_{cl} is the resistance of the current leads
- $R_i(t)$ is the resistance of the conductor. In absence of quench, the resistance is very low, and in practice, considered as being null. When a quench occurs, the resistance increases and depending on the sign of the current, it results in a positive of negative variation of the voltage across the conductor in which the quench occurs.

This equation is applied to a single magnet, therefore, the following subscripts and values must be defined:

- $N_{magnets}$ is the number of magnets in the tokamak. In ITER, as described previously, $N_{magnets}$ should comprise the TF, CS, CC, and PF systems. In this case:

$$N_{magnets} = 18 + 6 + 18 + 6 = 48$$

- The i index is the magnet index, depending on the context in which this equation is used.
- The j index stands for another magnet

The following coupling factors are also involved, expressed in henrys [H]:

- M_{ij} is the mutual inductance between i and j.
- L_i is the self inductance of the magnet i.
- $M_{i-plas}(t)$ is the mutual inductance of the plasma with magnet i. It must be noticed that since the plasma shape and position vary along time, the mutual inductance varies as well.
- M_{ijvv} is the mutual inductance of the element j_{vv} , part of the passive structures, with the magnet i. This factor will be described in details in a later paragraph. The distribution of the current in the passive structures is also varying along time.

Finally, the following currents, in amps [A] must be taken into account

- $I_i(t)$ is the current in the magnet i.
- $I_j(t)$ is the current in the magnet j.
- $I_{plasma}(t)$ is the plasma current.
- $I_{jvv}(t)$ is the current in the element j_{vv}, part of the passive structures.

The equation given above shows the impact of all the components taken into account in the presented study. Nevertheless, they do not have the same impact level regarding quench detection. In order to simplify the writing of the following paragraphs, the equation can be split into two parts:

$$U_{PSi}(t) = U_{cl-i}(t) + U_i(t)$$

And in this equation, the following voltages can be distinguished:

- $U_{cl\text{-}i}(t)$ is the voltage produced by the current leads
- $U_i(t)$ is the voltage along the conductor only

Hence, calling $U_{joints\text{-}i}(t)$ the sum of the voltages produced by the joints, the voltage across a magnet is finally:

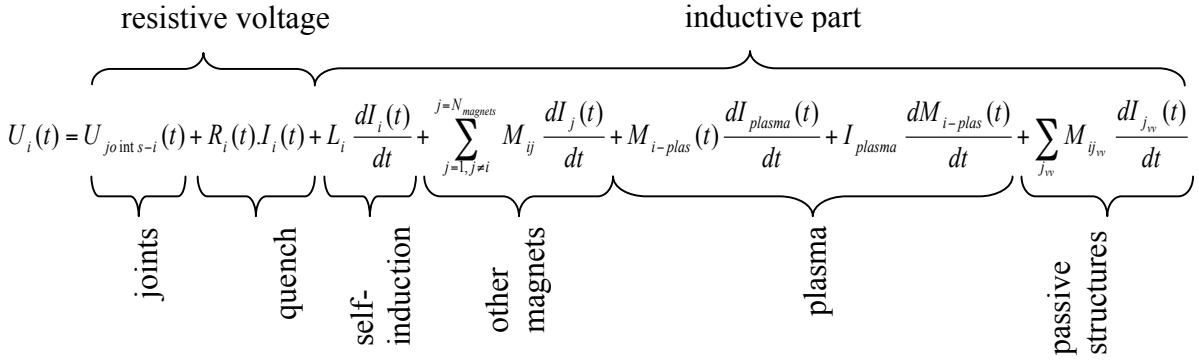

This last equation can be divided, into two parts:

- The resistive contribution, made by the resistance of the joints and the quench.
- The inductive part, made by the self-inductance and the coupling with the other contributors to the magnetic field.

Taking the CS as an example, on the one hand, the voltages expected across one module terminals are estimated up to 30 kV as a maximal value (and in case of fault). Studies of the maximum values are presented for each magnet in [36], [37], and [38].

On the other hand, in section 4.4 it is demonstrated that a typical quench can take a significant time to propagate. Considering that the voltage and the normal length are proportional (as it will be demonstrated later), reaching a few tenths of volt can take a significant time.

The conclusion is that due to the inductive part (around 12 kV during normal operation for the CS) which largely overwhelms the resistive one (due to the quench, below one volt), a direct observation of the signals $U_i(t)$ across each magnet cannot allow a systematically accurate quench detection (and reaction to it) within the detection and action time, τ_{da}, introduced in 3.5.. Indeed, a small voltage variation (around 1/12000) can be attributed to measurement errors.

In order to elaborate an efficient and reliable quench detection system, it is required to simulate in details the electromotive forces appearing during a plasma discharge across ITER magnets or their subcomponents. It is however not always possible (as explained in chapter 7). The objective of this examination is to propose a compensation of the inductive part of the observed voltage across a section of the magnet. This compensation will ideally cancel the inductive part of the voltage, and thus, make visible the resistive part of the voltage, due to the quench, as illustrated below in Figure 42 in an academic case.

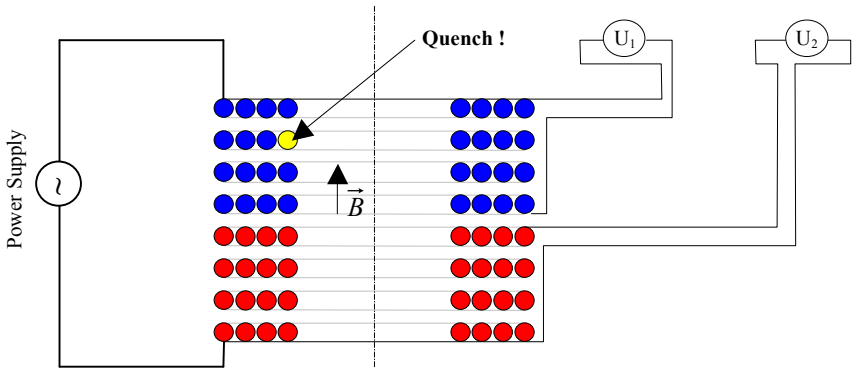

Figure 42: Typical balance of a solenoid halves

With such decomposition, U_1 is the voltage across one half of the solenoid, and U_2 is the second half. Each voltage can be decomposed, into two parts, an inductive part $U_{ind(i)}$, and a resistive part U_Q, in case of quench. According to Figure 42, only the first part is quenching, thus, it can be written:

$$U_1(t) = U_{ind(1)} + I(t).R_{quench}$$
$$U_2(t) = U_{ind(2)}$$

Considering the symmetry of the solenoid, it is reasonable to admit that:

$$U_{ind(1)} = U_{ind(2)}$$

Consequently, if we define $\Delta U(t)$ such as:

$$\Delta U(t) = U_1(t) - U_2(t)$$
$$\Delta U(t) = I(t).R_{quench} = U_Q(t)$$

The quench becomes visible once $\Delta U(t)$ has reached the detection threshold.

It has to be mentioned, that the compensation of signals is not the only possibility to detect a quench. Various systems have been designed for magnets used in various contexts, using different physical measurements, or even comparison of measured voltage with predicted

voltage. Due to the characteristics of ITER, (high voltage, electromagnetically noisy environment, reliability issues) comparison of elements has been chosen.

5.2. Calculation of inductive perturbations: TrapsAV

As described in the previous paragraphs, the modelling of all the contributors to the magnetic fields and time-varying fluxes responsible for the appearance of the induced electromotive forces present in the tokamak, is not trivial and requires the design and use of a dedicated software, TrapsAV.

In this section, the code Traps is presented, and a few applications are mentioned as examples. Then, the evolution of this code is presented, with its additional function used for quench detection studies purpose. Finally, the tests performed in order to qualify the code are presented.

5.2.1. Traps, a CEA code derived from the American code, EFFI

TRAPS or Traps (TRApeze, Rectangle and Scenarios) is a code developed in CEA (P. Hertout), and inspired by the code EFFI, presented in [39], designed to answer to several questions and issues related to magnetic fields. Its extension will be described in section 5.3

- Helping the dimensioning of the superconducting conductor constituting the coils
- Calculating Lorenz forces resulting from the magnetic field and helping a correct dimensioning of the structures and of the insulation
- Calculating the losses induced by field variations during plasma scenarios and causing eddy current losses in the structures, coupling current and hysteretic losses in the superconducting conductors

5.2.2. Method for magnetic field calculation in the Traps code

As said in the previous chapters, the magnetic systems of a tokamak are complex but as it is presented in Figure 14, it can be however seen that the systems are constituted of coils with rectangular sections and with uniform current density. Two sorts of elements can be distinguished for modelling:

- Straight conductor and arc of circles (TF and CC)

- Complete circles (PF and CS)

These are the basic conductor current elements considered in TRAPS code:

Contrary to what exists in many other codes, there is no calculation by finite element in TRAPS. The code is based on the use of the Biot and Savart law. The elementary magnetic field created at point P by a current of density at point M of the conductor j(M) in the differential element volume dM by Biot and Savart law is:

$$\overrightarrow{d\mathrm{B(P)}} = \frac{\mu_0}{4\pi} \frac{PM \times \overrightarrow{\mathrm{j(M)}}}{\mathrm{PM}^3} \mathrm{dM}$$

The magnetic field created at point P by a current of density j(M) circulating in a given volume Vol can be expressed under the form of a triple integral presented in the next paragraph.

5.2.3. Integration of Biot and Savart law over the conductor volumes.

Based on an idea developed for the EFFI code [39], the integration can be analytically carried out in the section Sec of the conductors if the section is symmetric trapezoidal (or rectangular). For curved conductors the integration along the conductor length is numerically carried out while for straight conductors an analytical calculation is again possible.

In comparison with finite element codes, this way to proceed makes the calculations extremely precise and also extremely fast.

$$\overrightarrow{B_{tot}(P)} = \frac{\mu_0}{4\pi} \int_{Long} \int_{(Sec)} \frac{\overrightarrow{PM} \times \overrightarrow{j(M)}}{PM^3} dM$$

For the curved conductor (arc of circle or complete circle), the three components of the magnetic fields are the following:

$$\begin{cases} \mathrm{B_x}(P) = \dfrac{\mu_0 I}{16\pi ab} \displaystyle\int_{\theta_1}^{\theta_2} d\theta \int_{R-a}^{R+a} \rho\, d\rho \int_{-b-k(\rho-R)-Z}^{b+k(\rho-R)-Z} \frac{-z\cos\theta\, dz}{(\rho^2 + r^2 + z^2 - 2\rho r\cos\theta)^{3/2}} \\ \mathrm{B_y}(P) = \dfrac{\mu_0 I}{16\pi ab} \displaystyle\int_{\theta_1}^{\theta_2} d\theta \int_{R-a}^{R+a} \rho\, d\rho \int_{-b-k(\rho-R)-Z}^{b+k(\rho-R)-Z} \frac{-z\sin\theta\, dz}{(\rho^2 + r^2 + z^2 - 2\rho r\cos\theta)^{3/2}} \\ \mathrm{B_z}(P) = \dfrac{\mu_0 I}{16\pi ab} \displaystyle\int_{\theta_1}^{\theta_2} d\theta \int_{R-a}^{R+a} \rho\, d\rho \int_{-b-k(\rho-R)-Z}^{b+k(\rho-R)-Z} \frac{(\rho - r\cos\theta) dz}{(\rho^2 + r^2 + z^2 - 2\rho r\cos\theta)^{3/2}} \end{cases}$$

with k, a parameter related to the trapezoidal shape of the cross section

The integration is carried out analytically in z and ρ and numerically in θ. The following Figure 43 shows the parameterization with the notation used in the calculation of an arc with a trapezoidal cross-section.

In this set of equations, a is the distance between the centre of the cross section and the inner edge of the cross section (or outer edge), ρ is the radius of the arc, R and Z are the coordinates of the centre of the arc (cylindrical system), μ_0 is the magnetic constant, and theta 1 and 2 are the angular extensions of the arc.

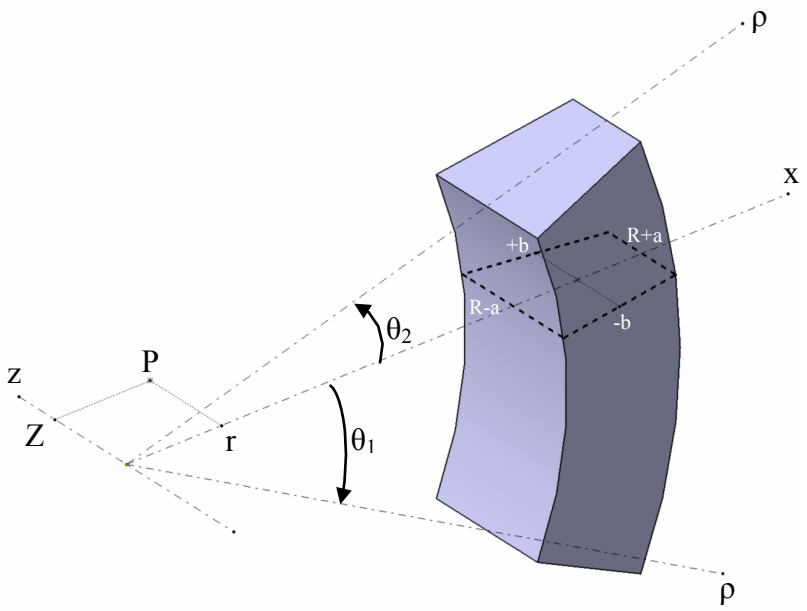

Figure 43: A curved conductor (arc), with its trapezoidal cross-section

For a straight conductor, the notation used in the calculation is presented in Figure 44. The three components of the magnetic fields are the following:

$$\begin{cases} B_x(P) = \dfrac{\mu_0 I}{16\pi ab}\displaystyle\int_{y_1}^{y_2} dy \int_{-a}^{+a} dx \int_{-b-kx-Z}^{b+kx-Z} \frac{-zdz}{((x-X)^2 + y^2 + z^2)^{3/2}} \\ B_y(P) = 0 \\ B_z(P) = \dfrac{\mu_0 I}{16\pi ab}\displaystyle\int_{y_1}^{y_2} dy \int_{-a}^{+a} dx \int_{-b-kx-Z}^{b+kx-Z} \frac{(x-X)dz}{((x-X)^2 + y^2 + z^2)^{3/2}} \end{cases}$$

In this equation, y_1, y_2, a, b, and k are respectively the geometrical descriptors of the conductor, and its cross section. X and Z (associated again with y_1 and y_2) define the position of the point where the field is calculated. μ is the magnetic permeability of the vacuum.

The integration is carried out entirely analytically.

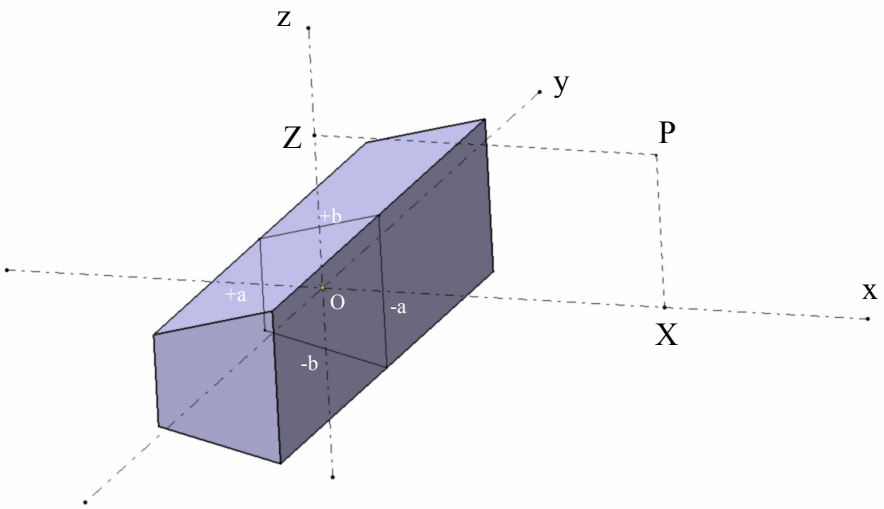

Figure 44: A straight conductor with a point P of calculation

5.2.4. Practical applications of Traps

- A good example of the use of the Traps code is the calculation of the magnetic field created by the TF system of ITER in its two successive versions of 1996 and 2000.

  The calculation has been done along the conductors of the TF coils, looking for the maximum magnetic field to dimension the superconducting material. This has been done with a simplified model with trapezoidal sections for the coils, and with a sophisticated model of the coils sections cut in rectangles in order to better account for the real winding geometry.

  - 5 rectangles for ITER 1996
  - 3 rectangles for ITER 2000

Table 11: Results of Traps code regarding the two versions of ITER

Tokamak	Model	Maximum magnetic field
ITER 1996	1 trapeze	12.66 T
	5 rectangles	12.64 T
ITER 2000	1 trapeze	11.74 T
	3 rectangles	11.71 T

- Traps has been used for the calculation of the toroidal magnetic field in Tore Supra [40]. The objective was a better knowledge of the magnetic field map of Tore Supra. The Traps code was used for the interpretation of magnetic field measurement obtained by extremely precise RMN probes in 1997 in the Tore Supra vacuum chamber.

- Calculation of ac losses in the superconducting conductor of the ITER PF system in the framework of an EFDA contract [41]. The objective of this study was to feed a thermohydraulic code with losses data along the conductor in order to estimate the temperature margin of the conductor

- Additionally, Traps code has been involved in the framework of the TFMC experiment [42]. The objective was, during the current sharing measurements, to make

a very precise magnetic field calculation along the conductor, to estimate the most probable location of the quench induced by the injected warm helium. An estimation of the degradation of the conductor and of the effective strain could be deduced from this estimation. Losses calculation was done over the coil for the thermal evaluation of the coil behaviour during a fast discharge.

The conclusions of these studies can be found in the associated references, and demonstrate the very good accuracy of Traps, and the close results to the experimental measurements.

5.3. Traps upgrade: TrapsAV (Advanced Version)

TRAPS stands for "Trapeze, Rectangles And Plasma Scenarios", and the suffix AV stands for "Advanced Version".

TrapsAV answered the need of estimations related to magnetic fluxes and voltage calculation in the specific case of ITER, taking into account the influence of the passive structures. Y. Takahashi has done similar calculations [43], with another code, and neglecting the passive structures.

The inputs for TrapsAV are basically the currents carried by each conductor, with the geometries of the coils and plasma. The batch of currents is usually called a scenario.

Its two main added features are:

- the possibility to describe in a simple way any passive structure whose carried currents are given as an input
- the possibility to calculate over a whole plasma scenario, the electromotive force produced by the time variation of the fluxes collected by any surface.

In order to meet the requirements needed for the foreseen use of Traps, many functions and upgrades have been made, and Traps has been modified in depth to solve in the most efficient way more complex problems. In the Table below (Table 12), the main new functions and abilities of TrapsAV are listed, or compared to those of Traps.

Table 12: Main features and improvements given by TrapsAV

	Traps	TrapsAV
Passive structures simulation	No	Yes
Plasma simulation	Yes	Yes
Flux and Voltages Calculation	No	Yes
Variable TF current	No	Yes
Additional Calculation points	Yes	Optimized
Post processing	Yes	Enhanced for other softwares
Losses calculation	Yes	Yes

Technically, the predecessor of TrapsAV, Traps, has been modified and modernized in depth, integrating the Fortran90 language. In addition, the structure of the internal data storage has been modified in order to store each result of field calculation. Doing so, any contribution of any magnet can be recalled after a calculation.

At the opposite to Ansys, TrapsAV does not compute the magnetic field over the total mesh of the modelled object which is in the present case, a tokamak in 3D, 360°. One of the main advantages of TrapsAV lies in its capability to run quick simulations with a model, which can be very simple.

5.3.1. Method for electromotive force calculation in TrapsAV

The major modification brought to Traps is the implementation of the electromotive forces induced by the varying magnetic fluxes collected by the surfaces delimited by the windings of the magnets, and associated measurement circuits. It is crucial to note that depending on the context, this electromotive force can be observed as a voltage, for instance, if there is a measurement device across the magnet terminals (it will be the case for the CS and the PF system), or as a change in the current (case of the TF), if the winding or coil is short-circuited.

In this paragraph, the method used to estimate such electromotive forces will be described, and the general assumptions to be done will be described. In order to reduce the time required for the calculation, they are specified in the TrapsAV input data. As for EFFI, the major advantage of Traps lays in its accuracy and calculation speed. According to the input file, a surface, the magnetic flux through which has to be calculated, is discretized, by TrapsAV and the calculation is automatically organized. The magnetic field computed by the TrapsAV core (Traps-like) is stored and processed, then integrated over the surface, and finally time-derived. The process can be described as follows:

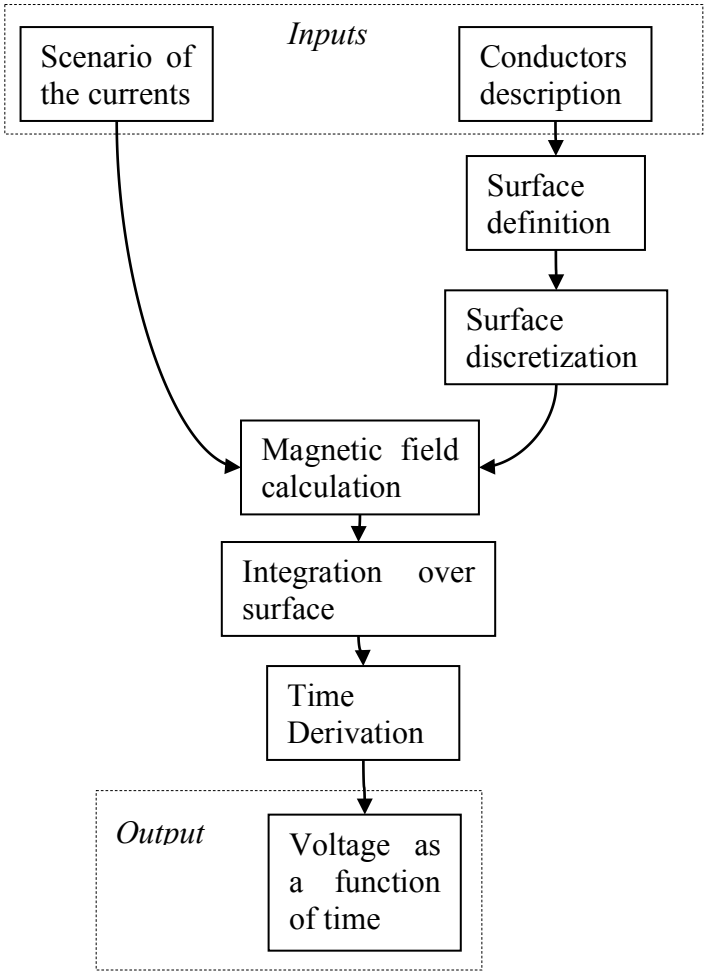

During the acquisition of the data related to the conductors or to the definition of the surface, which collects the magnetic flux, the time-derivative of which is responsible for the appearance of the electromotive force, it is possible to automatically simplify the problem, for instance, specifying that the field is supposed to be axisymmetric. It is also possible to specify in an additional input file, a user surface, defined by a list of points and the perpendicular vector. It is particularly useful for bent surfaces.

Starting from the Maxwell-Faraday equation:

$$\vec{E} = -\vec{\nabla}(V) - \frac{\partial \vec{A}}{\partial t}$$

Integrating this equation along the closed electrical circuit $C=C_{sup}+C_{dev}$, sup and dev standing respectively for superconductor and device, we obtain (see Figure 45):

$$\oint_{C_{dev}+C_{sup}} \vec{E}.\vec{dl} = -\oint_{C_{dev}+C_{sup}} \vec{\nabla}(V).\vec{dl} - \oint_{C_{dev}+C_{sup}} \frac{\partial \vec{A}}{\partial t}.\vec{dl}$$

Taking into consideration that the electric field is null in a superconductor (neglecting AC losses), and calling ε the electromotive force resulting from the Lenz law, it gives:

$$\oint_{C_{dev}+C_{sup}} \vec{E}.\vec{dl} = \int_{C_{dev}} \vec{E}.\vec{dl} = \varepsilon$$

Moreover, on a closed path:

$$\oint_{C_{dev}+C_{sup}} \vec{\nabla}(V).\vec{dl} = 0$$

It gives finally:

$$\varepsilon = -\oint_{C_{dev}+C_{sup}} \frac{\partial \vec{A}}{\partial t}.\vec{dl}$$

Thanks to the Ostrogradski theorem, and calling S the surface the contour of which is the circuit C, it can be written:

$$\varepsilon = -\iint_S \frac{\overrightarrow{dB}}{dt}.\overrightarrow{dS}$$

With $S=S_{sup}+S_{dev}$

This equation can be representative of a circuit such as presented in the Figure 45. In the top drawing, the device is a voltmeter. This voltmeter closes the path, and therefore, this

device measures the electromotive force, we obtain a voltage. This situation will be described in details in chapters 6 and 8.

In the bottom drawing, the circuit is closed by a power supply. The voltage measured is simply the voltage across the power supply, power supply which balances the electromotive force imposed by the time variation of the magnetic flux in the surface S. If this power supply were replaced by a wire (short circuit, unless the voltage caused by the resistance of the wire is significant), the voltage measured would be zero, and the electromotive force would be translated into a current change in the circuit. This case will be discussed in details in chapter 7.

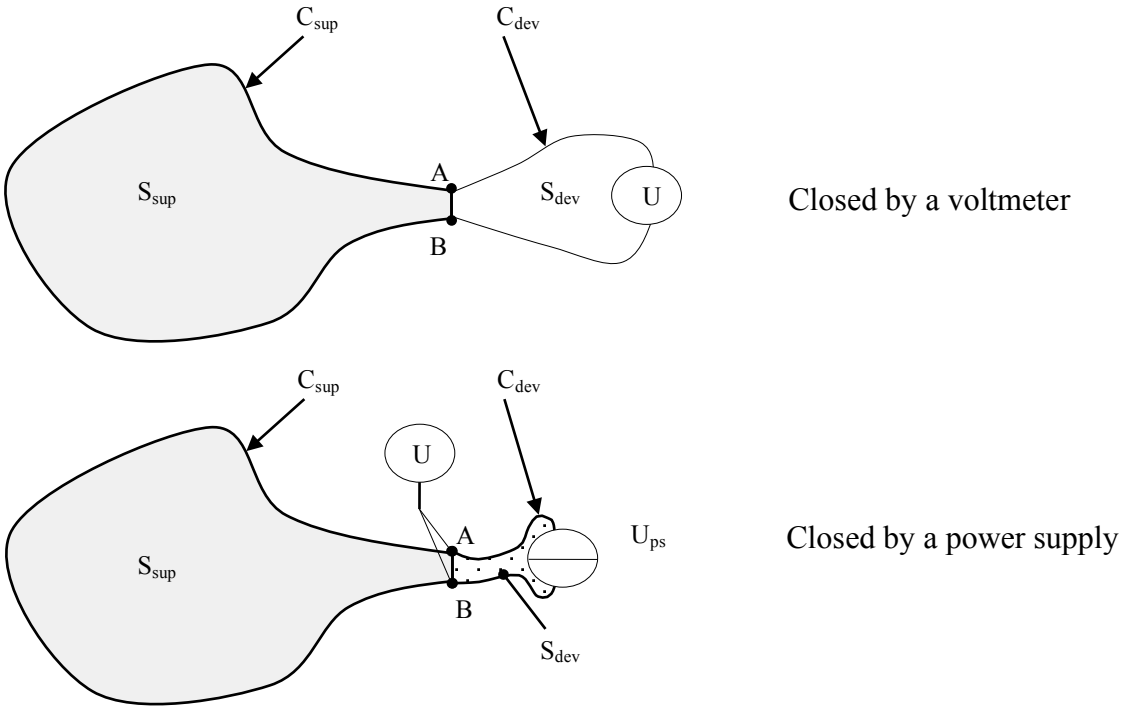

Figure 45: Closed circuit, by a voltmeter, and a power supply

Finally, we obtain, for the upper case of Figure 45, the voltage measured across the superconductor:

$$U = -\frac{\partial \Phi}{\partial t} = -\frac{\partial}{\partial t}\iint_S \vec{B}.\overrightarrow{dS}$$

With U the voltage, and Φ the flux of the magnetic flux B(x,y,z,t) through the surface S. In practice, in TrapsAV, the user has to give directly the parameters of the surface, the resolution of which has a great importance on the accuracy of the results, and can significantly affect the calculation time. A dedicated tool of TrapsAV has been developed to aid the user to build this surface.

a. Voltage calculation for a magnet single turn

The following equations represent the calculations done to calculate the voltage measured across a magnet turn which carries a current I(t), as represented in the following Figure 46.

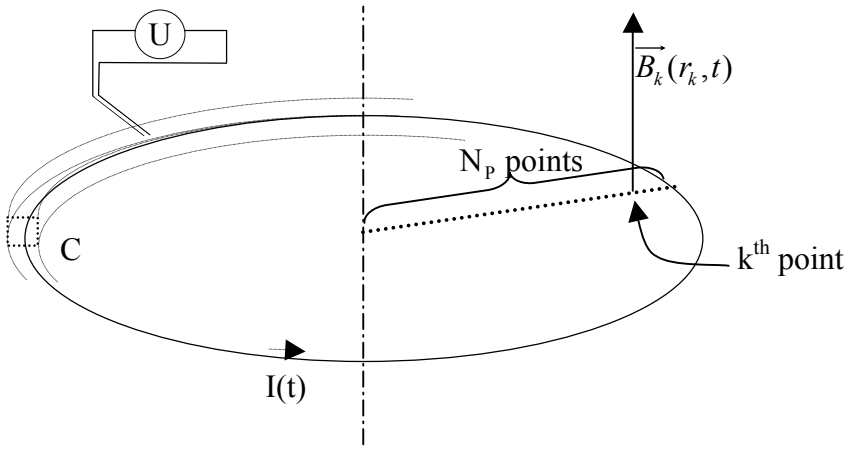

Figure 46: Voltage across a single turn of radius R_N

In this schematic, the conductor has a square cross section, represented in dots. The wires leading to the voltmeter are supposed to be twisted such that there is no flux between the two wires. This is equivalent to considering $S_{dev} = 0$. The voltage displayed in the voltmeter will be:

$$U = \frac{d}{dt}\int_0^{2\pi}\int_0^{R_N} \overrightarrow{B(r,\theta,z,t)}.\vec{n}.r\,dr\,d\theta$$

In the rest of this paragraph, for explanation and simplification purposes, certain assumptions are made, corresponding to the one used for the CS and PF studies, as described in the paragraphs concerning their TrapsAV model. These examples illustrate well the process used for the flux calculation. For the TF coils quench protection studies, TrapsAV has not been used. These assumptions and notations are:

- The surface S with normal $\vec{n}$ is such as $\vec{n} \times \overrightarrow{e_z} = \vec{0}$
- B depends only on the radius, and therefore, can be expressed as follow:

$$\vec{B}(r,z,\theta,t) = \vec{B}(r,t)$$

- The magnetic field with the subscript k is such as:

$$B_k = \overrightarrow{B(r_k,t)}.\overrightarrow{e_z} \quad \text{and} \quad r_k = k \times \frac{R_N}{N_P}$$

With N_P the input of TrapsAV allowing to optimize the accuracy of the calculation. R_N is the radius of the last turn of the pancake.

As explained in section 5.2.1, the magnetic field is provided by Traps, calculated with the geometrical characteristics of the conductors, in 3D. Knowing the details of the plasma discharge scenario in terms of currents, TrapsAV enables to calculate the flux along time. Several options of TrapsAV allow the user to modify and create surfaces involving simplifications of the model, but their use will not be described further in this thesis.

Here the discretization takes place, as it has been done:

$$U = \frac{\partial}{\partial t}\int_0^{2\pi}\left(\int_0^{r_1}\vec{B}(r,t).\overrightarrow{e_z}.r dr + \sum_{k=1}^{k=N_P-1}\left(\int_{r_k}^{r_{k+1}}\vec{B}(r,t).\overrightarrow{e_z}.r dr\right)\right).d\theta$$

Assuming linear interpolation between k and k+1. The field is assumed to be constant between r=0 and r_1.

$$U = \frac{\partial}{\partial t}\int_0^{2\pi}\left(\frac{r_1^2 B_1}{2} + \sum_{k=1}^{k=N_P-1}\left[\frac{B_{k+1}-B_k}{r_{k+1}-r_k}\times\frac{\left(r_{k+1}^{\ 3}-r_k^{\ 3}\right)}{3} + \left(B_k - \frac{B_{k+1}-B_k}{r_{k+1}-r_k}\times r_k\right)\times\frac{r_{k+1}^{\ 2}-r_k^{\ 2}}{2}\right]\right).d\theta$$

Due to the axisymmetry assumption, the integration on the angle can be done directly:

$$U = 2\pi\frac{\partial}{\partial t}\left(\frac{r_1^2 B_1}{2} + \sum_{k=1}^{k=N_P-1}\left[\frac{B_{k+1}-B_k}{r_{k+1}-r_k}\times\frac{\left(r_{k+1}^{\ 3}-r_k^{\ 3}\right)}{3} + \left(B_k - \frac{B_{k+1}-B_k}{r_{k+1}-r_k}\times r_k\right)\times\frac{r_{k+1}^{\ 2}-r_k^{\ 2}}{2}\right]\right)$$

The surface is discretized in N_p annular surfaces of index k in the formula above. The magnetic field B_k and B_{k+1} at the inner and outer radii r_k and r_{k+1} of each surface, calculated by Traps, is interpolated and integrated. Except for k=1, a linear interpolation is assumed for the magnetic field.

In addition, it is worth noting that in a tokamak, it is often useful knowing, in addition to the voltage across one turn, the voltage across a whole pancake. It is recalled that a pancake is a row of turns, located on the same plane perpendicular to the coil axis, as showed in Figure 47.

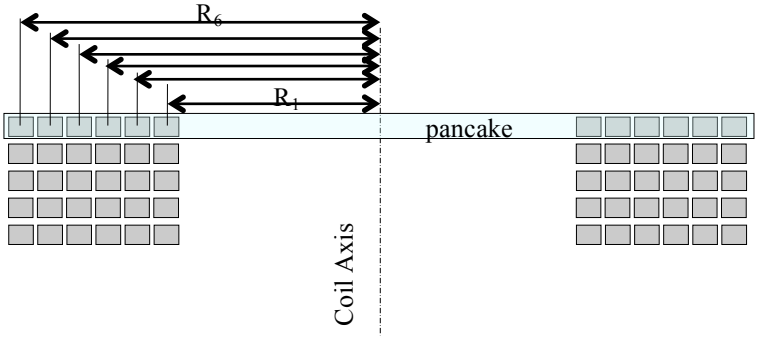

Figure 47: Coil with 5 pancakes and 6 turns

b. Voltage across a pancake (Figure 47)

The voltage U across one pancake can be seen as being the sum of the time derivative of the flux collected by each of the N turns of the pancake, it can also be observed that this electromotive force U is equal to N times the flux collected by the first turn, plus N-1 times the flux collected by the surface between turn 1 and turn 2, etc … as showed in Figure 48.

If Φ is the flux collected by the pancake, it can be written:

$$U = -\frac{\partial \Phi(t)}{\partial t}$$

This voltage can be expressed as the sum of the fluxes Φ_i collected by each turn i with a radius R_i:

$$U = -\frac{\partial}{\partial t}\left(\Phi_1 + \Phi_2 + \ldots + \Phi_{N-1} + \Phi_N\right)$$

On the other hand, calling $\Phi_{i/i+1}$ the flux collected by the area located between the turns i and i+1, the electromotive force U across one pancake can be expressed according to the following relationship:

$$U = N.\frac{\partial \Phi_1}{\partial t} + (N-1)\times\frac{\partial \Phi_{1/2}}{\partial t} + \ldots + (2)\times\frac{\partial \Phi_{(N-2)/(N-1)}}{\partial t} + (1)\times\frac{\partial \Phi_{(N-1)/(N)}}{\partial t}$$

The following Figure 48 illustrates these equivalent decompositions.

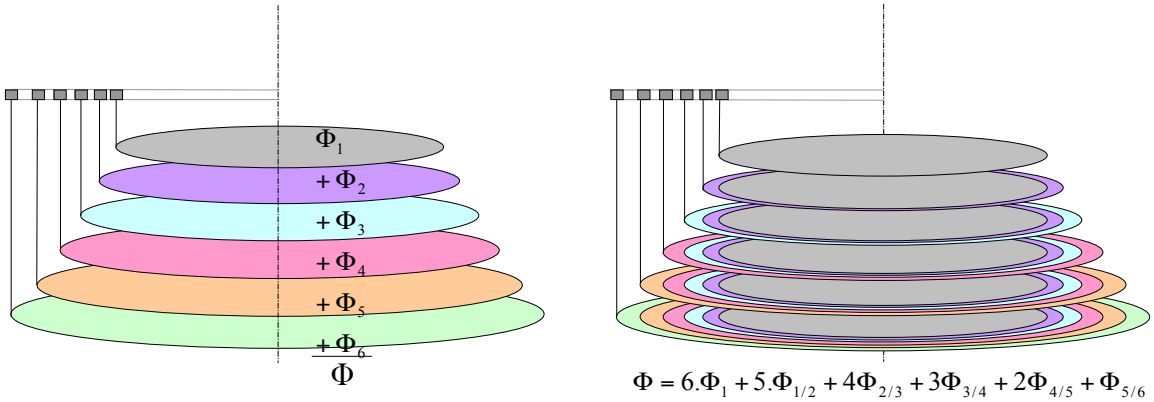

Figure 48: Decomposition of the flux collected by a succession of turns

The implementation of the right-hand side decomposition (visible in the figure above) in the TrapsAV code reduces strongly the calculation time. In addition, it can be seen in the ITER documentation, that the circuit which makes the voltage measurement makes, as shown before, a 360° turn with a radius R_i collects a flux Φ_i such that:

$$\Phi_i = \int_0^{2\pi}\left(\int_0^{R_i}\vec{B}(r,t).\vec{e_z}.rdr\right).d\theta$$

Assuming axisymmetry for the current field map, a turn which makes only f×360°, with f varying between 0 and 1 will collect:

$$f_i\Phi_i = f_i\times\int_0^{2\pi}\left(\int_0^{R_i}\vec{B}(r,t).\vec{e_z}.rdr\right).d\theta$$

Consequently, the coefficients f_i allow a finer description of a pancake than with entire turns. Taking into account the change of turns, and incomplete turns, the voltage U becomes:

$$U = \frac{\partial}{\partial t}\left[\left(f_1\Phi_1\right)+\left(\Phi_1+f_2\Phi_{1/2}\right)+\left(\Phi_1+\Phi_{1/2}+f_3\Phi_{2/3}\right)+\ldots+\left(\Phi_1+\sum_{i=1}^{N-2}\Phi_{i/i+1}+f_N\Phi_{N-1/N}\right)\right]$$

$$U = \frac{\partial}{\partial t}\left[(N-1+f_1).\Phi_1+(N-2+f_2).\Phi_{1/2}+\ldots+f_N.\Phi_{N-1/N}\right] \qquad \textbf{Eq. 7}$$

$$U = \frac{\partial}{\partial t}\left[(N-1+f_1).\Phi_1+\left(\sum_{i=2}^{i=N}(N-i+f_i).\Phi_{i-1/i}\right)\right]$$

Now, referring to Figure 47 for the limit radii R_i (index i refers to the index of the turns, and k refers to the points) involved in the description of the pancake:

$$U = \frac{\partial}{\partial t}\left[(N-1+f_1).\int_0^{2\pi}\left(\int_0^{R_i}\vec{B}(r,t).\vec{e_z}.rdr\right).d\theta+\left(\sum_{i=2}^{i=N}(N-i+f_i).\int_0^{2\pi}\left(\int_{R_{i-1}}^{R_i}\vec{B}(r,t).\vec{e_z}.rdr\right).d\theta\right)\right]$$

$$U = 2\pi\frac{\partial}{\partial t}\left[(N-1+f_1).\int_0^{R_i}\vec{B}(r,t).\vec{e_z}.rdr+\left(\sum_{i=2}^{i=N}(N-i+f_i).\int_{R_{i-1}}^{R_i}\vec{B}(r,t).\vec{e_z}.rdr\right)\right]$$

In TrapsAV, the integration along the variable r is made numerically. Despite the fact that several options in terms of discretization are available, the regular distribution has been used for the studies reported in this thesis. The regular distribution consists in locating N_P points at constant interval over the greatest radius R_N. Consequently, the spatial resolution Δr, and the radius r_k of each point of the distribution can be defined as follow:

$$\Delta r = \frac{R_N}{N_P},\ r_k = k.\Delta r$$

The numerical limits defining whether an interval $[r_k ; r_{k+1}]$ belongs to turn 1 or inter-turn i/i+1, are defined as follows:

$$N_i = k, r_{k-1} < R_i \le r_k$$

Then introducing the discretization, it comes:

$$U = 2\pi\frac{\partial}{\partial t}\left[(N-1+f_1).\left[\frac{r_1^{\,2}B_1}{2}+\sum_{k=2}^{k=N_1}\left(\int_{r_{k-1}}^{r_k}\vec{B}(r,t).\vec{e_z}.rdr\right)\right]+\left(\sum_{i=2}^{i=N}(N-i+f_i).\left[\sum_{k=N_{i-1}+1}^{k=N_i}\left(\int_{r_{k-1}}^{r_k}\vec{B}(r,t).\vec{e_z}.rdr\right)\right]\right)\right]$$

Finally, with the linear interpolation, the calculation of a voltage U across a pancake with N turns, with a resolution of R_N / N_p done in TrapsAV is:

$$\begin{aligned}U = \quad & 2\pi\frac{\partial}{\partial t}(N-1+f_1).\left[\frac{r_1^{\,2}B_1}{2}+\sum_{k=2}^{k=N_1}\left(\frac{B_{k+1}-B_k}{r_{k+1}-r_k}\times\frac{\left(r_{k+1}^{\,3}-r_k^{\,3}\right)}{3}+\left(B_k-\frac{B_{k+1}-B_k}{r_{k+1}-r_k}\times r_k\right)\times\frac{r_{k+1}^{\,2}-r_k^{\,2}}{2}\right)\right] \\ & +2\pi\frac{\partial}{\partial t}\left(\sum_{i=2}^{i=N}(N-i+f_i).\left[\sum_{k=N_{i-1}+1}^{k=N_i}\left(\frac{B_{k+1}-B_k}{r_{k+1}-r_k}\times\frac{\left(r_{k+1}^{\,3}-r_k^{\,3}\right)}{3}+\left(B_k-\frac{B_{k+1}-B_k}{r_{k+1}-r_k}\times r_k\right)\times\frac{r_{k+1}^{\,2}-r_k^{\,2}}{2}\right)\right]\right)\end{aligned}$$

Where the index i stands for the turn index ($1 \le i \le N$), k for the point index (automatically managed by TrapsAV), and where f_i is the fraction of the full turn made by the

conductor at the radius R_i. For instance, if the conductor just makes a half turn on the smallest radius, f_I is equal to 0.5. If the conductor just makes a tenth of the full turn at the largest radius, f_N is equal to 0.1.

5.3.2. Validation of TrapsAV

TrapsAV has been successively validated with respect to a few other codes, including its predecessor, Traps. In this paragraph, the tests performed on TrapsAV are partially described:

- Validation with Boboz, with and without inclusion of the passive structures
- After a previous study led by Y. Takahashi [44] with ITER model.

a. Validation with Boboz

Boboz is a code developed in CEA in the 80's, inspired from EFFI [39], which aims at simply and quickly calculating the magnetic field generated by a collection of coaxial vertical solenoids. It has been validated with EFFI, and therefore, can be considered as reliable. In TrapsAV, a command Genboboz returns files containing in the format of Boboz, the geometries and the currents used for the simulation. As the modification of Traps affected the way elementary data (including arcs and segments data acquisition) were processed, a validation was required, and several tests have been performed using comparisons with Boboz and Traps (older version).

At first, elementary tests have been conducted to check the validity of the field generated by the model elements named FILA used to represent the passive structures. The first test consists in a simulation of a coil divided in 10 pancakes, with 10 turns each. Each turn is modelled by Fila (Figure 49). Then the magnetic field is studied on 100 points, located everywhere around this coil. Then, a coil carrying the same current is simulated with Boboz.

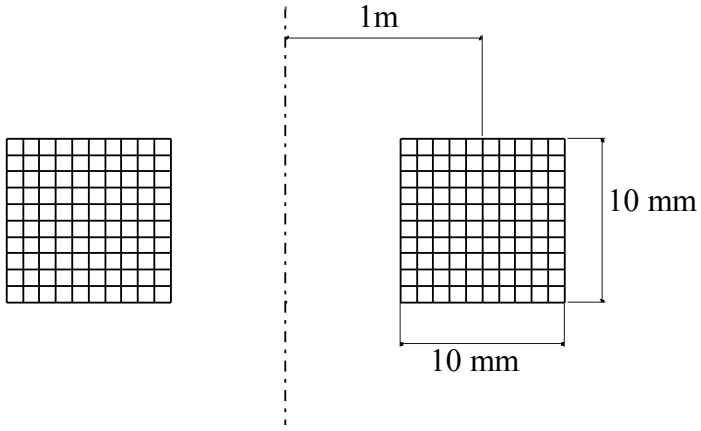

Figure 49: The coil modelled and simulated with 100 filas in TrapsAV

All the data and more tests are available in [77].

The difference between the TrapsAV models using a coil and the model using filas is negligible: values are different only at three points, where the field was minimal, and a decimal was missing. The results can therefore be considered as identical.

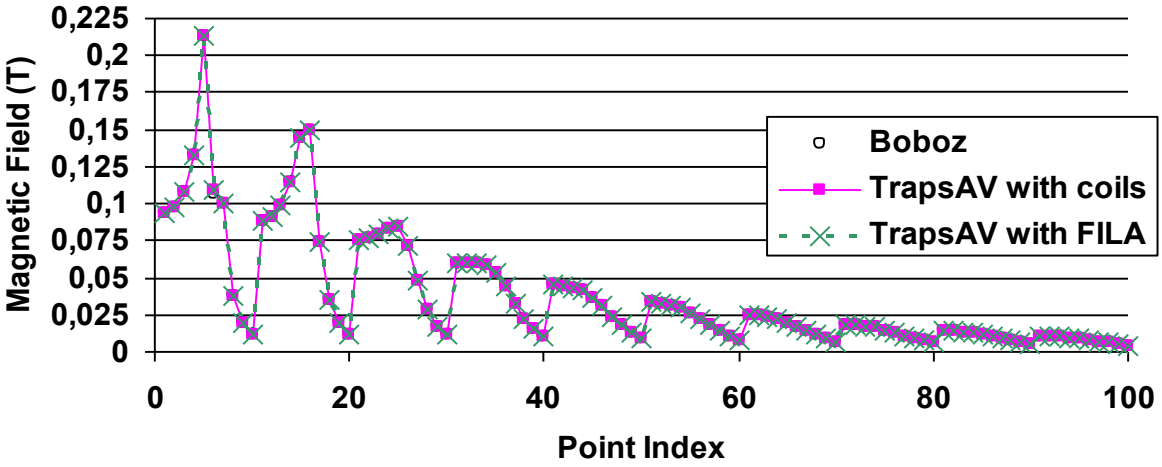

Figure 50: Magnetic field module calculated with Boboz and TrapsAV, using FILA and COILS elements

In Figure 50, the absolute magnetic field calculated with TrapsAV, with former method, with new objects (filas), and Boboz. The results are quasi-identical. The difference Between TrapsAV and Boboz is more interesting, and presented in Figure 51.

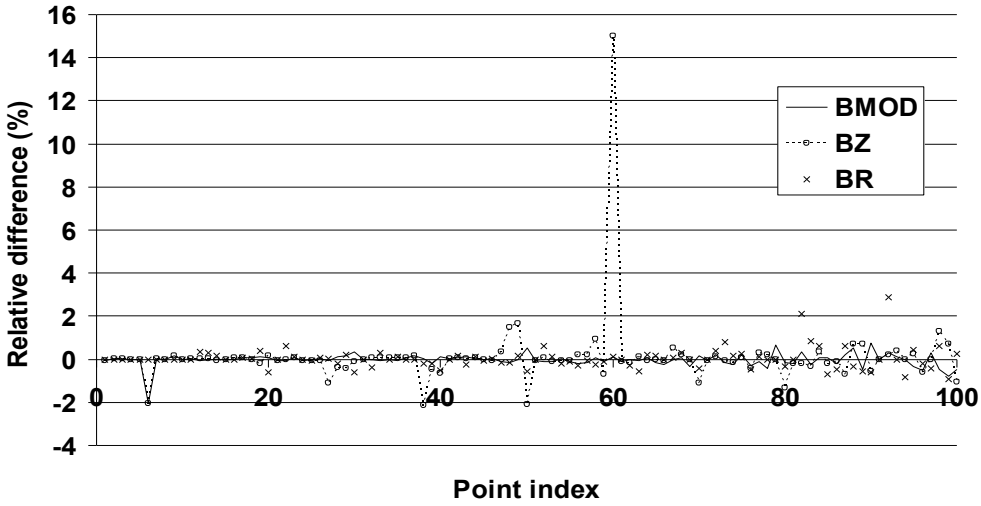

Figure 51: Relative error between TrapsAV with Filas and Boboz

This test shows that at a specific point, which is located far from the coil simulated with Boboz a non-negligible difference is observed. Anywhere else, the maximum error is at maximum 3%, and always at low field (due mainly to the output format of Boboz). It can be concluded that these discrepancies can be ignored, or multiplying the inputs can circumvent the problem by a power of 10, and then divide the output by the same factor.

The most evolved test, is run using the geometry of ITER poloidal system (CS + PF)[15], equilibriums 1, 15, and 36 of Reference scenario v1.10. In the following Figure 52, the dots represent the calculation points used for the validation, located on CS1U, PF1 and PF4. The detailed procedure and results are presented in [77].

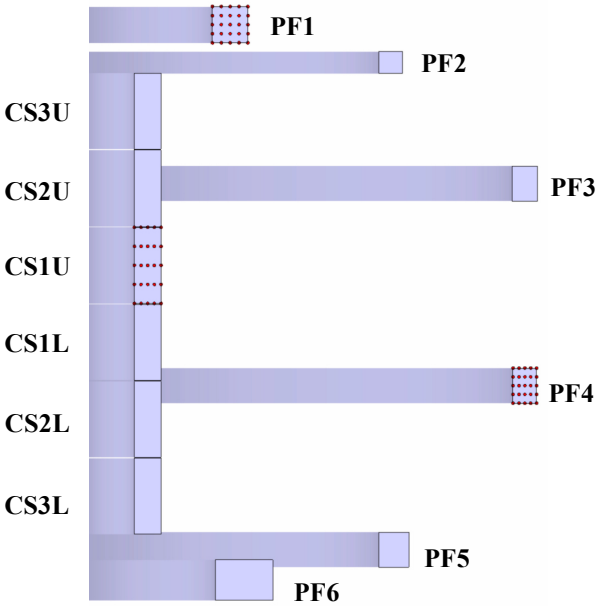

Figure 52: Control points for ITER simulation (passive structures are not represented)

This test has been performed without using passive structures and taking into account only the 12 coils of the poloidal field system. Boboz has been modified too, in order to make it work with up to 200 elements (it was formerly limited to 100 elements). In the following Figure **53**, the result of the test is presented for a given time in the reference scenario provided by Iter Organization, PF1, PF4, and CS1U. BR stands for Magnetic field in radial direction, BZ for vertical direction, BT for the modulus of the magnetic field. Some figures can show relatively high differences, but it happens only at low field producing 2,6 milliteslas at the point of maximum relative difference (points 10, 15 and 20 of CS1U). The figures summarizing the results can be found in [77]. The example of PF4 is shown in the following Figure **53**.

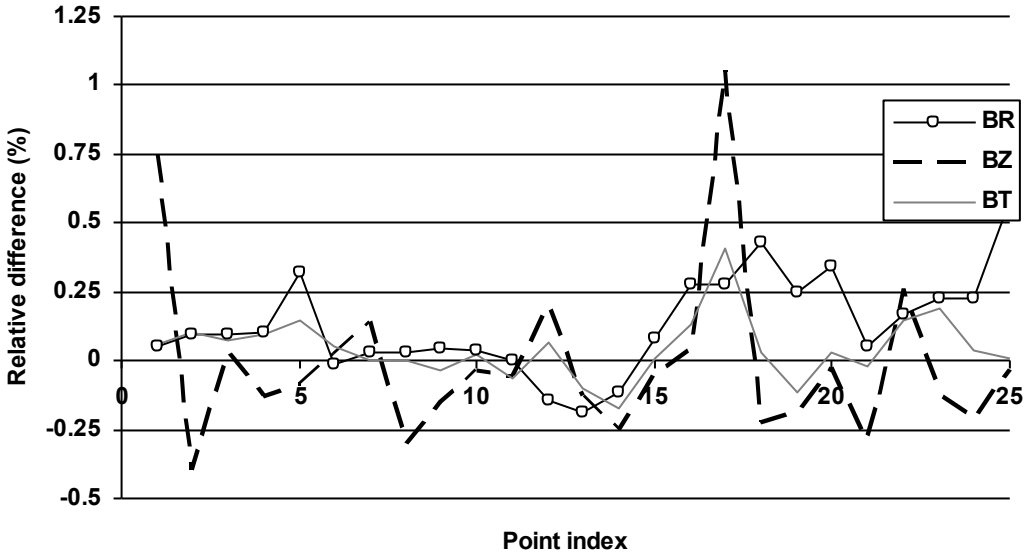

Figure 53: Magnetic field relative difference on PF4 with currents relevant of the reference scenario. The reference field is provided by Boboz.

TrapsAV gives the same results as Boboz, but for points located at very low field (about 0.01 T), the error is more important. Unfortunately, it is probably due to Boboz output format

which gives only 5 digits, where TrapsAV can give up to 11 digits. We can still notice that the error is most of the time below 2% and always at low field.

In order to validate the effects of passive structures (vacuum vessel, cryostat, ferromagnetic masses) on the magnetic field, a modification of Boboz was necessary, enabling it to model more coils (it was blocked at 100 elements maximum). It caused no observed decrease in terms of accuracy, and confirmed the effects announced by TrapsAV as seen in the following figures. Actually, this test is the same as the one described in the previous section, but with the insertion of passive structures (179 filaments, named FILA). The same conclusions follow this test, e.g., the impact of the output format of boboz in low field regions induces relative errors in the field calculation.

The general conclusion of this test campaign is that TrapsAV gives at high field the same results as Boboz. But in low field regions, uncertainties related to output format can induce high relative difference on very small values. In the foreseen applications of Traps in view of quench detection, these differences will not play a significant role (differences of 1.6 mT, -2.1 mT, and 1.7 mT for points 10, 15 and 20), because only TrapsAV, with more digits, will be used, and so low field will only be present on small areas.

b. Comparison Takahashi/TrapsAV for ITER plasma reference scenario

The first application of TrapsAV is to determine the electromotive forces induced by the fluctuations of the magnetic field the flux of which, is collected by the various magnets. Therefore, a comparison between results of the studies performed by Dr. Takahashi [43] [44] and results provided by TrapsAV using the same input data (old scenario for ITER with 36 equilibriums) has been made. In Figure 54, Figure 55 and Figure 56, representative curves showing the behaviour of the voltage measured across several Hexa-Pancakes (HP1, 3 and 6) of CS1U are presented. The scenario is described by 36 time steps, and is the same which has been used by Y. Takahashi.

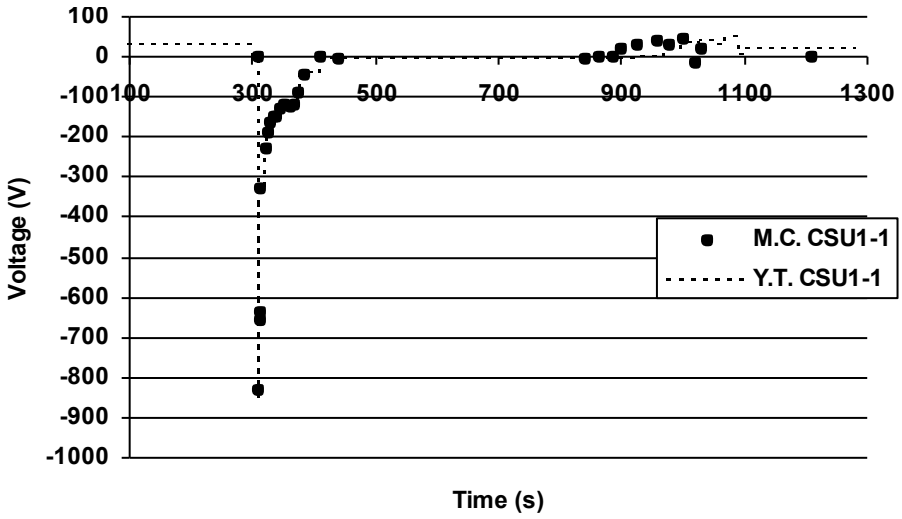

Figure 54: Voltage measured across Hexa-Pancake 1 (uppest) of ITER CS module CS1U. The results shown here are provided by TrapsAV (M.C.) and another code (Y.T.)

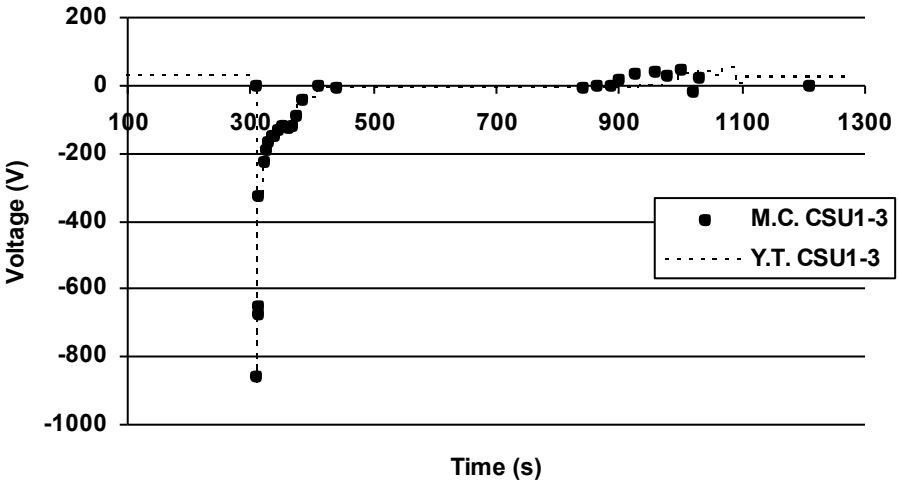

Figure 55: Voltage measured across Hexa-Pancake 3 of ITER CS module CS1U

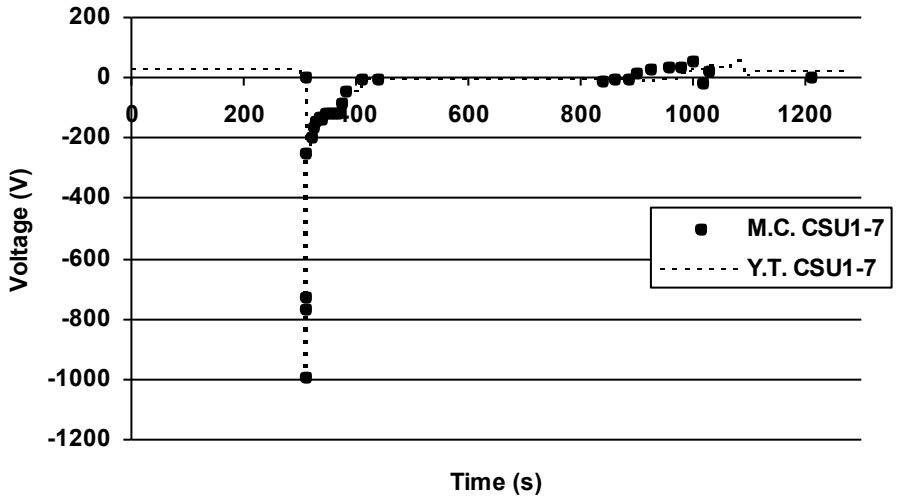

Figure 56: Voltage measured across Hexa-Pancake 6 (lowest) of ITER CS module CS1U

As shown in Table 13, the maximum difference is less than 4%, which is an additional proof of reliability of TrapsAV in terms of voltage calculation.

Table 13: Statistics and values obtained while monitoring the voltage across CS modules

TrapsAV	(M.C.)					
	CS3U	CS2U	CS1U	CS1L	CS2L	CS3L
MaxPeak (V):	165.21	323.19	331.88	307.56	226.53	165.72
MinPeak (V):	-7587.06	-8056.86	-5951.55	-6004.44	-8214.70	-7949.45
Y.Takahashi						
	takCSU3	takCSU2	takCSU1	takCSL1	takCSL2	takCSL3
MaxPeak (V):	170.55	336.91	340.08	313.72	232.91	171.32
MinPeak (V):	-7848.63	-8248.68	-6105.11	-6141.17	-8395.12	-8243.37
Differences	CS3U	CS2U	CS1U	CS1L	CS2L	CS3L
Max (V)	-5.34	-13.72	-8.20	-6.17	-6.38	-5.60
Min (V)	261.57	191.82	153.56	136.73	180.42	293.92

% :	-3.45%	-2.38%	-2.58%	-2.28%	-2.20%	-3.70%

Some probable reasons for these differences have been pointed out:

- Different principles of calculation (potential vector or field calculation)
- Different derivatives used
- Different resolutions
- Different geometries
- Different plasma simulations

And concerning TrapsAV:

- Uncertainties about control points localization (outer part, centre, or inner part of the conductor)

c. Conclusion of the validation process

The cross checkings described above are the most significant. Nevertheless, more detailed studies have been made, involving for instance analytical calculations, improving the reliability of TrapsAV. Taking into account the similarity of the results, it can be concluded that TrapsAV is a reliable tool designed to calculate the electromotive forces which can be measured across the magnets or subcomponents of the ITER magnets.

5.3.3. Exploration of the effect of the passive structures of the tokamak

The first step in the estimation of the induced electromotive force across a magnet, is to estimate the effect of the passive structures on the results of the calculation across a pancake, for instance. This effect has been mentioned in [46] by A.L. Radowinsky, in 2006. This effect has been checked in the CS pancakes, using nevertheless, a different scenario, closer to the reference scenario used for magnet studies. The effects are quite visible, and the effect on the magnetic field is showed as an example, in Figure 57.

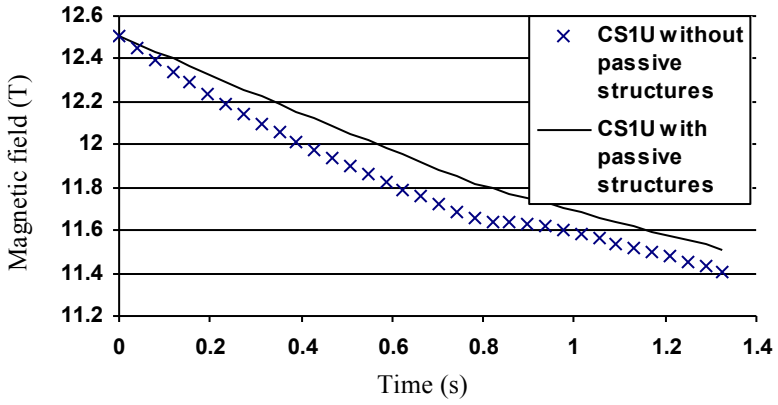

Figure 57: Magnetic field observed during reference scenario v10 at the inner side of CS1U

In this figure, one can notice that eddy currents have a weak influence on the magnetic field itself but act more like a smoother, to counteract the variation of the magnetic field. As

the voltage induced in the coils is a function of the time variation of the current, this smoothing will have an effect on it.

Indeed, the voltages across several pancakes of the CS have been calculated, and will be discussed later. However, the effect of the passive structures on the voltage is illustrated in the following Figure 58.

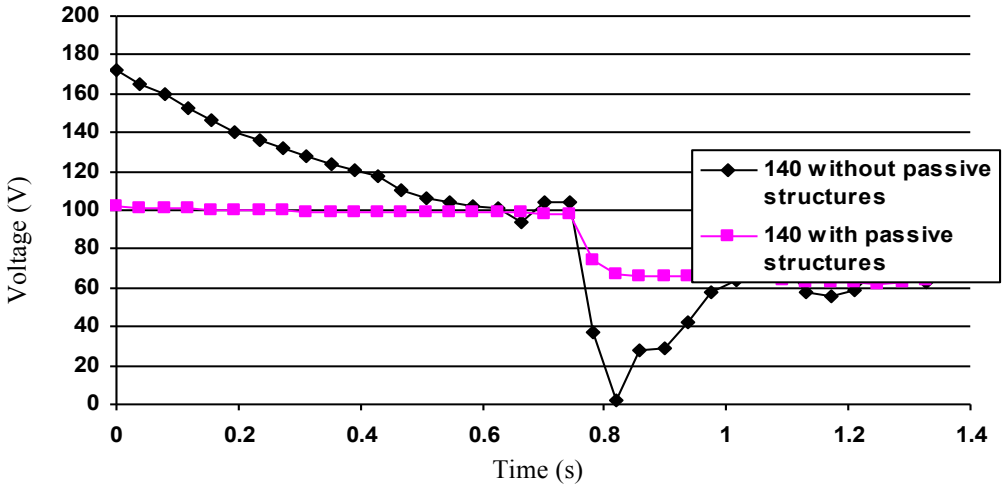

Figure 58: Voltage across pancake 140, upper of DP70 (CS1U)

It can be shown, that the passive structures act as a smoother of the electromotive force across the pancake. This result has a strong impact for the detection. This example shows that the expected maximum voltage is almost divided by two. For the rest of the studies, unless specified, the passive structures will be used in the simulations, during plasma initiation only, when they have a significant impact due to the large drop of magnetic flux in the CS.

5.4. Relation between inductive perturbation and quench propagation time τ_p

The set of parameters which describes the quench detection system must account for dependencies between parameters. One of the most significant is the relationship which exists between the resistance generated by the quench, and the propagation time.

It has been explained in 3.4, in Figure 30, that in order to be detected, the quench must produce a resistive voltage sufficiently high such that it becomes visible among the compensated voltage ΔU(t), as explained in 5.1. The countdown to the FSD is started as soon as:

$$\left|\Delta U(t)\right| \geq \left|U_t\right|$$

It must be pointed out that U_t is theoretically equal to U_Q only in case of perfect magnetic symmetry of the components which are balanced (case presented in 3.4, the plateau). In practice, it cannot be the case in a tokamak, due to the asymmetry of the magnetic configuration. Different compensation schemes exist, aiming at improving the compensation, and making the resistive voltage play a more important role in ΔU(t).

Depending on the chosen scheme, the relationship between U_Q and U_t varies.

In the following example, it is shown that for a chosen detection voltage threshold U_t, a propagation time corresponding to a resistive voltage U_Q as specified below must be estimated.

$$U_Q = 2 \times U_t$$

The following lines explain why there is a factor 2 in the above formula. Taking the example corresponding to the detection system described in Figure 42, page 65 (compensation of the voltages measured across two halves of a solenoid).

The voltages across two elements, one of them with a voltage due to the resistance, can be expressed as follow:

$$U_1(t) = -\frac{\partial \Phi_1(t)}{\partial t} + I(t).R_{quench}$$
$$U_2(t) = -\frac{\partial \Phi_2(t)}{\partial t}$$

If the two compensation units are perfectly magnetically symmetrical, in absence of quench:

$$\frac{\partial \Phi_1(t)}{\partial t} = \frac{\partial \Phi_2(t)}{\partial t}$$

Therefore, it can be written at any time:

$$\Delta U(t) = U_1 - U_2 = I(t).R_Q = 0$$

Now, if an asymmetry exists:

$$\Delta U(t) = -\frac{\partial \Phi_1(t)}{\partial t} + \frac{\partial \Phi_2(t)}{\partial t} + R_Q.I(t)$$

In addition, the voltage threshold U_t can be equal to the highest value of $\Delta U(t)$; in this case, the countdown to the FSD is not triggered while $\Delta U(t)$ is in the range:

$$-U_t < \Delta U(t) < U_t$$

Due to the asymmetry, $\Delta U(t)$ is not null anymore, even in the absence of a quench. To be conservative, it must be assumed that $\Delta U(t)$ can be close to the limit $-U_t$, in the example here below, by negative value:

$$\Delta U(t) = -\frac{\partial \Phi_1(t)}{\partial t} + \frac{\partial \Phi_2(t)}{\partial t} + R_Q.I(t) = -U_t + R_Q.I(t)$$

Supposing the current in the conductor positive, the appearance of the quench will result in a voltage increase. The quench will have to produce a resistive voltage of two times the threshold value, in order to exceed it. The corresponding propagation time in this case, is $\tau_p(2U_t)$. This case is the worst in this situation.

$$U_Q = 2 \times U_t$$

On the other hand, if the current is negative, the resistive voltage varies negatively, and the threshold value is immediately reached. U_Q is therefore the highest resistive voltage that must be produced in order to start the countdown to the FSD.

Consequently, the choice of the compensation influences the perturbation attenuation, but also the propagation time, at a given threshold value. For each proposed system, CS, TF, and PF, the case will be studied.

6. Quench detection in the ITER CS system

In previous chapters, the basics of the quench have been presented. In chapter 6, the methods presented before will be applied to the ITER central solenoid.

As explained in details in the first chapters of this manuscript, a quench is a fast superconducting-to-resistive state transition, which is, if not detected, likely to cause permanent damage to the coil.

In case of a quench, a fast safety discharge (FSD) of the current is triggered such as to extract the magnetic energy of the coil into external dump resistors and protect the coil. The detection and action time, which is the time between the quench initiation and the FSD triggering, must be sufficiently small to limit the temperature increase in the coil and avoid any damage. Quench detection using voltage measurements is likely to be the fastest technical available solution, but, for the resistive voltage, a specific processing is required to discriminate the inductive voltage due to the variations of the magnetic field, which has to be detected. This is one of the specificities of the quench detection in the ITER PF and CS systems, which makes it particularly difficult.

In this chapter, the first section will focus on the description of the ITER central solenoid and its surroundings.

The second part of this chapter will render the quench propagation aspects, including a specificity occurring at the early times of the quench propagation, in the first seconds.

The following section will be dedicated to a critical point of the CS quench protection, the strategy of balancing the sub-elements of the CS, which plays a great role in the efficiency of the quench detection system. It is recalled that very high voltages will appear during plasma discharges (up to 12 kV across one single module in normal operation), and the quench voltage order of magnitude is around the 10th of volt. This discussion will be supported with the results from TrapsAV.

To complete the two elements mentioned above, in a specific section, the hot spot criterion will be applied.

Finally, this chapter will be concluded by the proposal of a solution consisting in the monitoring of one Double-Pancake, balanced with the weighted average of the voltage across the two adjacent Double-Pancakes. It will be explained how the routing of the measurement wires has been taken into account, and how the plasma initiation phase characterized by very fast current variations has been treated.

6.1. Description of the ITER Central solenoid magnet system

The CS magnet system can be decomposed into two parts: the CS itself, and the other part, the pipes, structures, and instrumentation. These two parts are described in the two next paragraphs.

6.1.1. The Central Solenoid

The main role of the CS is to drive a current in the plasma, by induction. It is also involved in the control of the plasma shape and stabilization. Therefore, it carries high and fast varying currents, and consequently, very high voltages appear across the terminals of the modules. The main characteristics of the CS system are presented in the following table.

Table 14: Main CS characteristics (from [15])

	CS Modules
Maximum coil current (MA.turn)	21.9 MA at PI (13 T)
Number of turns per CS module: - Radial - Vertical - Total (incomplete turns taken into account)	 14 40 549
Conductor Unit length (m)	895 (for 6 pancakes) 594 (for 4 pancakes)
Turn voltage in normal operation (V)	20 (PI)
Ground/ terminal voltage in normal operation (including fast discharge) (kV)	19.5/19.5
Ground/ terminal voltage in faulted operation(kV)	19.5/19.5
Coil DC ground test voltage (kV)	41
Number of current lead pairs	6

In the table above, PI stands for Plasma Initiation, which is the first 3 seconds of the studied reference scenario.

The CS is a stack of 6 modules as presented in Figure 59 with the denomination of the modules. They are independently powered except for CS1L and CS1U, which are series connected.

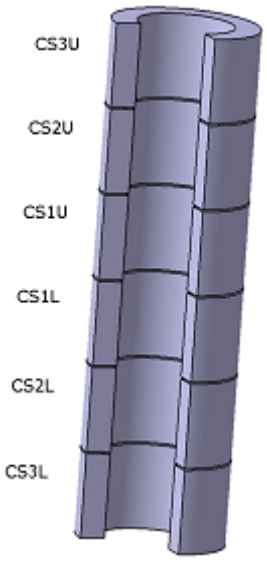

Figure 59: ITER CS with its 6 modules

Each of the CS modules is by itself composed of seven sub-elements: six Hexa-Pancake (HP, a stack of 6 pancakes wound together) and one Quad-Pancake (QP, a stack of 4 pancakes wound together), separated by joints as showed in Figure 60, with the names of these sub-elements.

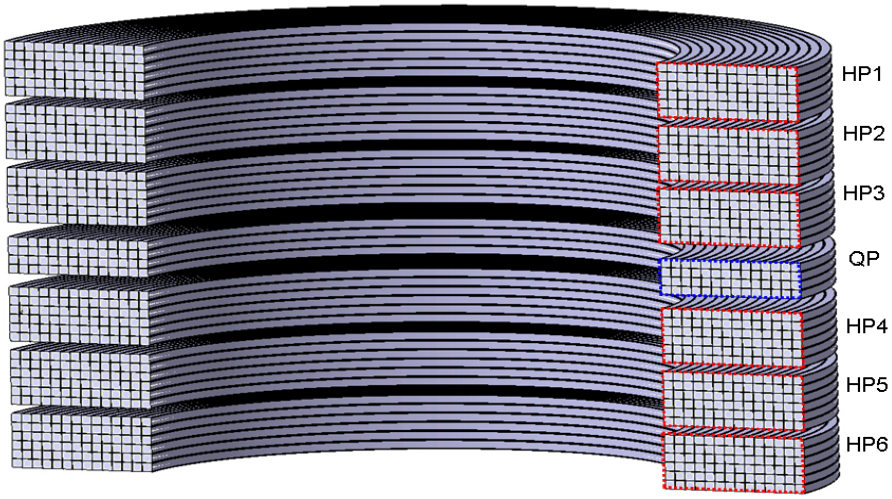

Figure 60: ITER CS module showing 6 Hexa-Pancakes and 1 Quad-Pancake

In addition, each Hexa-Pancake and the Quad-Pancake can be decomposed in terms of Double-Pancakes (DP). A single module, with its 40 pancakes, is a stack of 20 Double-Pancakes. This decomposition allows to locate each DP in the CS. DP 1 is the bottom Double-Pancake, and DP 120 is located at the top of the CS. In this section, for instance, CS2L-DP3 designates the third DP of the module CS2L starting from the bottom, which is also the 23rd DP of the CS, DP23.

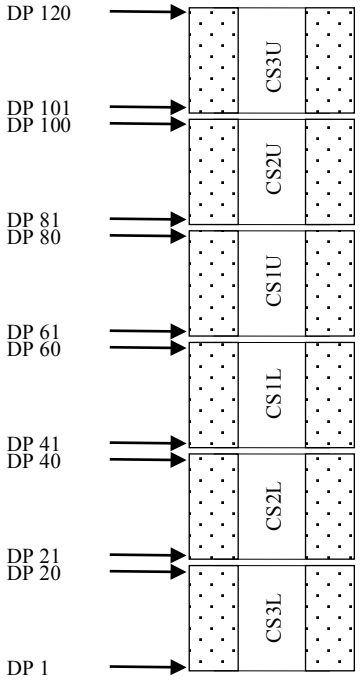

Figure 61: Central Solenoid with appropriate designation of the Double-Pancakes

6.1.2. CS equipments and surrounding components

The decomposition presented in Figure 61 is adequate regarding the locations where sensors can be placed (visible in Figure 62). Indeed, between each Double-Pancake, voltage taps can be installed on the helium outlets, and in the middle of a Double-Pancake, on the helium inlets, as showed in the following Figure 63. In addition, away from the CS itself, thermohydraulic sensors are installed, for monitoring, and secondary detection purpose. Further explanations are given in [16].

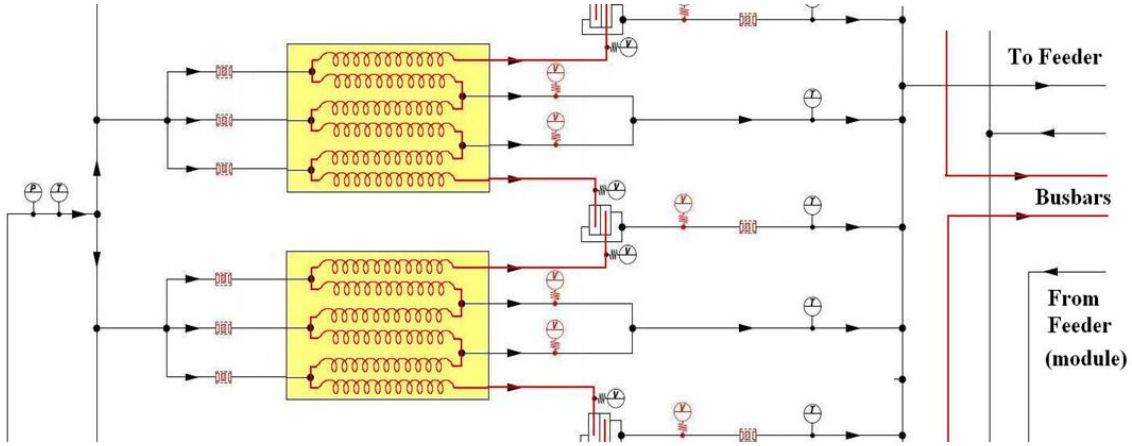

Figure 62: Instrumentation of 2 Hexa Pancakes of the CS

The Central Solenoid is equipped with several kinds of sensors, and structural components aiming at reinforcing the assembly, which has to face very large Lorentz forces. They take obviously space and must be dodged by the instrumentation cables and wires.

Between each pancake, a voltage measurement wire can be drawn from the voltage tap (in green in Figure 63, such as it becomes possible to measure the electromotive force induced in the circuit composed by the DP conductor, and the measurement wires. A view of the simulated practical assembly is given Figure 63.

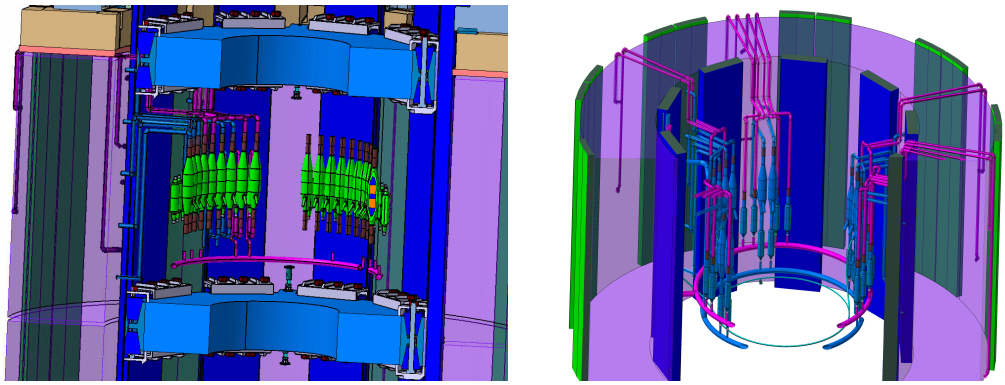

Figure 63: A CS module, with helium pipes.
Inlets in blue, Outlets in violet, voltage taps in green (left-hand side).

It should be noticed that the effect of the routing of the wire is not negligible, because it contributes depending on its trajectory, to the voltage measured, unless the wires are perfectly twisted together to avoid flux collection.

6.1.3. CS plasma discharge scenario

In this thesis, only a reference scenario has been examined. This scenario has been provided by ITER ORGANIZATION, for studies purposes. It is assumed to be very demanding on many points. Indeed, the proposed cycle shows very large currents, and current variations. According to section 5.1, these variations induce high electromotive forces in the magnets, making the discrimination of the resistive voltage associated with the quench difficult to detect.

The reference to scenario is made of two packages, which can be found in the following documents:

- Magnets:

  Scenarios_for_Coil,_Power_Supply_and_Cry_2FTVKV_v1_10.xls (2FTVKV)

- Passive structures:

  data_related_to_scenarios_of_plasma_init_2M745L_v1_0.zip (ITER_D_2M745L).

In these documents, several versions of the plasma discharge are given, and the scenario, which has been studied, is the baseline scenario with plasma current at 15 MA. The initial CS flux is 120 Wb and the plasma initiated outboard.

The following Figure 64 presents the currents in the CS modules.

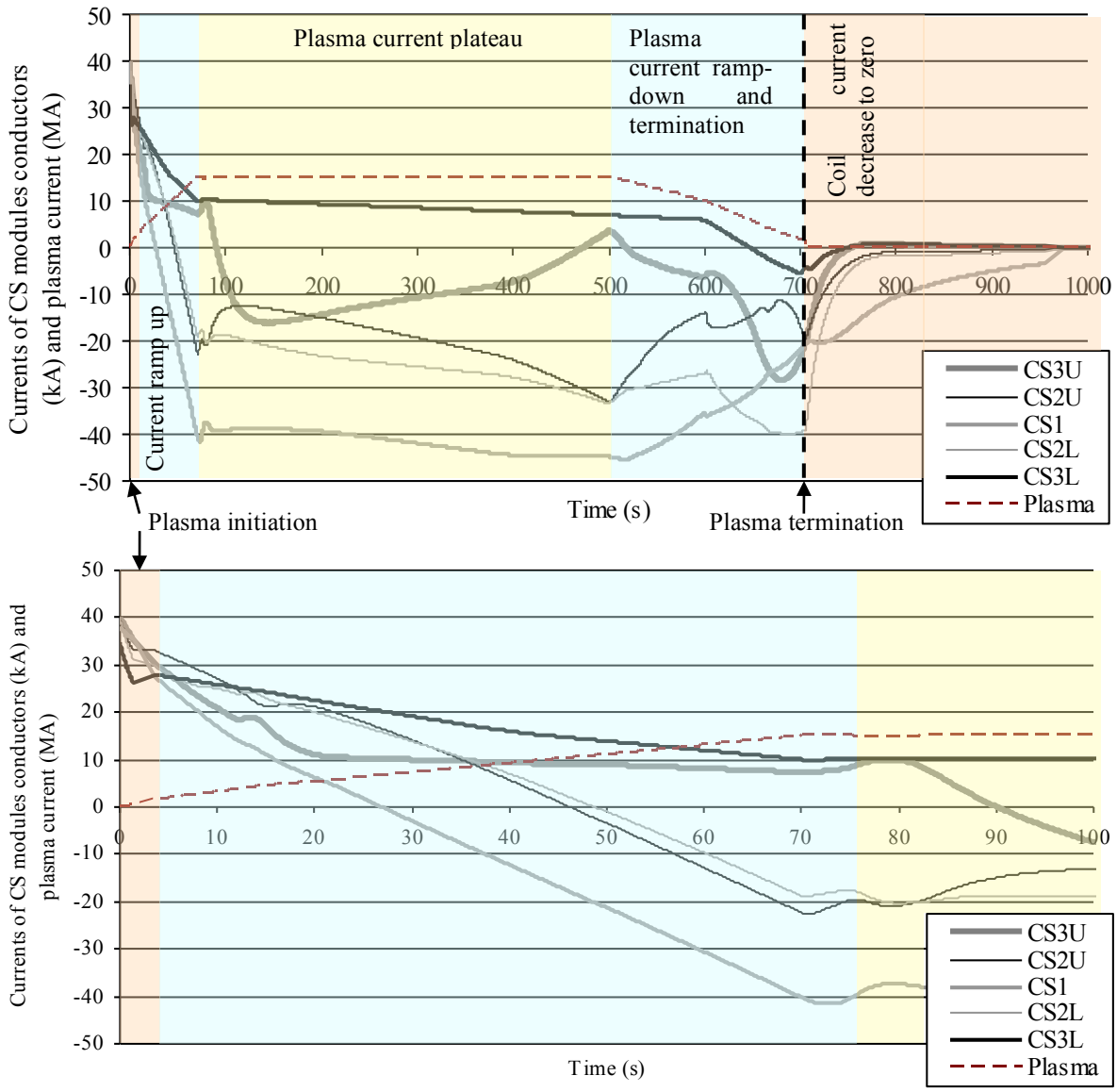

Figure 64: Whole CS current scenario. In the upper figure, the whole scenario, in the lower figure, just the plasma initiation phase is represented.

It can be observed that during the initiation phase, CS1U and CS1L experience a complete inversion of the current. Moreover, during the first seconds, the current decrease in the CS modules is extremely rapid, approaching -10 kA.s^{-1}. Indeed, during this phase, the plasma is initiated, and this requires great flux changes.

6.2. Quench propagation in the ITER Central Solenoid

General considerations about quench propagation have been given in chapter 4, including a description of the main parameters influencing the quench velocity: magnetic field, current length of the zone affected by the quench initiation. This was given for a virtual model at constant magnetic field. In this section, the quench propagation in the CS will be studied on a more realistic model taking into account the magnetic field variation along the pancake.

The influence of the deposited energy has been explored and the influence of the quench location for three typical turns of the pancake.

6.2.1. Description of the model

As explained in the section 4.3, Gandalf code is not able to model several thermally coupled pancakes. In the present study, the pancake 101, the lower pancake of DP51, in the middle of CS1L module, has been modelled. This pancake is the most loaded in terms of heat deposition during the scenario. Moreover, it is located in the module which carries the highest current (45.7 kA).

The length of the pancake is 151.4 m, and the current is 38.047 kA corresponding to the current plateau before Plasma Initiation (PI). The distribution of the magnetic field inside the pancake is presented in Figure 66.

In Figure 65, P101 is represented. The pancake is supposed alone and closed on an external downscaled circuit modelled by flower [45]. The critical properties of the conductor as a function of magnetic field, temperature and strain are taken similar as in [45].

The electrical conditions of the pancake are the one existing after current increase, during the plateau just before the plasma initiation (PI).

The helium inlet temperature is 4.3 K and the pressure inlet is 3 bar.

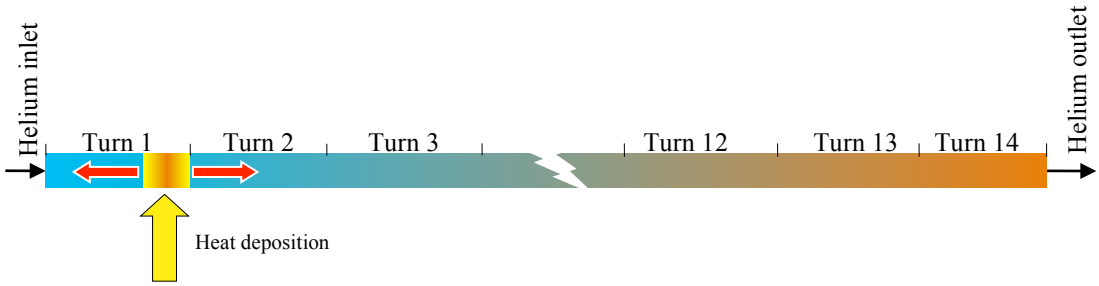

Figure 65: Quench initiation zone localization. The colour represent the increasing temperature of the helium, due to its circulation in the bundle of.

The location of the quench in the model and the question of boundaries will play an important role in comparison with the virtual model of section 4. The quench will be triggered at the end of the first turn of the P101. Indeed, at the inner radius of the central solenoid, the magnetic field is maximal and therefore the margin in temperature is the lowest. Consequently, this is the location where a quench is the most likely to occur.

It is to be noted that the model such as presented in Figure 65, is not fully representative of the real circuit. In this model, there is intrinsically no possibility of propagation on the left side once the normal (quenched) zone reaches the helium inlet region, while in reality the propagation following the quench initiation can further take place in the following pancake as there is no discontinuity of the conductor.

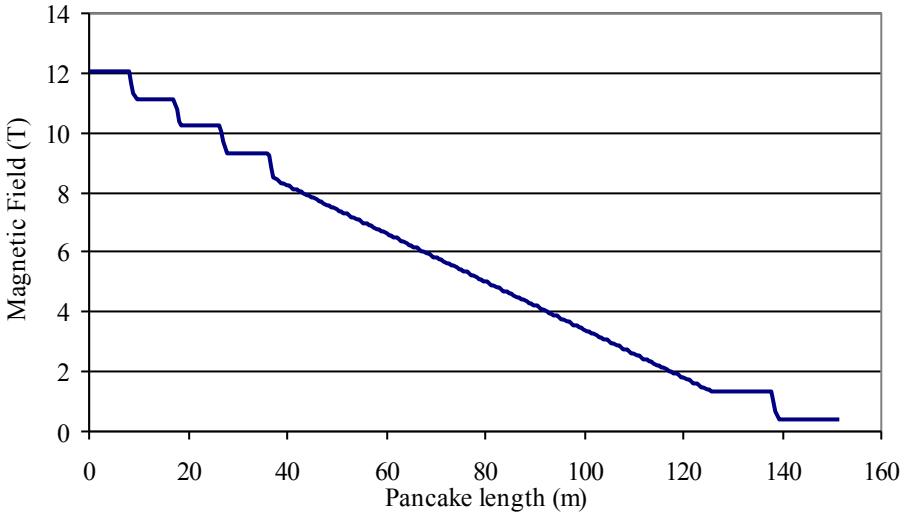

Figure 66: Model of magnetic field along the length of pancake 101

6.2.2. Assumptions on the quench initiating perturbation

Independently of the quench location, the conditions of the quench initiation are certainly influencing the quench propagation as already introduced in chapter 4.

The propagation velocity and consequently, the time needed to reach the detection level, is a function of the parameters characterizing the quench initiation. These are:

- The length of the conductor affected by the initial quench
- The energy deposited in the conductor for the quench initiation
- The (constant) power at which this energy is injected in the conductor (duration of the disturbance)

Depending on these characteristics the propagation speed can be very different. Therefore from the beginning, some of them have been fixed, as discussed in sections 4.4 and 4.4.3.

The length of the conductor is 1 meter, and the duration of the disturbance is 0.1 s.

As presented in Figure 65, the quench is initiated by injecting a given power at time 0.1 s during 0.1 s on one meter of conductor situated between x=7.12 m and 8.12 m, the origin is taken at the helium inlet. (x=8.12 m is the abscissa where the transition to the second turn is taking place)

Main characteristics of the quench which are the resistive voltage U(t), the normal length L(t) and the temperature of the hot spot T_{hs} (t) are observed during the time following the quench initiation. They are observed for 3 values of the quench energy initiation corresponding to 1.MQE, 2.MQE and 4.MQE.

MQE is the minimum quench energy. It is recalled that the MQE, for a given conductor and heat deposition location and duration, is a function of the magnetic field, the strain, and the current in the conductor.

The minimum power deposited to initiate a quench in 0.1 s is 2410 W/m, which corresponds to MQE = 521 mJ/cm^3. As visible in Figure 67, Figure 68 and Figure 69, the propagation corresponding to 1.MQE is very different from the propagation corresponding to 2.MQE and 4.MQE. In the propagation corresponding to 1.MQE there is a delay of about 2.8 s before real propagation. It does not correspond to any real heating at the hot spot, as showed in Figure 69.

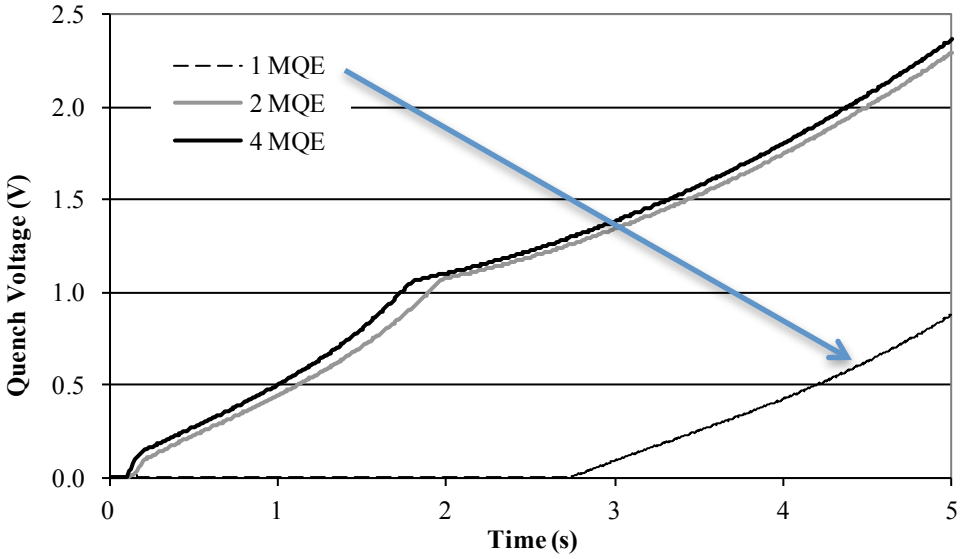

Figure 67: Quench Voltage on P101 (Gandalf)

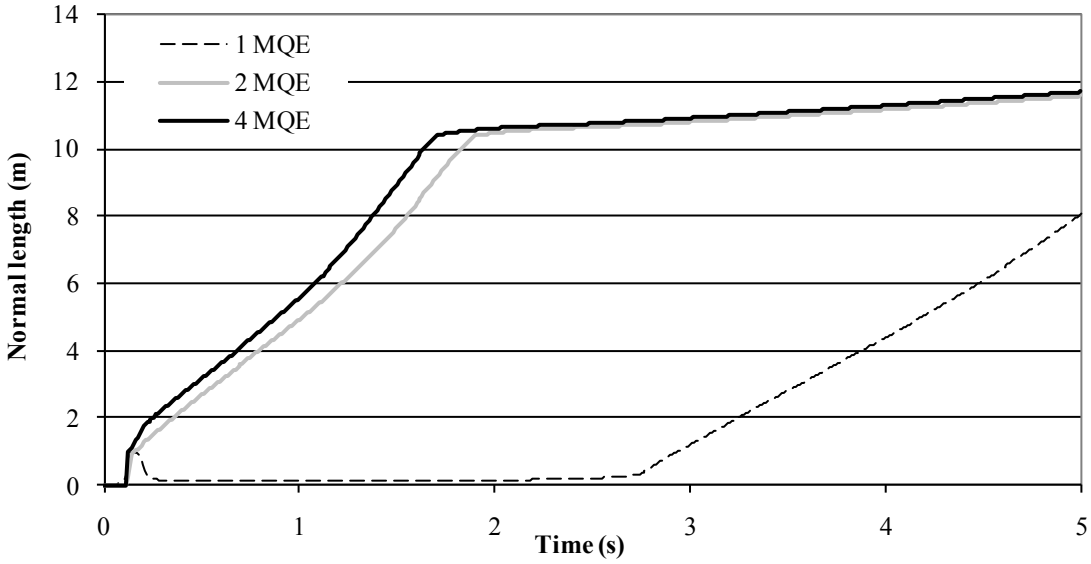

Figure 68: Normal zone on P101 (Gandalf)

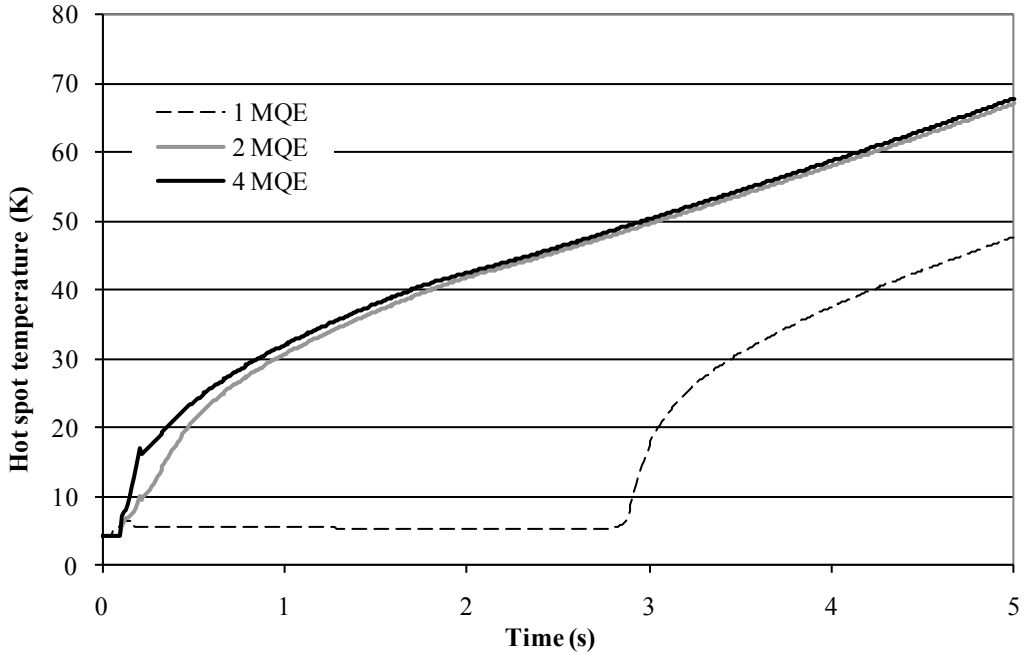

Figure 69: Temperature at the initially quenched zone on P101 (Gandalf)

The propagations corresponding to 2.MQE or 4.MQE are not very different from each other. It is therefore decided to select a heat deposition equal to 2.MQE for the rest of the study.

P101 is the pancake where the quench is the most probable, because the other pancakes are subject to lower magnetic field (lower magneto-resistance, and higher minimum quench energy). However during the scenario, P101 experiences large variations in terms of magnetic field along the conductor, but also current variations, and consequently, Lorentz force, and finally, variation of strain ε. A complete modelization of this strain is difficult, and it is not the aim of the present study. Only a variation of 10% of the strain has been simulated. Indeed, as shown in Figure 70, the strain, which is mostly due to thermal contractions, has a weak impact on the quench propagation. Therefore, in the following studies the strain scaling law given in [45]. The strain effect on the quench propagation velocity had been studied, since it has a significant influence on the temperature margin.

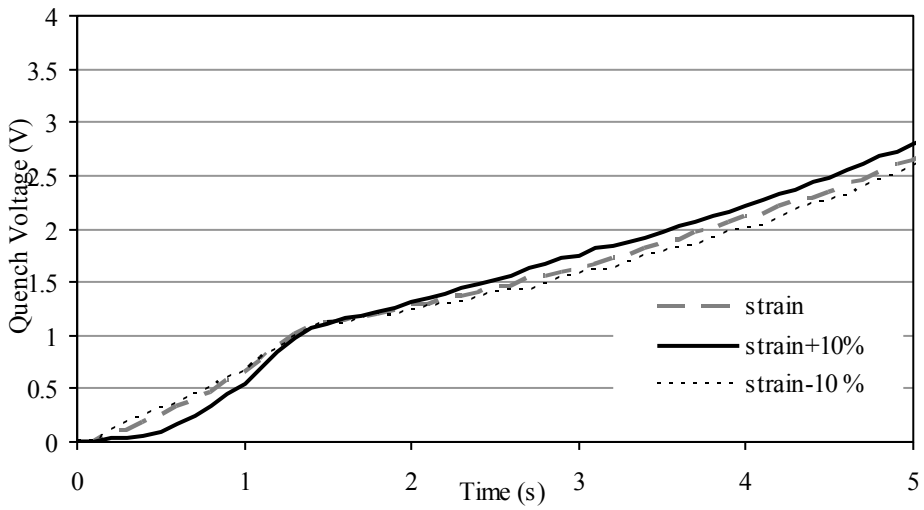

Figure 70: Influence of strain on quench propagation (P101)

It can be noted that there is an inflexion point in the curves related to propagation. It can be shown, that this is due to the fact that the first propagation front (on the left direction, in Figure 65), reaches the helium inlet. Therefore, it cannot develop in this direction any longer, and the resulting expansion of the normal zone becomes only depending on the propagation front velocity on the right.

6.2.3. Influence of the quench location on the quench propagation

As it is said in paragraph 6.2.1 it is supposed in the study that the quench is initiated at the inner radius of the CS, which is the most probable situation: for instance a quench during the ramp of the current up to the plateau before PI.

With the hypotheses previously given, heat deposition duration of 0.1 s and power equivalent to 2 times the minimum quench energy (2.MQE), quenches have been initiated on the two first turns of the CS.

Firstly, the impact of the deposition length has been highlighted, as shown in Figure 71 (initial heat deposition length of 1 m) and Figure 72 (8 meters) on turn 1. This illustrates that the voltage increase is very depending on the initial heated length.

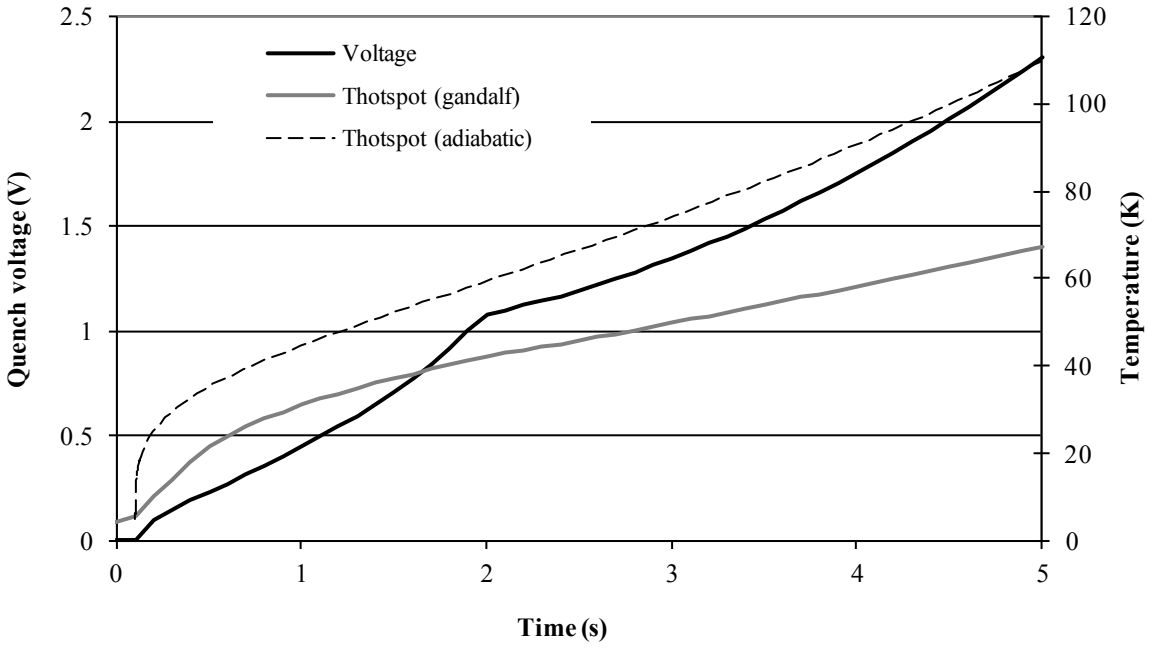

Figure 71: Characteristics of quench propagation
(P101 quench initiation between 7.12 m and 8.12 m, turn 1)

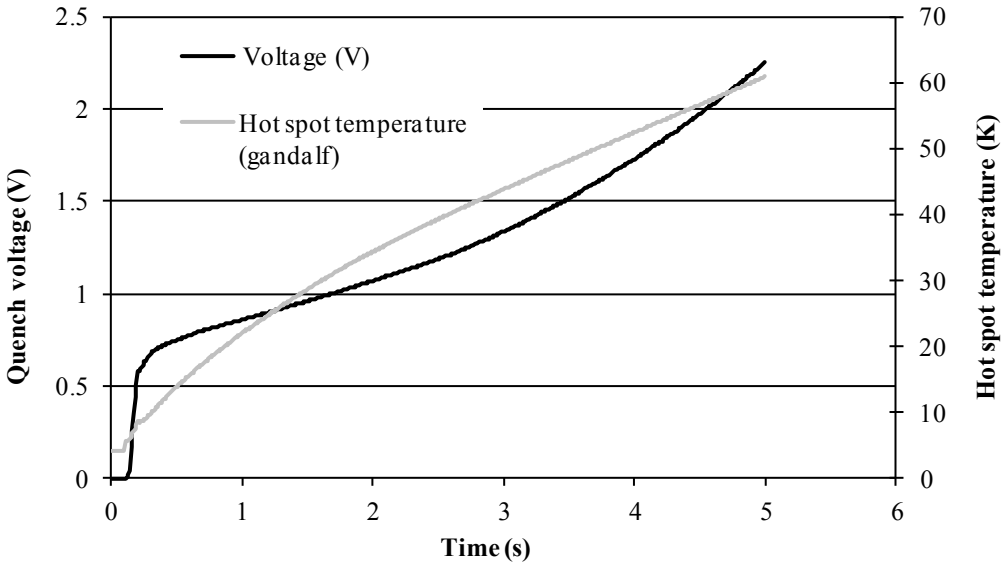

Figure 72: Characteristics of quench propagation (P101 quench initiation on the full turn 1)

In order to stay within conservative hypotheses, an initial heated length of one meter has been assumed for the rest of the study. 1 m is considered as being conservative, since the length exposed to high field (lowest temperature margin) is about 8 m.

A quench initiation corresponding to 1 meter of conductor at the end of turn 2 has been simulated with Gandalf and compared to a similar quench initiation in turn 1. The compared quench voltages are presented in Figure 73. It can be seen that the inflexion does not exist for turn 2 which confirms that this inflexion is due to the Gandalf model for turn 1 (artificial end of the pancake at x = 0 m).

At the beginning of the quench initiation the propagation is slower in turn 2 due to the lower field, but the two curves are crossing at t=3.4 s, the propagation in turn 2 being more realistic in the time range useful for quench detection (i.e. first 2 seconds), because the actual conductor does not contain a discontinuity at x=0 m. Turn 2 has no discontinuity even in the Gandalf model (no inflexion before 4 s propagation).

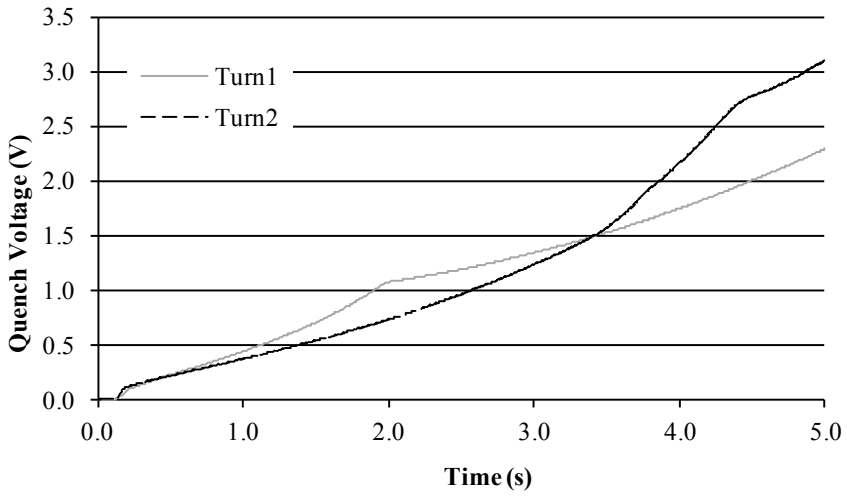

Figure 73: Compared characteristics of quench propagation (P101) in turn 1 and turn 2

Using Gandalf it is possible to compare the characteristics of the quench at turn 1 (inner radius) and at turn 14 (outer radius) of pancake P101 (Figure 76).

In order to have an estimation of the quench behaviour at low field, quenches have also been triggered at turn 14, as showed in Figure 74, Figure 75 and Figure 76.

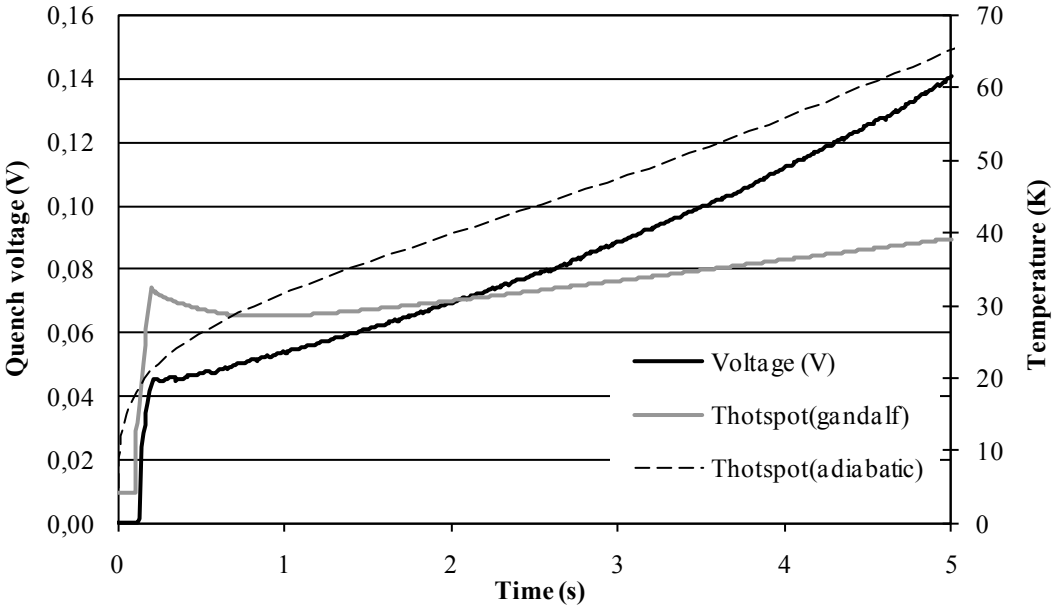

Figure 74: Characteristics of quench propagation (P101 quench initiation on one meter, turn 14)

In turn 1 the average voltage per second corresponding to the propagation is 0.5 V/s.

The quench energy (heat deposited on the cable to initiate a quench) on turn 14 is deposited with a power of 14500 W/m, over one meter within 0.1 s, corresponding to 6 times the quench energy on turn 1, and about 3132 $mJ.cm^{-3}$. After 0.5 s the voltage is still very low (around 0.3 V) leaving little chance to detect the quench. Note that for turn 14, τ_{da} (related to the hot spot criterion) is large, due to the small value of the magnetic field. There is an appreciable difference between the adiabatic hot spot estimation and the hot spot by Gandalf showing that cooling is efficient to reduce the temperature in case of initiation on a small portion of conductor, this will be illustrated later in the manuscript, in section 6.4.

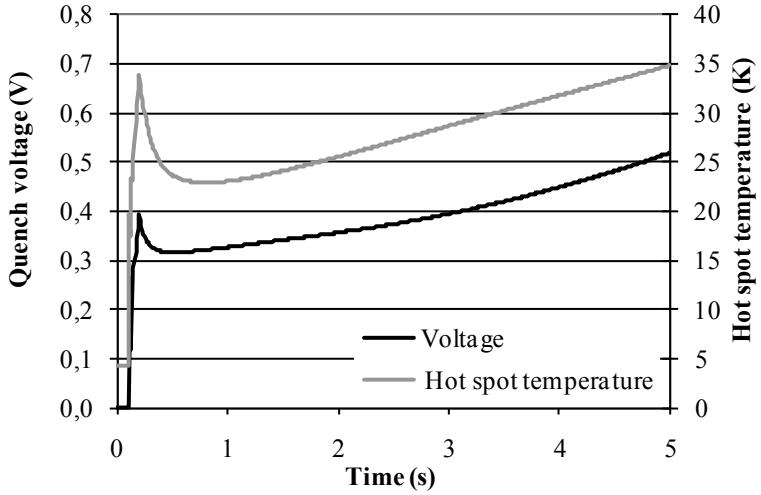

Figure 75: Characteristics of quench propagation (P101 quench initiation on the full turn 14)

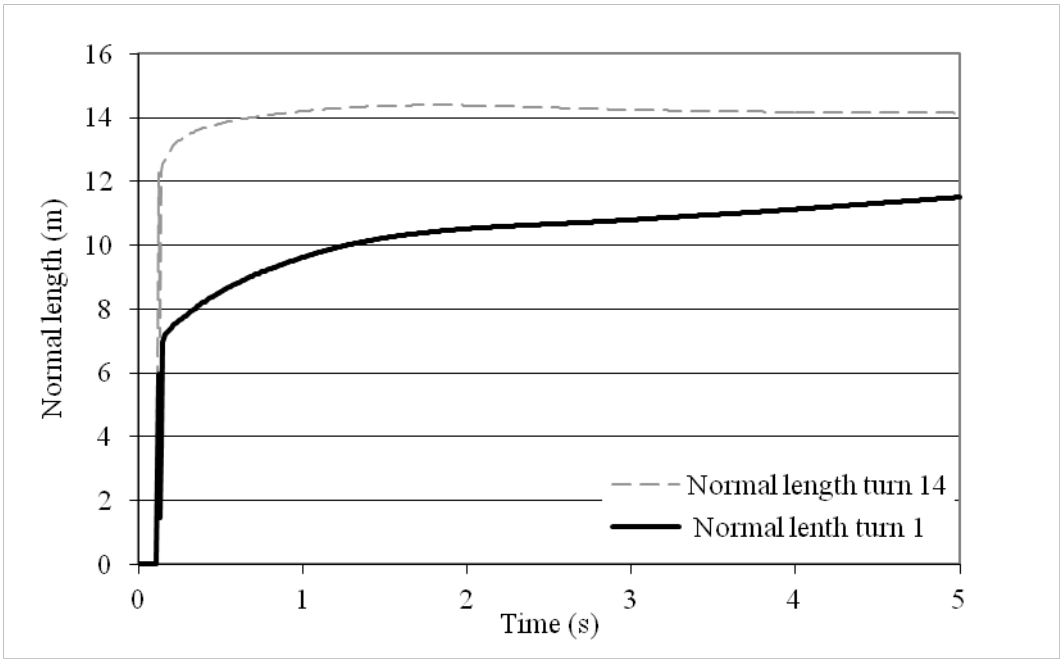

Figure 76: Compared characteristics of quench propagation (P101) in full turn 1 and full turn 14

The difference between turn 1 and turn 14 is large. While the normal zone is propagating in turn 1 at a velocity of about 3 m/s there is no propagation on turn 14. The hot spot temperature calculated with Gandalf is very similar for 1 m initial quench length and for a full turn quenched.

6.2.4. Conclusions on CS quench propagation for the detection

In Figure 77, a zoom is given about the first two seconds of the propagation, which are decisive for detection. An inflexion corresponding to a decrease of the propagation velocity is observed on the voltage trace and on the normal length at about 1.9 s and 1 V and 10 meters. This is due to the model of Figure 65. When the normal zone reaches the helium inlet the propagation is no longer possible in this direction and the velocity is divided by a factor 2.

This does not correspond to the reality because the quench can still propagate in the adjacent pancake. This approach is therefore conservative for the detection.

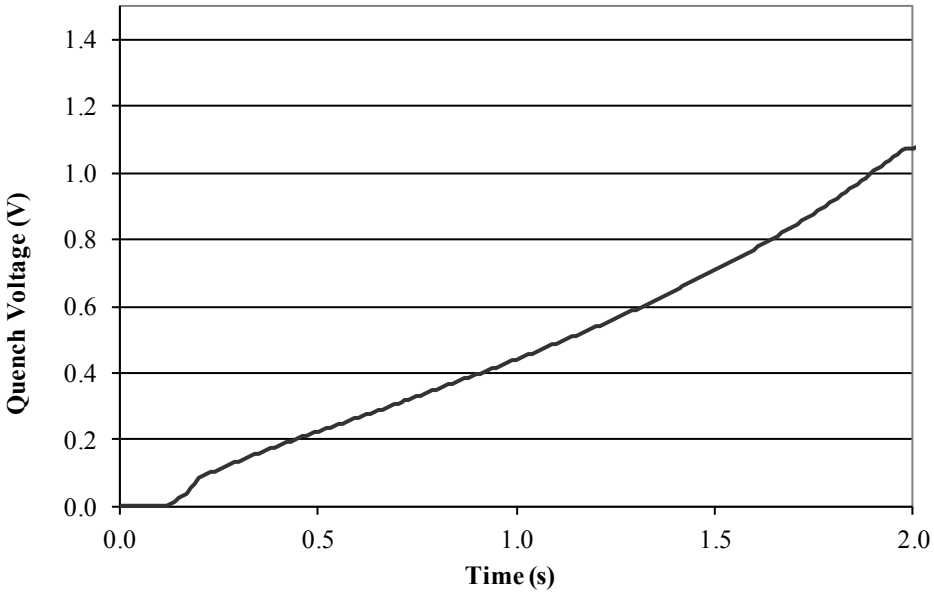

Figure 77: Zoom on quench voltage during the first two seconds on P101

In Table 15, the propagation time is given as a function of the voltage. It corresponds to $\tau_p(U_t)$ such as described in section 3.4. In addition, it is crucial to consider that as the power deposition starts at t=0.1 s, there is an offset in the times. Table 15 takes this offset into account.

Table 15: Summary of quench propagation characteristics on P101

Quench voltage (V)	Time (s)	Normal length (m)
0.1	0.13	1.4
0.2	0.34	2.4
0.3	0.58	3.5
0.4	0.81	4.5
0.5	1.02	5.5
0.6	1.22	6.5
0.7	1.39	6.95
0.8	1.54	8.67
0.9	1.68	9.69
1.	1.79	10.4

As from this Table 15 it can be seen that a typical voltage detection of 0.5 V can be reached in 1 second (1.02 s). It has been noted that the strain has a weak influence on these values, and the times indicated above increase when the quench is initiated at lower fields. As a quench initiated in the first turn is the most probable, the values of Table 15 will be selected for quench detection system design, as proposed in this thesis.

6.3. Investigations about electromagnetic disturbances in the CS system

With TrapsAV, the electromotive forces which can be collected across each pancake have been estimated. The tokamak model has been constructed, using the names given in the first paragraph, in Figure 61. The first subsection of this section describes the model used in TrapsAV with more details.

As presented in the introduction of chapter 6, the primary quench detection in ITER magnets is based on voltage, but the voltage has to be compensated to eliminate transient inductive effects. Several methods in terms of compensations have been tested, with increasing level of definition. The different trials are described in the second subsection, starting by the module-to-module compensation.

In the third subsection, the selected solution is presented which is based on the Central Difference Averaging.

The fourth subsection sums up this part of the study, highlighting the problem of the plasma initiation phase.

6.3.1. Description of the Central Solenoid Model by TrapsAV

In this study, all the components of the tokamak are not required, because some of them have no impact on the CS. The TF system especially, has a quasi-null mutual inductance with the CS. Moreover, the CC systems have a very weak influence, and in consequence, these components have not been modelled. The following figure illustrates the model, which has been used.

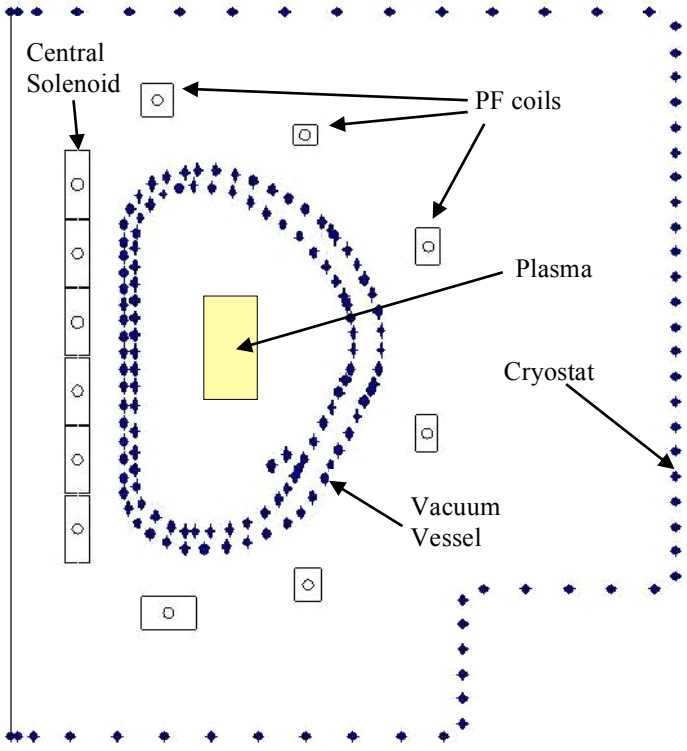

Figure 78: Components involved in the model for the estimation of the inductive forces in the Central Solenoid

The designation of the Double-Pancakes, Quad-Pancakes, and Hexa-Pancakes, is made in concordance with Figure 60 and Figure 61. The model described in the section 6.3.2 has been used for the first steps of the electromotive forces estimation across the CS sub-elements. Nevertheless, this simple model does not correspond to the reality. A correction of the model is therefore introduced in the paragraph 6.3.3. Nevertheless, the simplified model of section 6.3.2 allows a simple estimation of the orders of magnitude of the voltages appearing across the elements, hence, has been used to discard potential solutions.

In order to obtain the voltages across modules or subcomponents of the CS modules, TrapsAV has been used, and the scenario presented in 6.1.3 has been used.

6.3.2. Presentation of some compensation solutions

The more global is the solution to be used for quench detection, the more reliable it is, due to the reduced number of critical components. According to this principle, there were several attempts, going from the coarsest to the finest detection system, involving more and more detectors.

- The first attempt consisted in balancing the voltage appearing across whole modules. Unfortunately, the voltage difference was too high to ensure a residual voltage ΔU(t) (introduced in section 5.1) sufficiently low such that a quench could be detected in time. For this solution, the voltage taps are supposed to be located at the top and bottom of each module. The voltage U_{CSxx} is then available to be used in a real time compensation such that the resulting compensated voltage is:

$$\Delta U_i(t) = U_{CS3U}(t) - \alpha_i . U_{CS2U}(t)$$

The compensated voltage ΔU(t), one example of which is given in Figure 79, shows peaks of significant duration.

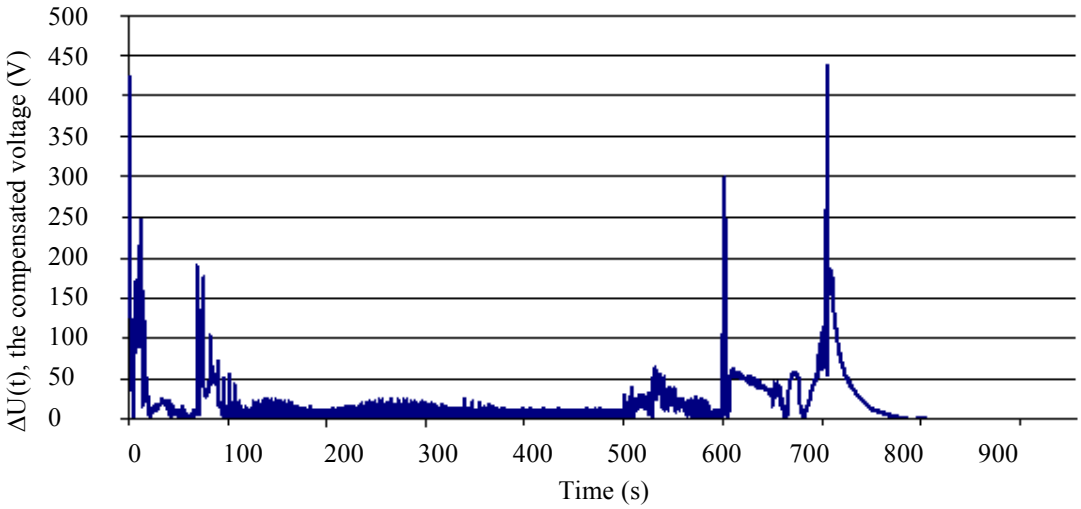

Figure 79: Example of CS1U-CS1L compensation, showing peak voltages up to 500V

It can be concluded thanks to the example shown in Figure 79, that further exploration of the possibilities of this compensation has to be excluded. Indeed, CS1U and CS1L

are the modules, which were the most likely to compensate each other, because they are powered by the same generator.

- The next step has been to use the "natural" decomposition according to the hexa-pancakes and quad pancakes. This compensation has been used by Y. Takahashi, and presented in [43]. It is useful to do this simulation again: contrary to the study of Takahashi, the passive structures (and their smoothing effect) are included in the model. Moreover, the plasma discharge scenario is far more detailed in the study presented here. It consists in balancing the voltage across an Hexa-Pancake i with a linear combination of the voltages measured across the adjacent Hexa-Pancakes i-1 and i+1, according to the following relationship:

$$\Delta U_i(t) = U_{HPi}(t) - \alpha_i . U_{HP(i-1)}(t) - \beta_i . U_{HP(i+1)}(t)$$

The corresponding cabling is presented in Figure 80. In this figure, HPi stands for Hexa-Pancake index i. α_i and β_i are weighting coefficients aiming at reducing static side effects. They effectively reduce the residual voltage.
The Hexa-Pancakes are closer to each other in terms of collected magnetic flux than the modules were. Therefore, the results are lower in terms of compensated voltage, as illustrated in Figure 81, when applied to the three top Hexa-Pancakes of CS3U (HP1, 2, and 3), which have been estimated as being the worst case regarding quench detection.
As expected, the resulting compensated voltages are much lower than for module compensation, even at the worst place. Nevertheless, this compensated voltage remains much more above an acceptable solution (which would be less than 1 V concerning the threshold and up to 3 seconds in terms of holding time).

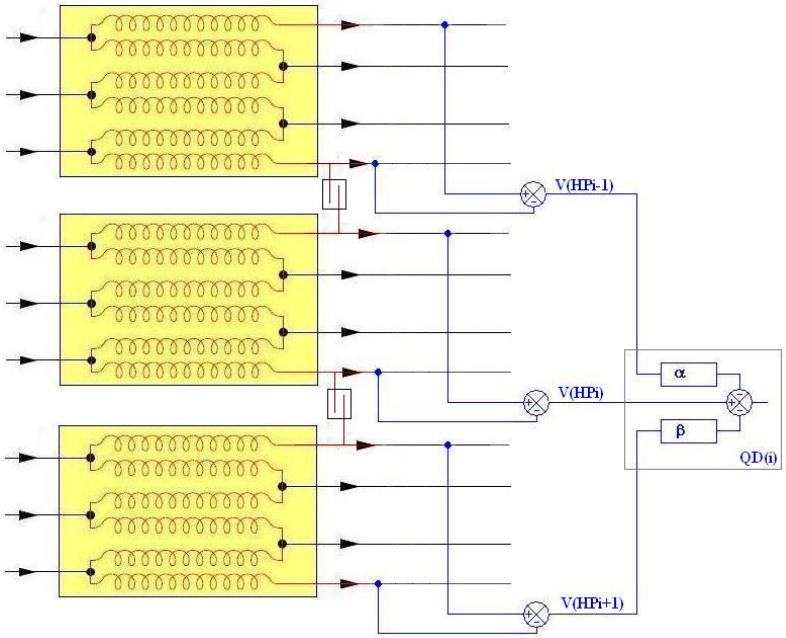

Figure 80: Cabling of the Hexa-Pancake to Hexa-Pancake with Central Difference Averaging compensation

An example of this compensation is shown in the following Figure 81.

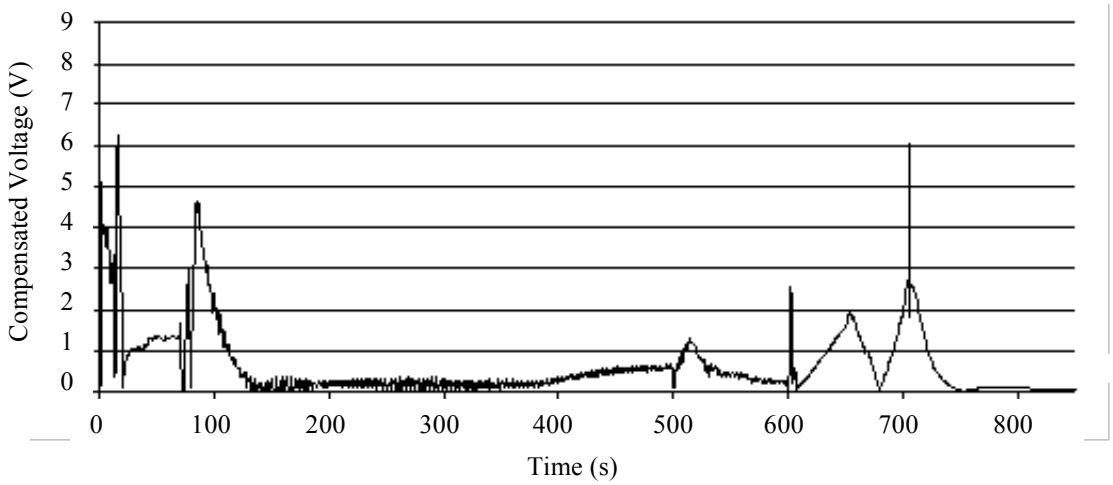

Figure 81: Compensated voltage using the three adjacent Hexa-Pancakes of CS3U

- A variant of the compensation of the voltage across an Hexa-Pancake by the voltages across the two adjacent Hexa-Pancakes does exist. It consists in taking a HP as being the quantity to be observed, and compensated with the weighted average of its top and bottom DP. Despite the fact that it provides much better results than module compensation and Hexa-Pancake compensation, the results still show that a significant holding time would have to be set. As it would require as many voltage taps as the Double-Pancake to Double-Pancake compensation described in the next paragraph, this solution brings the advantage of having a "wider" view (based on the measurement across three Pancakes).

6.3.3. Double Pancake compensation, model completion, and central difference averaging

The previously potential solutions which require a few numbers of detectors and voltage taps, do not achieve a sufficiently good attenuation of the compensated voltage, which cannot be kept under a few volts. This section presents one of the most refined solution, the compensation of a Double-Pancake, DP, by an average of the weighted voltages across the two adjacent Double-Pancakes. The monitored Double-Pancake has the index i, the upper has the index i+1 and the lower, the index i-1. The following relationship is called Central Difference Averaging, or CDA.

$$\Delta U_{DP(i)}(t) = U_{DP(i)}(t) - \frac{\alpha_i . U_{DP(i-1)}(t) + \beta_i . UDP_{(i+1)}(t)}{2} \qquad \text{Eq. 8}$$

In this equation, $U_{DP(i)}$ stands for the voltage across the Double-Pancake i, α_i and β_i are the weighting coefficients involved in the compensation unit of the Double-Pancake i, applied to the voltages respectively of the lower Double-Pancake (i-1) and the upper (i+1). These weighting coefficients are constant along time. It can be easily understood, that for the Double-Pancakes located at the extremities of the modules, such compensation is not possible, because one adjacent Pancake is missing. For this situation, depending on the location, top or bottom of the module, one of the following equations will be used.

For the Double-Pancake located at the top of the module:

$$\Delta U_{DP(i)}(t) = U_{DP(i)}(t) - \alpha_i . U_{DP(i-1)}(t) - \beta_i . U_{DP(i-2)}(t) \quad \text{Eq. 9}$$

For the Double-Pancake located at the bottom of the module:

$$\Delta U_{DP(i)}(t) = U_{DP(i)}(t) - \alpha_i . U_{DP(i+1)}(t) - \beta_i . U_{DP(i+2)}(t) \quad \text{Eq. 10}$$

Using TrapsAV, it has been possible, like for the other solutions, to calculate the voltage induced by the variation along time of the magnetic flux collected by the loop constituted by the winding of each Double-Pancake supposed closed by a voltmeter in the simplest way, which is explained in the first part of this section.

In a second part, the effect – not negligible – of the extended loop created by the measurement circuit will be discussed.

Then, the final optimized arrangement will be described, as well as the redefinition of the weighting coefficients.

a. Voltage across the winding of each Double-Pancake

Using the formulations given in 5.3.1, the voltage has been calculated across the windings of each Double-Pancake (DP) of each module. The voltage across a DP is assumed to be the sum of the voltages across the two Pancakes constituting the DP. In a first approach, the DP terminals are supposed to be infinitely close to each other, and the voltmeter is located at this place. The associated scheme can be observed in Figure 82.

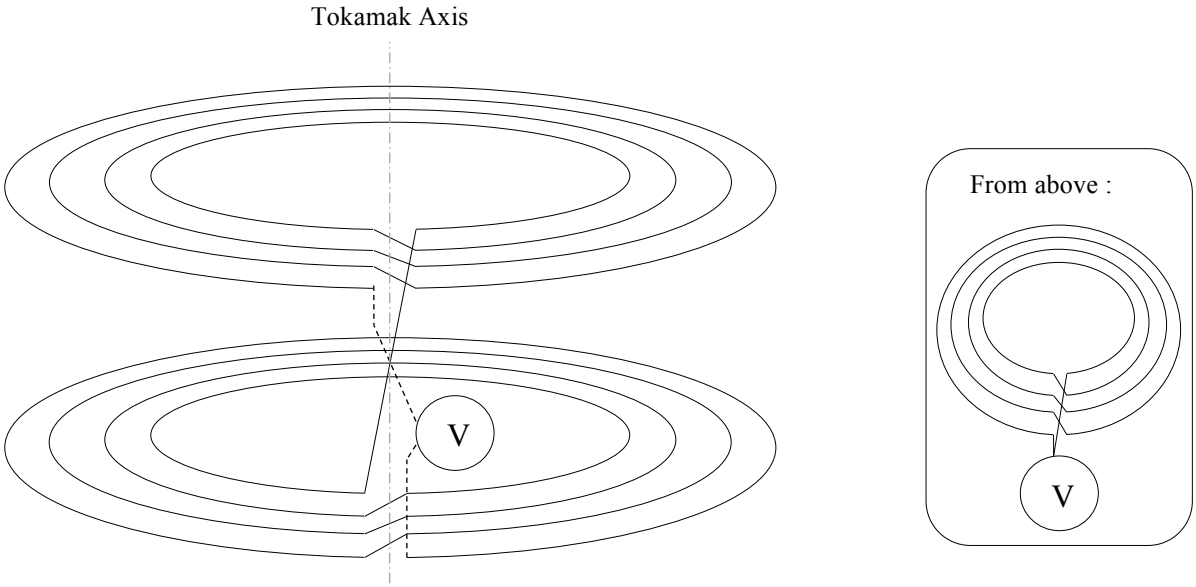

Figure 82: Double-Pancake routing in a first approach

Then with weighting coefficients α and β equal to 1, the compensation by CDA has been tested successfully, the residual voltage ΔU(t) being far lower than for the previously presented solutions. In the Figure 83 and Figure 84, the examples of CS3L and CS1L are given. These signals correspond to the maximum of the compensated voltages $|\Delta U_i(t)|$, for i

such as DP(i) belongs to the corresponding CS module. It can be concluded, that except during plasma initiation, a voltage threshold U_t of 0.55 V is not exceeded.

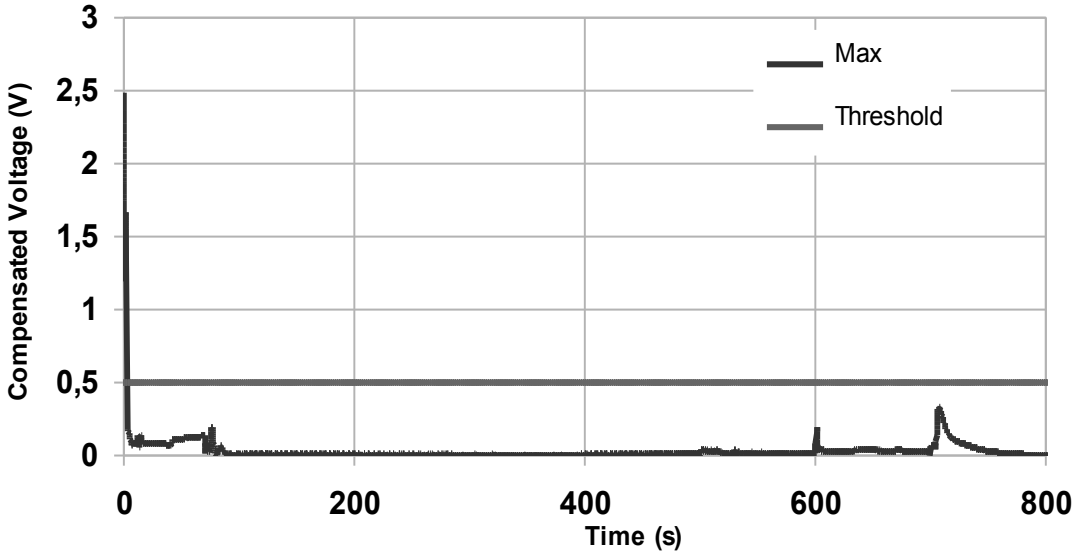

Figure 83: Envelope of the maximum of the absolute values of the compensated voltages in CS3L double Pancakes

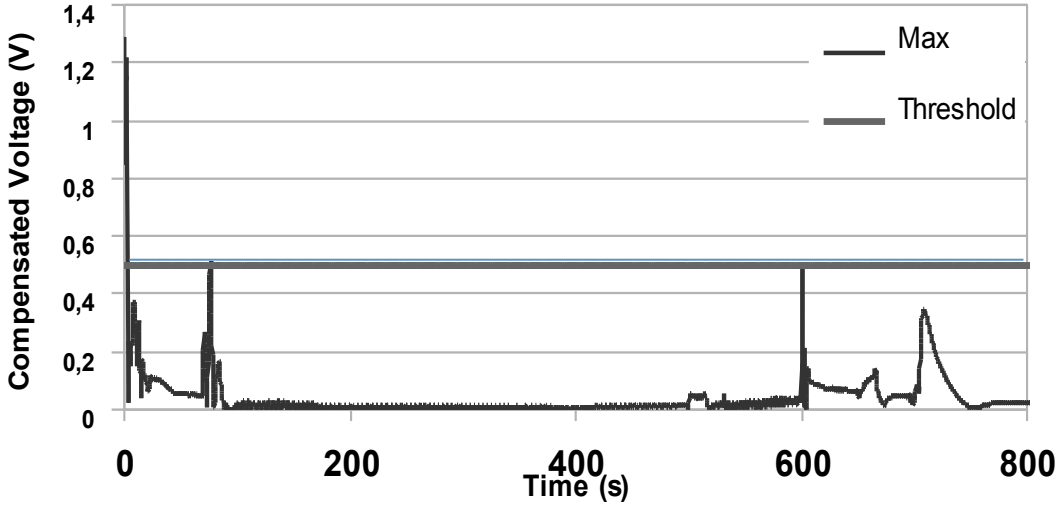

Figure 84: Envelope of the maximum of the absolute values of the compensated voltages in CS1L double Pancakes

However, weighting coefficients can further reduce the compensated voltage, but it is pointless, because the model does not take into account the measurement wires, and the model must be adapted to allow a finer study of the compensation.

b. Voltage including external routing

Figure 63, page 91 represents the CS, with its helium pipes and on them, the voltage taps. It has been demonstrated in section 5.1, that the voltage across a part of the magnet is depending on the observed winding, a pancake for instance, but also on the path taken by the measurement wires until the loop is closed. In the previous paragraph, it has been assumed that the measurement wires were stuck on the outer radius of the CS, and consequently, introduced no modification of the voltage.

Actually, the measurement wires and voltage taps are not located as assumed before, but are fixed on the helium pipes, in the inner bore of the modules, as represented in the left-hand side image of Figure 63. Figure 85, shows that the surfaces involved in the calculation

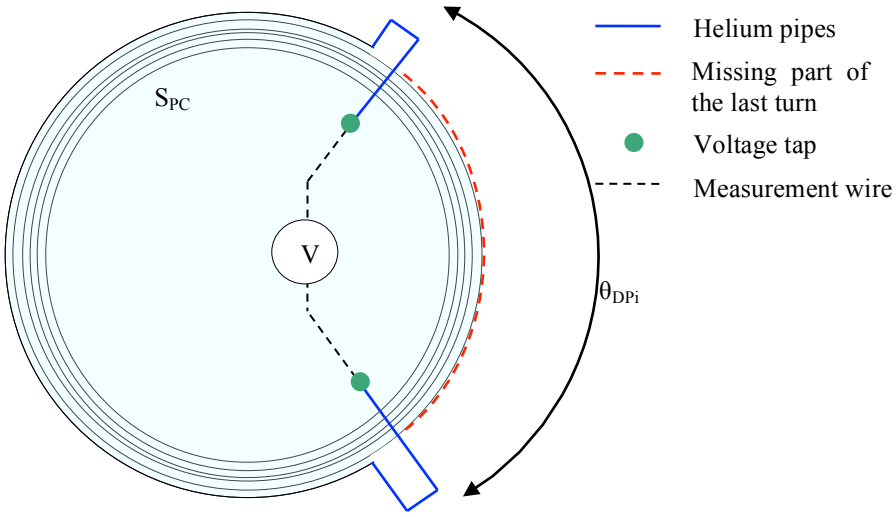

Figure 85: Projected surfaces and contours involved in the calculation of the Voltage across a circuit including the measurement wires

The voltages calculated thanks to the expressions given in section 5.3.1 are used to compute the flux through the surface S_{PC}, the contour of which, is the conductor, last turn of the Double-Pancake assumed being complete. Then, this flux is completed by the addition the flux enclosed in a surface delimited by the helium pipes, the theoretical missing part of the last turn, and the missing wires. In the CS, due to the presence of the structural components of the magnet (tigh plates), the angle θ_{DPi} refering to DPi, is depending on i, and strongly varies. This has been taken into account. It can be added, that during this part of the study, different possibilities in terms of pipes management have been studied, with the contribution of ITER organization, in order to equalize the fluxes collected by the different DPs, to ease the compensation, and thus reduce the residual voltage. The following Figure 86 gives a detail of the additional surface various locations, with respect to the position of the DP.

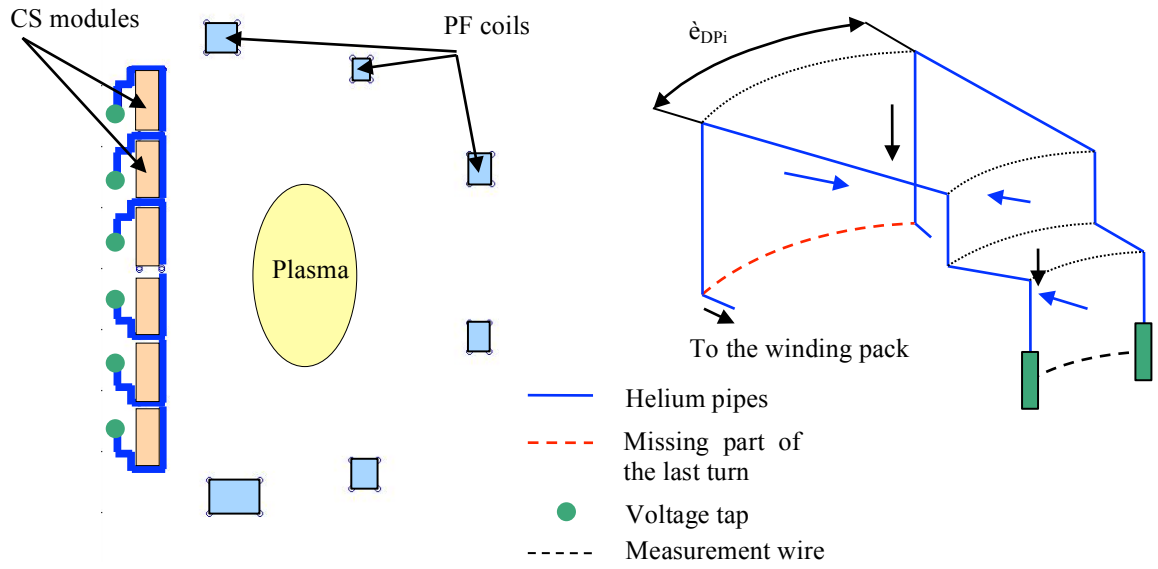

Figure 86: Additional flux collecting loop, delimited by helium pipes, and measurement wires

In this figure, it can be seen that the surface shape depends not only on the angle θ_{DPi}, but also of the elevation of the Double-Pancake, and the module in which the Double-Pancake is located. The arrows of the right-hand side scheme symbolise the vectors perpendicular to the surfaces, counting the flux as positive.

This surface has been modelled with TrapsAV, and the flux calculation has been done. The final voltage takes into account the electromotive force induced in the winding pack, the helium pipes, and the measurement wires.

The voltages $U_{DP(i)}(t)$ are obtained for each Double-Pancake, and a redefinition of the α_i and β_i has been done, trying to minimize the peak of voltage during the scenario. It has been observed that there are two events in the scenario, which cause exceptional peaks in the observed voltages, as it can be seen in Figure 83 and similar. The compensated voltages signals show peaks during the plasma initiation, and after the plasma termination, (indicated in Figure 64), due to the fast evolution of the currents in the module, which creates large variations in the magnetic field.

The plasma initiation phase has a limited duration, and the decrease of the current after plasma disappearance is controllable. For these reasons, the scenario has been studied with three versions, with adapted α and β. The difference between the versions is the duration during which the quench detection is activated. This point will be discussed in section 6.5.1. These versions are:

- Whole plasma scenario
- Plasma scenario without plasma initiation
- Plasma scenario without plasma initiation, and currents after plasma termination assumed to be decreasing slowly.

On the following Table 16 and Table 17, a summary of the key values found during this calculation has been done. Only the first and third version mentioned above are presented.

Typical signals of three DPs are represented in Figure 87. The peak voltages after compensation are located at the beginning and at then end of the plasma discharge.

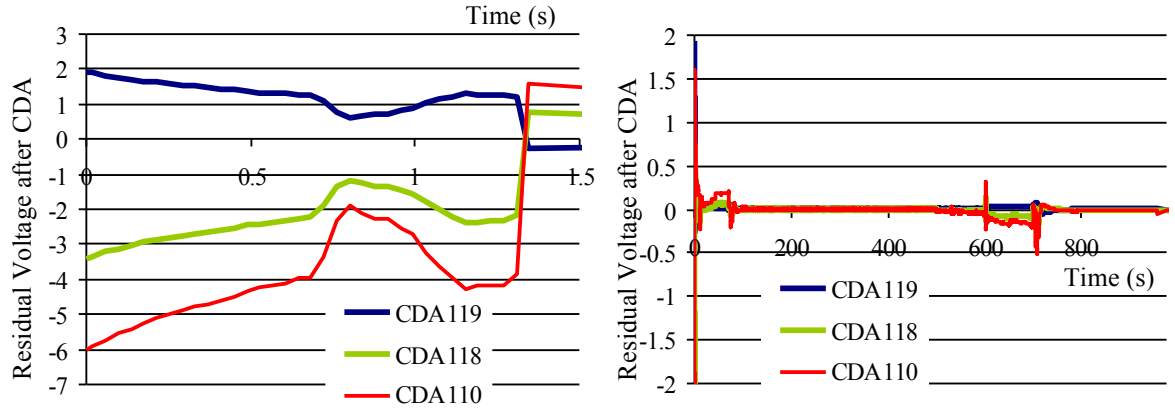

Figure 87: Compensated voltage drop across three DPs of CS2L

It can be observed thanks to the Figure 88 that the voltage across the DPs during the whole plasma current increase (~100 first seconds) is not null. In can be also observed that the phases during which the maximums of the compensated signals occur are the ones during which the maximum uncompensated voltage is obtained. These phases are the plasma initiation, and after the plasma termination (at ~700 s).

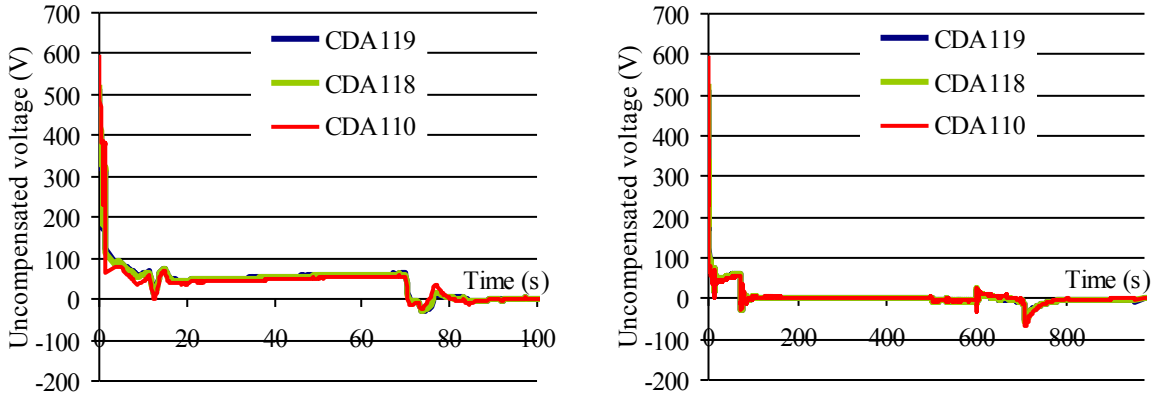

Figure 88: Uncompensated Voltage across three DPs of CS2L

In the following tables, "Threshold" is the maximum absolute value reached by the compensated signal.

Table 16: Data about voltage compensation by CDA during plasma discharge, plasma initiation and post-plasma termination included

		DP2	DP3	DP4	DP5	DP6	DP7	DP8	DP9	DP10	DP11	DP12	DP13	DP14	DP15	DP16	DP17	DP18	DP19
Angular difference (deg)		-80	-120	-40	-80	-120	-40	-80	-120	-40	-200	-40	-80	-120	-40	-80	-120	-40	-80
CS3U	Threshold	0.114	0.595	0.313	0.155	0.688	0.333	0.186	0.599	0.775	1.037	0.387	0.143	0.347	0.246	0.096	0.297	0.339	0.295
	Alpha	0.976	0.732	1.114	0.890	1.042	0.898	1.020	1.224	0.762	1.542	0.812	1.096	1.196	0.958	1.082	1.124	1.022	1.092
	Beta	1.048	1.224	0.926	1.110	0.936	1.126	0.982	0.760	1.288	0.406	1.220	0.904	0.786	1.064	0.918	0.856	1.000	0.888
CS2U	Threshold	0.289	0.869	0.432	0.191	0.892	0.402	0.299	0.701	0.689	1.106	0.405	0.192	0.427	0.315	0.166	0.348	0.324	0.331
	Alpha	0.898	0.964	0.880	0.918	0.938	0.842	0.920	1.252	0.730	1.320	0.872	1.068	1.114	0.980	1.068	1.100	1.048	1.066
	Beta	1.116	1.016	1.140	1.084	1.042	1.178	1.082	0.730	1.320	0.622	1.164	0.932	0.866	1.044	0.932	0.878	0.978	0.912
CS1U	Threshold	0.274	0.838	0.481	0.159	0.780	0.514	0.147	0.776	1.287	1.876	0.927	0.148	0.750	0.510	0.129	0.790	0.434	0.647
	Alpha	0.904	0.976	0.900	0.936	0.954	0.930	0.940	0.918	1.100	1.072	0.890	0.932	0.976	0.918	0.902	0.928	0.700	1.564
	Beta	1.114	0.996	1.126	1.064	1.018	1.096	1.060	1.054	0.956	0.864	1.148	1.070	1.000	1.106	1.100	1.048	1.324	0.414
CS1L	Threshold	0.628	0.713	0.443	0.129	0.460	0.462	0.133	0.515	1.505	1.598	0.839	0.146	0.649	0.603	0.173	0.580	0.504	0.629
	Alpha	0.212	1.862	0.346	1.208	1.654	0.542	1.110	1.452	0.126	1.770	0.706	1.086	1.224	0.934	1.066	1.144	1.016	1.088
	Beta	1.798	0.128	1.670	0.790	0.330	1.480	0.888	0.526	1.946	0.160	1.332	0.914	0.750	1.094	0.932	0.830	1.012	0.886
CS2L	Threshold	0.318	0.648	0.405	0.096	0.581	0.360	0.116	0.475	0.810	0.900	0.495	0.159	0.338	0.287	0.199	0.374	0.405	0.328
	Alpha	0.846	1.042	0.804	0.940	1.068	0.796	0.942	1.166	0.584	1.408	0.740	0.996	1.140	0.854	1.010	1.122	0.952	1.100
	Beta	1.168	0.938	1.216	1.062	0.912	1.226	1.060	0.816	1.470	0.532	1.296	1.006	0.838	1.172	0.992	0.854	1.076	0.876
CS3L	Threshold	0.413	0.503	0.510	0.088	0.529	0.377	0.043	0.515	0.844	1.116	0.299	0.149	0.261	0.163	0.140	0.036	0.321	0.113
	Alpha	0.858	0.952	0.912	0.952	1.092	0.892	0.910	1.034	0.778	1.306	0.518	0.942	1.402	0.730	1.108	1.278	0.934	1.166
	Beta	1.152	1.036	1.104	1.050	0.896	1.124	1.094	0.954	1.260	0.650	1.520	1.064	0.568	1.304	0.888	0.690	1.098	0.804

In this figure, it can be seen that this compensation is likely to be not effective enough to ensure a sufficiently low threshold such that the propagation time needed to reach this value could be done in less than τ_{da}. In the following Table 17, the statistics are updated, with α and β recalculated for the scenario without the plasma initiation phase. The possibility of ignoring the plasma initiation will be confirmed later, in paragraph 6.5.2.

Table 17: Data about voltage compensation by weighted CDA during plasma discharge, plasma initiation and post-plasma termination excluded

		DP2	DP3	DP4	DP5	DP6	DP7	DP8	DP9	DP10	DP11	DP12	DP13	DP14	DP15	DP16	DP17	DP18	DP19	
Angular difference (deg)		-80	-120	-40	-80	-120	-40	-80	-120	-40	-200	-40	-80	-120	-40	-80	-120	-40	-80	
																				Max
CS3U	Threshold	0.080	0.321	0.142	0.078	0.294	0.117	0.078	0.203	0.236	0.361	0.123	0.054	0.127	0.058	0.042	0.115	0.060	0.114	0.36
	Alpha	0.942	1.032	0.930	0.990	1.156	0.888	1.064	1.286	0.742	1.422	0.916	1.086	1.152	1.020	1.082	1.110	1.066	1.082	
	Beta	1.076	0.960	1.092	1.016	0.840	1.130	0.942	0.712	1.294	0.544	1.114	0.918	0.836	1.000	0.920	0.876	0.954	0.904	
CS2U	Threshold	0.065	0.269	0.103	0.082	0.316	0.095	0.126	0.412	0.346	0.905	0.233	0.159	0.298	0.084	0.097	0.223	0.087	0.203	0.41
	Alpha	0.920	0.912	0.930	0.916	0.866	0.958	0.912	0.940	1.044	0.878	0.884	1.102	1.218	1.030	1.094	1.132	1.064	1.092	
	Beta	1.096	1.066	1.092	1.086	1.112	1.064	1.090	1.040	0.998	1.068	1.148	0.898	0.766	0.992	0.906	0.850	0.958	0.890	
CS1U	Threshold	0.053	0.064	0.058	0.030	0.059	0.049	0.034	0.057	0.105	0.130	0.087	0.024	0.085	0.059	0.036	0.141	0.094	0.182	0.18
	Alpha	0.900	0.948	0.908	0.938	0.924	0.952	0.950	0.882	1.090	0.652	1.186	0.926	0.708	1.132	0.976	0.786	1.186	0.780	
	Beta	1.114	1.030	1.114	1.064	1.054	1.070	1.052	1.096	0.954	1.292	0.854	1.076	1.270	0.890	1.026	1.196	0.836	1.204	
CS1L	Threshold	0.179	0.287	0.171	0.049	0.164	0.077	0.034	0.083	0.131	0.127	0.062	0.026	0.038	0.043	0.029	0.042	0.057	0.040	0.29
	Alpha	0.640	1.512	0.518	0.984	1.654	0.582	1.080	1.444	0.212	1.844	0.686	1.064	1.240	0.918	1.066	1.170	0.996	1.118	
	Beta	1.368	0.482	1.494	1.018	0.330	1.436	0.920	0.538	1.842	0.100	1.346	0.936	0.740	1.104	0.934	0.808	1.028	0.860	
CS2L	Threshold	0.070	0.144	0.091	0.031	0.140	0.079	0.027	0.138	0.158	0.266	0.045	0.108	0.072	0.220	0.106	0.073	0.256	0.087	0.27
	Alpha	0.878	0.982	0.848	0.922	0.994	0.828	0.904	0.998	0.652	1.178	0.618	0.966	1.248	0.766	1.162	1.152	1.262	1.050	
	Beta	1.132	1.006	1.168	1.080	0.994	1.188	1.100	0.990	1.392	0.778	1.414	1.040	0.732	1.266	0.832	0.826	0.742	0.934	
CS3L	Threshold	0.086	0.188	0.124	0.023	0.170	0.095	0.026	0.143	0.206	0.253	0.034	0.038	0.049	0.058	0.041	0.019	0.120	0.051	0.25
	Alpha	0.868	1.000	0.832	0.916	1.044	0.772	0.924	1.130	0.428	1.630	0.582	0.972	1.264	0.702	0.998	1.250	0.844	1.180	
	Beta	1.142	0.992	1.182	1.088	0.948	1.244	1.080	0.858	1.620	0.312	1.456	1.030	0.710	1.330	1.004	0.720	1.192	0.790	

In this Table 17:

- the monitored DP index is shown on the first line. DP1 is the double Pancake at the bottom of the considered Module
- The angular difference is θ_{DPi} indicated in Figure 86
- Threshold line contains the maximum value reached by the compensated signal. A green cell just indicates that this value is under 0.55 V. This value will be explained in the next section 6.3.4.
- The alpha and beta lines contain the values for α and β.

The algorithm used for determination of the α and β coefficients has another step consisting in determining the accuracy of the coefficients. Starting from the general formula which is recalled:

$$\Delta U_{DP(i)}(t) = U_{DP(i)}(t) - \frac{\alpha.U_{DP(i-1)}(t) + \beta.U_{DP(i+1)}(t)}{2}$$

α is the weighting coefficient associated with the adjacent lower DP

β is the weighting coefficient associated with the adjacent higher DP

$U_{DP(i)}(t)$ is the potential difference across the DP number i voltage taps. The couple (α ; β) which minimizes the maximum of the compensated voltage attained during the scenario is determined. In a second step, the maximum allowable deviation by positive and negative value is determined after the following equation:

$$\Delta U_{DP(i)}(t) = U_{DP(i)}(t) - \frac{\alpha.(1+\varepsilon).U_{DP(i-1)}(t) + \beta.(1+\varepsilon).U_{DP(i+1)}(t)}{2}$$

ε is a deviation: if ε is equal to 0, the α or β is considered as exact. If it is non null, the coefficient is exact with ε % tolerance.

If the negative value of ε is called ε_{min} and the positive one ε_{max}, these values can be calculated with S being the threshold, here 0.55 V, this choice is justified later:

$$\varepsilon_{mini}(t) = \frac{2.(U_{DP(i)} - S)}{\beta.U_{DP(i+1)} + \alpha.U_{DP(i-1)}} - 1$$

and

$$\varepsilon_{maxi}(t) = \frac{2.(U_{DP(i)} + S)}{\beta.U_{DP(i+1)} + \alpha.U_{DP(i-1)}} - 1$$

$$\varepsilon_{min} = \min(\varepsilon_{mini}(t))$$

$$\varepsilon_{max} = \min(\varepsilon_{max\,i}(t))$$

And finally

$$\text{Accuracy} = \min(\varepsilon_{mini}; \varepsilon_{maxi})$$

The final result of this study, is that α and β must be defined at their optimal values plus or minus 0.24%

6.3.4. Conclusion of the electromagnetic study

This study aimed at finding a signal processing allowing a reduction of the residual compensated voltage on a CDA compensation during the ITER reference scenario. This study includes practical and technological aspects of a quench detection system at a large scale, including options of redundancy, cabling, tolerances of the parameters, reliability of the model, and many other aspects. It has been shown that the compensation does not prevent the compensated signals from reaching important voltage peaks but with limited duration (3 seconds during plasma initiation).

Moreover, with the CDA as defined in 6.3.3, the link between U_Q and U_t can be defined. Assuming that the DPi is quenching, the current positive, and ΔU_i closer to $-U_t$ than to U_t, such as presented in the following Figure 89.

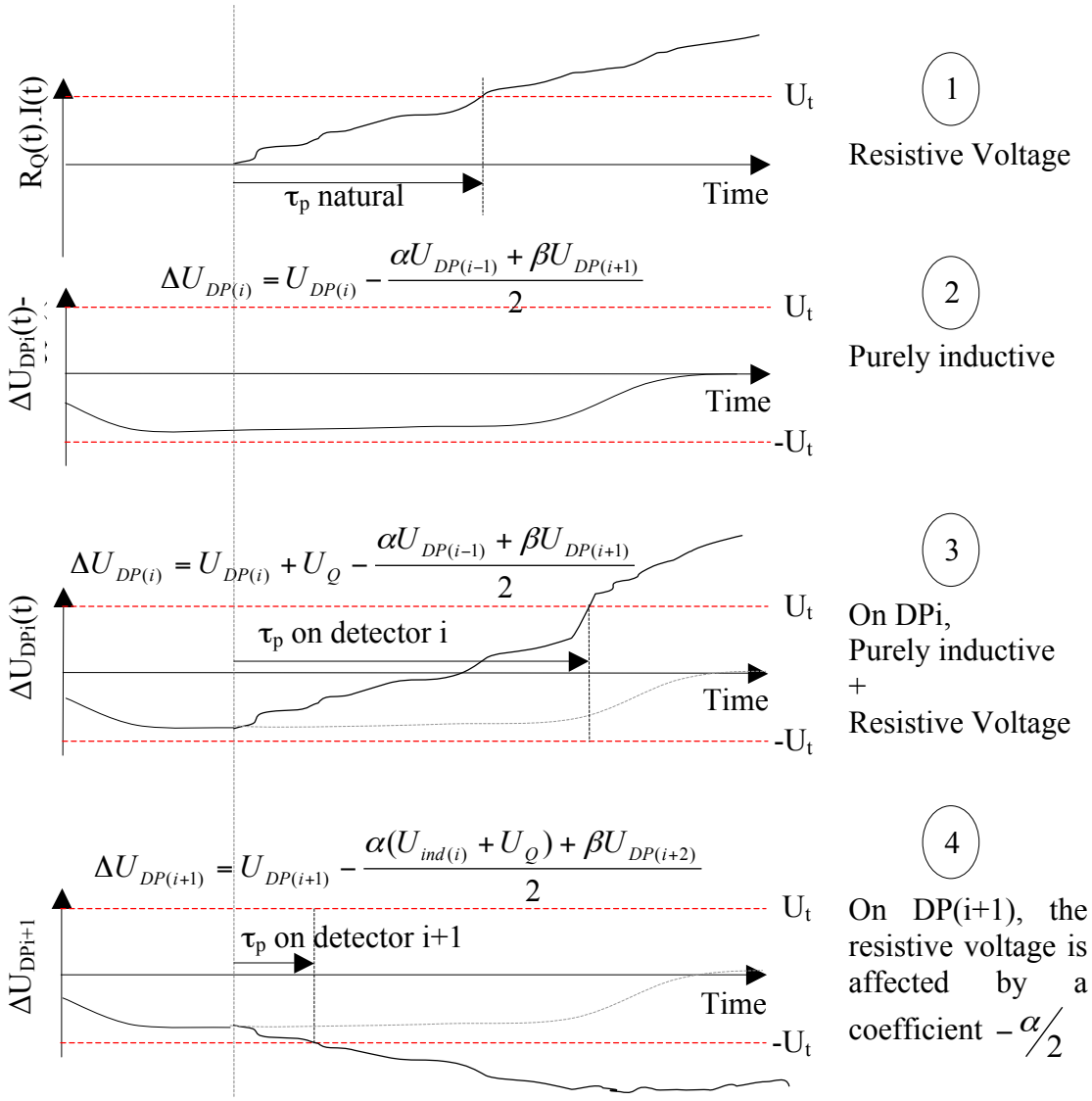

Figure 89: The voltage across DP(i) is involved in the CDA of DPi+1 and DP(i-1)

The Figure 89 can be explained as follows:

- 1. In the first curve, a quench voltage $R_Q(t).I(t)$ is represented. The voltage increases, as the quenched length becomes wider. In addition, the increasing temperature reinforces the resistivity of the copper.

- 2. The second curve is the compensated voltage delivered by the detector which monitors the DPi, in absence of a quench. It is called ΔU_{DPi}. It is shown, that due to the magnetic asymmetry, the compensation is not perfect, and the residual voltage is close to $-U_t$. It causes no trigger of the countdown to the FSD, since $|\Delta U| < |U_t|$.

- 3. If a quench occurs, the signals presented in drawings 1 and 2 must be added. The curve in 3 illustrates the observed effect on detector monitoring DPi. The compensated voltage needs a long time to reach the threshold U_t.

- 4. In the equation which rules the detector monitoring the adjacent double pancake (i+1), the voltage across DPi is affected by a coefficient $-\alpha/2$. Consequently, the compensated voltage does not increase, but decreases, and reaches rapidly the lower threshold $-U_t$.

In conclusion, in some cases, the quench is detected faster by a detector monitoring the adjacent double pancake than by the detector of the quenching double pancake. This effect helps the detection, since in the worst case, the quench voltage U_Q does not need to reach 2 U_t such that it can be detected.

This principle, illustrated above in Figure 89, can be explained analytically as follows, considering:

$\Delta U_{DP(i)}$ is the compensated voltage such as presented in Eq. 8, page 106

U_t is the absolute value of the threshold

$U_{ind(i)}$, the voltage induced by a magnetic flux change across a double Pancake i

$R_Q(t).I(t)$ the voltage caused by the quench

$$U_{DP(i)} = U_{ind(i)} + R_Q(t).I(t)$$

In absence of a resistive signal (no quench):

$$\Delta U_{DP(i)}(t) = U_{DP(i)} - \frac{\alpha U_{DP(i-1)} + \beta U_{DP(i+1)}}{2} = U_{ind(i)} - \frac{\alpha U_{DP(i-1)} + \beta U_{DP(i+1)}}{2}$$

In presence of a quench, a resistive signal is superposed which is $R_Q(t)I(t)$:

$$\Delta U_{DP(i)}(t) = U_{DP(i)} - \frac{\alpha U_{DP(i-1)} + \beta U_{DP(i+1)}}{2} = U_{ind(i)} + R_Q I(t) - \frac{\alpha U_{DP(i-1)} + \beta U_{DP(i+1)}}{2}$$

In presence of a positive inductive compensated signal as it is the case for DP23 just before 700 s (see Figure 90), as the current is negative at that time, the resistive voltage has to decrease 1.5 times the threshold value U_t, in order to reach negatively the threshold at $-U_t$.

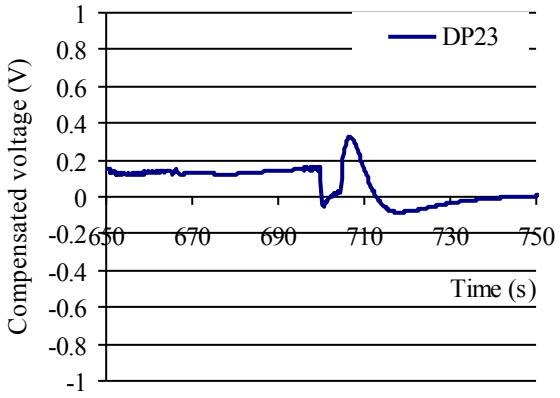

Figure 90: Compensated voltage across DP23 (CS2L)

Let us examine the situation on the next double Pancake where the decreasing resistive voltage is also playing a role, but divided by a factor α/2 and counted negatively.

$$\Delta U_{DP(i+1)}(t) = U_{DP(i+1)} - \frac{\alpha U_{DP(i-1)} + \beta U_{DP(i+1)}}{2} = U_{ind(i+1)} - \frac{\alpha(U_{ind(i)} + R_Q.I(t)) + \beta U_{DP(i+2)}}{2}$$

$$\Delta U_{DP(i+1)}(t) = U_{DP(i+1)} - \frac{\alpha U_{ind(i)} + \beta U_{DP(i+2)}}{2} - \frac{\alpha}{2} R_Q I(t)$$

The threshold is reached this time positively, assuming that the compensated voltage across DP(i) and DP(i+1) is approximately the same in absence of quench:

$$U_{ind(i)} - \frac{\alpha U_{DP(i-1)} + \beta U_{DP(i+1)}}{2} \approx U_{DPi+1} - \frac{\alpha U_{ind(i)} + \beta U_{DP(i+2)}}{2}$$

According to the residual voltage $\Delta U_{DP(i)}$ and $\Delta U_{DP(i+1)}$ the quench can be detected earlier on Double-Pancake i or Double-Pancake i+1. It is simultaneously detected on the two detectors (which is the worst case) when:

$$U_t - \Delta U_{DP(i)} = -U_t - \Delta U_{DP(i+1)}$$

$$U_t - \left(U_{ind(i)} + R_Q I(t) - \frac{\alpha U_{DP(i-1)} + \beta U_{DP(i+1)}}{2} \right) = -U_t - \left(U_{DPi+1} - \frac{\alpha U_{ind(i)} + \beta U_{DP(i+2)}}{2} - \frac{\alpha}{2} R_Q I(t) \right)$$

Finally:

$$U_t - R_Q I(t) = -U_t + \frac{\alpha}{2} R_Q I(t)$$

$$2U_t = \left(1 + \frac{\alpha}{2} \right) U_Q$$

The resistive voltage to reach the threshold is:

$$U_Q = \frac{4}{2+\alpha} U_t$$

Considering that in a first approach, the weighting coefficients are close to 1., it comes:

$$U_Q \approx \frac{4}{3} U_t$$

6.4. Hot spot criterion applied to the Central Solenoid conductor

The last unknown to be estimated, is the maximum τ_{da} allowed, such as the temperature at the end of the fast discharge stays below 250 K, as explained in 3.5. To estimate τ_{da} per module it is necessary to calculate the hot spot criterion according to the modules. The calculations are classically done using the conductor parameters presented in Table 18 and assuming an exponential discharge of the current module of 7.5 s. The magnetic field of the pancake is assumed to decrease proportionally as a function of the current for the calculation of the copper magnetoresistivity along the safety discharge. The hot spot has to be, according to the criterion, at a maximum temperature of 250 K at the end of the FSD.

Table 18: Characteristics of CS conductor

	CS conductor	
Type of strand	Nb_3Sn	
ITER cycle phase	SOD	EOB
Maximum operation current (kA)	40.	46
Peak field (T)	13	12.7
Operating temperature (K)	@ peak field 4.5	
Non copper (mm^2) untwisted [twisted]	154.3 [160.8]	
Total copper (mm^2) untwisted [twisted]	308.6 [321.5]	
Time constant of the fast safety discharge (s)	7.5	
Cooling channel length, (m)	150	

As the power dissipated by joule heating evolves with the square of the current, the limiting τ_{da} will be found at the time of the plasma discharge when the current is maximal.

The scenario for currents carried by the CS modules conductors are presented in Figure 64. In the following Table 19, the maximum values of the current carried by the various CS modules.

Table 19: Maximum current in the CS modules

	CS module conductor maximum current (kA)	Corresponding scenario phase	Maximum magnetic field
CS3U	40.0	t = 0 s	13 T
CS2U	40.0	t = 0 s	13 T
CS1U	45.4	t = 516 s	12.7 T
CS1L	45.4	t = 516 s	12.7 T
CS2L	40.0	t = 0 s	13 T
CS3L	34.85	t = 0 s	13 T

It is recalled, that the electrical resistance of a material is also depending on the magnetic field. Consequently, this dependence has been shown for the two representative cases, CS1U and L on one hand, and the other modules in the other hand, as depicted in Figure 91. The hot spot has been calculated with the current kept constant at its maximum value.

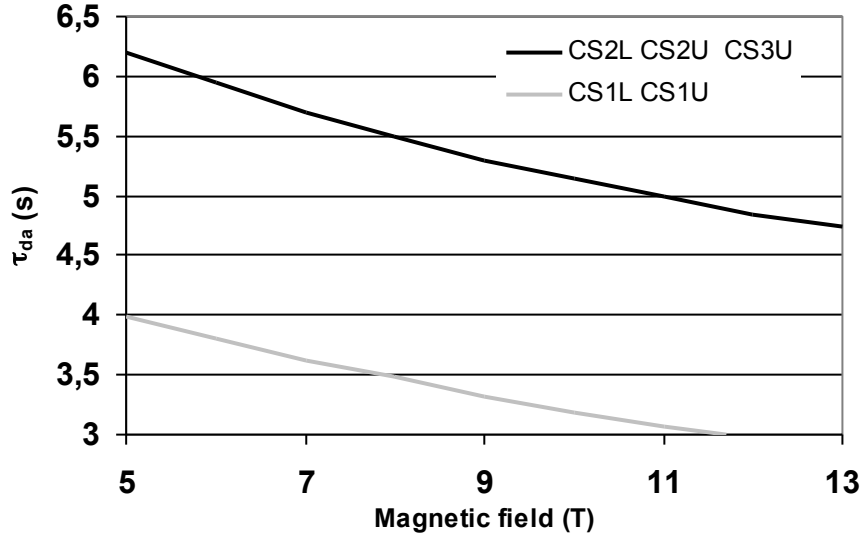

Figure 91: Maximum allowed detection and action time with respect to the magnetic field

It can be seen in this figure, that the higher the magnetic field is, the lower the maximum detection and action time is. Consequently, the values to be used are the τ_{da} corresponding to the maximum field of the considered module. These figures also help appreciating the evolution of the τ_{da} in case of quench deeper in the winding, in the other turns. The following table sums up the values taken for τ_{da}. It is to be noted that in spite of the lower value of the maximum current for CS3L, τ_{da} will be taken conservatively at the same value as the modules CS2U and L, and CS3U. In conclusion, the most restrictive modules are CS1U and CS1L, due to their higher currents.

Table 20: Selected values of τ_{da} for the various CS modules

Module	τ_{da} (s)
CS1U, CS1L	3
CS2U, CS2L, CS3U	4.75
CS3L	7.5

6.5. Selected Solution for the ITER CS for regular double pancake detectors (RDPD)

The results presented in this section can be found in [58].

According to the observations resulting from the use of TrapsAV, no inductive voltage should exceed significantly 0.55 V and it is decided to set up the threshold voltage at ± 0.55 V.

The minimum resistive voltage to overcome positively or negatively the threshold voltage is approximately $4U_t/3$, which corresponds to 0.73 V. The propagating time to reach this value supposing a quench initiated at the CS inner radius depends on the module and has been

evaluated in section 6.2.4. Knowing τ_{da} , τ_p and τ_{cb} (0.5 s at maximum) it is possible to deduce the maximum threshold time τ_h, which is the filtering time aimed at avoiding any false activation of the FSD according to the formula below presented in Eq. 1, section 3.4.

$$\tau_h \leq \tau_{da} - \tau_p(U_t) - \tau_{cb}$$

In the next sections, the values of τ_{da} will be given according to each module, and the selected solution will be presented.

6.5.1. A solution to eliminate inductive disturbance at plasma initiation: the blanking

It has been seen in section 6.1.3, in Figure 64 that the plasma initiation duration exceeds 3 seconds, which is the total available detection and action time. Therefore, whatever the selection of τ_p and U_t is, the FSD would be triggered during every plasma discharge beginning. However, it can be observed in Figure 92 that the current decrease rate is very high during plasma initiation. Therefore, the assumption, which has been made for the hot spot criterion, (i.e. a current at constant value before the fast safety discharge), is not valid anymore, and a dedicated study has been performed, to recalculate the available τ_{da} taking into account this decrease of current. The aim of this study is to prove that the quench monitoring could be suppressed during this special phase only.

This idea came from the fact that the current decrease rate during plasma initiation is similar to the beginning of a FSD, as shown in Figure 92. It can be deduced that if a quench is initiated during, or before the plasma initiation, this phase would not endanger the magnet integrity, because no significant more energy would be released during this phase, than it would be during a FSD.

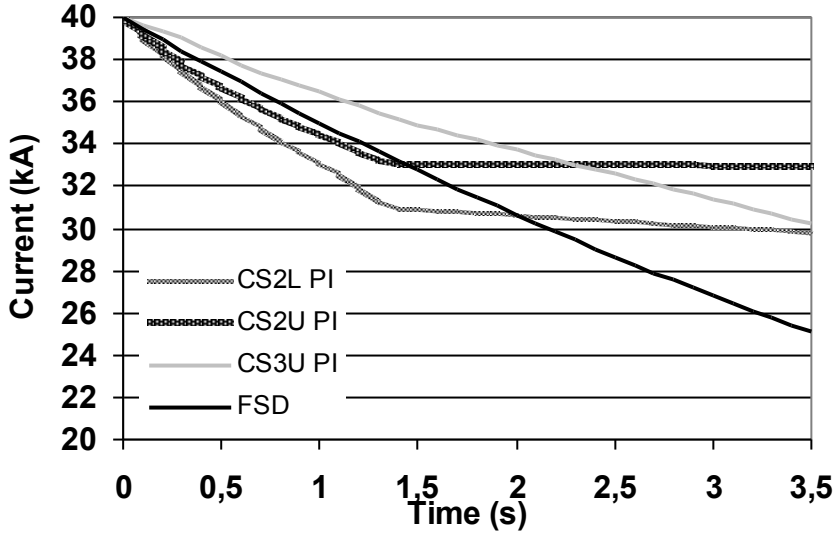

Figure 92: current during a FSD and during PI for CS2L, CS2U and CS3U

It can be also calculated that the integral of $j(t)^2$ during the 3.5 first seconds of a FSD starting at 40 kA (called FSD3.5) has the same order of magnitude as during the 3.5 first seconds of the scenario plasma initiation (called PI). This is shown in Table 21.

Table 21: Integration of the square of the current density during first seconds of the FSD and PI

Modules	CS3L	CS2L	CS1	CS2U	CS3U
I_0	34 kA	40kA	38.05 kA	40kA	40kA
$\int_{FSD3.5} j^2(t)dt$	$2.76\ 10^9$	$3.64\ 10^9$	$3.30\ 10^9$	$3.64\ 10^9$	$3.63\ 10^9$
$\int_{PI} j^2(t)dt$	$2.88\ 10^9$	$3.84\ 10^9$	$4.10\ 10^9$	$4.26\ 10^9$	$4.48\ 10^9$

6.5.2. Practical application of blanking during plasma initiation

In the worst possible scenario, a quench is triggered a few seconds before the plasma initiation, when the current is maximum for the modules (except for CS1 U&L). The quench starts propagating, reaches the U_t value within $\tau_p(U_Q)$, and the holding time τ_h starts elapsing. At the moment when a quench is identified, instead of triggering the FSD, the plasma initiation starts, and the quench alert signal is ignored for the 3.5 s duration of the plasma initiation. Then, taking back the quench signal into account, which is still present and even larger, the τ_h must be elapsed again, before triggering the opening of the current breakers. This process is illustrated in the following Figure 93.

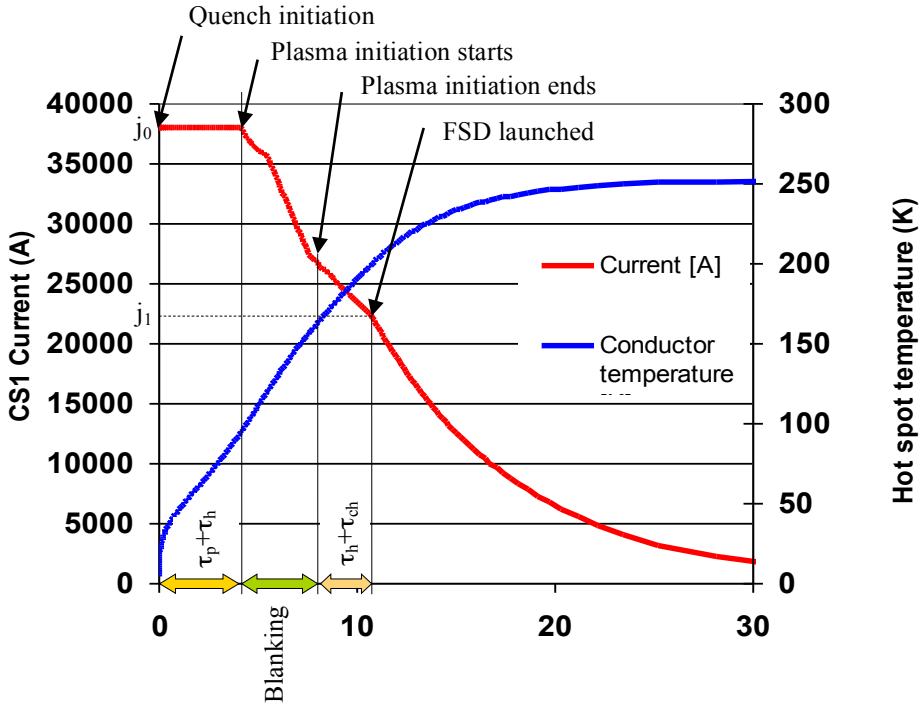

Figure 93: History of the quench detection with blanking, with varying current along time

It is possible to calculate the hot spot using classically an excel file for the normal case of the fast safety discharge or for the case with blanking. In case of blanking the plasma scenario is integrated according to the modules.

τ_p and τ_{cb} are known and the maximum. τ_h can be calculated according to the hot spot. Note that for τ_p in case of blanking a resistive voltage of 0.55 V is considered (instead of 0.73 V for a normal FSD) as during the plateau, the inductive disturbances are supposed negligible.

$$\tau_{da} \geq \tau_p + \tau_{cb} + \tau_h$$

The maximum τ_h is presented in Table 22 according to the modules. It can be seen that τ_{da} is lower in case of blanking as in the case of a normal fast safety discharge, for all the modules excepted CS1L and CS1U, which have higher current somewhere else in the scenario (end of plasma current flattop). It is understandable from Figure 92 and Table 21. Note also that τ_h is applied two times in case of blanking. The consequence is that τ_h is lower for the case when blanking is considered. It means that it is the reference case for the detection parameters.

Table 22: Maximum τ_h according to the CS modules when blanking during plasma initiation

Modules	CS3L	CS2L	CS1L CS1U	CS2U	CS3U
τ_{da}	7.5 s	4.75 s	3 s	4.75 s	4.75 s
$\tau_{dablanking}$	5.6 s	3.7 s	4.4 s	2.8 s	3.8 s
τ_p (0.55 V)	2.1 s	1.1 s	1.1 s	1.1 s	1.4 s
τ_{cb}	0.5 s	0.5 s	0.5 s	0.5 s	0.5 s
τ_h	3.0 s	2.1 s	2.8 s	1.2 s	1.9 s

It can be seen that Table 22 is consistent with the choice of τ_h =1.2 s, for all the modules to simplify the detection system. CS2U is at the limit due to the slowest decrease of coil current for this module and a kind of plateau starting at t=1.5 s (see Figure 93).

The number of quench detection units (QDUs) of this type is 108. The same solution will be adopted for all the QDUs: U_t = ±0.55 V and τ_h = 1.2 s with a blanking of the detection during the first 3.5 s of the plasma discharge.

6.5.3. End double pancake detectors (EDPD)

For the pancakes situated at the extremities of the modules, the ones that are situated at the top and at the bottom of each module, it is not possible to apply Eq. 8. As a matter of fact these double pancakes are not inserted between two Double Pancakes of the same module on which the compensation can be made.

Two new relations Eq. 9 and Eq. 10 presented in 6.3.3 are proposed, involving the two pancakes located in the vicinity of the pancake. This cannot be done in this case without using balance coefficients α and β.

Using TrapsAV it can be shown that it is possible to find α and β such as the inductive signal does not exceed 0.5 V except during the 3.5 seconds which leads to a situation similar to the one observed on the regular double pancakes.

The number of QDUs of this type is 12. The same solution will be adopted for all the QDUs: U_t = ±0.55 V and τ_h =1.2 s with a blanking of the detection during the first 3.5 s of the plasma discharge.

6.5.4. Module quench detector (MQD)

The most critical simultaneous quench that can happen, is the quench of the whole CS module. In the case where all the quenches are supposed to be developing at the same rate, none of the QDUs will detect the quench, as every compensated voltage will remain between the thresholds.

At this moment, the module located under the quenched one (or the module over it), is considered as not quenched. The compensation will be made thanks to the voltage of the last pancakes of the not quenched modules. With the same logic as described for the DP located at the extremities of the modules. For instance, for CS2L/CS3L:

$$\Delta U_{DP20} = U_{DP20} - \alpha_{20} U_{DP21} - \beta_{20}(U_{DP21} - U_{DP22}) \qquad \alpha_{20}=1.001 \qquad \beta_{20}=1.6$$

$$\Delta U_{DP21} = U_{DP21} - \alpha_{21} U_{DP20} - \beta_{21}(U_{DP20} - U_{DP19}) \qquad \alpha_{21}=1. \qquad \beta_{21}=2.$$

The number of QDUs of this type is 10. The same solution will be adopted for all the QDUs: $U_t = \pm 0.55$ V and $\tau_h = 1.2$ s with a blanking of the detection during the first 3.5 s of the plasma discharge.

6.5.5. Conclusion for CS quench detection

To detect a quench in the ITER CS, a solution has been selected based on the differential voltage monitoring of the 120 double pancakes. This solution consists in compensating the inductive differential voltage of each CS double pancake by the differential voltage of the two neighbouring double pancakes (RDPD). This generic solution does not require additional pick up coils, the insulation of which is difficult in the environment of the ITER CS. The access to the double pancake differential voltages is easy as they are all located at the external radius of the CS.

12 additional detectors based on the same principle are necessary for the double pancakes situated at the extremities (EDPD) and 10 other additional detectors are necessary to monitor the quench detection of a whole CS module (MQD).

The threshold voltage is chosen at a level which should never been exceeded during the plasma discharge, which is ±0.55 V for the RDPDs and EDPDs and ±1.V for the MQDs.

The holding time has been conservatively set at 1.2 s for all detectors to be sure that a quench detection is not falsely activated.

As recommended by ITER Organization, the parameters of the detection do not change along the scenario, however a blanking of the detection has been selected for the first 3.5 seconds of the plasma discharge, which corresponds to large inductive signals, the exact description of which is difficult. As the CS is experiencing a fast discharge during this phase which is not so different from the FSD, it has been demonstrated that a quench initiation in this phase or during the current plateau just before this phase will result in an adiabatic hot spot at a temperature under 250 K on the cable. Moreover, if needed, the detection and action time can be recalculated, taking into account the wraps and central spiral. They are part of the cable, and provide additional enthalpy above 50 K. Doing so will extend the holding time, or allow a higher voltage threshold.

To select this solution, tools have been developed such as TrapsAV. A method has been followed: calculation of inductive voltage, use of Gandalf to calculate propagation time, calculation of adiabatic hot spots associated with normal FSD or including the plasma initiation with blanking. This method is available for further studies regarding other scenarios or particular plasma events. The parameters selected for the detections include a certain flexibility, which can be used for further refinement. Nevertheless the following values can be retained:

$U_t = 0.55$ V

And

$\tau_h = 1.2$ s

7. Quench detection in the ITER TF system

Iter CS is a strongly pulsed magnet, but TF has the smallest available detection and action time. Chapter 7 will present a solution for the quench detection in this crucial system.

The main roles and a general description of the TF system are given in section 1.1.4.

At variance with the PF and the CS systems (refer to [16] and [18]), the TF system of a tokamak is a steady state system. Except during the ramping phase of the current, which should occur less than daily (1000 TF charging cycles in the DDD), the TF current is almost constant during normal operation. Inductive voltages should therefore be less important across the TF than across the PF and the CS and the quench easier to be discriminated.

However, due to the large stored energy and the small allowed number of fast discharges (50), more severe requirements are put in the DDD [15] for the TF system in comparison with the PF and CS systems, aiming to avoid any fast discharge not related to a quench[19]:

"The magnet quench detection system will be able to distinguish between superconductor quench and the electromagnetic perturbations caused by a plasma disruption with a reliability of >90% for the CS, CC and PF coils for type I and II disruptions and type II and III VDEs and >99.9% for the TF coils for type I and II disruptions and type II and III VDEs. The quench detection system of the coils (particularly the TF) must be designed to allow possible tuning during commissioning as experience with plasma behaviour is obtained.

The TF quench detection system will be able to distinguish between a fast discharge of the CS, PF and CC coils and a TF superconductor quench with a reliability >99.9%.

A fast discharge of the TF system will require a fast discharge of all coils (TF, CS, PF and CC). Fast discharge of a CS or PF coil will require an associated fast discharge only of the CS and PF system. A quench of the CC will require a fast discharge only of the CC system."

As explained in [15] the quench detection system protecting the TF Coils system relies on the surveillance of the electrical signature of the quench, introduced in section 3.1.2. Moreover, a proposition based on a redundant co-wound tape, which is described in section 7.2.3 is proposed in the ITER design description document. The aim of this chapter is to examine whether a quench detection based on a co-wound tape is compulsory to ensure the inductive voltage compensation (EAST system) [60] or whether the balance of the voltage of two TF coils is sufficient (Tore Supra, KSTAR) [59]. This co-wound tape, tightly bound to the TF conductor, is expected to provide the best compensation of any induced electromotive force in the TF winding. Nevertheless, it is very convenient being able to rely on a maintainable system (voltage taps are accessible, under the TF coils, and not in the depth of the winding).

A difficulty for the TF quench detection is that the inductive voltage cannot be estimated as easily as for the PF and the CS system. For the CS and PF systems, it is possible in theory to calculate the voltage across the different components during for instance a plasma discharge. It will be shown that the voltage is more difficult to predict for the ITER TF system, thanks to observations of signals coming from the French tokamak Tore Supra.

7.1. ITER TF system description

The ITER TF coils system is composed of 18 D-shaped coils, the details of which are given in [19]. Each coil is made of 14 pancakes, usually decomposed in Double Pancakes (DP), and designated according to the figure shown in Figure 94.

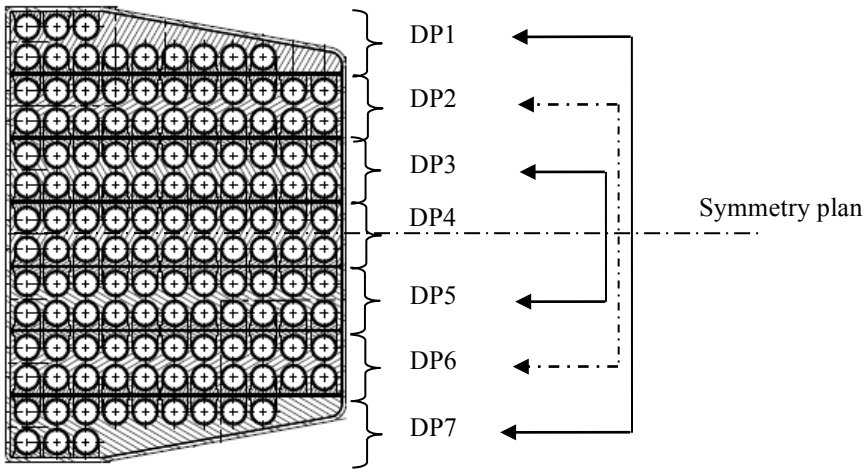

Figure 94: ITER TF coil winding pack decomposition in 7 Double Pancakes

The TF CICC details are given in [17], [95]. However, when used, the required information is given in the following sections.

7.2. Perturbations induced in the ITER TF coils

Flux variations due to the plasma, in normal plasma discharge or in case of disruptions or Vertical Displacement Event (VDE) can be at the origin of an inductive voltage across the TF coils.

It is estimated that there is probably a possibility to compensate for the inductive voltage in case of disruption or VDE by adjusting the holding time τ_h at a time sufficiently long to eliminate their effects (1-1.5 s). Effect of disruptions and VDE will be therefore neglected in a first approach. This point will have to be confirmed.

Flux variations in TF coils can be linked to other causes. This point will be detailed in the next section.

For a short-circuited coil of inductance L and current I, such as represented in Figure 95, a flux variation $d\Phi/dt$ cannot induce a voltage across the coil.

$$L\frac{dI}{dt}+\frac{d\Phi}{dt}=0 \quad \Rightarrow \quad \frac{dI}{dt}=-\frac{1}{L}\frac{d\Phi}{dt}$$

The reaction of the coil to maintain constant the flux is to vary the current at zero voltage. There is no voltage induced across the coil.

This is the reason why the expression “voltage induced to the flux variation” is not adapted to this kind of phenomenon. dΦ/dt can be seen as an electromotive force and not as a voltage.

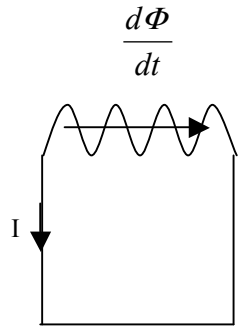

Figure 95: Short-circuited coil submitted to flux variation

7.2.1. Reactions of the TF coils to inductive flux variations

A simplified scheme of the ITER TF electrotechnical circuit is presented in Figure 96 with 18 TF coils in series.

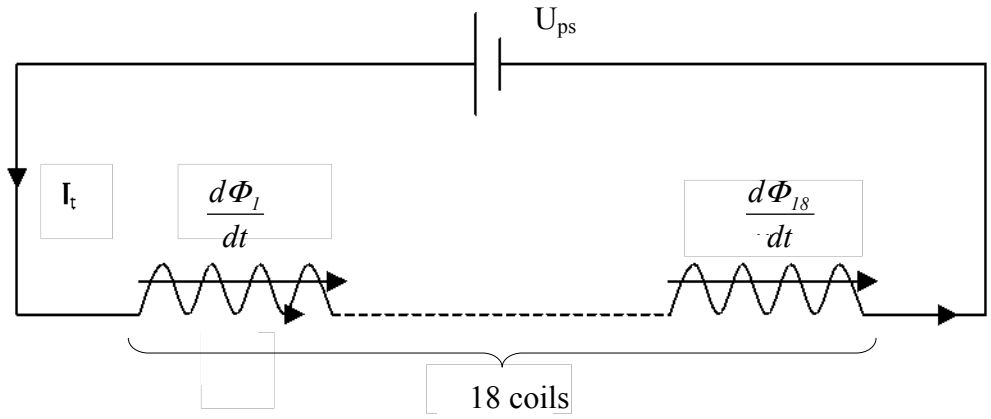

Figure 96: simplified electrical scheme for the ITER TF system

Eq 11. stands for the 18 coils, submitted to flux variations. In this equation:

L is the equivalent inductance of each of the 18 coils supposed identical.
L_k is the self inductance of the coil k
$M_{kk'}$ is the mutual inductance of coil k and k’
I_k is the current in the coil k
And Φ_k is the flux collected by the coil k.

Finally, $\overline{d\Phi/dt}$ is the average of the fluxes, defined as follows:

$$\frac{\overline{d\Phi}}{dt} = \frac{1}{18} \times \sum_{k=1}^{k=18} \frac{d\Phi_k}{dt}$$

Then, it can be written:

$$L_k + \sum_{k'=1,k\neq k'}^{k'=18} M_{kk'} = L$$

The voltage across the 18 coils in series is equal to power supply voltage U_{ps}:

$$\sum_{k=1}^{k=18} \sum_{k'=1}^{k'=18} M_{k,k'} \frac{dI_{k'}}{dt} + \sum_{k=1}^{k=18} \frac{d\Phi_k}{dt} = U_{ps}(t) \qquad \text{Eq. 11}$$

$$\frac{dI_{k'}}{dt} = \frac{dI}{dt} \qquad \forall k'$$

$$18L\frac{dI}{dt} + \sum_{k=1}^{k=18} \frac{d\Phi_k}{dt} = U_{ps}(t) \qquad \text{Eq. 12}$$

Eq. 13 gives the voltage across one coil k :

$$U_k = L\frac{dI}{dt} + \frac{d\Phi_k}{dt} \qquad \text{Eq. 13}$$

Using Eq. 12, Eq. 13 translates :

$$U_k = \frac{U_{ps}(t)}{18} + \frac{d\Phi_k}{dt} - \frac{1}{18}\sum_{k=1}^{k=18} \frac{d\Phi_k}{dt}$$

$$U_k = \frac{U_{ps}(t)}{18} + \frac{d\Phi_k}{dt} - \overline{\frac{d\Phi}{dt}} \qquad \text{Eq. 14}$$

It can be seen in Eq. 14 that the distribution of voltage U_k is linked to the distribution of flux variation in the coils $d\Phi_k/dt$. The voltage U_k appearing across a coil k is not $d\Phi_k/dt$ but a more complex form Eq. 14, which takes into account the other coils. However the voltage difference between two coils is a function only of the difference of the flux variations.

All $d\Phi_k/dt$ are equal $\rightarrow U_k = U_{ps}(t)/18 \quad \forall k$ (according to Eq. 14)

$$U_k - U_i = \frac{d\Phi_k}{dt} - \frac{d\Phi_i}{dt} = 0$$

Supposing all $d\Phi_k/dt$ equal to $d\Phi_k/dt$ then $U_k = U_{ps}/18$.

$$\frac{U_{ps}}{18} = L\frac{dI}{dt} + \frac{d\Phi}{dt} \qquad \text{Eq. 15}$$

The voltage across the coil is due to the power supply, which regulates the current to re-establish the nominal current. The voltage distributes identically across the coils if the flux variations are equal.

7.2.2. Perturbations due to the plasma

The plasma generates both a toroidal and a poloidal magnetic field respectively associated with the poloidal and the toroidal component of the plasma current:

- The plasma poloidal flux Φ_p is due to the toroidal current component associated with the plasma current

- The plasma toroidal flux Φ_φ results from two distinct phenomena associated with the plasma magnetism, which are presented in this section.

a. the diamagnetic flux due to cyclotronic motions of the plasma charged particles

Due to the cyclotronic motions of the electrons and of the ions around the magnetic field lines, a toroidal flux $\Phi_{\varphi d}$ is produced in the opposite direction to the main toroidal field. This effect is generally negligible compared to the second one.

b. the magnetic flux associated with tokamak equilibrium

There must be an internal balance between the plasma pressure P and the forces due to the magnetic field. The basic equation for plasma equilibrium is that the force on the plasma be zero at all points [4]. This requires that the magnetic field force balances the force due to plasma pressure (Eq. 16).

The axis, the plasma and the different magnetic field and current densities are presented in Figure 97.

$$\vec{j} \times \vec{B} = \overrightarrow{\nabla p}$$
$$\overrightarrow{j_p}.\overrightarrow{B_\varphi} + \overrightarrow{j_\varphi}.\overrightarrow{B_p} = \overrightarrow{\nabla p} \qquad \text{Eq. 16}$$

Where J_φ is the toroidal current density (plasma current), B_p is the poloidal magnetic field created by the plasma current, B_φ is the toroidal magnetic field generated by the external TF system. P is the plasma pressure.

J_p is the poloidal induced current density in the plasma, which is the magnetization current. It is presented here as paramagnetic, which is the most common case.

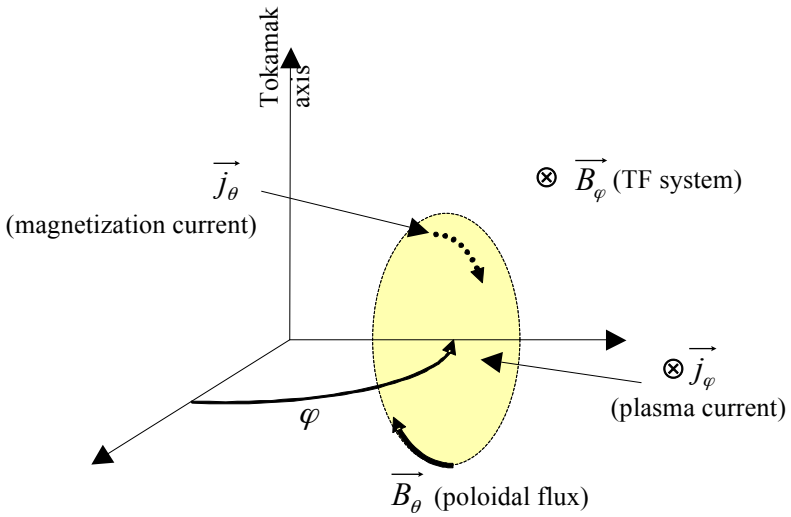

Figure 97: Different current densities and magnetic fields associated with plasma equilibrium.

An important parameter of the equilibrium is β_p, which is the ratio of the thermal pressure to the poloidal magnetic pressure on the reference surface.

$$\beta_p = \frac{\int pdS / \int dS}{B_p^2 / 2\mu_0}$$

It can be seen from (Eq. 16) that, if there is no poloidal (magnetization) J_p current, the toroidal magnetic field does not play a role in confining the plasma pressure, the radial magnetic confining inward force density being applied by the poloidal field combined to the plasma current. This corresponds to β_p=1. The current lines in the plasma are helicoidal except when β_p=1.

Eq. 16 can only be solved numerically and β_p depends on the pressure and current distribution inside the plasma.

In many cases (e.g. Tore Supra and ITER), the reference inductive plasma discharge, β_p <1 which means that the toroidal field is applying an outward force density in a direction opposite to the confining force density associated with the poloidal magnetic field. In this case the magnetization currents are paramagnetic. The poloidal component of the plasma current generates a toroidal flux $\Phi_{\varphi p}$, which is in the same direction as the main toroidal field.

This flux is linked to the parameter μ:

$$\mu = \frac{50B_0}{\pi . I_p^2} \Delta\Phi_{\varphi p}$$

$$\Delta\Phi_{\varphi p} = \frac{50B_0}{\pi I_p^2} \mu$$

$$\mu = \beta_p - S_1 - S_2\left(1 - \frac{R_p}{R_0}\right)$$

S_1 and S_2 are Shafranov moments, which can be estimated only numerically.

Note that the toroidal magnetism of the plasma induces symmetrical effects in all the coils.

7.2.3. Perturbations due to the poloidal flux [71]

The twisted petals of the Cable-In-Conduit conductors such as presented in Figure 98 are natural pick up coils for the plasma poloidal flux.

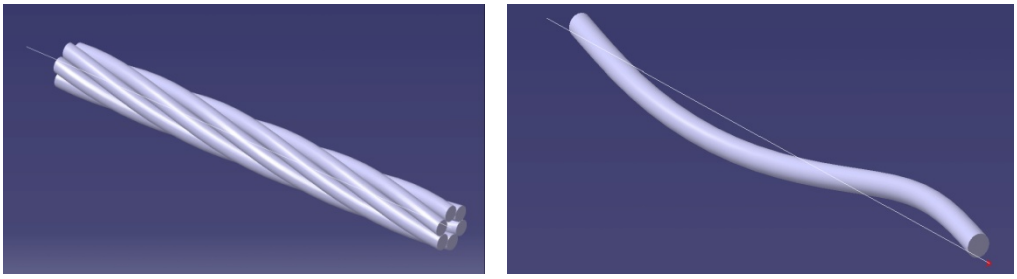

Figure 98: Left-hand side figure: A pitch or the conductor (450 mm). Round petals are represented. Right-hand side figure: A single petal with its axis and the path of the centre of its cross section (assumed to be circular). The general shape of the petal is a helix

Due to this shape a poloidal flux can be induced into the winding, which behaves as a Rogowski coil during a plasma discharge or a plasma disruption.

a. Principle of estimation of the flux induced by a plasma current variation across a conductor petal

The toroidal magnetic field is assumed to be constant as well as the conductor current I_{cond}.

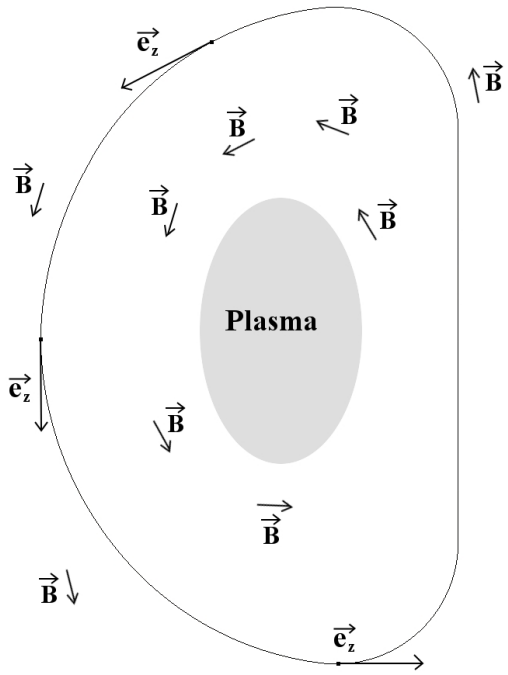

Figure 99: The general shape of a TF coil showing the magnetic field due to the plasma current

In order to calculate the flux induced by a plasma current variation, the poloidal field only is to be taken into consideration, neglecting the effect of the poloidal components of the plasma current. In the next pages, the vector $\vec{e_z}$ is considered as parallel to the axis of the conductor as shown in Figure 99 and Figure 100.

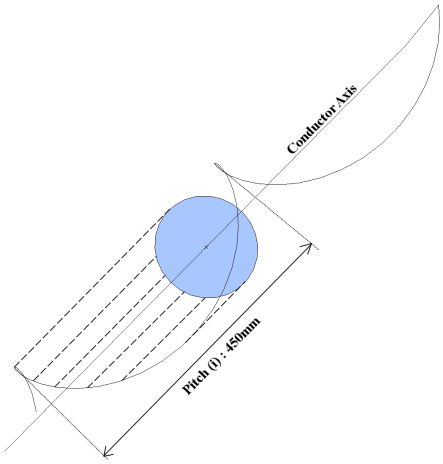

Figure 100: the projection of a 0.450 m (pitch of the conductor) section of the petal centres path (the helix) is assumed to be circular

Assuming that the projection of the path of the centres of a petal on a plan perpendicular to $\vec{e_z}$ is a circle, as illustrated on Figure 100, the magnetic flux is calculated through the surface (disk) S so designed, in order to determine Φ_p.

b. Analytical calculation of the flux induced by the plasma current variations into a conductor petal (Figure 101)

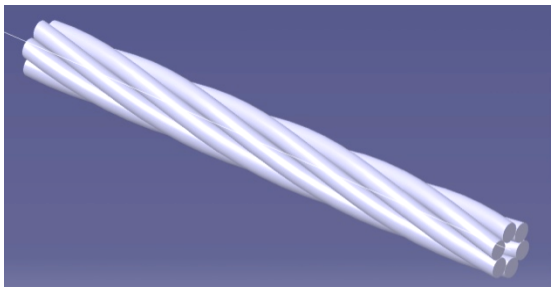

Figure 101: a pitch of the conductor, full scale, with round petals

The petals being electrically in parallel, in this study, we will assume that all the petals collect the same poloidal magnetic flux due to the plasma current variation. In [78], the calculations are more detailed, but the main conclusions are given in this section.

At first, it can be derived from the Maxwell-Faraday equation that the poloidal flux across one petal pitch is:

$$\frac{\partial \Phi_{pi}}{\partial t} = \frac{\partial}{\partial t}\iint_S \vec{B} d\vec{S}$$

S_i being the projected circular section of the petal such as illustrated in Figure 100.

Then:

$$\Phi_{petal} = \sum_{i=1}^{i=L/p_{petal}} \Phi pi$$

In the following equation, L is the considered length of the conductor, p_{petal} the twist pitch of the conductor, and R_{petal} is the radius of the helix.

$$\frac{\partial \Phi_{petal}}{\partial t} = \pi . R_{petal}^2 . \frac{L}{p_{petal}} \frac{\partial}{\partial t} \sum_{i=1}^{i=L/p_{petal}} B_i \qquad \text{Eq. 17}$$

With

$$B_i = \vec{B}.\vec{e_z}$$

Then, as $\vec{B}$ is supposed constant over each surface S_i and as all the surfaces S_i are equal to S :

$$S = \pi . R_{petal}^2$$

Supposing that $\frac{L}{p_{petal}}$ is very large, the sum term can be approximated:

$$\sum_{i=1}^{i=L/p} B_i = \frac{1}{L} \int_L \vec{B}.\vec{e_z}.dl$$

To satisfy the requirements of Ampère's theorem integral form, the conductor is considered as re-closing geometrically on itself by its ends:

According to Ampère's theorem (N_t being the number of turns of the conductor, and I_{p+vv} being the total existing toroidal current in the vacuum vessel and in the plasma).

$$\frac{1}{L} \oint_L \vec{B}.\vec{e_z}.dl = \frac{1}{L} \mu_0 . N_t . I_{p+vv}$$

And Finally, after (Eq. 17):

$$\frac{\partial \Phi_{petal}}{\partial t} = \mu_0 . N_t \frac{\pi R_{petal}^2}{p_{petal}} \frac{\partial I_{p+vv}}{\partial t} \qquad \text{Eq. 18}$$

c. The particular case of the co-wound tape envisaged for ITER TF quench detection.

The reference ITER system to balance the inductive voltage of the circuit to be monitored is to use a co-wound tape, which therefore follows exactly the same path as the circuit and

will see the same flux variations. The twisted co-wound tape is installed during conductor production within the conductor insulation (see Figure 102). It has to be carefully insulated from the jacket of the conductor.

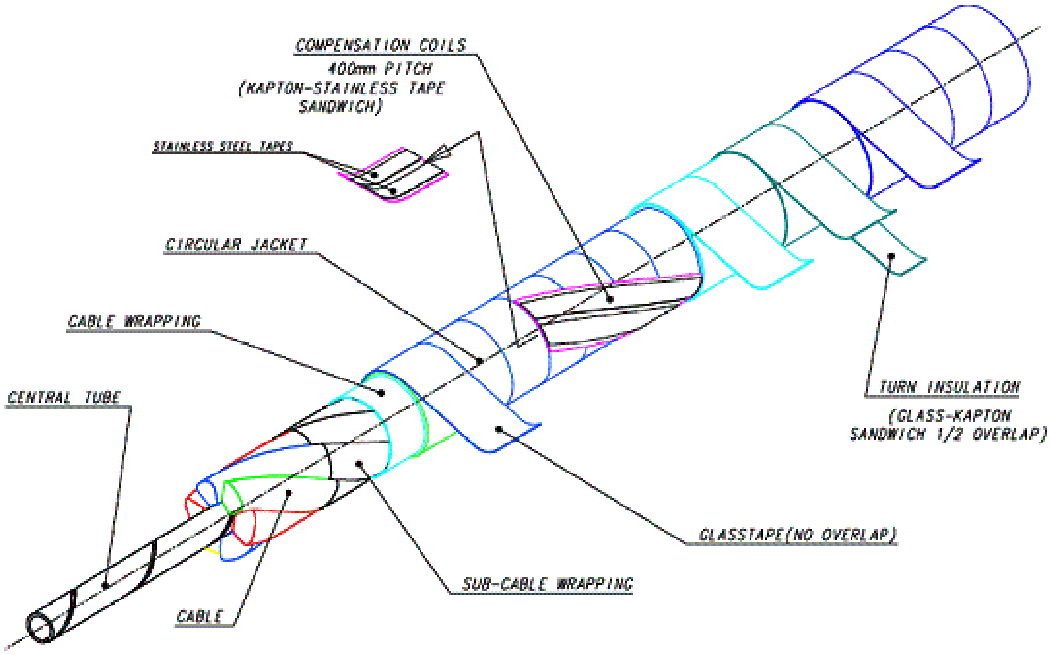

Figure 102: ITER TF conductor showing two redundant co-wound tapes located in the conductor insulation (from [3]).

Similarly to Eq. 18 the same formula can be derived for the co-wound tape, depending on the square of the radius. It is to be noticed that Φ_{petal} and $\Phi_{co\text{-}wound}$ are both related to the plasma current variations.

$$\frac{\partial \Phi_{co-wound}}{\partial t} = \mu_0 . N_t \frac{\pi R^2_{co-wound}}{p_{co-wound}} \frac{\partial I_{p+vv}}{\partial t}$$

- Translation of the flux variations into voltage

In Figure 103 is represented the simplest quench detection circuit associated with a co-wound tape for a TF double pancake where a current I_{cond} is circulating. This system is supposed to be very effective during current TF ramp. The inductive voltage across the double pancake $U_1=(V_1- V_0)$ is balanced by the voltage across the co-wound tape $U_2=(V_2-V_0)$. The quench detection voltage ΔU is such as:

$$\Delta U = (V_1 - V_0) - (V_2 - V_0)$$

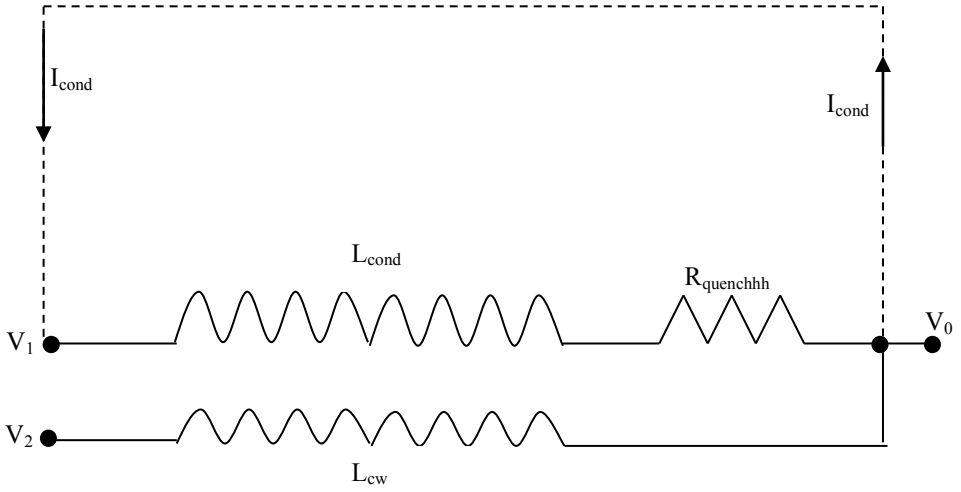

Figure 103: Double pancake envisaged detection system with a co-wound tape

$$(V_1 - V_0) = U_{PS} = \frac{d\Phi_{petal}}{dt} + L_{cond}\frac{dI_{cond}}{dt} + R_{quench}.I_{cond}$$ according to Eq. 12

$$(V_2 - V_0) = \frac{d\Phi_{co-wound}}{dt} + M\frac{dI_{cond}}{dt}$$

Supposing that the co-wound is perfectly coupled to the TF double pancake then L~M:

$$(V_2 - V_0) = \frac{d\Phi_{co-wound}}{dt} + L\frac{dI_{cond}}{dt}$$

Let us now observe the behaviour in case of plasma current variation.

It can be seen that the voltage differences (V_1-V_0) and (V_2-V_0) are not equal to the electromotive forces $d\Phi_{petal}/dt$ and $d\Phi_{co\text{-}wound}/dt$ but takes a more complex form which depends on the regulation parameters of the power supply which tries to maintain the courant at the nominal value (see further chapter). In ITER, the voltage across the double pancake (126 double pancakes) is certainly very small due to the limited capacity of the power supply in voltage regulation (about 50 V/ 126 =0.4 V).

The compensated voltage becomes:

$$\Delta U = U_1 - U_2 = \frac{d\Phi_{petal}}{dt} - \frac{d\Phi_{co-wound}}{dt} + R_{quench}.I_{cond}$$

- Disruption

  The example of a disruption at full plasma current is taken. In case of a plasma disruption the plasma is terminated within 1 ms, but the currents dissipate in the vacuum vessel through eddy currents, which dissipate within typically 100 ms. An approximation of a linear decay of the current within 100 ms will be taken for the estimation.
  R_{petal} is taken arbitrary at the centre of a petal, considering it has a circular cross section and $R_{co\text{-}wound}$ is the radius on which the co-wound tape is wrapped.

The considered length is the length of a double pancake, on which the co-wound tape is planned to be monitored. So the number of associated turns is 22, which is the number of turns of a double pancake. The numerical application is summarized in Table 23. In this table, the variables depends on the considered circuit, co-wound tape or petal

Table 23: Electromotive forces across petal and co-wound tapes due to plasma disruption

Variable	Petal	Co-wound Tape
N_t	22 turns	22 turns
R	0.0125 m	0.024 m
p	0.45 m	0.45 m
$\frac{\partial I_{p+vv}}{\partial t}$	$\frac{15.10^6}{50.10^{-3}}$ A.s^{-1}	$\frac{15.10^6}{50.10^{-3}}$ A.s^{-1}
$\Delta\Phi$	0.45 Wb	1.67 Wb
$\frac{d\Phi}{dt}$	9.04 V	33.35 V
ΔU	~24 V	

- Plasma initiation

In case of plasma initiation it takes about 70 s to increase the current.
During ITER scenario, plasma current increase can cause significant electromotive forces for longer periods. This is presented in Figure 104. The level of the signals is low in comparison with the envisaged detection level, which is higher than 0.1 V.
However during the first two seconds, substantial electromotive forces appear across the co-wound tape, induced by the currents circulating in the vacuum vessel (Figure 105).

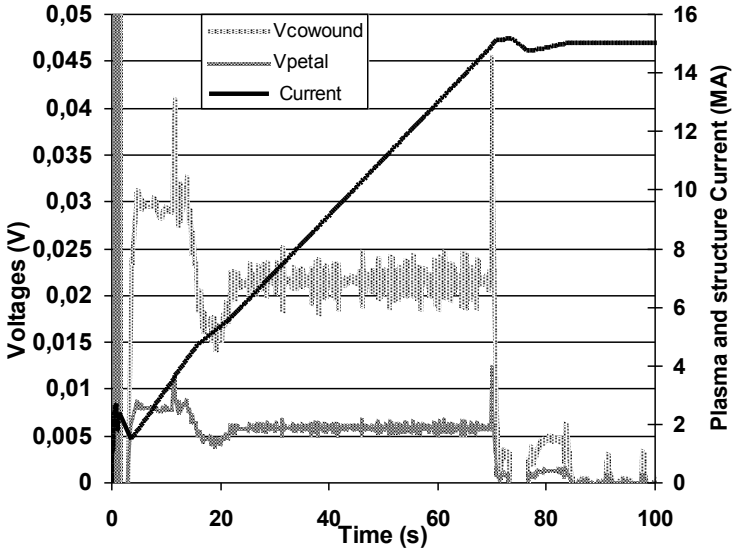

Figure 104: Estimation of electromotive forces and ΔU during ITER reference scenario v10

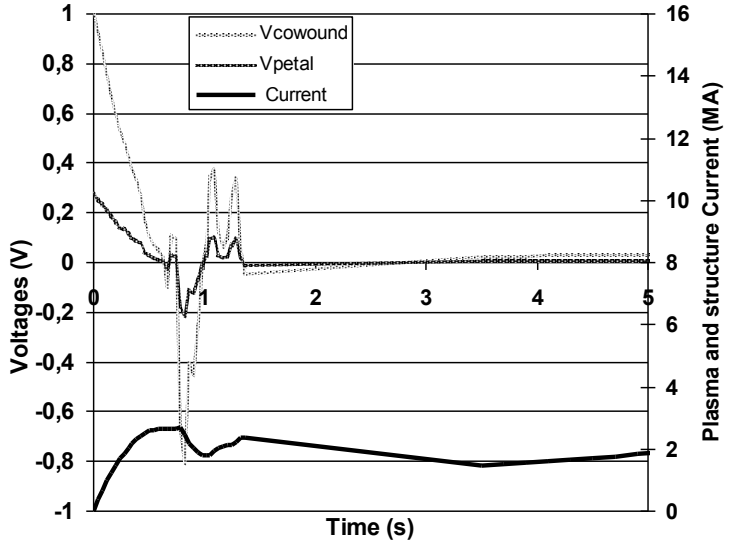

Figure 105: Estimation of electromotive forces and ΔU during early times of ITER reference scenario v10. It can be seen that the peak voltage difference will reach 0.7 V

7.3. Observations of inductive voltage in Tore Supra during plasma discharge

In principle, if all the coils were perfectly positioned, there would be no coupling between the TF and the PF system except through the connexions between double pancakes. Two types of positioning defaults can be taken into consideration:

- Inclination of the TF coil plane resulting from a rotation around its horizontal axis
- Displacement of the meridian plane of the coil parallel to itself, which is equivalent to a rotation around its vertical axis.

The driving parameter of the voltage distribution is the series of parameters α_k, Φ_k being the flux induced into the coils (see Eq. 14).

$$\alpha_k = \frac{d\Phi_k}{dt} - \frac{1}{18}\sum_{k=1}^{k=18}\frac{d\Phi_k}{dt}$$

$$U_k = \frac{U_{ps}(t)}{18} + \alpha_k$$

In fact $d\Phi_k/dt$ is the sum of the contribution from the paramagnetism and from the PF coupling:

$$\frac{d\Phi_k}{dt} = \frac{d\Phi_{pk}}{dt} + \frac{d\Phi_{PFk}}{dt}$$

If $d\Phi_{PFk}/dt << d\Phi_{pk}/dt \ \forall$ k the influence of the PF coupling will be small as observed in Tore Supra (see 7.3.3).

An estimation of $d\Phi_{PFk}/dt$ can be done estimating the positioning defaults from fabrication analysis and it can be compared to an estimation of $d\Phi_{pk}/dt$.

The observation of the voltage signals across the TF coils in Tore Supra can help.

And again, if $d\Phi_{PFk}/dt << d\Phi_{pk}/dt \ \forall k$ during plasma discharge, the voltages across the coils are identical and equal to the voltage delivered by the power supply divided by the number of coils.

The coupling between the PF and the TF coils can be in theory observed during the preparation of the plasma discharge, the premagnetization phase when the current in the PF and CS system are increased to their plateau values.

7.3.1. Introduction of the studied plasma discharges

Two plasma discharges of Tore Supra have been examined in details in order to check whether the analysis made in the previous section drives the behaviour of the voltage across the coils or not. Only plasma discharge #46010 is represented here.

Plasma discharge #46010, performed on the 20/10/2010 is a "short" one; the current plateau of the plasma lasts for 8.5 s at 1 MA, as shown in Figure 106.

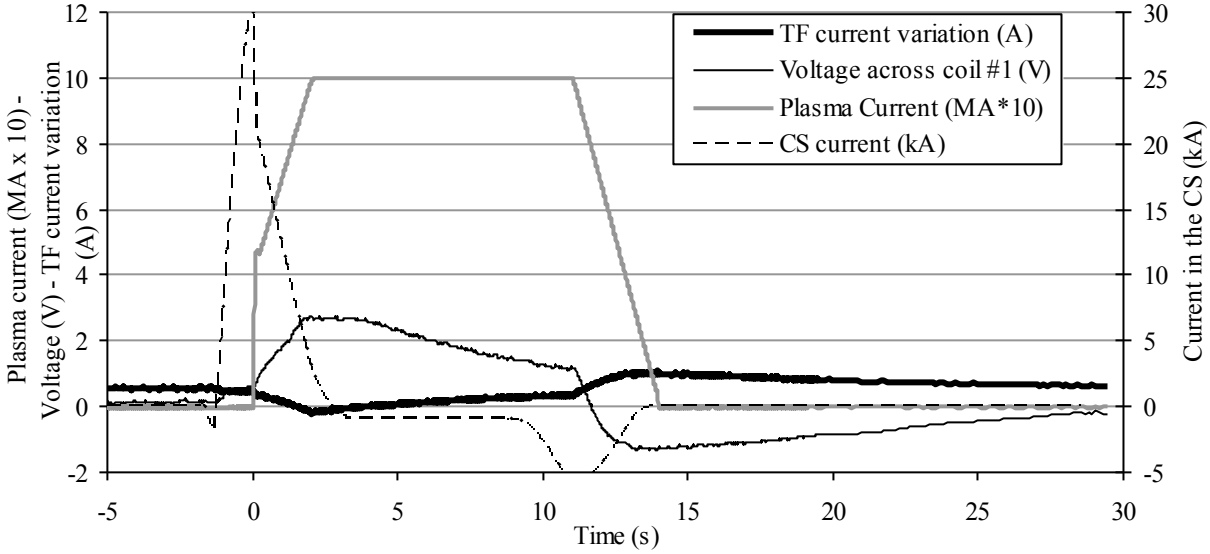

Figure 106: Plasma discharge 46010. The plasma current has been multiplied by 10 to make it more visible on the figure.

In Figure 106, the plotted TF current (in thick black) is the variation, taking its value before the plasma discharge as reference (here, 1225 A). Nevertheless, there is a residual offset of 0.54 A, as visible on the figure. On this graph, the voltage across one coil (BT1) is given. The last provided data is the current carried by the Central Solenoid (CS in dashed line).

7.3.2. Signal processing

The signals used for these studies come from the database of Tore Supra. The sample rates and the resolutions used for the storage or from the sensors do not enable a direct use of the signals. The signals are basically coming from two distinct systems.

- The "continuous acquisition" is mainly used for the monitoring of the Tore Supra superconducting system. This system continuously records the voltage across the coils

and power supply, quench detection balances, as well as auxiliary cryogenic systems (temperatures …). The acquisition frequency is about 6 Hz, and the resolution is 0.1 V. The quench detection threshold in Tore Supra is set at 2 V for 1s. The interest for the present study of these signals is that the power supply voltage is recorded, and the voltage across each coil can be extracted.

- The second system, which collects information from Tore Supra, is called "standard acquisition". The standard sensors, whose data are stored in TSbase are far more numerous, and deliver signals less coarse, as shown in Figure 107. Unfortunately, the sample rate can be different according to the sensors. Some processing is needed before using these signals. The voltage is not recorded across each coil of the TF system, but only across BT1. For comparison between signals coming from two different coils (hypothetically to check if a coil-to-coil bridge for quench detection is a potential candidate), the signals from "continuous acquisition" are the only available ones.

  In addition, the multiple galvanic insulations give offsets to the signals coming from the sensors. Many of them are compensated, before the storage, but not all of them. Therefore, offsets have to be removed before use.

7.3.3. Examination of plasma discharge 46010

In Figure 107 the main physics parameters of the plasma discharge are presented: β_p, Li (plasma internal inductance), plasma current and the so-called diamagnetic flux $\Phi_{\varphi p}$ (see section7.2.2).

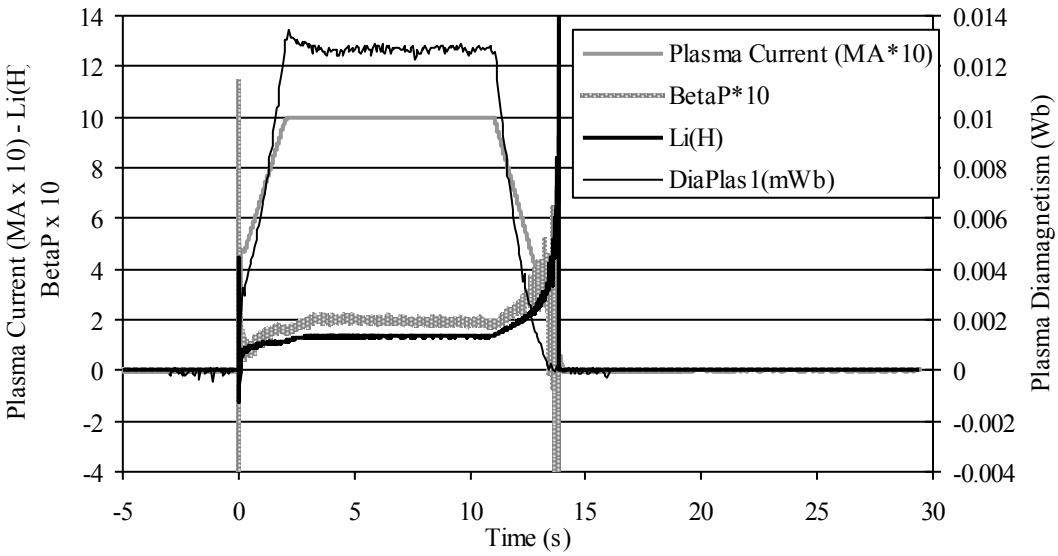

Figure 107: Physics parameters in plasma discharge #46010

As seen in section 7.2.1, if all the flux variations through the coils were the same, it would have been theoretically possible to predict the current change in the coils thanks to the following Eq. 19:

$$\frac{U_{ps}(t)}{18} = L\frac{dI(t)}{dt} + \frac{d\Phi(t)}{dt}$$

L being the effective inductance of 1/18 of the Tore Supra TF system inductance: L=34 H. (There are 18 TF coils in TS), and Φ being the total flux collected by the coil surface. The conductor is not a cable in conduit as in ITER, therefore, it will be assumed that Φ_p=0.

Assuming that the coils are purely vertical, the only induced flux is Φφ. The coil is supposed in a first approach short-circuited (no power supply), It gives (N_{TF} is the number of turns of the TF coil, N_{TF}=2028) and I_{no} the coil current :

$$\frac{dI_{no}(t)}{dt} = -\frac{N_{TF}}{L}\frac{d\Phi_{\varphi}(t)}{dt} \qquad \textbf{Eq. 19}$$

$$I_{no}(t) = -\frac{N_{TF}}{L}\Phi_{\varphi}(t)$$

This relationship is applied to the signals extracted from Tore Supra database, TSbase, for discharge #46060 (Figure 106).

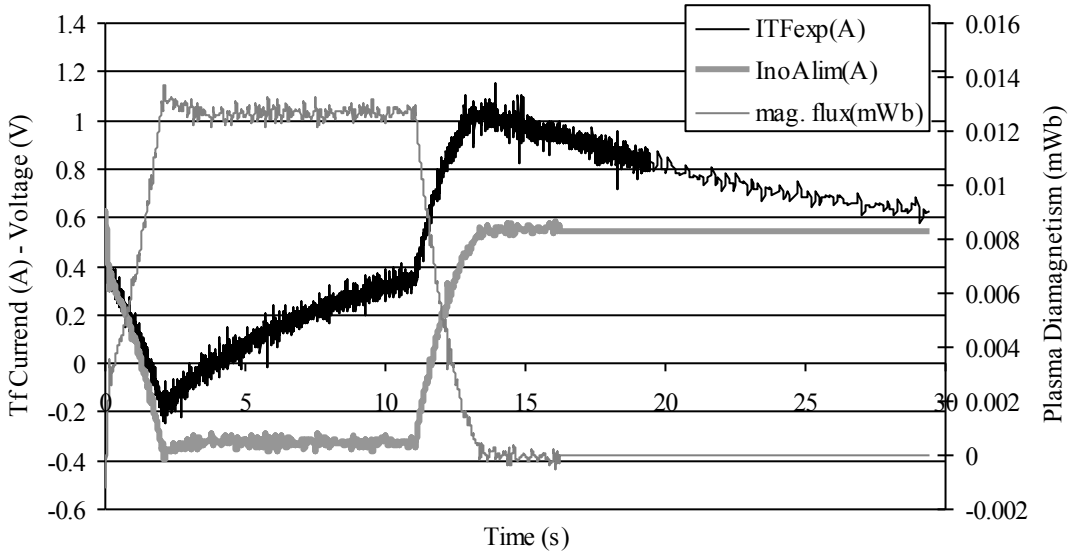

Figure 108: Prediction of current variation in plasma discharge 46010 without taking into account the effect of the power supply

ITFexp is the actual voltage measured in TS coils and InoAlim is the calculated current, considering that there is no power supply, just a short circuit. mag. Flux (mWb) is the flux collected by the measurement loop implemented at the inner radius of a TF coil.

Figure 108 shows a good correlation in the early times and after a certain time following the disappearance of the plasma. The difference between ITFexp and InoAlim is due to the regulation of the power supply.

By adding the effect of the power supply to the relationship Eq. 19, and assuming that all the coils are correctly positioned and sense the plasma the same way, it comes:

$$\frac{U_{ps}(t)}{18} = U_{coil}(t)$$

The relationship Eq. 19 can be written as follows:

$$U_{coil}(t) = L\frac{dI(t)}{dt} + \frac{d\Phi(t)}{dt}$$
$$\left(U_{coil}(t) - \frac{d\Phi(t)}{dt}\right)\frac{1}{L} = \frac{dI(t)}{dt}$$

By doing a step by step integration, it comes:

$$\Delta I = \frac{1}{L}.\left(U_{coil}(t).\Delta t - \Delta\Phi\right)$$

And finally:

$$\Delta I = \frac{1}{L}.\left(U_{coil}(t).\Delta t - N_{TF}\Delta\Phi_{\varphi}\right)$$

The result is shown below in Figure 109:

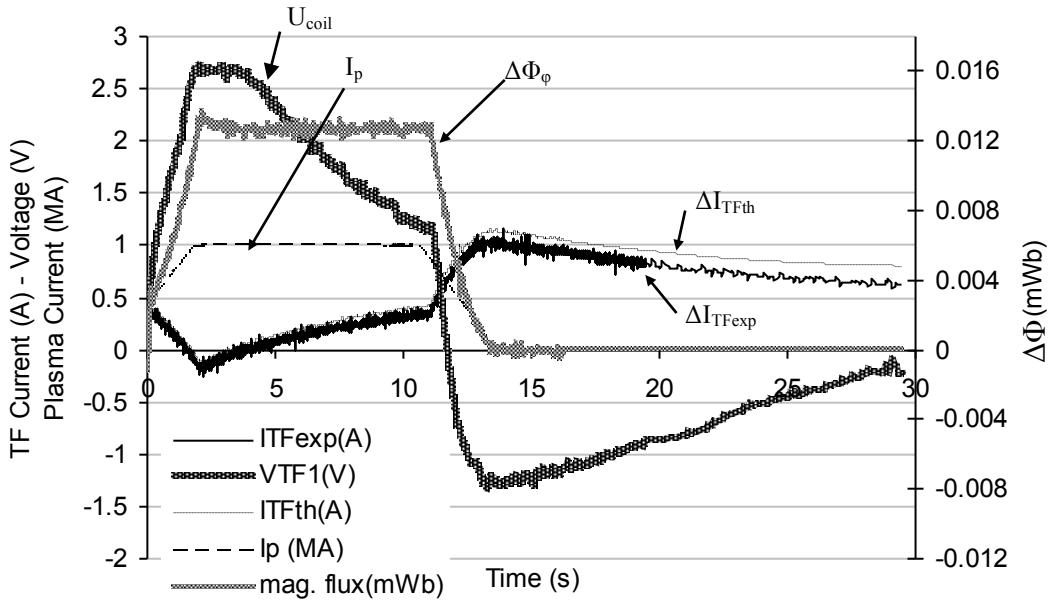

Figure 109: Prediction of current variation in plasma discharge 46010, taking into account the effect of the power supply

ITFexp is the current measured in the coil. ITFth is the current calculated, taking the power supply reaction U_{coil} into account.

I_{TFth} and I_{TFexp} are in perfect agreement, proving that the plasma magnetism, actually plasma paramagnetism, plays a great role on the voltages measured across the coils.

Several factors which can influence the behaviour of the voltage across the coils have been pointed out (poloidal flux collection by the coil thickness, by a potential tilt of the coil …). Nevertheless, it seems that the plasma paramagnetism has the greatest effect on the voltage across the coil.

Moreover, this plasma paramagnetism is sensed the same way by all the coils, as shown in the Figure 110. All the signals coming from the machine have been recalibrated (time offset and offset value compensated):

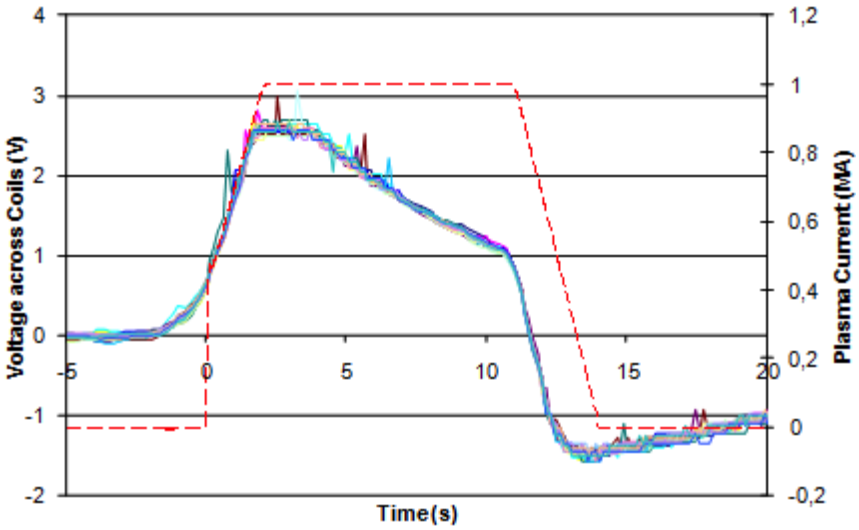

Figure 110: Experimental observations of same voltages in the 18 Tore Supra TF coils during plasma discharge #46010

In this figure, it can be seen that all the curves have the same behaviour, showing that the currents variation induced by the magnetic flux variation, decrease the same way. This demonstrate that the plasma paramagnetism is sensed the practically the same way by all the coils.

7.3.4. Other factors which can influence the voltage across the coils

Some of them have been described in the previous sections. A tilt of coils can be envisaged, but is it practically observable in a real operating machine? In Figure 111, it can be seen that there are misalignments existing in Tore Supra.

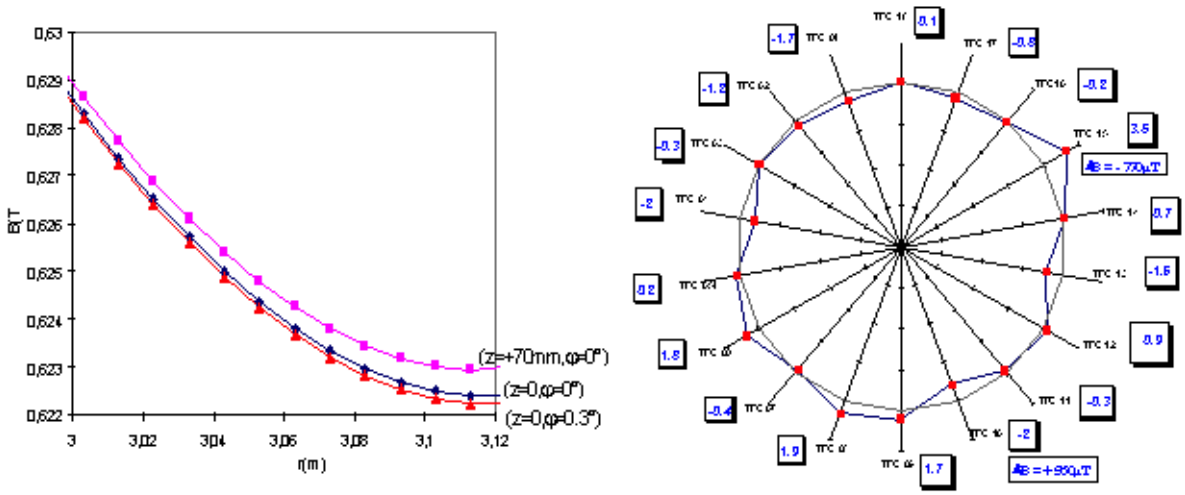

Figure 111: Experimental observations of misalignments in Tore Supra by magnetic measurements

Despite the fact that the coils are not absolutely well positioned, as seen in Figure 111, all the voltages across them are the same. Nevertheless, it can be seen that the behaviour of the coils cannot be predicted thanks to plasma paramagnetism observation only, as shown in the next Figure 112.

Before plasma initiation, corresponding to a situation where there is no paramagnetism, it can be seen in Figure 112 that there is already a drift in TF current and a voltage across the coil. There is only one event that can cause this, the field variation caused by the current rise in the CS (or PF). In Figure 110, it can be seen that all the voltages are the same, so, the misalignments of the coils cannot be responsible for this flux collection.

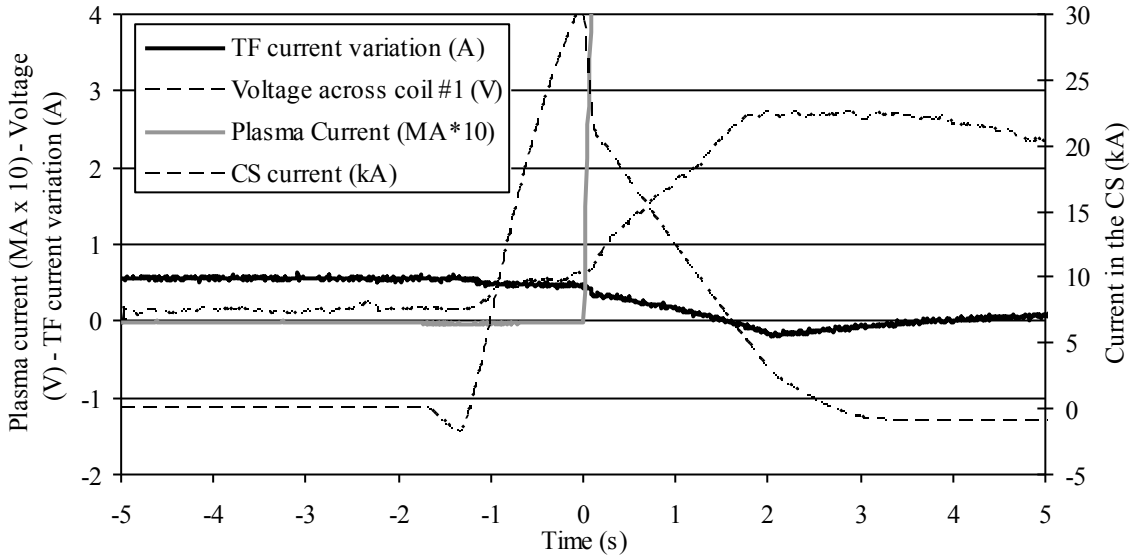

Figure 112: Experimental observations of TF coil voltage during premagnetization of plasma discharge 46010

7.4. Possible detection system for the ITER TF system

The two major systems to be compared are:

- quench detection system based on the balance of the voltage of two coils or the balance of coil subcomponents, which is supposed to be more sensitive (pancakes, double pancakes, half coils)

- quench detection based on a co-wound tape. This choice will result in a drastic complication of the conductor insulation and must be examined carefully.

The two existing machines with a TF quench detection system based on balance of two coils (Tore Supra and KSTAR) did not show any disturbance linked to the PF system.

In

Table 24 are shown the solutions on existing machines in construction or in operation.

Table 24: TF quench detection system for several machines in operation or in project

	Tore Supra (in operation)	KSTAR (in operation)	EAST (in operation)	ITER (project)	JT-60SA (project)
Co-wound tape			X (not twisted)	X	
Balance of similar coils	X	X		X	X

In Table 25, the expected sensitivity of the two quench detection systems against the characteristic envisaged flux variations is presented.

Mainly one has to consider:

- Sensitivity to TF ramp up
- Sensitivity to plasma variation due to plasma toroidal magnetism $\Phi_{\varphi p}$ (Plasma initiation or disruption)
- Sensitivity to plasma current variation due to plasma poloidal flux Φ_p (Plasma initiation or disruption)
- Sensitivity to PF and CS system Φ_{PF} (PF and CS safety discharges, plasma initiation)

Table 25: sensitivity of TF quench detection systems according to different types of flux variation

	Sensitivity to TF ramping	Sensitivity to $\Phi_{\varphi p}$	Sensitivity to Φ_{PF}	Sensitivity to Φ_p
Co-wound tape	perfectly coupled	perfectly coupled	perfectly coupled	deviations predicted
Balance of similar coils or subcomponents	perfectly balanced	perfectly balanced	deviations predicted due to misalignments	perfectly coupled

"perfectly coupled" means that just third order variations are expected.

"deviation expected" means that a deviation in the order of magnitude of several hundred millivolts can be observed.

7.5. Considerations on TF current ramp up

7.5.1. Quench detection with a co-wound tape integrated in the insulation

The different voltages are expressed during TF ramp up, with the denominations associated with Figure 103.

In this case the voltages are particularly simple:

$U_1=(V_1-V_0) = U_{ps} = L\ dI_{cond}/dt + R_{quench}.I_{cond}$

$U_2=(V_2-V_0) = M.dI_{cond}/dt$

Suppose that the co-wound tape is perfectly coupled to the TF double pancake then L~M. It is certainly the case for the co-wound helix tape such as envisaged in ITER (Figure 102) as the magnetic axis of the tape is the same as the conductor magnetic axis.

$U_2=(V_2-V_0) = L.dI_{cond}/dt$

$\Delta U = U_1-U_2 = R_{quench}.I_{cond}$

It is shown that in theory the quench detection is nearly insensitive to TF ramp up.

7.5.2. Drawback associated with non twisted co-wound tape

A co-wound tape not twisted will avoid the Rogowsky effect described in 7.2.3 and is easier to implement. Then the perfect coupling is somehow destroyed, as it is the case in EAST (see Figure 113). By the way, that the Rogowsky effect is not present in EAST nor in any existing Tokamak. It is possible to roughly estimate the bias introduced by this arrangement in comparison with the co-wound twisted tape.

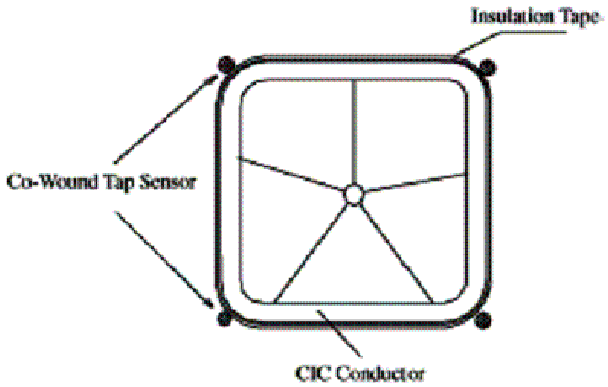

Figure 113: EAST TF conductor showing four redundant co-wound tapes located inside the conductor insulation.

The model used for this estimation is the classical ideal D-shape thin torus where the turns are supposed concentrated on a thin continuous torus, this model retrieves the correct magnetic energy and the inductance of the TF coils.

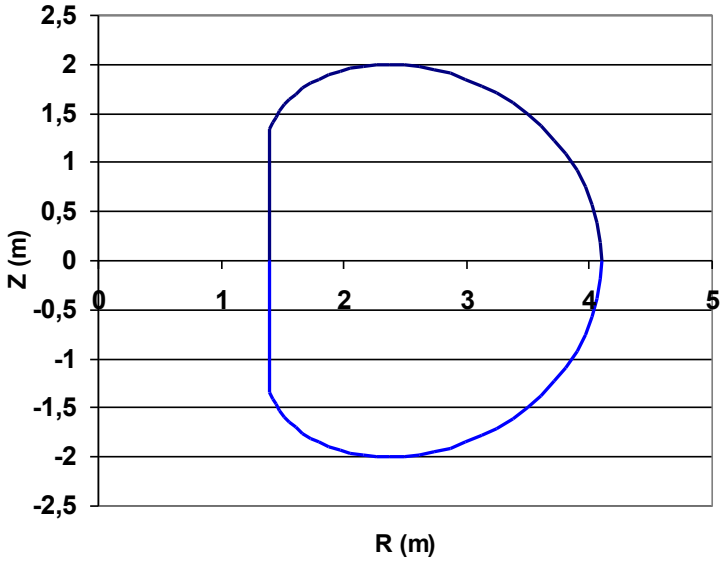

Figure 114: EAST TF system represented as a D-shape ideal thin torus

The bias introduced by the co-wound tape of EAST conductor can be modelled by shifting the curve of Figure 114 by the distance between the tape and the conductor axis, which is typically 10 mm. The area reduction corresponding to this 10 mm shift can be estimated to: 0.11 m^2

Supposing the TF coil inductance reduction proportional to the surface the corresponding inductance reduction can be estimated for a double pancake to:

$$\Delta L=2.2 \text{ mH}$$

The inductive voltage can be estimated:

$$\Delta U = \Delta L.\frac{dI}{dt} = 145mV \quad \text{(corresponding to 80 A/s)} \qquad \text{Eq. 20}$$

For certain type of faults, there is a need to accelerate the ramp down of the EAST TF coils using the power supply, up to – 80A/s. Using Eq. 20, it can be seen that the quench detection voltage threshold is exceeded in this phase, triggering a fast safety discharge (see below and Figure 115). The above calculation can account for this effect reported in the following note by the EAST team:

"Considering the huge stored energy of TF coils that the maximum of stored energy is 298 MJ, the safest operation mode for TF coils is ramping up and ramping down current slowly. When the stability of vacuum chamber or cryogenic system is transiently deteriorated, fast ramping down TF current will be initiated and the maximum rate of ramping down current can reach 80 A/s. In this process, the co-wound voltage signals cannot eliminate self-coupling noise voltage completely, inductive noise may make detection system misjudgement to trigger protective action. During the first engineering commission of East Tokamak, a false quench trigger occurred due to un-eliminated inductive voltage in the process of fast discharge current of TF." (from YL Hu and EAST quench team) [60].

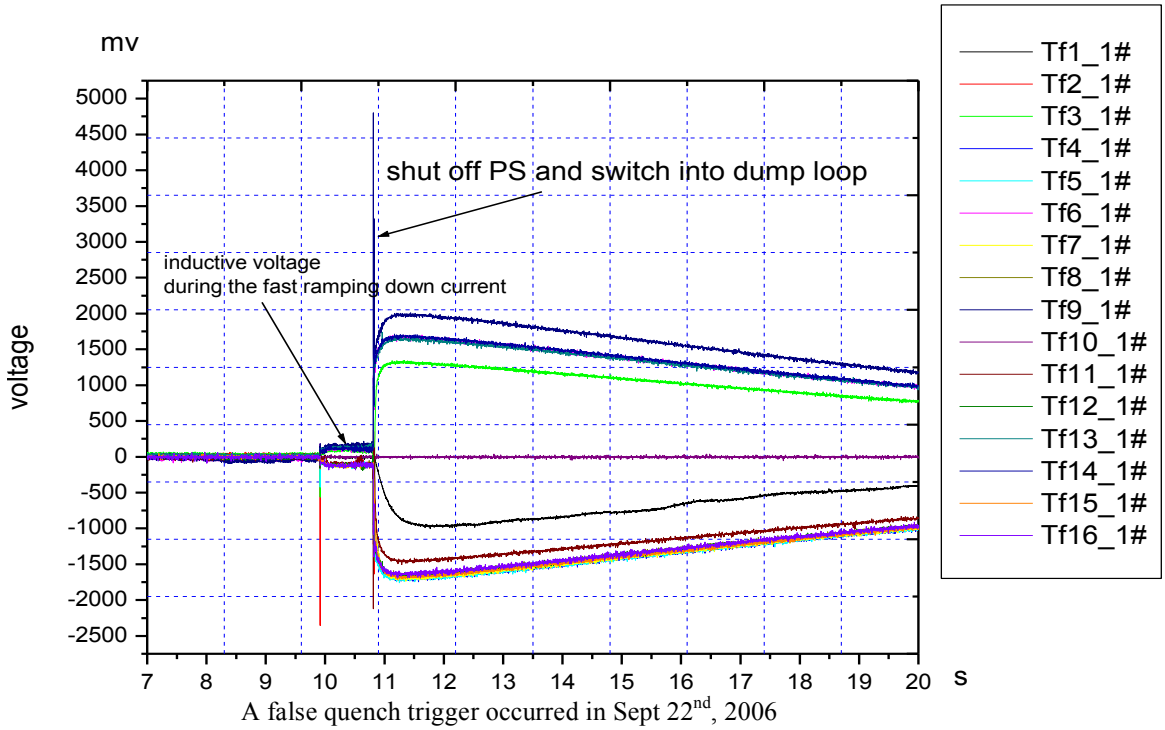

Figure 115: Illustrations of fast discharge in EAST TF coils triggered by a detection voltage due to fast ramp down (80 A/s).

It can be seen in this figure, that the fast ramping down induces a flux variation, which is not perfectly compensated by the co-wound tape. EAST threshold voltage is to low for this kind of event. This voltage has been exceeded during about 0.7 s, which has led the quench detector to trigger the fast safety discharge.

7.5.3. Estimation of ITER TF coil imbalance during ramp due to cable different internal inductances.

Evaluating the consequences of abandoning the co-wound tape, to adopt balance of TF coil voltage such as it is performed in KSTAR TF system, the possibility to have two different coils made from two different cables has to be estimated. If the two cables are made from two different composites having different effective filament diameters d_{eff} (say 20 μm and 60 μm for instance), the internal inductance is affected, which can cause a coil imbalance in case of comparison of two coils.

The diamagnetism of the superconducting filaments, excluding magnetic flux from the conductor, affects the internal inductance of the conductor (Figure 116).

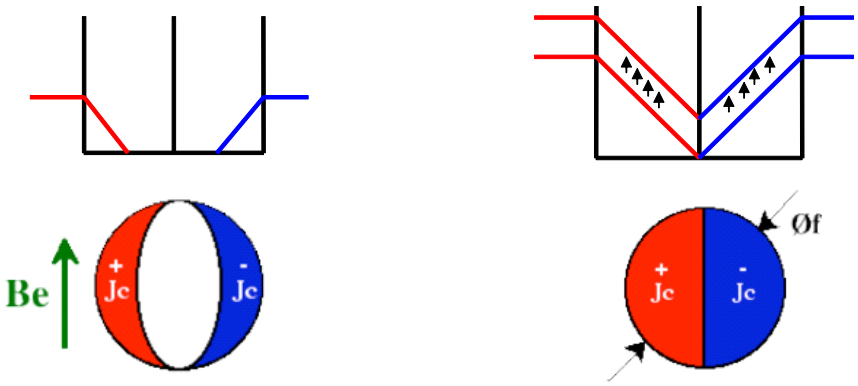

Figure 116: Diamagnetism of superconducting filaments according to their magnetization [67]

The analysis is done for ITER using the same model as in section 7.5.2. The model used is the classical ideal D-shape thin torus where the turns are supposed concentrated on a thin continuous torus.

Clearly the thickness and the discontinuity of the coil is ignored to consider only "average turns" subject to an average magnetic field.

$$M = -\frac{2J_c(B)d_{eff}}{3\pi}$$

It is possible to calculate the magnetic field at any point of the D-shape thin torus as presented in Figure 117 and to deduce the associated local magnetization, assuming half the calculated magnetic field, to take into account the linear variation of the magnetic field inside the thickness of the winding. The magnetization is a function of J_c, which depends of B, it is larger at low magnetic field.

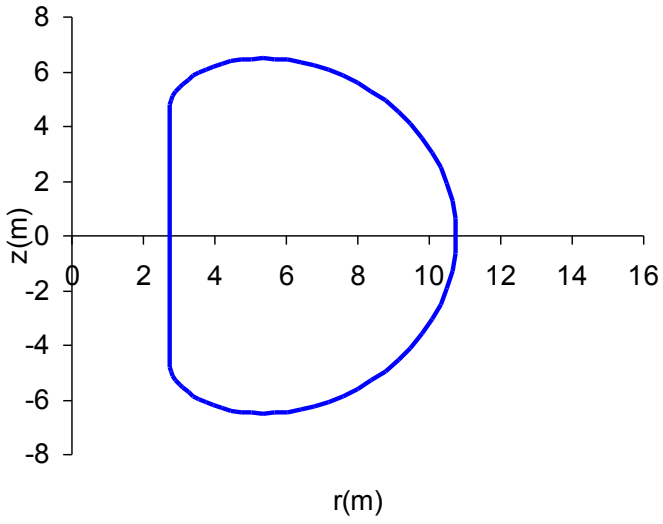

Figure 117: ITER TF system represented as a D-shape ideal thin torus

It is numerically possible to calculate the conductor magnetic energy W_{cond} as a function of d_{eff}, which affects the conductor magnetization. The volume affected by the diamagnetism is only the non-copper volume. The non-copper volume is 20.7 m^3.

$$W_{cond} = \iiint_{cond} \frac{B_{cond}^2}{2\mu_0} dv = \iiint_{cond} \frac{\left(B_{loc} + \mu_0 M(d_{eff})\right)^2}{2\mu_0} dv$$

$$\Delta L = \frac{2W_{cond}(d_{eff1}) - 2W_{cond}(d_{eff2})}{I_{cond}^2} \quad \text{Eq. 21}$$

a. No diamagnetism (conservative assumption)

The internal inductance of the non-copper volume coil is calculated supposing no diamagnetism.

W_{cond} =1.19 10^8 J W_{TF} = 40.8 GJ

L_{condTF}= 52 mH L_{TF}= 17.65 H

To estimate possible imbalance, it is supposed in the rest of the section that the coil is energized up to 68000 A within 1800 s, corresponding to the nominal current of the TF conductor.

The corresponding ramp up voltage respectively across one DP U_{DP}, across one TF coil, U_{TFcoil} and across the TF system U_{TF} is:

U_{TFcoil}=37 V U_{DP}= U_{TF}/(18*7)= 5.3 V U_{TF}= 667 V

$L_{condTFcoil}$= 52 mH/18=2.89 mH

The corresponding voltage, which is a source of imbalance, supposing full diamagnetism in the other coil ($L_{condcoil}$= 0 mH) is:

$\Delta U = L_{condcoil} dI_{cond}/dt$

ΔU= 109 mV

This is the maximum voltage in the very conservative assumption of full diamagnetism.

b. Different diamagnetism in two coils

Considering two coils with respective d_{eff} of 20 μm and 60 μm, it is possible to estimate the voltage imbalance between two coils as a function of the current in the TF system (Figure 118) using Eq. 21. This voltage is decreasing with the current due to the decrease of J_c.

The maximum expected voltage is in the range of 20 mV which demonstrates that this effect is negligible.

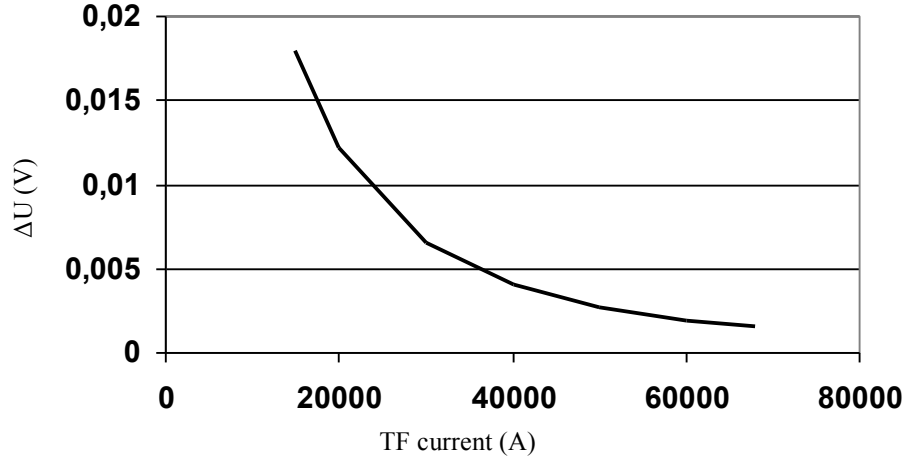

Figure 118: Voltage imbalance between two TF coils with different d_{eff} (20 µm and 60 µm)

In conclusion, it is proven that the diameter of the filaments has no influence on the voltage difference between two coils at nominal current.

7.6. Voltage threshold and holding time [72]

As for the CS presented in chapter 6, in order to describe a quench detection system, the characteristic times mentioned in section 3.3 are recalled in the next paragraph.

7.6.1. Main characteristic times of the quench detection and fast discharge

The main phases of the detection process are illustrated in Figure 30 for a quench resistive signal typical of the TF system, starting from a quench initiation and highlighting the values, which have been selected for the detection, namely:

- the voltage threshold U_t above which the quench is detected
- the holding time τ_h during which U_t has to be continuously exceeded before opening of the current breaker and initiation of the Fast safety Discharge (FSD).

The main purpose of this study is to determine U_t and τ_h, after calculation of the maximum allowed detection and action time, which plays a leading part for the hot spot considerations, as explained in 3.5.

7.6.2. The detection and action time

a. The Hot spot criterion

As explained, in section 3.5, the heat equation must be solved to compute the maximum detection and action time τ_{da}.

For the TF system, J(t) can be decomposed in two phases, the phase when J stays constant during τ_{da} at J_{op} and the phase associated with the fast discharge according to (Eq. 22):

$$J_{op}^2 \tau_{da} + \int_{\tau_{da}}^{\infty} J^2 dt = \int_{T_0}^{T\,max} \frac{\gamma C(T)}{\rho(T)} dT = U(T_{max}) \qquad \text{Eq. 22}$$

To estimate τ_{da} in Eq. 22, knowing $U(T_{max})$ it is necessary to evaluate the equivalent time constant of the discharge τ_{fsd} such as:

$$\int_{\tau_{da}}^{\infty} J^2 dt = J_{op}^2 \frac{\tau_{fsd}}{2}$$

b. Fast safety discharge in ITER TF system

The fast safety discharge in the TF system is not as simple as for the CS and the PF system. During the fast safety discharge (FSD) of the TF superconducting system of ITER, the TF system discharges its magnetic energy into a resistor bank within a time constant τ_{fsd}. During this phase, eddy currents are induced in the metallic parts surrounding the TF system mainly (see Figure 119):

- The vacuum vessel
- The coils casings
- Other metallic parts like the radial plates

These eddy currents disturb the discharge and accelerate it at the beginning; part of the magnetic energy is dissipated in the metallic parts. Stresses appear under Lorentz forces in particular in the vacuum vessel.

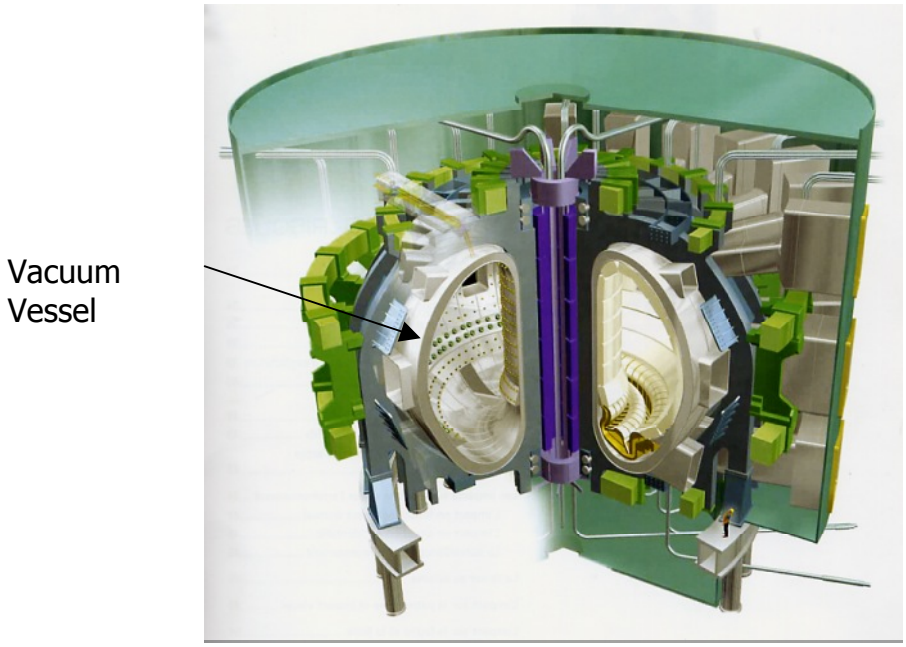

Figure 119: View of the ITER magnet system surrounding the vacuum vessel in the cryostat

In order to minimize the constraints in the vessel (magnetic pressure), a variable discharge resistor is selected to lower the initial coil voltage. The discharge resistor is adjusted at the end of the discharge such as [61]:

$R_{df} = 2.35\ R_{df0}$ corresponding to a final temperature of the resistor of 250 °C.

$R_{df0} = 0.88\ \Omega$

It is possible to calculate the inductances and the mutual inductances of the four electrical circuits d, c, p and v. Knowing in addition the resistances of these circuits R_d, R_c, R_p and R_v, it is possible to calculate the currents in the circuits during the FSD according to the following matricial equation.

d: winding pack
c : casing
p : plates
v : vacuum vessel

$$\begin{bmatrix} L_d & M_{dc} & M_{dp} & M_{dv} \\ M_{cd} & L_c & M_{cp} & M_{cv} \\ M_{pd} & M_{pc} & L_p & M_{pv} \\ M_{vd} & M_{vc} & M_{vp} & L_v \end{bmatrix} \begin{bmatrix} dI_d/dt \\ dI_c/dt \\ dI_p/dt \\ dI_v/dt \end{bmatrix} + \begin{bmatrix} R_d(T) & R_c & R_p & R_v \end{bmatrix} \begin{bmatrix} I_d \\ I_c \\ I_p \\ I_v \end{bmatrix} = 0$$

The characteristic values for the matricial equation are presented in Table 26.

Table 26: self inductance, mutual inductance and resistance of the circuit involved in a TF fast safety discharge

	Inductance Matrix (H)				Resistance
	TF winding	TF casing	TF plates	Vacuum Vessel	
TF winding	17.7	$6512\ 10^{-6}$	$6898\ 10^{-6}$	$4414\ 10^{-6}$	0.87Ω -2.04 Ω
TF casing	$6512\ 10^{-6}$	$2.7\ 10^{-6}$	$2.7\ 10^{-6}$	$1.87\ 10^{-6}$	$2.8\ 10^{-6}\ \Omega$
TF plates	$6898\ 10^{-6}$	$2.7\ 10^{-6}$	$2.86\ 10^{-6}$	$1.87\ 10^{-6}$	$4.5\ 10^{-6}\ \Omega$
Vacuum vessel	$4414\ 10^{-6}$	$1.83\ 10^{-6}$	$1.83\ 10^{-6}$	$1.87\ 10^{-6}$	$6.10^{-6}\ \Omega$

The influence of structures is highlighted in Figure 120 showing the current decay with and without structures. The accelerated initial phase due to structure is quite visible. The TF current of Figure 120 is very similar to the one presented in [62].

Overall the equivalent time constants of the discharge are quite different with structure τ_{fsd1} and without structure τ_{fsd2}.

$$\tau_{fsd1} = 11.6\ s \qquad \tau_{fsd2} = 13.3\ s$$

Knowing τ_{fsd1} it is possible to deduce τ_{da} from Eq. 22 taking into account the material properties of the conductor: τ_{da}=2.2 s

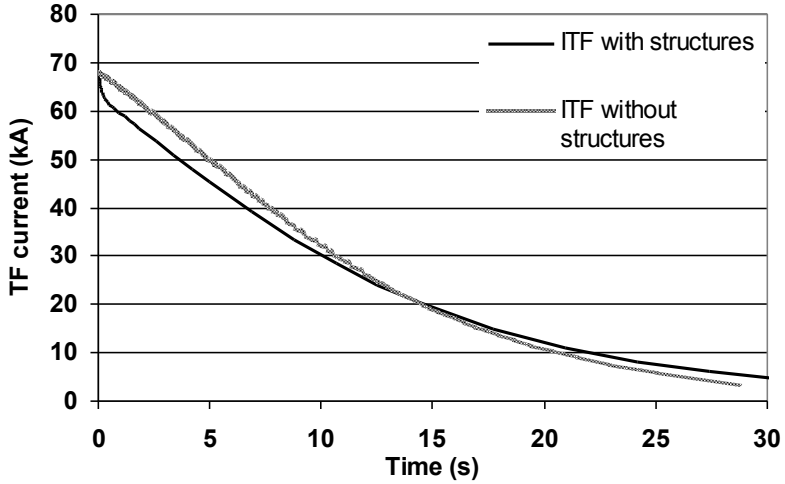

Figure 120: Influence of the TF structures on the TF current decay

7.6.3. The propagation time

For the reference case, the magnetic field is chosen at the point of abscissa = 25.85 m which corresponds to a zone of high magnetic field in DP3 and high temperature because of the distance of the helium inlet (see Figure 122). So this zone is at the lowest temperature margin. A quench at this location is therefore the most probable (see Figure 121).

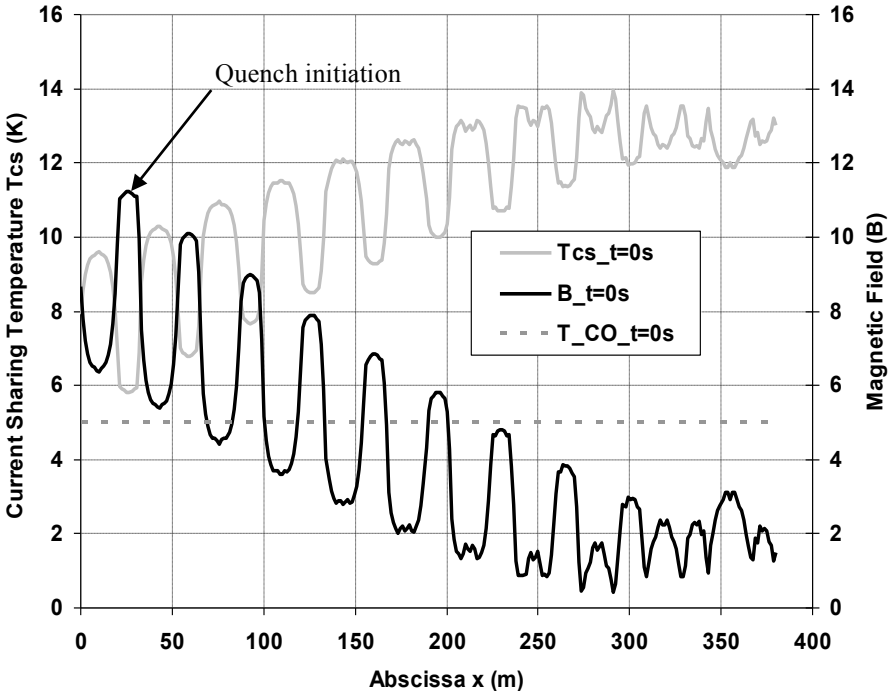

Figure 121: Magnetic field and current sharing temperature along TF DP6 (abscissa taken at helium inlet)

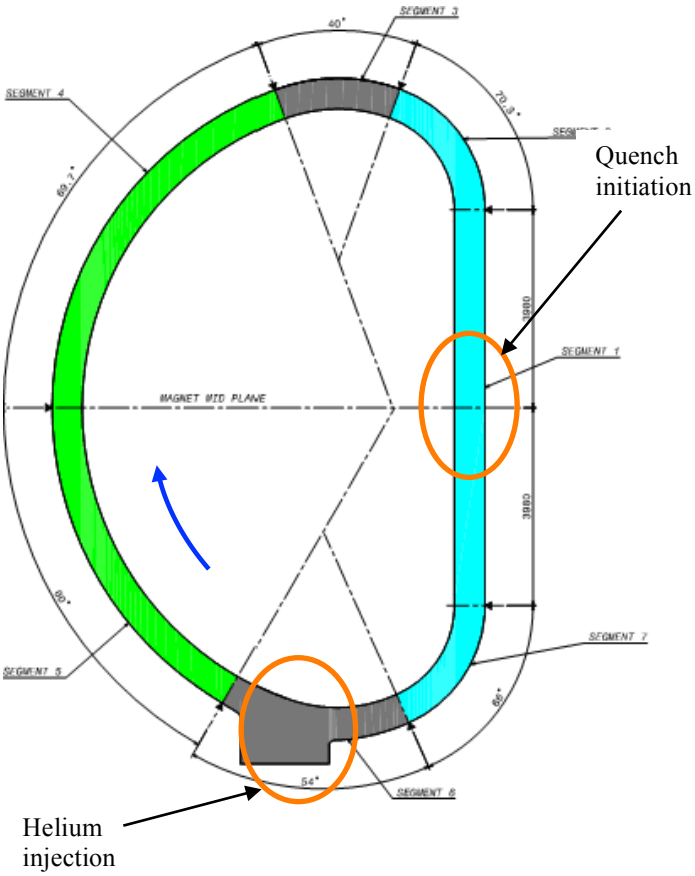

Figure 122: Location of quench initiation in ITER TF with respect to helium injection

As for the CS system the initial reference quenched length has been taken equal to 1 m, in relationship with the extension of the conductor length at the highest magnetic field which is around 12 meters .

Gandalf offers refined possibilities to numerically monitor the quench development and quench propagation by dynamic adaptive refinement of the mesh in the quench development zone.

A study has been made to adjust at best the Gandalf parameters. This study has shown the impact of the parameters on the results [63].

Following this study a mesh of type 2 (adaptive) with the parameter sizmin and sizmax respectively set at 0.01 m and 1 m has been selected.

Regarding the temporal resolution, the time step is automatically adapted by Gandalf in a range between stpmin and stpmax defined by the user, respectively taken equal to 1 μs and 0.1 ms.

In these studies the quench energy is provided through a square shape power. It is selected as two times the minimum quench energy (MQE).

a. Influence of the heat deposition duration on quench propagation

The voltage and normal length increases are very dependent on the heat deposition duration such as illustrated in Figure 123 and Figure 124 (taken from [63]), and already demonstrated in chapter 4 for an initial quenched length of 1 meter.

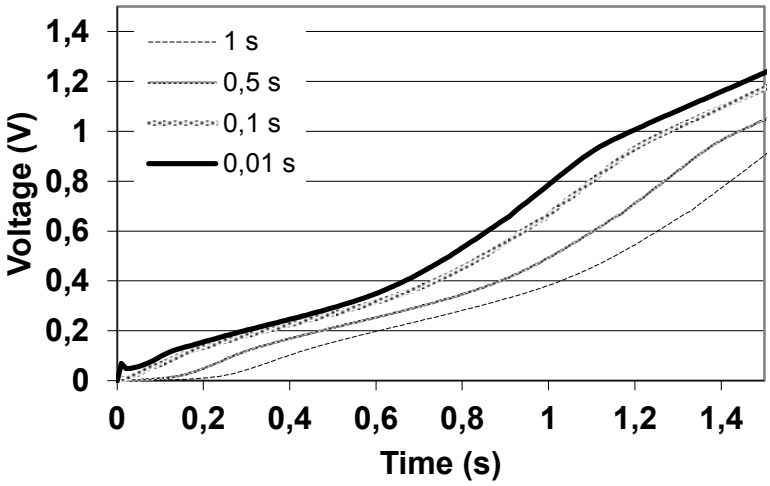

Figure 123: Influence of the heat deposition duration on the voltage increase after a quench initiation in the ITER TF (1 m heat deposition).

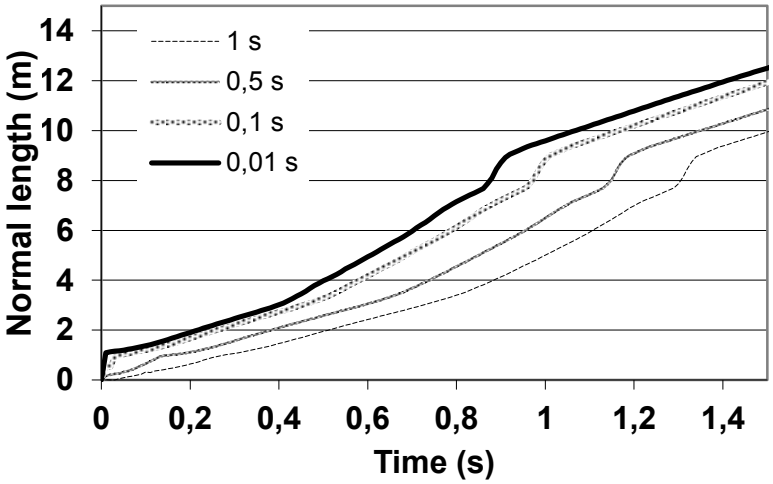

Figure 124: Influence of the heat deposition duration on the normal length increase after a quench initiation in the ITER TF (1 m heat deposition).

The main characteristics of the voltage development are presented in Table 27.

Deposition duration	0,01 s	0,1 s	0,5 s	1 s
Power	16000 W/m	1900 W/m	420 W/m	205 W/m
MQE	160 J	190 J	210 J	205 J
Time for reaching 0,1 V (s)	0,1	0,14	0,27	0,39
Time for reaching 0,3 V (s)	0,51	0,57	0,71	0,83
Time for reaching 0,5 V (s)	0,77	0,84	1.01	1,15

Table 27: Voltage increase as a function of heat deposition duration in ITER TF

This table will be used for the selection of the threshold voltage, in coherence with the other quench detectors parameters. Beyond these considerations, this table can be used for review of the quench detection system, and its robustness regarding particular quenches.

b. Influence of the length of the initial quenched length on the voltage propagation

The voltage and normal length increases are very dependent on the initial quenched length such as illustrated in Figure 125 and Figure 126 obtained from for a heat deposition within 1 s.

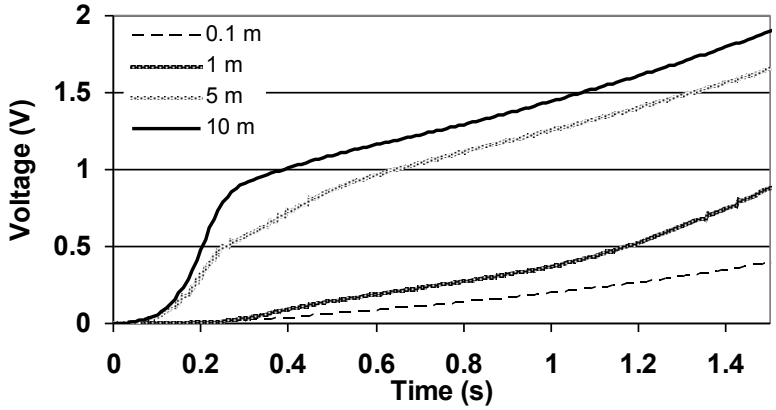

Figure 125: Influence of the heat deposition duration on the voltage increase after a quench initiation in the ITER TF (1 s heat deposition).

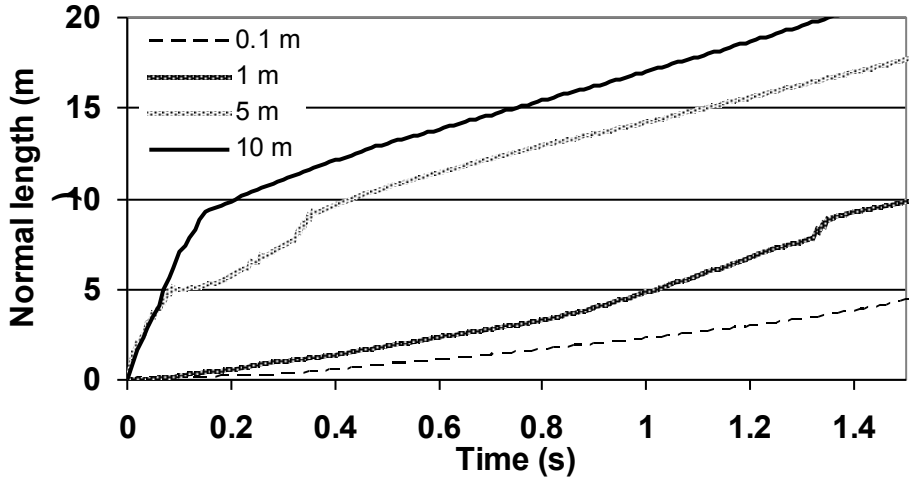

Figure 126: Influence of the initial quenched length on the normal length increase after a quench initiation in the ITER TF (1 s heat deposition).

7.6.4. Selection of the holding time

The detection and action time, τ_{da} has been estimated 2.2 s (from 7.6.2b). The propagation time τ_p needed to reach a value of $U_t = 0.5$ V is 0.84 s and $\tau_p = 0.57$ s for $U_t = 0.3$ V, as shown in Table 27.

The opening time of the current breaker ($\tau_{cb} = 0.5$ s), is driven by the time to commute the current from the by-pass to the vacuum current breaker before opening the vacuum current breaker. τ_h Can be derived from Eq. 1, which is recalled here after:

$$\tau_h \leq \tau_{da} - \tau_{cb} - \tau_p$$

It can be easily deduced that the holding times corresponding to the two threshold values U_t previously given, are:

$$\tau_h = 0.86 \text{ s} \quad \text{for } U_t = 0.5 \text{ V} \quad \text{and } \tau_h = 1.13 \text{ s} \quad \text{for } U_t = 0.3 \text{ V}$$

The recommended parameters for the quench detection based on balance of coils or coils sub-elements could be:

$$\boxed{\tau_h = 1. \text{ s} \quad \text{for } U_t = 0.4 \text{ V}}$$

7.7. Selection of a solution for the TF primary quench detection

7.7.1. Description of the reference solution of ITER

As it can be seen in Figure 127, the TF coil feeders consist of 9 cryostats placed around the machine perimeter, feeding a pair of TF coils each. The 18 TF coils are connected in series. Each of the 9 feeder cryostats houses bus bars, He piping and instrumentation wire corresponding to the following pairs of coils 5 [18]:

(18,1), (2,3), (4,5), (6,7), (8,9), (10,11), (12,13), (14,15), (16,17).

The indicated couple of coils are cold series connected within the TF cryostat.

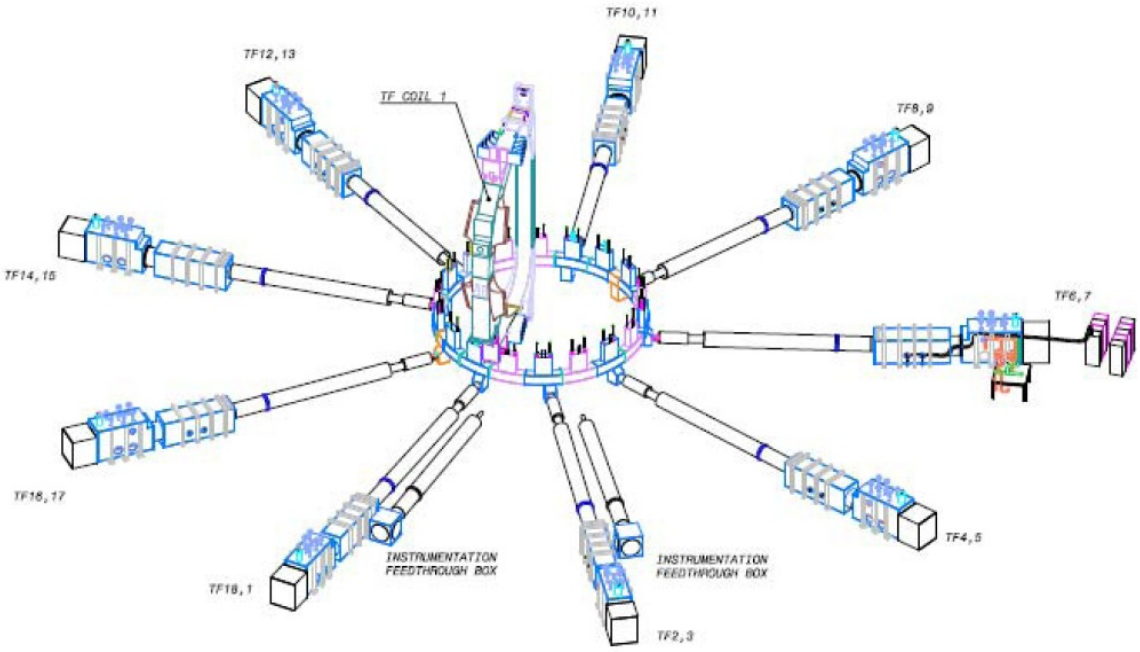

Figure 127: organization of feeders around the ITER cryostat [65]

A zoom on the distribution of current, He pipes and instrumentation wire for two coils is presented in Figure 128.

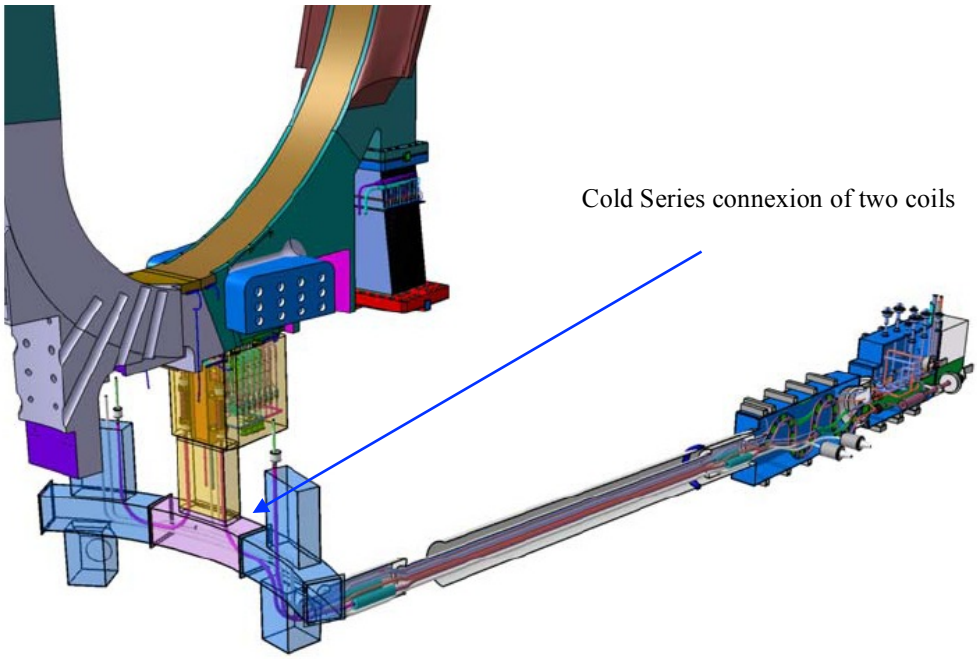

Figure 128: distribution of two coils by one feeder

A scheme of the instrumentation for one coil and per double pancake is presented in Figure 129. The helium distribution is represented with triangles on the pipes.

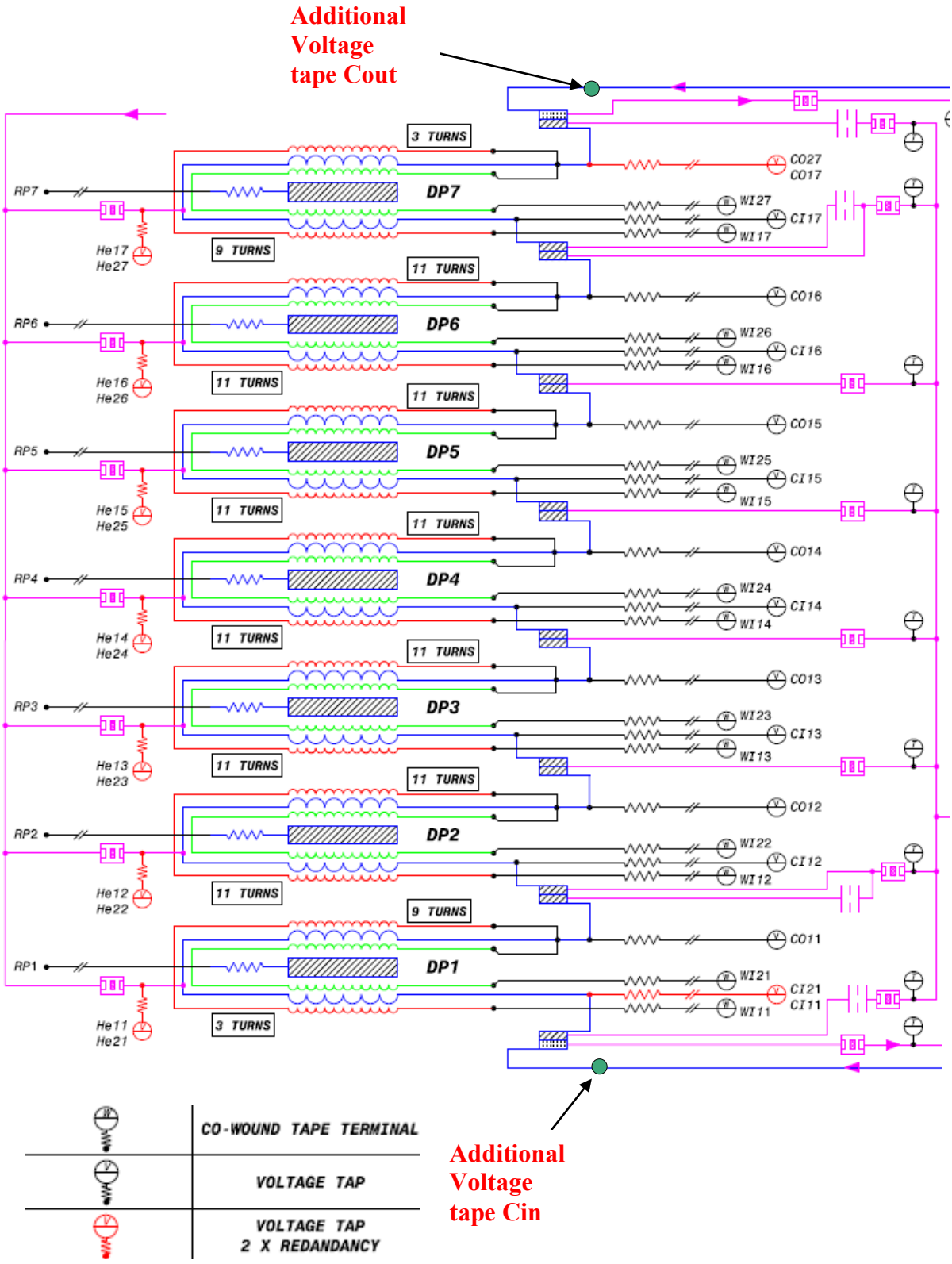

Figure 129: TF winding pack schematic instrumentation diagram [66]

The voltage sensors per double pancake are presented in Table 28. This makes a total of 4 voltage taps and 2 co-wound tapes per double pancake and a total of 28 voltage taps per coil and 14 co-wound tapes per coil (7 double pancakes per coil).

In addition there are two special voltage taps at the inlet of the coil (CI21) and at the outlet (CO27). It is proposed to implement two additional voltage taps Cin and Cout allowing monitoring the two corresponding joints at the inlet and outlet which is not possible with the present scheme. The two special voltage taps could be suppressed and replaced by respectively Cin and Cout. This makes a total of 30 voltage taps. The rest of the document is taking into account this configuration.

This is presented in Table 28 with the same denomination as in Figure 129 with an extension to mention the number of the considered coil y ($1 \leq y \leq 18$).

Table 28: Voltage sensors for ITER TF reference solution for a given double pancake x and for a given coil y

Denomination	sensor	location
CI1x_y	Voltage tap	On conductor jacket (double pancake x inlet)
WI1x_y	Co-wound tape	Merging from conductor (double pancake x inlet)
WI2x_y	Co-wound tape	Merging from conductor (double pancake x inlet)
He1x_y	Voltage tap	On helium inlet (mid double pancake x)
He2x_y	Voltage tap	On helium inlet (mid double pancake x)
CO1x_y	Voltage tap	On conductor jacket (double pancake x outlet)

7.7.2. Which solution for the primary quench detection in the ITER TF system?

It has been shown in the previous sections, that detection by coil balance could be acceptable for TF ramping and for plasma operation as well. It has been shown in particular in Tore Supra, that the main source of induced flux is coming from the plasma magnetism and the observed induced flux seems identical in every coil.

The method by coil balance is also successfully applied in KSTAR.

For eliminating the voltage, which appears across coil or subcomponents of coils, the most appropriate solutions is to balance TF coils or subcomponents of coils (pancake or double pancakes) against each other.

It is recommended to choose subcomponents, which are symmetrical regarding the poloidal field system and the plasma, which means that they are situated at the same distance from the vertical axis of the tokamak. This will minimize the difference of induced fluxes. This is the case for the following couple of double pancakes (DP1, DP7), (DP2, DP6), (DP3, DP5) (see Figure 130). DP4 is the central double pancake and no full symmetrical component can be found within a coil, it has to be balanced against another central pancake from another coil.

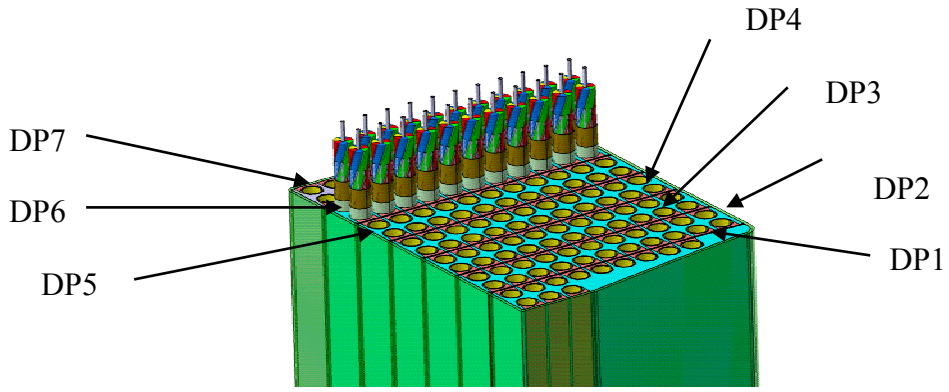

Figure 130: Double pancakes within an ITER TF coil

On another hand from an analytical approach, it has been shown that the twisting of the co-wound tapes and of the conductor, being performed on different radius, could result in substantial inductive voltages during plasma initiation and plasma discharge. In addition the implementation of such a co-wound tape within the TF conductor insulation, will further complicate the insulation process, which is already complex. There is also a risk to damage the insulation. As the method by coil balance seems to work, it is suggested to abandon the co-wound taps.

The method by coil balance can have different degrees of sophistication according to the components in associations (coils like in KSTAR or Tore Supra) or subcomponents (half coils, double pancakes or even pancakes) as it is the case in W7-X. This is what is examined in section 7.7.3.

7.7.3. Description of a solution for the quench detection in a coil couple

a. Balance of two coils

The simplest solution consists in balancing the voltage across the two coils against each other according to Table 29 and Table 30, which give an illustration for the particular couple (1,18). In the following Table 29, for simplicity, the name of the voltage tap is identified with the voltage measured from this voltage tap.

Denomination	Voltage taps association	Denomination	Voltage taps association
U_{coil_18}	CI11_18- CO17_18	U_{coil_1}	CI11_1- CO17_1

Table 29: Composition of voltage across coil 1 and 18 from voltage taps

Denomination	Characteristic Voltage association	Comments
$\Delta U_{coil\_18\text{-}1}$	U_{coil_1}- U_{coil_18}	Two coils 1-18 balance

Table 30: Composition of voltage across coil 1 and 18 from voltage taps

In this solution the total number of detectors is 1 per couple, which can be multiplied by 2 by balancing each coil to another one outside the couple for redundancy.

It has been shown in section 7.5.3 that the presence of strands of different filaments diameters should not introduce a significant voltage unbalance between two coils.

b. Balance of coils and half-coils

A more refined solution is presented, introducing in addition balance of half coils within the same feeder.

In the following Table 31, the characteristic voltages are given for a coil y, which are the voltage across the coil y and the voltage across its 2 half coils.

Denomination	Voltage taps association	Comments
U_{coil_y}	Cout_y- Cin_y	Voltage across coil y
U_{HC1_y}	CI11_y-He14_y	Voltage across half-coil 1
U_{HC2_y}	He24_y-CO17_y	Voltage across half-coil 2

Table 31: Characteristic voltages to be monitored in TF coil y

The envisaged solution is based on characteristic voltages taken in the couple of coils such as presented in section 7.7.1 . For this solution the wiring is circulating in the feeder dedicated to the given couple. The solution, illustrated on the coil couple (18,1), is presented in Table 32 and Table 33. This allows in particular twisting certain wires in order to minimize the electrical noise.

Denomination	Voltage taps association	Denomination	Voltage taps association
U_{coil_18}	Cout_18- Cin_18	U_{coil_1}	Cout_1- Cin_1
U_{HC1_18}	CI21_18-He14_18	U_{HC1_1}	CI21_1-CO11_1
U_{HC2_18}	He24_18-CO17_18	U_{HC2_1}	CI12_1-CO12_1

Table 32: Characteristic voltages on the coil couple (18,1)

The 3 detectors ΔU are presented in Table 33 for this coil couple (18,1).

Denomination	Voltage taps association	Comments
$\Delta U_{coil\_18\text{-}1}$	U_{coil_1}- U_{coil_18}	Two coils 1-18 balance
ΔU_{HC_18}	U_{HC1_18}- U_{HC2_18}	Two Half coils of coil 18
ΔU_{HC_1}	U_{HC1_1}- U_{HC2_2}	Two Half coils of coil 1

Table 33: Composition of detectors in coils (18,1) from characteristic voltages

In this solution the total number of detectors is 3 per couple of coils. In addition balancing each coil to another one outside from the couple for redundancy is recommended.

c. Balance of coils and Double-Pancakes

In the following Table 34, the characteristic voltages are given, which are the voltage across the coil y and the voltage across its 7 Double Pancakes.

Table 34: Characteristic voltages to be monitored in TF coil y

Denomination	Voltage taps association	Comments
U_{coil_y}	Cout_y- Cin_y	Voltage across coil y
U_{DP1_y}	CI11_y-CO11_y	Voltage DP1_y
U_{DP2_y}	CI12_y-CO12_y	Voltage DP2_y
U_{DP3_y}	CI13_y-CO13_y	Voltage DP3_y
U_{DP4_y}	CI14_y-CO14_y	Voltage DP4_y
U_{DP5_y}	CI15_y-CO15_y	Voltage DP5_y
U_{DP6_y}	CI16_y-CO16_y	Voltage DP6_y
U_{DP7_y}	CI17_y-CO17_y	Voltage DP7_y

The envisaged solution is based on characteristic voltages taken in the couple of coils such as presented in section 7.7.1. For this solution the wiring is circulating in the feeder dedicated to the given couple. The solution, illustrated on the coil couple (18,1), is presented in Table 35 and Table 36. This allows in particular twisting certain wires in order to minimize the electrical noise.

Table 35: Characteristic voltages on the coil couple (18,1)

Denomination	Voltage taps association	Denomination	Voltage taps association
U_{coil_18}	Cout_18- Cin_18	U_{coil_1}	Cout_1- Cin_1
U_{DP1_18}	CI11_18-CO11_18	U_{DP1_1}	CI11_1-CO11_1
U_{DP2_18}	CI12_18-CO12_18	U_{DP2_1}	CI12_1-CO12_1
U_{DP3_18}	CI13_18-CO13_18	U_{DP3_1}	CI13_1-CO13_1
U_{DP4_18}	CI14_18-CO14_18	U_{DP4_1}	CI14_1-CO14_1
U_{DP5_18}	CI15_18-CO15_18	U_{DP5_1}	CI15_1-CO15_1
U_{DP6_18}	CI16_18-CO16_18	U_{DP6_1}	CI16_1-CO16_1
U_{DP7_18}	CI17_18-CO27_18	U_{DP7_1}	CI17_1-CO27_1

The 8 detectors ΔU are presented in Table 36 for this coil couple (18,1), they are based on:

- whole coil monitoring (including joints) by balancing coil 1 against coil 18
- double pancake monitoring by balancing symmetrical pancakes within a coil, except for the central double pancakes which are balanced against each other.

It could be envisaged to include a joint in the monitoring of a double pancake, Table 33 should be then slightly changed to take into account this and include a joint in the characteristic voltage.

Table 36: Composition of detectors in coils (18,1) from characteristic voltages

Denomination	Voltage taps association	Comments
$\Delta U_{coil\ 18\text{-}1}$	U_{coil_1}- U_{coil_18}	Two coils 1-18 balance
ΔU_{DP1_18}	U_{DP7_18}- U_{DP1_18}	Two symmetrical DPs 7-1 balance in coil 18
ΔU_{DP2_18}	U_{DP6_18}- U_{DP2_18}	Two symmetrical DPs 6-2 balance in coil 18
$\Delta U_{DP3\ 18}$	U_{DP5_18}- U_{DP3_18}	Two symmetrical DPs 5-3 balance in coil 18
ΔU_{DP1_1}	U_{DP7_1}- U_{DP1_1}	Two symmetrical DPs 7-1 balance in coil 1
ΔU_{DP2_1}	U_{DP6_1}- U_{DP2_1}	Two symmetrical DPs 6-2 balance in coil 1
ΔU_{DP3_1}	U_{DP5_1}- U_{DP3_1}	Two symmetrical DPs 5-3 balance in coil 1
ΔU_{DP4}	U_{DP4_1}- U_{DP4_18}	Two symmetrical DPs 4 balance from coil 1 and 18

In this solution the total number of detectors is 8 per couple of coils. In addition balancing each coil to another one outside from the couple for redundancy is recommended.

d. Balance of coils, pancakes and half-coils

Similarly a solution can be described based on pancake monitoring using the implemented voltage taps on the helium inlet of each double pancake.

In this solution the total number of detectors is 15 per couple. In addition, balancing each coil to another one for redundancy is recommended.

Using these voltages taps, an interesting option by balancing half coils of the same coil can also be implemented.

e. Summary for the TF detection

The different solutions are summarized in Table 37. It can be seen that the number of detectors are quite different according to the solutions.

	Balance of coils Solution 1	Balance of coils And half coils Solution 2	Balance of coils and double pancakes Solution 3	Balance of coils and pancakes Solution 4
Number of detectors per couple of coil	1	3	8	15
Number of detectors for the TF system (9 couples)	9	27	72	135
Additional detector by coil balance for redundancy	9	9	9	9
Total number of detectors in ITER TF system	18	36	81	144

Table 37: Number of TF quench detectors according to solutions

It is not straightforward to select one of the 4 solutions presented in Table 37. It is suggested to keep all the voltage taps and the associated wiring as presented in Figure 129.

It is however quite sure that solution 4 will not be necessary. This can be considered as an ultimate back up solution not to be implemented at the beginning of the ITER TF commissioning.

The final solution between solution 1, solution 2 and solution 3 has to be selected after further observations on EAST and KSTAR as suggested in section 7.5.2.

For each solution, a redundant scheme has also been proposed.

7.7.4. Monitoring of joints

As illustrated during the LHC commissioning, it is important to monitor the joints of the coils at least during commissioning. This is especially recommended if the resistance of the joints has not been measured during the coil acceptance tests, before the assembly into the ITER cryostat.

If a joint resistance happens to be not according to specifications during operation, it will be possible to discriminate which joint is concerned thanks to the joint monitoring. Note that the monitoring of the temperature outlet is not sufficient to state that the cause of abnormal heating is a deficient joint.

The joint monitoring is delicate because the resistive voltage to observe is low. The voltage taps associated with this measurement have to be twisted together all along the circulation in the feeder.

Resistance of a superconducting joint: 2 nΩ, corresponding voltage at 68 kA: 136 μV

Power in the joint: 9.24 W

Resistance of a resistive joint: 75 nΩ, corresponding voltage at 68 kA: 5 mV

Power in the joint: 350 W

The joint monitoring can be performed according to Table 38.

Table 38: Composition of the 8 joint voltages of coil y from characteristic voltages

Denomination	Voltage taps association	Comments
V_{joint_1y}	CI11_y-Cin (twisted)	Monitoring of 1 st joint of coil y
V_{joint_2y}	CI12_y-CO11-y (twisted)	Monitoring of 2 nd joint of coil y
V_{joint_3y}	CI13_y-CO12-y (twisted)	Monitoring of 3 rd joint of coil y
V_{joint_4y}	CI14_y-CO13-y (twisted)	Monitoring of 4 th joint of coil y
V_{joint_5y}	CI15_y-CO14-y (twisted)	Monitoring of 5 th joint of coil y
V_{joint_6y}	CI16_y-CO15-y (twisted)	Monitoring of 6 th joint of coil y
V_{joint_7y}	CI17_y-CO16-y (twisted)	Monitoring of 7 th joint of coil y
V_{joint_8y}	CIout_y-CO17-y (twisted)	Monitoring of 8 th joint of coil y

In Figure 131 is schematically presented a joint of praying end type.

The question is how the measurement of the joint resistance is affected by the position of the voltage taps.

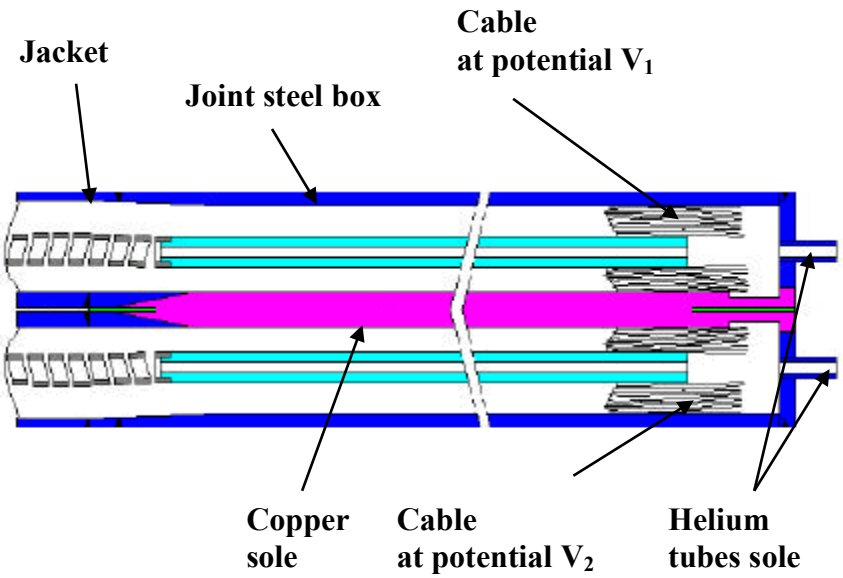

Figure 131: Praying hand type joint to illustrate the potentials

Both conductors can be considered at respective equipotentials V_1 and V_2. The resistance of the joint is by definition:

$$R_{joint} = \frac{V_2 - V_1}{I_{cond}}$$

The voltage difference is appearing at the interface between the cable and the copper sole. The two copper soles can be considered to be at the same potential.

It has been shown in [42] and [68] that the resistance measurement is very dependent on the position of the voltage taps. At a characteristic length from the joint, the voltage on the jacket is equal to the voltage on the cable.

It can be seen the helium outlet tubes are at an intermediate potential between the copper sole and the cable. So the voltage measurement taken from the helium outlet tubes is smaller than the voltage corresponding to the joint resistance.

In addition the two helium tubes are generally short-circuited at a certain distance from the joint, very near the short-circuit point the voltage measurement is zero and there is no longer any information about the joint resistance. If the voltage is taken on the helium tubes it has to be taken sufficiently far from this point.

7.8. Conclusion for the TF quench detection system

In this chapter it has been demonstrated that balance of TF coils or of symmetrical subcomponents of TF coils is a possible solution for the primary quench detection of the ITER TF system. The detectors are built from the implemented voltage taps and the precise constitution of these detectors is described in the document. This conclusion was deduced from theoretical considerations about the origin of the induced flux in the TF coils of a tokamak. These considerations are confirmed by experimental observation on Tore Supra, KSTAR and EAST TF systems. Further experimental observations are however recommended on KSTAR and EAST to finalize the solution for the detection and decide

which level of subcomponents (pancake, half coils, double pancake) it is necessary to balance in addition to TF coils.

It is therefore recommended not to implement co-wound tapes, which appear as not necessary and even can trigger false quench detections during plasma initiation. They introduce also an additional difficulty in the TF conductor insulation which can be avoided.

It is recommended, in a conservative approach, to keep all the voltage taps foreseen in the reference ITER document. The implementation of the corresponding electronics can be adjusted during the commissioning as a function of the ITER TF system behaviour.

According to a study of quench propagation in a realistic case the recommended parameters for the quench detection are:

$\tau_h = 1.\ s$

And

$U_t = 0.4\ V$

8. Quench detection in the ITER PF system

The 6 PF composing the vertical field system of the tokamak are all different. Again, the following chapter will show how a quench can be detected in time, and a solution is presented.

8.1. Introduction [94]

Similarly to the CS system [16], the PF system [18] of a tokamak is a pulsed system.

The magnet quench detection system will be able to distinguish between superconductor quench and the electromagnetic perturbations caused by plasma scenarios or plasma disruption with a reliability of >90% for the CS, CC and PF coils for type I and II disruptions and type II and III. A difficulty for the study of the PF system is the flexibility of the system.

This study will focus on the 15 MA baseline scenario (see Figure 132), giving the conceptual approach for defining for each coil, in this case, the couple (U_t, τ_h) which are the main parameters of the quench detection [51], as presented in section 3.3.

In the rest of this chapter, a couple of common abbreviations and denominations are used and detailed in Table 39.

Abbreviation	Meaning
CS	Central Solenoid
PF	Poloidal Field Coils
TF	Toroidal Field Coils
PS	Passive structures. Includes Cryostat, Vacuum Vessel inner and outer shells, divertor supports
DP	Double Pancake
T, B, SCC	Top, Bottom, and Side Correction Coils
DP-C1	Conductor 1 (which is connected to the double pancake joint with upper double pancake)
PF3-DP4-C1	Conductor 1 of the 4th double pancake of PF3. The index refers to the upper DP
PC	The index of the PC refers to the upper pancake of the coil.

Table 39: commonly used abbreviations

8.2. The ITER PF system

The PF system consists in 6 coils, PF1 through PF6 that serve to shape and stabilize the position of the plasma in the tokamak. All coils are built by stacking 6 to 9 Double Pancake (DP) windings wound with two-in-hand NbTi superconducting CICCs (cable-in-conduit-conductors). The outer diameters of the coils vary between ~ 8 m and ~ 24 m. Figure 133 shows the sizes and relative positions of all PF coils.

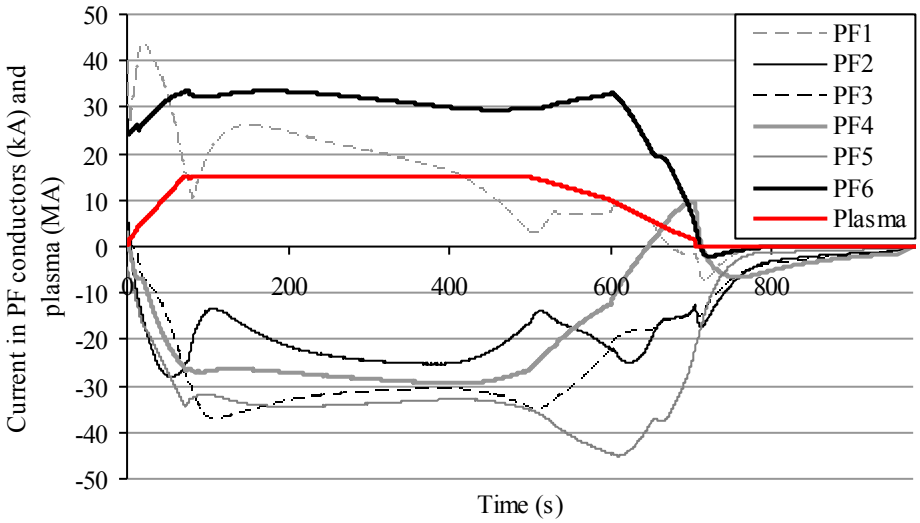

Figure 132: ITER PF currents during the 15 MA reference scenario

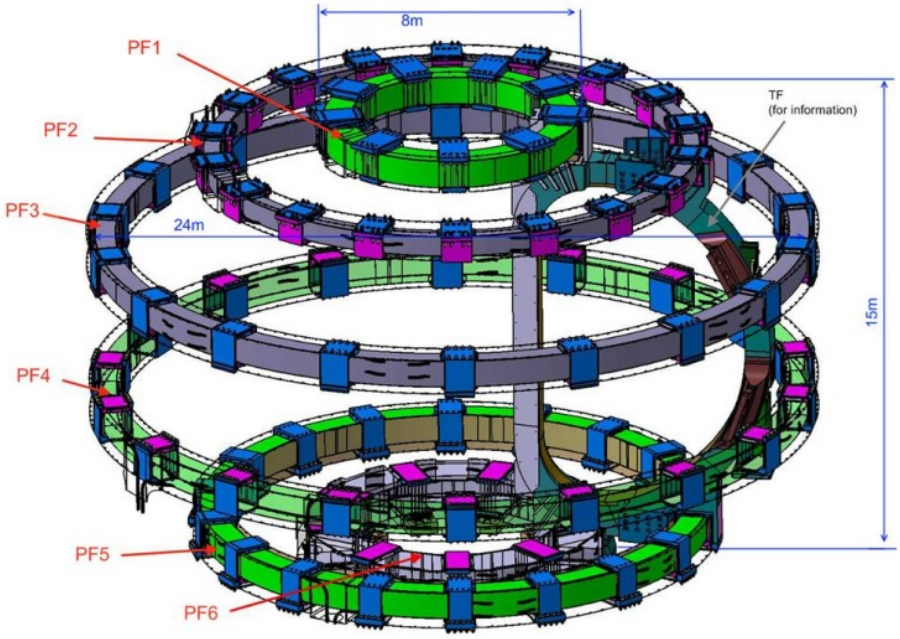

Figure 133: Layout of the ITER PF system

Operating conditions of the PF conductors in terms of I, dI/dt, B, dB/dt have been analysed for the 15 MA baseline scenario. For each of the 6 PF coils a search is carried out in space, to find out the highest values of field and dB/dt as a function of time. The peak values occurring during the 15MA baseline scenario are reported in Table 40 (from [18]).

	PF1	PF2	PF3	PF4	PF5	PF6
I_{max} (kA)	43.73	10.00	1.08	9.47	0.00	33.50
I_{min} (kA)	-7.17	-28.14	-37.05	-29.48	-45.08	-2.13
$(dI/dt)_{max}$ (kA/s)	1.64	20.03	7.13	5.79	9.13	0.39
$(dI/dt)_{min}$ (kA/s)	-11.55	-11.31	-4.21	-5.85	-5.60	-3.55
B_{peak} (T)	5.27	2.35	3.49	2.69	4.91	4.91
$(dB/dt)_{max}$ (T/s)	0.30	0.98	0.30	0.41	0.38	0.23
$(dB/dt)_{min}$ (T/s)	-1.24	-0.87	-0.22	-0.34	-0.91	-0.62

Table 40: Peak values of I, dI/dt, B, dB/dt for the 15 MA baseline scenario

8.3. ITER PF conductors

The ITER PF conductors are presented in Table 41. There are three types of conductors respectively for:

- PF1-6
- PF5
- PF2,3,4

There are only two types of strands: type 1 for PF1-6, type 2 for PF 2-3-4-5

Characteristic	PF1-6	PF5	PF2,3-4
Sc strand type	NbTi (Type 1)	NbTi (Type 2)	NbTi (Type 2)
Cable pattern	$3sc \times 4 \times 4 \times 5 \times 6$	$(3sc \times 4 \times 4 \times 4)$ + $1\,Cu\ core\ 3$	$\left(\begin{array}{c} (3sc + 1\,Cu) \times 3 \times 4 \\ + \\ 1\,Cu\ core\,1 \end{array} \right) \times 5$ + $1\,Cu\ core\ 2$
Central spiral	10 x 12 mm		
Petal wrap	0.05 mm thick, 50% cover		
Cable wrap	0.10 mm thick, 40% overlap		
Ni coated strand diameter	0.73 mm	0.73 mm	0.73 mm
NbTi strand Cu-to-non-Cu ratio	1.6 type 1	2.3 type 2	2.type 2 strand3
Number of sc strands	1440	1152	720
Non copper (mm^2) untwisted [twisted]	229.3 [238.8]	144.5 [150.5]	90.3 [94.1]
Total copper (mm^2) untwisted [twisted]	366.8 [382.1]	370.5 [385.1]	424.7 [440.9]
Copper strand/core diameter (mm)	none	Cu strand: 0.73 Cu core 3: 2.85	Cu core 1: 1.20 Cu core 2: 2.70
Void fraction (annulus)	34.3	34.1	34.2
Cable diameter	37.7 mm	35.3 mm	35.3 mm
Circle in square 316L Jacket (mm)	53.8 x 53.8	51.9 x 51.9	51.9 x 51.9

Table 41: PF conductors according to PF coils

The scaling law used for the strands is the Bottura scaling law [53], [54].

$$J_c(B,T) = \frac{C_0}{B}\left(1 - \left(\frac{T}{T_{c0}}\right)^{1.7}\right)^{\gamma}\left(\frac{B}{B_{c2}(T)}\right)^{\alpha}\left(1 - \frac{B}{B_{c2}(T)}\right)^{\beta}$$

$$B_{c2}(T) = B_{c20}\left(1 - \left(\frac{T}{T_{c0}}\right)^{1.7}\right)$$

The coefficients of the scaling law are given in Table 42 according to the type of strand.

	C_0	B_{c20}	T_{c0}	α	β	γ
Strand type 1 (PF1-6)	$1.132\ 10^{11}$	12.97	9.15	1	0.96	2.91
Strand type 2 (PF 2-3-4-5)	$1.52\ 10^{11}$	13.72	8.79	1.	0.98	1.96

Table 42: Coefficients of scaling law according to strand type

8.4. Models construction for voltage calculation

8.4.1. Tokamak model

For this study, taking into account the large calculation time, several models have been tested in order to select the level of details of the model, in terms of geometry and scenario, acceptable regarding accuracy vs. calculation time.

Three models have been tested, as presented in Figure 134.

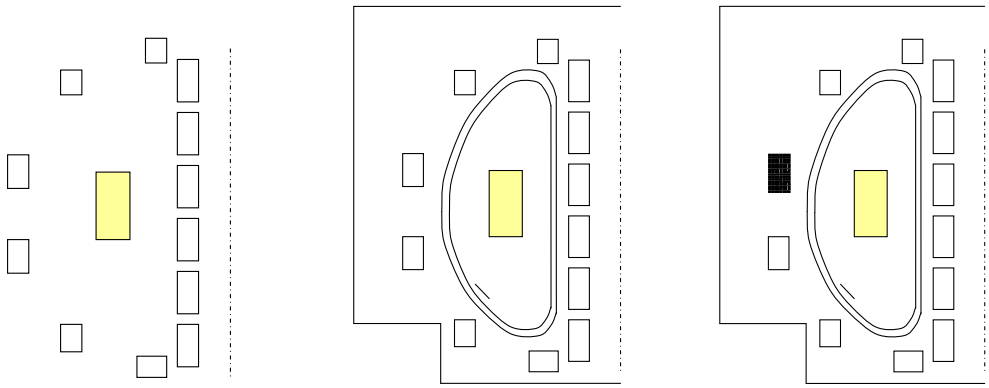

a. CS and PF + Plasma b. CS + PF + Plasma + PS c. CS + PF + Plasma + PS + Discrete studied coil

Figure 134: Models built for QD studies. Model (c) is used in this studies

Starting from first calculations using coarse models for the routing and DP winding patterns, it appeared clearly that the passive structures play a significant role on the measured voltage, as showed in Figure 135 hereafter.

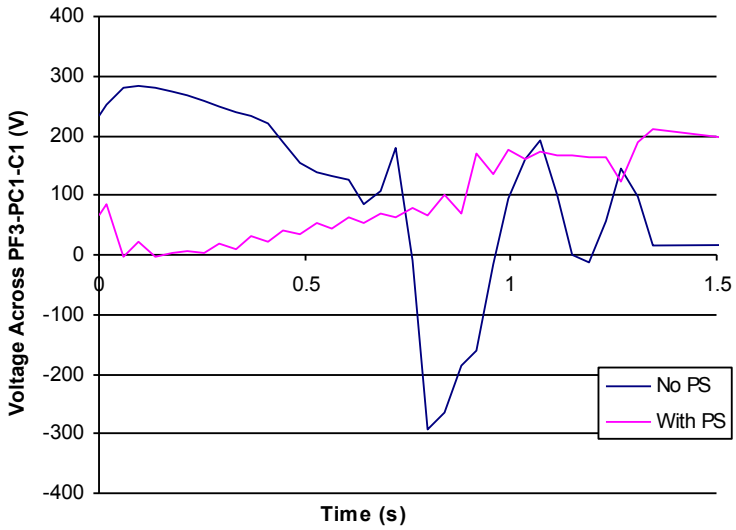

Figure 135: Voltage across PF3-PC1-C1 during plasma initiation with and without passive structures

Passive structures representing the cryostat, the vacuum vessel and the divertor support have been included during plasma initiation for each calculation.

8.4.2. Detailed model for the studied coil

The construction and use of the third model (with vacuum vessel and turn by turn discrete coils) requires the implementation of a refined coil model for the studied coil. The refinement consists in the decomposition turn to turn of the studied coil (see Figure 136), instead of a uniform current density in a coil cross section as it is the case for the other coils. With such a description the calculation accuracy can really be high.

Each turn of PF3 has been modelled with a plain cable whose cross section is a square (edge of 3.53 cm, the diameter of the actual cable). Each turn of PF3 is a horizontal planar coil, centred on the machine axis. It is perfectly circular (no joggles). This last point could be adjusted if needed.

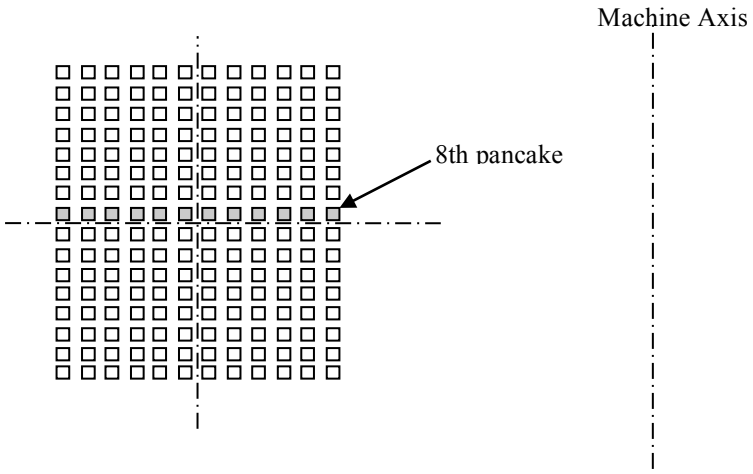

Figure 136: Discretization turn by turn of PF3

In Figure 137, the impact of different parameters is studied.

- Influence of the coil refinement (discrete or block),
- Influence of the scenario discretization: 73 points (reduced) and 4797 (Allplas)

1061 and 2122 correspond to the number of radial divisions for voltage integration. It does not affect the result, highlighting that 1061 divisions are sufficient regarding the accuracy.

It is shown that the model choice has a strong impact on the voltage response across conductors. The 73 points scenario is not acceptable and the coil refinement has a high impact on the result. Therefore, for the rest of the study on quench detection in the PF coils, the refined model has always been adopted for the studied coil. In the following Figure 137 a, some signals seem not to be visible. Actually, they are superimposed with others. Basically, the “Discrete” are all together in the lower part of the graph.

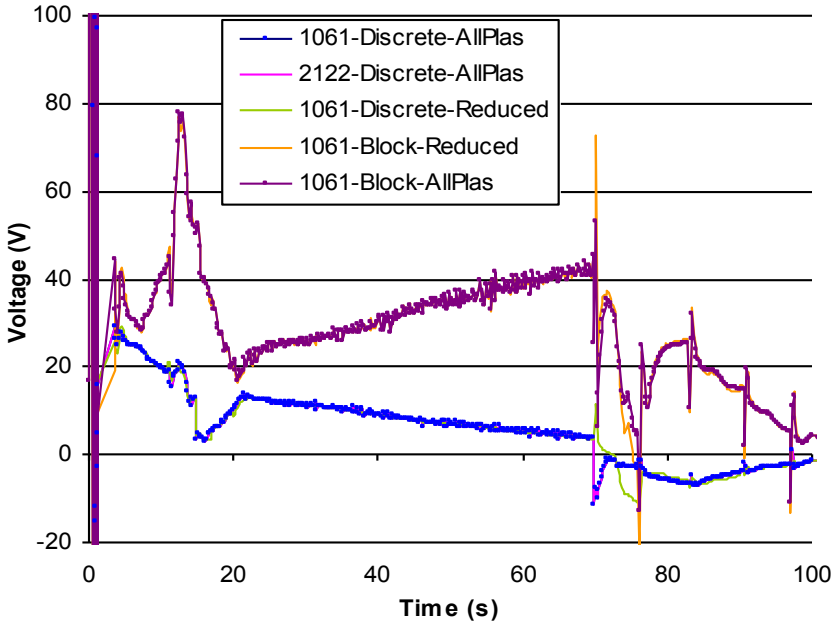

a- Plasma initiation and ramp-up

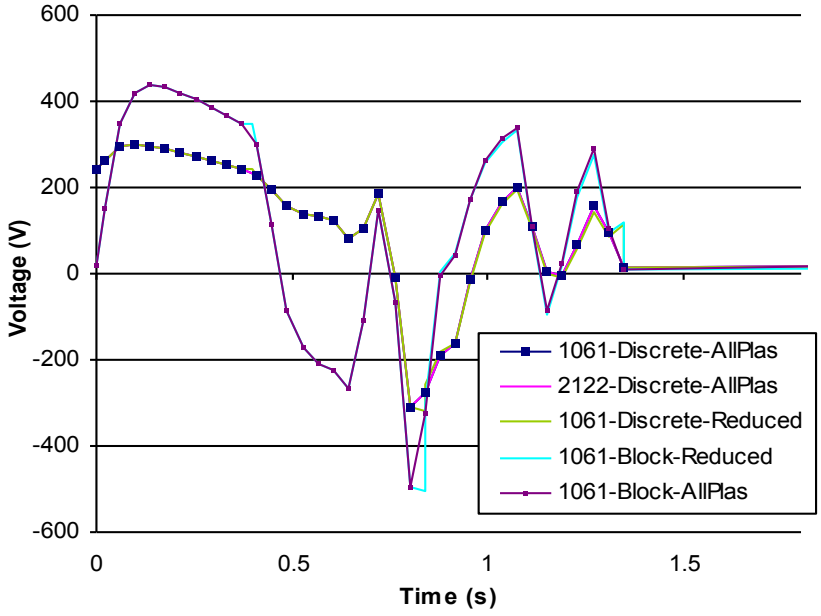

b- Plasma initiation

Figure 137: Voltage drop across conductor of PF3 during plasma initiation and current ramp-up

8.4.3. Scenario definition

Plasma and scenario: The refinement in time of the plasma scenario has also been adapted to the study. By reducing the time interval during plasma current flattop, and keeping all its details during plasma initiation, current ramp up and down, and plasma termination. The initial file contains 4797 equilibriums; it has been reduced to 648 equilibriums (eqs in the graphs). The equilibriums that have been suppressed are mainly concentrated during the plasma current flattop. Concerning all coils, no reduction has been made, since they do not move (contrarily to the plasma). As presented in the following Figure 138, this reduction had no impact on the definition of the plasma current along the scenario, but allows a great

reduction of the calculation time. In the figures, the dots represent the 73 equilibriums, and the superposition of the lines representing the scenario in the reduced and detailed versions, show that the plasma scenario simplification will not affect the result.

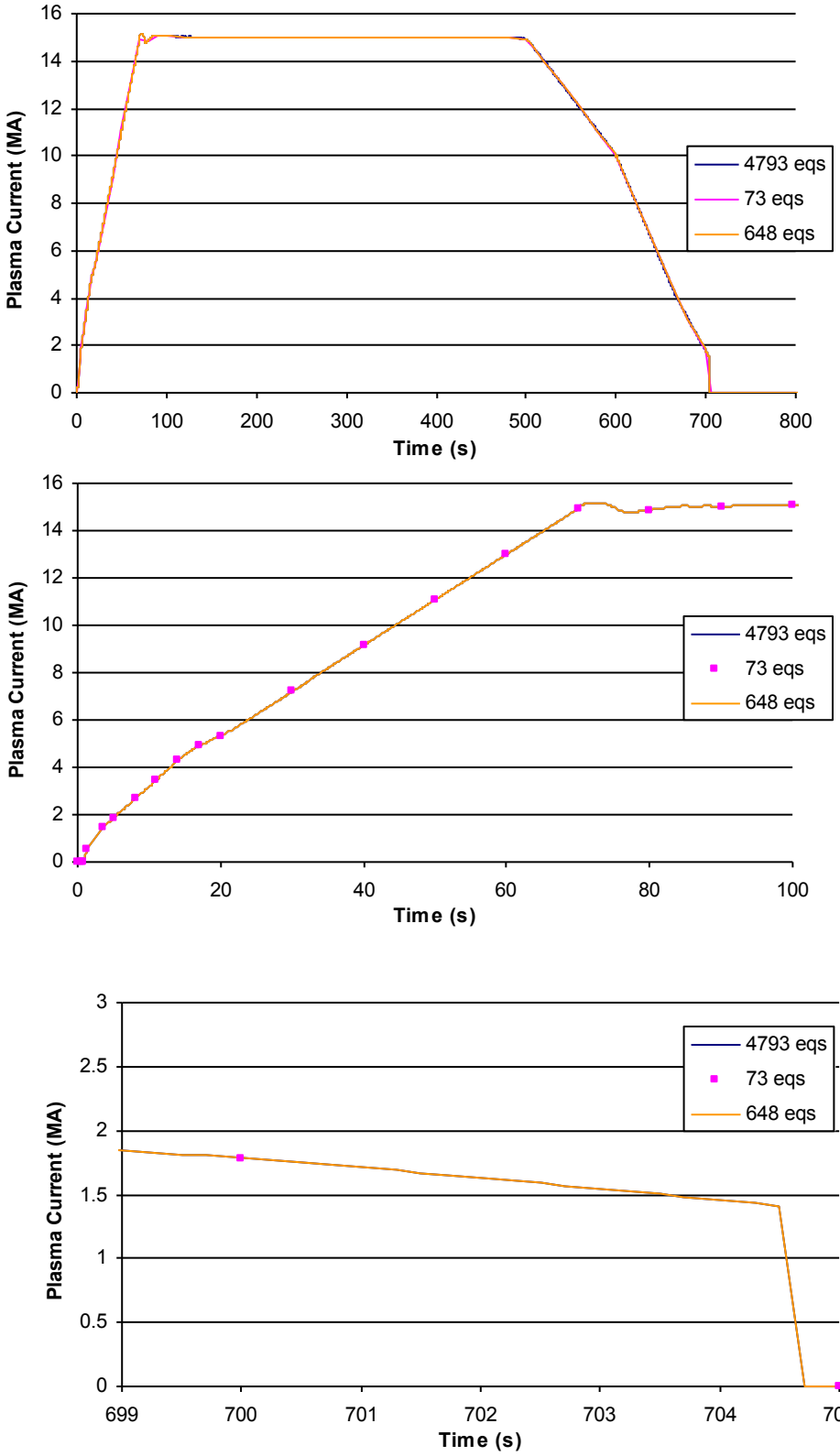

Figure 138: Plasma scenario and model definition

The reduction of the scenario permits a great reduction in terms of calculation efforts, hence, the 648 equilibriums scenario will be used.

8.4.4. Presentation of the reference solution

As presented in [18], DDD version 2009, the reference solution for quench detection is made by comparison of the voltages across each two-in-hands conductors:

"As seen in Figure 139*(a), a bridge quench detector is made by comparison of the voltages in two-in-hand double pancake winding. Voltage taps for quench detection (red dots) are located on the coolant outlet tube. Voltage taps for the measurement of the joint voltage are installed at the transition lengths between the conductor and the joint.*

Two quench detectors are available for each DP. The quench voltage taps cover the resistive voltages of two joints in each hand that are cancelled by the bridge circuit. This also provides indirect back up information of the joint resistance. The cancellation of inductive voltage is affected by differential winding lengths in different hands. Tentatively, this will be compensated numerically once the differential inductance is measured in a DP.

A protection resistor is connected in between the voltage tap and the diagnostic wire to protect the coil in case the instrumentation wire is grounded. Redundant cold resistors wrapped in ground insulation at each voltage tap location are used in the present design."

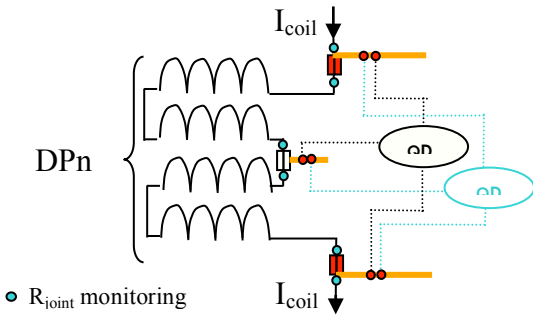

a) Quench Detection Voltage Taps

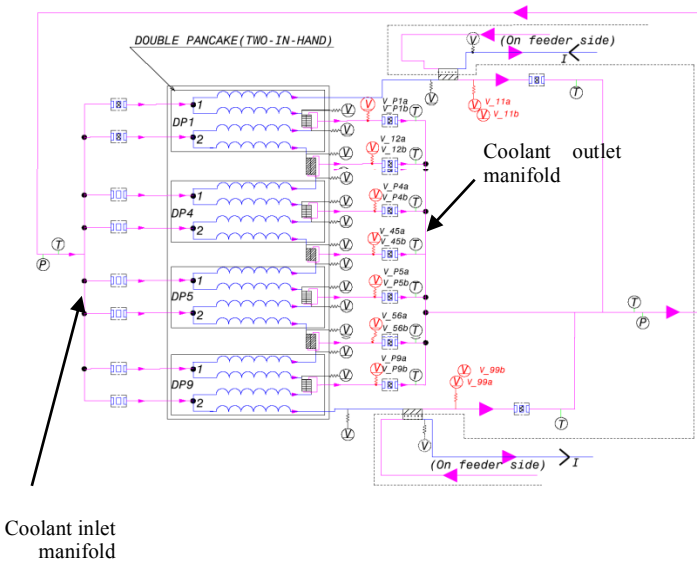

b) Temperature and pressure measurements of cooling system

Figure 139: Quench Detection Voltage Taps

8.4.5. Implementation of the reference solution in TrapsAV

The voltage calculation with TrapsAV cannot be done directly across one double pancake (due to the different winding patterns and associated different inductances). The voltage in TrapsAV is calculated across each conductor, for each pancake. Therefore after calculation, voltages across C1-Upper pancake and C1-Lower pancake have to be properly added in order to estimate the voltage which can be measured in reality for quench detection. In Figure 139

and Figure 141 it is showed the way C1 and C2 are wound and connected together, and consequently, determines the way voltages should be added.

At the opposite of the "simplified" model used for the model of the coil which is being studied (turn to turn defined, but with circular conductors – cylindrical geometry, no joggles), for the flux calculation, the real loops have been taken into account, with terminals and radial joggles. It is also useful to note that correction coils are not included in the simulation, because they are oppositely powered, and consequently, the flux induced by one CC is compensated by the one diametrally opposed (if included, they would slightly slow down the calculations…).

As specified in 11P3WP_000439E (ITER_D_245574 v5.0), the different pancakes and double pancakes do not have the same winding pattern and this has been taken into account. The following Table 43 shows the difference introduced by the change of patterns in PF3.

UDPJ : Azimutal angle between Upper Double Pancake Joint and Pancake joint
J1 : Azimutal angle between Joggle zone 1 and Pancake joint
J2 : Azimutal angle between Joggle zone 2 and Pancake joint
J3 : Azimutal angle between Joggle zone 3 and Pancake joint
J4 : Azimutal angle between Joggle zone 4 and Pancake joint
LDPJ : Azimutal angle between Lower Double Pancake Joint and Pancake joint

A Joggle zone is the zone where the turn to turn transition occurs for both C1 and C2. There are four Joggle zones in each Double Pancake.

	Pattern	UDPJ	J1	J2	J3	J4	LDPJ
DP1	K-T1	230	70	270	90	290	140
DP2	K	220	70	270	90	290	140
DP3	L	240	70	270	90	290	140
DP4	K	220	70	270	90	290	140
DP5	L	240	70	270	90	290	140
DP6	K	220	70	270	90	290	140
DP7	L	240	70	270	90	290	140
DP8	M-T2	220	70	270	90	290	130

Table 43: Differences introduced by the change of pattern in PF3

Other angles were used to calculate the difference between voltages across C1 and C2 of the same pancake. These angles are given in Figure 140 which illustrates the pattern K-T1, the winding of the first two pancakes of PF3.

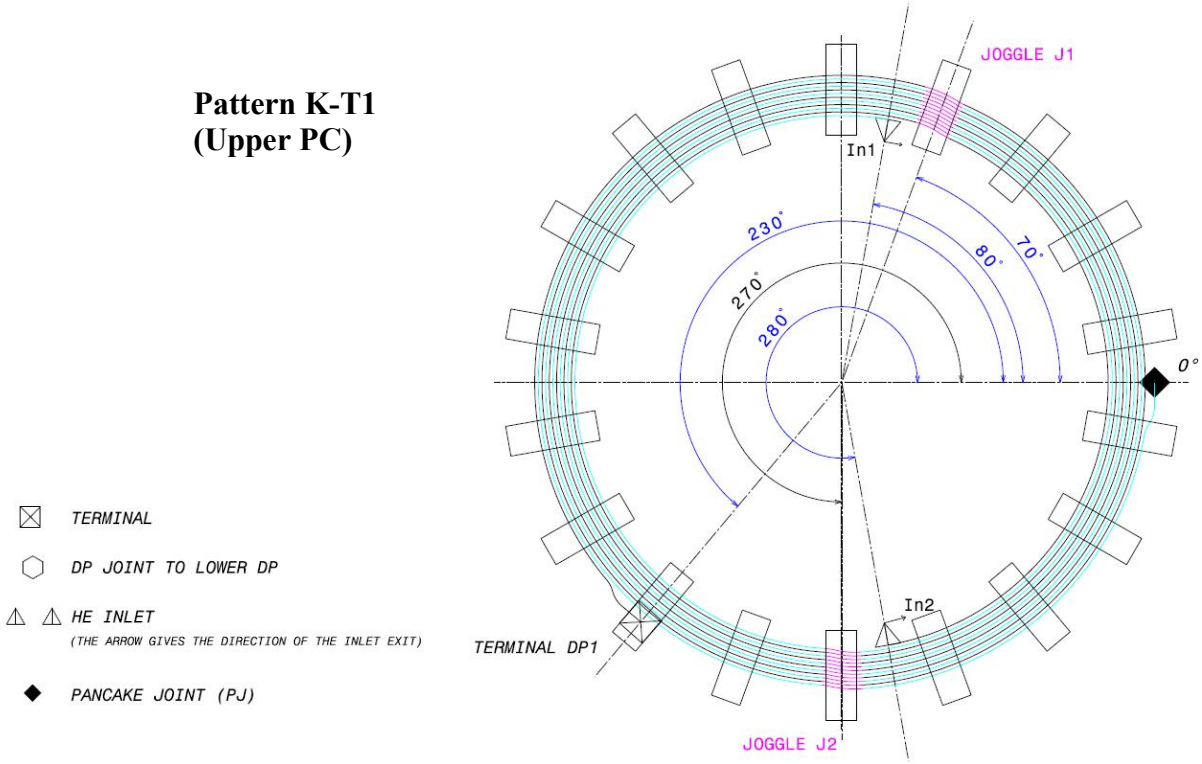

Figure 140: Upper pancake winding (PC) of PF3

This kind of winding introduces differences between the voltages appearing across the two conductors of the same pancake, and the f_i coefficients used in Eq.7 (page 77) illustrate the interface between the technological problem, and the input data for voltage calculation. The method used for this voltage calculation is explained in section 5.3.1.

The following Figure 141 show how the conductors are electrically connected in the same double pancake. The voltage taps are located at the DPJ (Double Pancake Joints) and PCJ (Pancake Joint).

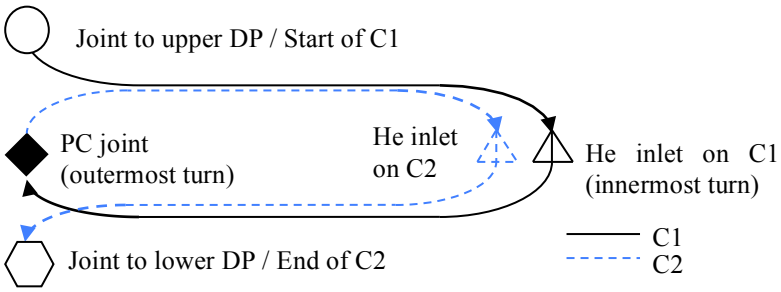

Figure 141: DP winding pattern

Therefore, for each double pancake DPi, 4 voltages are calculated:

- $U_{DPi\text{-}C1\text{-}upper}$: voltage across C1-Upper pancake
- $U_{DPi\text{-}C1\text{-}lower}$: voltage across C1-Lower pancake
- $U_{DPi\text{-}C2\text{-}upper}$: voltage across C2-Upper pancake
- $U_{DPi\text{-}C2\text{-}lower}$: voltage across C2-Lower pancake

These voltages should be added as follow, in order to estimate the measured voltages between each pair of voltage taps:

$$U_{DPi-C1} = U_{DPi-C1-upper} + U_{DPi-C1-lower}$$

and

$$U_{DPi-C2} = U_{DPi-C2-upper} + U_{DPi-C2-lower}$$

This calculation has been run for scenario 2 baseline 15 MA, whose link is given :

Scenarios_for_Coil,_Power_Supply_and_Cry_2FTVKV_v1_10.xls (2FTVKV)

With the following description of the PF coils (except PF3, whose geometry has been adapted to refine the calculation).

Size_and_Position_of_the_PF_Coils_2ABBBD_v2_2.doc (ITER_D_2ABBBD v. 2.2)

The CS has been modelled according to the DDD figures:

DDD11-3: CS Coils and Pre-Compression Structure (ITER_D_2NHKHH v1.5)

Note that for calculation time reduction, the amount of plasma equilibriums has been decreased down to 648, as explained before. Indeed, during the plasma current flattop, the plasma does not play a significant role regarding voltages across windings.

It is recalled that the given voltage is not the actual voltage which appears across the conductors, since the flux collection loops are not closed in the vicinity of the conductors, but in a bundle of instrumentation wires located above or under the coil (depending on the coil)…

The example of PF6 is given in Figure 142. Therefore, the voltage given in the following paragraphs should be completed by an additional circuit for the loop closure. This circuit has a shape strongly depending on the external structures of the coils, like the tie-plates and separation plates are for the CS. This circuit and associated extra voltage will be given in the next section (section 8.9 in particular). The equivalent approach has been used for the CS, and is explained in section 6.3.3.

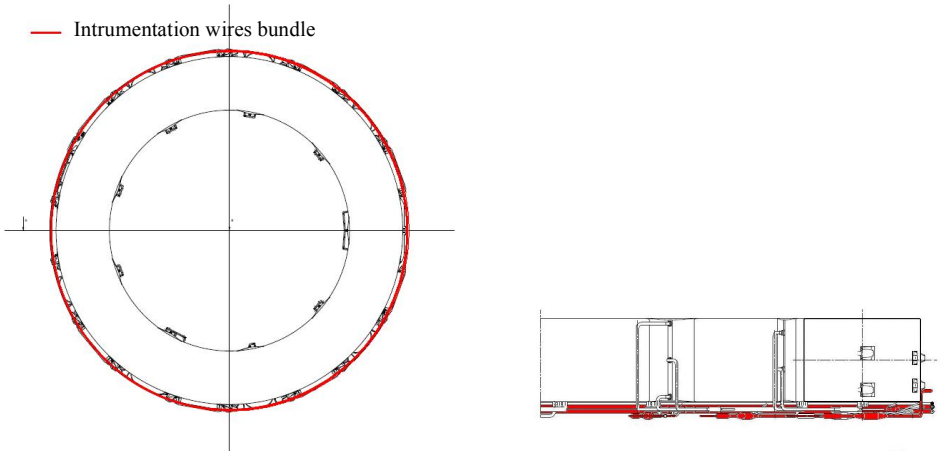

Figure 142: PF6 localization of the bundle of instrumentation wires

Nevertheless, in a first approach which gives a correct view of the actual voltages order of magnitude, the model ignoring the real routing of the wires is explored. The calculations the

results of which are given in section 8.7, correspond to the circuit described in Figure 143. In this figure, only one conductor is represented. The dashed line is the virtual closure of the circuit. This closure is to be replaced taking into account the real path of the instrumentation wires. The principle of the additional calculations is described in section 8.10.

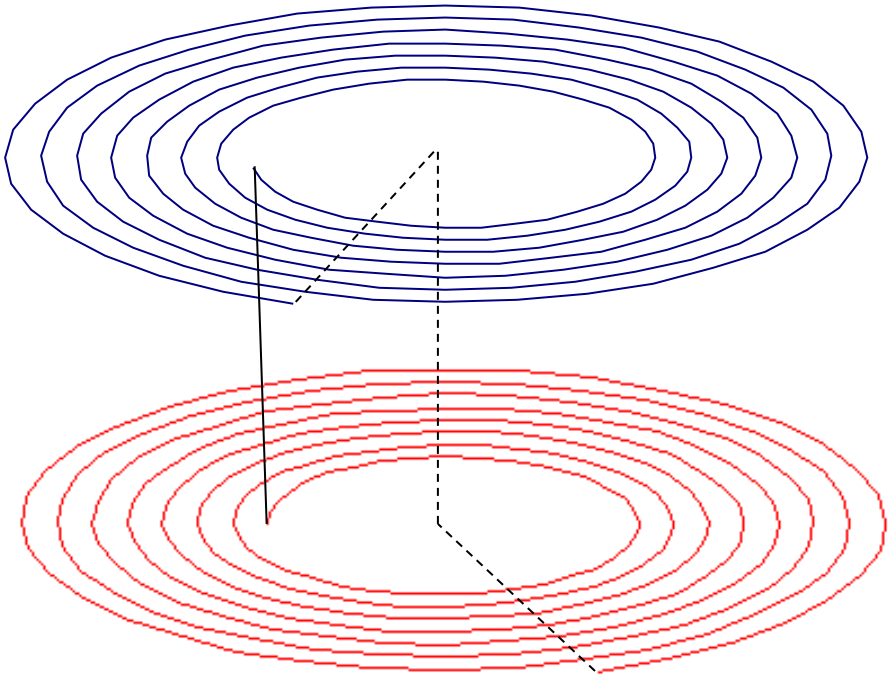

Figure 143: Double pancake circuit with virtual closure

The inductive signal due to the flux collected by the loop previously represented is calculated along the scenario, and the compensation is applied according to section.

8.5. Quench Detection hypotheses and methodology

8.5.1. Main hypothesis for the present study

The PF system is a very flexible system. It is not possible to study all the various scenarios, corresponding to different current scenarios in each PF coil. It has been decided to limit this study to the 15 MA reference scenario, as explained in section 8.4.3. The followed method and hypothesis are described in the next paragraphs. They are quite general and it is possible to further reconsider the quench detection parameters in the framework of other scenarios using TrapsAV.

Similarly and conservatively the equivalent time constant of the FSD has been taken equal to 14 s for all the PF coils [17]. In reality the coupled discharge of the PF coils, in case of a FSD, has to be solved specifically in case of every scenario. The resolution takes into account the matrix of the inductances and mutual inductances of the PF and the CS coils.

The quench propagation duration $\tau_p(U_t)$ is studied using Gandalf

It has been seen in the previous quench detection studies regarding the TF and the PF system that the quench propagation is very depending on the location of the quench.

A quench occurring in the low field zones of the magnets is very slow in propagation and consequently very difficult to be detected. The study has focused on a quench occurring in the high field region as [56], [57], and [58]. It is initiated at the inner radius, when the current is maximal.

It has been also seen that the quench propagation is very depending on the way the quench is initiated (initiated quench length, and power deposition). They are summed up in the following Table 44.

Length	Energy deposited to initiate the quench	Duration and mode of heat deposition	Location
1 m	2.MQE	0.1 s Constant power	Inner turn field just before transition to second turn

Table 44: Main characteristics of reference quench initiation

8.5.2. Method of selection of (U_t, τ_h)

The followed method is very similar to the one used for the CS system [58]. Nevertheless, the currents and contents in terms of materials of the conductors are different for each PF coil. Therefore, a dedicated study has been performed, using the conductor parameters defined in Table 41.

Knowing τ_{da} and $\tau_p(U_t)$ respectively from hot spot criterion application (solving the Eq. 2, section 3.5), and using Gandalf, it is then possible to deduce $\tau_h(U_t)$ from Eq. 1

Due to the high symmetry in terms of geometry and current distribution in the conductors two-in-hand, and following the principles expressed in 5.4., in absence of inductive noise, the compensated voltage is approximately equal to the quench voltage. Taking into account that the inductive voltage can be either positive or negative, it is conservative to take into account the propagating time corresponding to $2U_t$.

Several couples (U_t, τ_h) are still possible but the most appropriate one is selected through the examination of the inductive signal along the scenario.

The inductive signal is calculated along the scenario, and the compensation is applied according to the following formula, using a weighting coefficient α, which depends on the routing of the wires, as it was for the CS (see 6.3.3).

$$\Delta U_{DPi} = U_{DPi-C1}(t) - \alpha_i . U_{DPi-C2}(t)$$

It is recalled that the given voltage is still virtual, since the flux collection loops are not closed. in average, 150° of the outer turn is missing. Therefore, the voltage given in this paragraph should be completed by an additional circuit for the loop closure. This circuit is likely to have a shape strongly depending on the external structures of the coils. This circuit and associated extra voltage will be given in the next chapters.

8.6. Detection and action time, and quench propagation in the PF conductors

As the coils are very different from each other, there is no common result for all the coils in terms of detection and action time. Consequently, the overall volume of results is very large,

and the signals obtained from Gandalf and TrapsAV are not included in this document, they are presented in [79].

In Figure 132, the currents in the PF conductor are given.

For each coil, the main characteristics relevant for propagation time τ_p and detection and action time τ_{da} estimation, are summarized in the following Table 45. τ_{da} has been calculated according to the hot spot criterion 3.5.

	Current (kA)	Magnetic Field (T)	T_{ma} (K)	τ_{da} (s)	
PF1	42.6	4.53	1.88	6.6	(T_{op} = 5 K)
PF2	-27	2.16	2.77	26	(T_{op} = 5 K)
PF3	-37	3.51	2.12	10.8	(T_{op} = 5 K)
PF4	-30	2.68	2.52	20	(T_{op} = 5 K)
PF5	-45	4.93	1.55	3.8	(T_{op} = 4.6 K)
PF6	33.5	4.8	1.81	16	(T_{op} = 4.6 K)

Table 45: First turn of PF characteristics

In addition, the quench propagation has been studied with conductor parameters given in Table 41. A quench of 1m has been initiated on the first turn of each coil, with 2.MQE deposited within 0.1 s.

The main results of the propagation are given in Table 46.

U_q(V)	τ_p PF1 (s)	τ_p PF2 (s)	τ_p PF3 (s)	τ_p PF4 (s)	τ_p PF5 (s)	τ_p PF6 (s)
0.1	0.95	8.2	2.65	5.85	0.7	2
0.2	2.45	13.6	4.55	10.55	1.85	4.4
0.3	3.55	17.5	6.1	13.9	2.8	6

Table 46: Quench propagation time vs resistive voltage for the different PF coils

It can be observed that τ_{da} and τ_p are very different from one coil to another. This is due to the very different values of the currents and temperature margins.

8.7. Electromagnetic disturbances along the reference scenario.

As for the CS, with TrapsAV, the voltages across each conductor of the PF coils Double Pancakes have been calculated, and combined according to Figure 143. It is recalled that the voltage must be completed by another contribution collected by the measurement wires, shown in Figure 142, and expressed in terms of calculation in section 8.10. The compensation applied in the present section, corresponds to the following relationship:

$$\Delta U_{DPi}(t) = U_{C1-i}(t) - \alpha_i . U_{C2-i}(t) \qquad \text{Eq. 23}$$

In Eq. 23, $U_{C1\text{-}i}$ and $U_{C2\text{-}i}$ are the voltages described in Figure 141. The following figures from Figure 144 to Figure 149 show the voltage along the plasma scenario. Each figure contains on the left, the whole scenario, on the right, only the plasma initiation is shown.

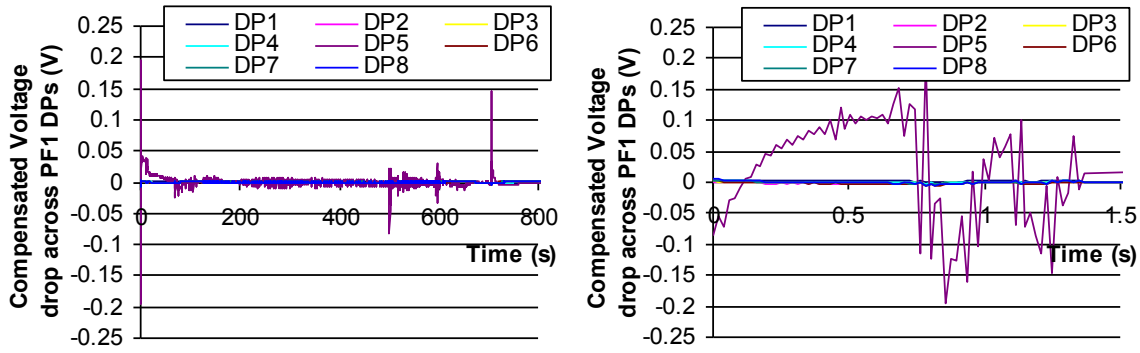

Figure 144 : Compensated voltage across PF1 along time

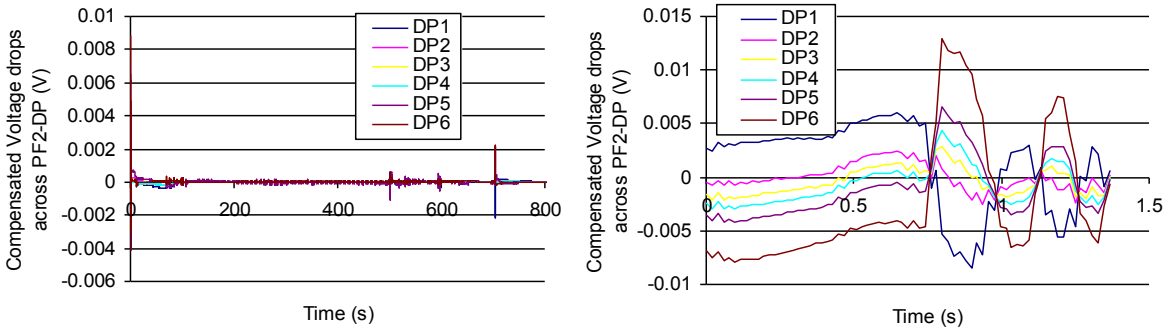

Figure 145 : Compensated voltage across PF2 along time

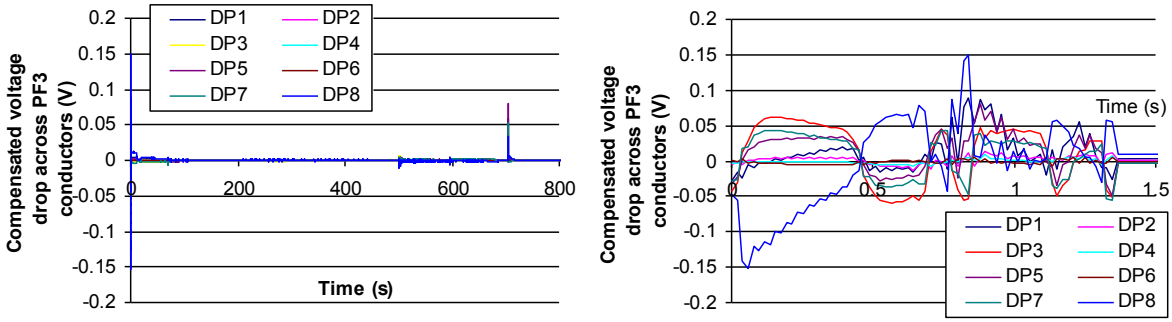

Figure 146 : Compensated voltage across PF3 along time

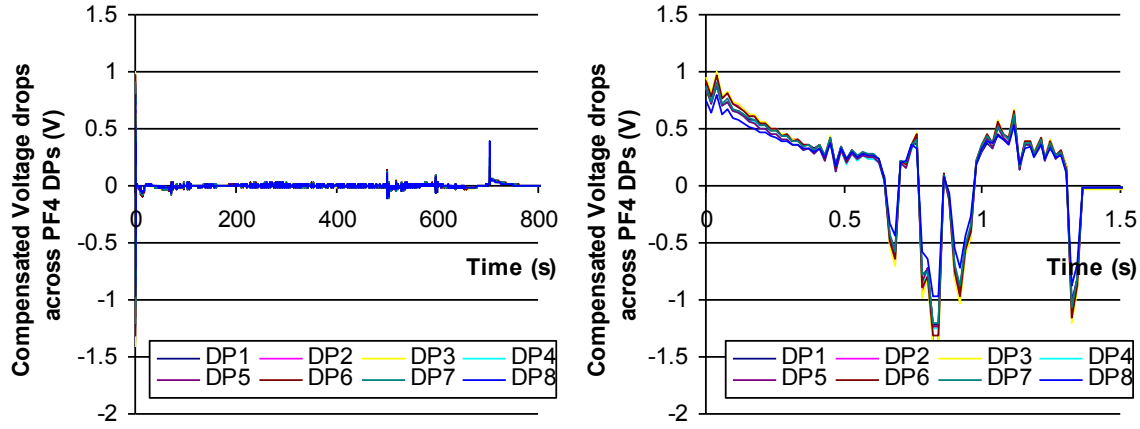

Figure 147 : Compensated voltage across PF4 along time

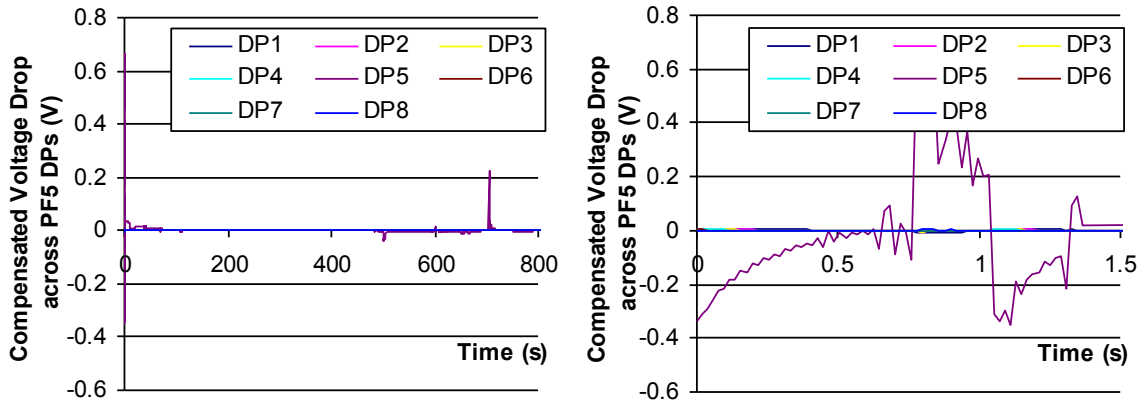

Figure 148 : Compensated voltage across PF5 along time

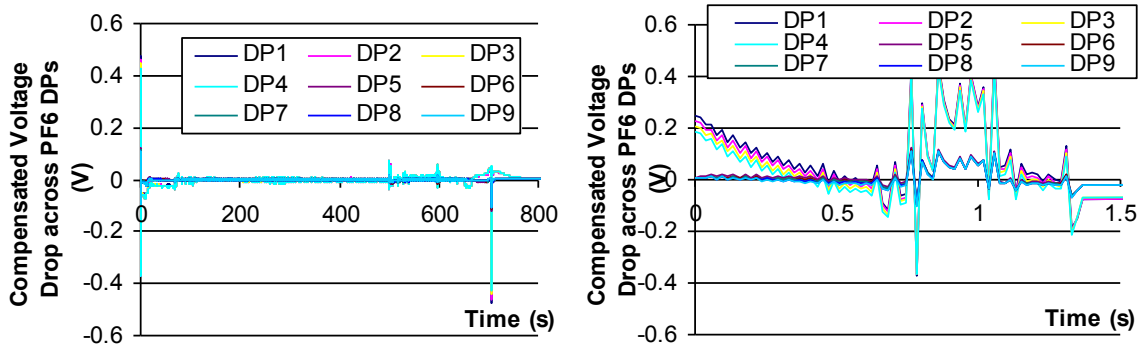

Figure 149 : Compensated voltage across PF6 along time

The examination of the signals represented in the previous figures allows determining as a function of a voltage threshold, the maximum consecutive time spent over this value (in absolute). This calculation, as well as the choice of the weighting coefficient is done by a program dedicated to this unique purpose. The method used to choose the weighting coefficient consists in minimizing the peaks, in absolute value, of the compensated signals. The result of this study is shown in the tables hereafter: for each coil and each Double Pancake, the maximum consecutive time spent out of the limits is given.

Limit			DP1	DP2	DP3	DP4	DP5	DP6	DP7	DP8
over	0.1	V	0.0000	0.0000	0.0000	0.0000	**0.4000**	0.0000	0.0000	0.0000
under	-0.1	V	0.0000	0.0000	0.0000	0.0000	**0.0196**	0.0000	0.0000	0.0000
over	0.2	V	0.0000	0.0000	0.0000	0.0000	0.0000	0.0000	0.0000	0.0000
under	-0.2	V	0.0000	0.0000	0.0000	0.0000	0.0000	0.0000	0.0000	0.0000
over	0.3	V	0.0000	0.0000	0.0000	0.0000	0.0000	0.0000	0.0000	0.0000
under	-0.3	V	0.0000	0.0000	0.0000	0.0000	0.0000	0.0000	0.0000	0.0000

Table 47: Maximum consecutive time spent out of the indicated voltage limit for PF1

Limit			DP1	DP2	DP3	DP4	DP5	DP6
over	0.1	V	0.0000	**0.0391**	0.0000	**0.0391**	**0.0391**	0.0000
under	-0.1	V	0.0000	**0.2000**	0.0000	**0.2000**	**0.2000**	0.0000
over	0.2	V	0.0000	0.0000	0.0000	0.0000	0.0000	0.0000
under	-0.2	V	0.0000	0.0000	0.0000	0.2000	0.2000	0.0000
over	0.3	V	0.0000	0.0000	0.0000	0.0000	0.0000	0.0000
under	-0.3	V	0.0000	0.0000	0.0000	0.0000	0.0000	0.0000

Table 48: Maximum consecutive time spent out of the indicated voltage limit for PF2

Limit			DP1	DP2	DP3	DP4	DP5	DP6	DP7	DP8
over	0.1	V	**0.0390**	0.0000	0.0000	0.0000	0.0000	0.0000	0.0000	**0.0390**
under	-0.1	V	**0.0000**	0.0000	0.0000	0.0000	0.0000	0.0000	0.0000	**0.2000**
over	0.2	V	0.0000	0.0000	0.0000	0.0000	0.0000	0.0000	0.0000	0.0000
under	-0.2	V	0.0000	0.0000	0.0000	0.0000	0.0000	0.0000	0.0000	0.0195
over	0.3	V	0.0000	0.0000	0.0000	0.0000	0.0000	0.0000	0.0000	0.0000
under	-0.3	V	0.0000	0.0000	0.0000	0.0000	0.0000	0.0000	0.0000	0.0000

Table 49: Maximum consecutive time spent out of the indicated voltage limit for PF3

Limit			DP1	DP2	DP3	DP4	DP5	DP6	DP7	DP8
over	0.1	V	**0.4000**	**0.4000**	**0.4000**	**0.4000**	**0.4000**	**0.4000**	**0.4000**	**0.4000**
under	-0.1	V	**0.0196**	**0.2000**	**0.2000**	**0.2000**	**0.2000**	**0.2000**	**0.2000**	**0.2000**
over	0.2	V	0.0391	0.0391	0.0391	0.0391	0.0391	0.0391	0.4000	**0.4000**
under	-0.2	V	0.0196	0.0196	0.0196	0.0196	0.0196	0.0196	0.0196	**0.0196**
over	0.3	V	0.0391	0.0391	0.0391	0.0391	0.0391	0.0391	0.0391	**0.4000**
under	-0.3	V	0.0196	0.0196	0.0196	0.0196	0.0196	0.0196	0.0196	**0.0196**

Table 50: Maximum consecutive time spent out of the indicated voltage limit for PF4

Limit			DP1	DP2	DP3	DP4	DP5	DP6	DP7	DP8
over	0.1	V	0.0000	0.0000	0.0000	0.0000	**0.4000**	0.0000	0.0000	0.0000
under	-0.1	V	0.0000	0.0000	0.0000	0.0000	**0.0196**	0.0000	0.0000	0.0000
over	0.2	V	0.0000	0.0000	0.0000	0.0000	**0.4000**	0.0000	0.0000	0.0000
under	-0.2	V	0.0000	0.0000	0.0000	0.0000	**0.0196**	0.0000	0.0000	0.0000
over	0.3	V	0.0000	0.0000	0.0000	0.0000	**0.0390**	0.0000	0.0000	0.0000
under	-0.3	V	0.0000	0.0000	0.0000	0.0000	**0.0196**	0.0000	0.0000	0.0000

Table 51: Maximum consecutive time spent out of the indicated voltage limit for PF5

Limit			DP1	DP2	DP3	DP4	DP5	DP6	DP7	DP8	DP9
over	0.1	V	**0.0391**	**0.0391**	**0.0391**	**0.0391**	**0.0391**	**0.0391**	**0.0391**	**0.0391**	**0.0391**
under	-0.1	V	**0.2000**	**0.2000**	**0.2000**	**0.2000**	**0.2000**	**0.2000**	**0.2000**	**0.2000**	**0.2000**
over	0.2	V	**0.0391**	**0.0391**	**0.0391**	**0.0391**	0.0000	0.0000	0.0000	0.0000	0.0000
under	-0.2	V	**0.2000**	**0.2000**	**0.2000**	**0.2000**	0.0000	0.0000	0.0000	0.0000	0.0000
over	0.3	V	**0.0391**	**0.0391**	**0.0391**	**0.0391**	0.0000	0.0000	0.0000	0.0000	0.0000
under	-0.3	V	**0.2000**	**0.2000**	**0.2000**	**0.2000**	0.0000	0.0000	0.0000	0.0000	0.0000

Table 52: Maximum consecutive time spent out of the indicated voltage limit for PF6

8.8. Selection of the detection parameters for the PF coil system

From Table 47 to Table 52, it possible to deduce the maximum time τ_{dis} during which ΔU_{DP} is exceeded. This time is different for each PF coil. In agreement with ITER team, it has been decided in a first approach, to select the same detection parameters for all the coils and Double Pancakes. Due to the very low value of τ_{da} of PF5, this coil is considered as the most demanding. Consequently, a low threshold is applicable, U_t = 0.1 V has been chosen. The corresponding propagating time, is $U_Q = 2.U_t$ = 0.2 V (refer to 8.5.2).

The time range of τ_h is adjusted according to the following:

On one hand due to the maximum time spent over the limit, τ_{dis}, the holding time τ_h must be such as:

$$\tau_h > \tau_{dis}$$

On the other hand the maximum value of τ_h is imposed by τ_{da} according to:

$$\tau_h < \tau_{da} - \tau_p(2U_t) - \tau_{cb}$$

Coil	Detection threshold U_t (V)	$\tau_p(2.U_t)$ (s)	τ_{dis} (s)	τ_{da} (s)	τ_h Range (s)
PF1	0.1	2.45	0.4	6.6	0.4 s<τ_h< 3.65 s
PF2	0.1	13.6	0.2	26	0.2 s<τ_h< 11.9 s
PF3	0.1	4.55	0.2	10.8	0.2 s<τ_h< 5.75 s
PF4	0.1	10.55	0.4	20	0.4 s<τ_h< 8.95 s
PF5	0.1	1.85	0.4	3.8	0.4 s<τ_h< 1.45 s
PF6	0.1	4.4	0.2	16	0.2 s<τ_h< 11.1 s

Table 53: Possible range of τ_h according to the PF coils

A range of τ_h can be defined for each PF coils. However, a single value for U_t and a single value for τ_h which match the requirements can be selected:

$U_t = 0.1$ V

And

$\tau_h = 1.4$ s

8.9. Influence of the accuracy of the weighting coefficient

As presented before, a weighting coefficient should be used in order to minimize the maximum voltage reached during the scenario. In the study presented before, this coefficient has been set to $1. \pm 10^{-5}$. Note that after the choice made for U_t and τ_h , the method for choosing the coefficient can be not the best: there are at least two different ways to optimize a weighting coefficient. Here, the coefficients have been chosen such that they minimize the maximum voltage peak. The other option, is to choose them, such that they allow large voltage peaks, but minimize the maximum consecutive time spent over or below a given threshold value. It is recalled that for each PF coil, the compensation effectiveness has been tested according to the following relationship:

$$\Delta U_{DPi}(t) = U_{C1-i}(t) - \alpha_i . U_{C2-i}(t)$$

In the previous equation, α_i is constant in time, and different for each Double Pancake i, for each PF coil. However, this coefficient is always very close to 1. Therefore, the relationship between U_Q and ΔU is:

$$U_Q = \Delta U$$

Consequently, the propagation time must be calculated with a voltage $2.U_t$, according to the principle explained in 5.4.

8.10. ITER Additional flux collecting loops

As described in chapter 8.4.5, the voltages presented above do not represent the actual design of the ITER machine. As the conductors are not considered as closed in the previous sections, additional flux-collecting loops must be taken into account, which represent the way the circuit used for voltage measurement is closed. The closed circuit C is shown in Figure 150. In the previous sections, the voltages presented are due to the circuit represented in Figure 143 (page 181).

In order to have a first view on the influence of the wires routing, drawings have been obtained from IO.

Despite the fact the real loops including all the details of their paths are not easy to do and likely to change with any modification of the coils, it is still possible to include them in a general way. This has been done, and for 3 over 6 coils, the conclusions in terms of voltage threshold and holding time could change. However, it is possible to modify the routing to adjust the inductances of C_{wires} (for C_1 and C_2) so they fit the previous given parameters.

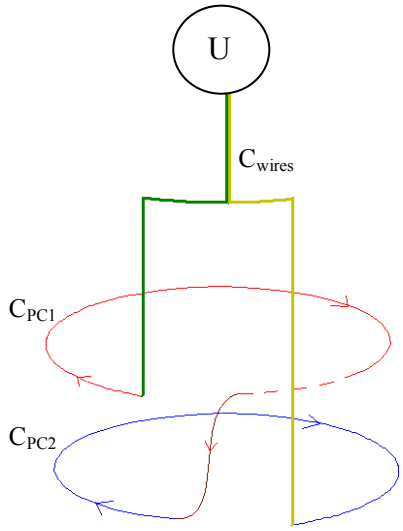

Figure 150: Actual voltage, across winding plus instrumentation wires

The circuit C is decomposed as explained in the previous chapters into two parts. One is the winding (presented on Figure 143 and the left-hand side of Figure 151), and the other is the wires including the routing to the location where they are assembled to form a twisted pair (see Figure 151, right-hand side).

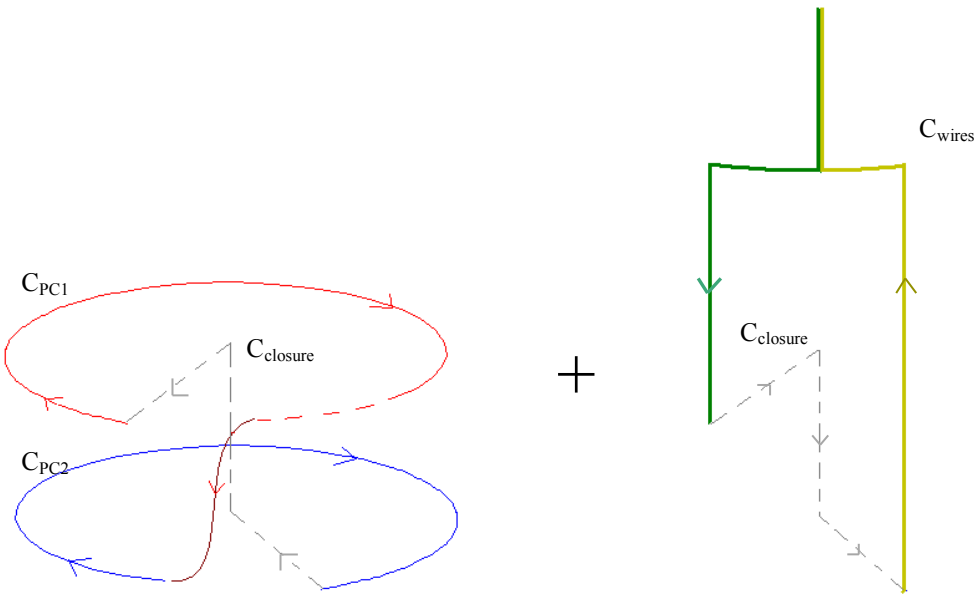

Figure 151: Decomposition of circuit C

The following relationships show the way the routing has been taken into account, and how it influences the final result.

The basic law used for voltage estimation, which includes the routing and winding.

$$U_C = \oint_C \vec{E}.\vec{dl} = \iint_C \frac{d\Phi(t)}{dt}$$

$$C = C_{PC1} + C_{PC2} + C_{closure} - C_{closure} + C_{Wires}$$

The loop made by the wires has a shape strongly depending on the localization of the pancake, in terms of elevation and angular aperture (due to the fact that the last turns are not completed).

$$\vec{\nabla}\vec{B} = 0$$

This expresses that through a closed surface, the magnetic flux is null.

The loop formed by the wires (right-hand side of Figure 151, and Figure 152) is the loop through which the additional flux has to be calculated to estimate the actual voltage U_c.

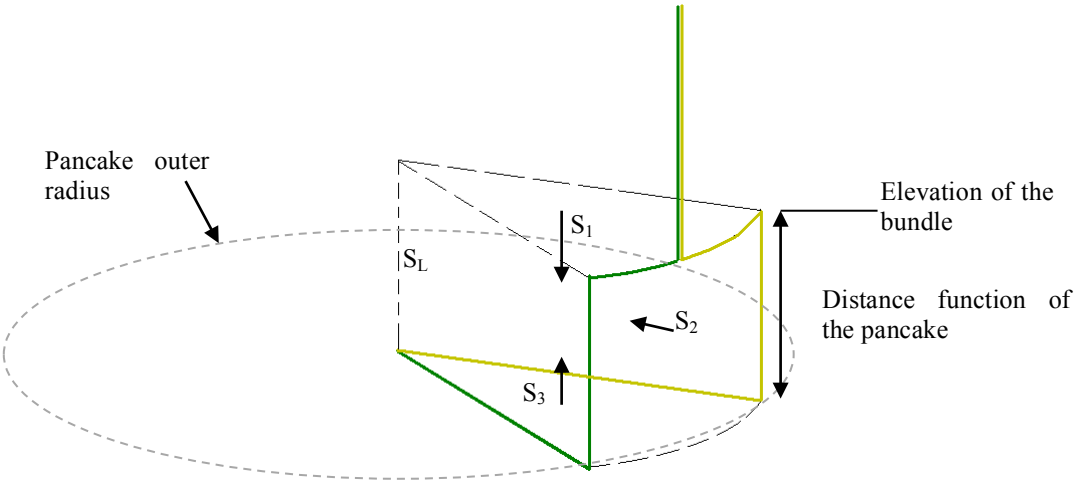

Figure 152: Closed surface, the contour of which is formed by $C_{closure}$ and C_{wires}

This surface ($S_1 + S_2 + S_3 + S_L$), presented in Figure 152 is closed.

S_1 is the surface at the top of the coil where the bundle of instrumentation wires is. S_2 is the surface located at the outer radius of the coil

S_3 is an angular sector at the pancake elevation.

S_L are the lateral surfaces, which collect no flux since the problem is considered as being axisymmetric.

$$\Phi_1 + \Phi_2 + \Phi_3 + \Phi_L = 0$$

We try to estimate $\Phi_2(t) + \Phi_3(t)$, which is equivalent to calculate $-(\Phi_1(t) + \Phi_L(t))$.

But $\Phi_L = 0$

Therefore, calculating the flux collected by $S_3 + S_2$ is equivalent to calculate the flux through S_1.

Preliminary calculations have been done using this method. They show that the external wires introduce significant additional voltage for all the PF coils (max 10%, which makes the compensation far less effective). The compensation of paragraph 8.4.4 cannot be applied anymore for coils PF3, PF4, and PF6. Adaptations of the routing have to be envisaged to recover the previous compensation.

8.11. Case of the simultaneous quench of C_1 and C_2

Is it possible to detect a quench affecting simultaneously the two conductors C_1 and C_2 of a single pancake with a threshold voltage of 0.1 V?

As for the CS, the case of a quench that is initiated on the whole inner turn of one pancake has been envisaged. As explained in previous sections, the conductors of a pancake are not symmetric; they do not have the same exposed length. In average, their angular extension has 40° of difference. This causes a heat deposition length difference of ΔL. Such an asymmetry induces a difference of ΔU immediately visible at quench initiation. These voltage differences

are shown below, in Table 54. In this case, the propagation time given in the previous chapters is not valid anymore, since more than 1 m is heated.

Coil	I	B	U_q	ΔL	ΔU
PF1	42.6 kA	4.53 T	0.043 V/m	2.43 m	0.11 V
PF2	27 kA	2.16 T	0.016 V/m	5.6 m	0.092 V
PF3	37 kA	3.51 T	0.028 V/m	8.15 m	0.23 V
PF4	30 kA	2.69 T	0.02 V/m	8.15 m	0.16 V
PF5	45 kA	4.93 T	0.047 V/m	5.6 m	0.26 V
PF6	33.5 kA	4.78 T	0.035 V/m	2.5 m	0.087 V

Table 54: Voltage difference U_{C1}-U_{C2} due to a heat deposition on the full first turn

These voltages will increase along time up to the $2U_t$, and continue to grow after that, and probably faster than presented before.

In conclusion, it is highly probable that such a quench can be detected, but further studies should be made about this particular case of quench propagation.

8.12. Conclusions about quench detection in the ITER PF system

The design of the quench detection of the ITER PF system has been made following a methodology very similar to the one followed for the ITER CS system, despite the final architecture of the detection is different, and does not rely on a CDA style compensation, but simply on a bridge compensation.

The solution for the detection voltage related to a double pancake, is made by comparison of the voltage across each two in hands conductors of a double pancake.

Using TrapsAV it is possible to have, for each double pancake of the PF system, the inductive voltage detection signal along the reference 15 MA ITER scenario. This signal does not take into account the external routing of the detection wires.

There are different possibilities for the voltage threshold in the range of 0.1 V - 0.3 V it is possible to adjust the holding time of the detection.

The PF coils in the reference 15 MA ITER scenario are far from their theoretical capacity in current. The protection is therefore easy because the detection and action time is large except for PF5 where the current is 45 kA.

Several couples (U_t, τ_h) are possible for the parameters of the quench detection, varying U_t from 0.1 V to 0.3 V. However having in mind the maximum capacity of the PF coils, it is suggested to select a level 0.1 V as a reference detection level for the electronics.

It has been pointed out, that further studies should be made to take into account a better routing of the instrumentation wires to mitigate inductive voltages.

9. Conclusion

The quench of one of the ITER superconducting magnet system induces the development of a resistive zone associated with large heat dissipation. In spite this event is very unlikely, it has to be envisaged and mitigated. Therefore this resistive transition has to be rapidly detected to dump the magnetic energy, and avoid permanent damage of the magnet. This is particularly challenging for some of the ITER coils due to the large inductive components of the voltage during the plasma scenario. The primary quench detection is based on voltage detection in ITER. The major purpose of the thesis was to propose a conceptual design of the quench detection based on voltage measurements. For this, a clear methodology was developed. It includes the classical hot spot criterion, the propagation using the code Gandalf and the estimation of the inductive disturbances by developing the TrapsAV code.

A solution was proposed for the main ITER magnet systems.

a. CS and PF ITER coils

The compensation of the very large inductive components is decisive in the case of these two systems because of their pulsed behaviour linked to the plasma scenario.

This is by the way the first time that the quench detection of such pulsed systems is studied in details.

The proposed compensation is based on a system of double pancakes voltage opposition, which is different for the two coil systems.

To theoretically study the resulting detection voltage and adjust the solution, it has been necessary to develop within the thesis a special code TrapsAV, dedicated to voltage estimations during plasma scenarios, which is an extension of an existing CEA code Traps, for very accurate magnetic field calculations for fusion magnets.

For the CS system, it turned out to be necessary, in addition, to blank the detection during the 3.5 first seconds of the plasma initiation phase. It has been proven that this very special operation was possible while respecting dynamically the usual hot spot criterion.

If the selected threshold was considered as being too high, the routing of the instrumentation wires could be adapted such that the circuits are more equilibrated, allowing a better compensation. The examination of new circuits can be done easily with TrapsAV.

b. TF coil

The ITER TF magnet system will be the largest magnet system in the world presenting a magnetic stored energy of 40 GJ. The protection of this system is really crucial for ITER operation and also for safety.

The TF system of ITER is not pulsed and it is practically impossible to predict the inductive electromotive forces induced by the plasma and the scenario taking place in the surrounding PF and CS coils. These electromotive forces are partly due to positioning errors resulting from tolerances during the fabrication phase. In theory the electromotive forces are null, in practice their actual values will be estimated during the commissioning phase of the system.

Instead of compensating the electromotive forces by a co-wound strip, it is proposed to compensate them by opposing coils or coil subcomponents, adjusting the level of refinement and the number of detectors during the commissioning phase. This is the solution selected for most of the fusion projects in the world (Tore Supra, KSTAR, SST-1, JT-60SA).

For the first time the manifestation of another electromotive force due to the plasma paramagnetism has been observed in Tore Supra superconducting TF system. This takes place during plasma initiation and results in a TF current decrease which is compensated by the power supply voltage. This electromotive force can be perfectly compensated in theory by coil balance and it is the case in Tore Supra.

c. Quench propagation

The quench propagation during the early times of the quench plays a very important role for the detection. As soon as the quench is initiated the initial point of the quench is adiabatically heating according to the classical hot spot criterion. Depending on the quench velocity, the detection voltage threshold can be reached rapidly or less rapidly.

Starting from the classical adiabatic velocity, it is well known that the helium of the cable in conduit is decreasing the quench velocity, which is detrimental to quench detection. The quench propagation has been therefore academically studied on a virtual model, to point out the main factors influencing the quench velocity such as the quench initiation, the current and the magnetic field comparing the simulations with Gandalf to the few existing experiments.

Using the results of the quench propagation (using Gandalf) and the calculations of the inductive electromotive forces (using TrapsAV) it is possible to propose a quench detection system characterized by a voltage threshold (in the range of 0.1 V – 0.55 V) and a holding time (in the range) depending on the different systems. The proposed solutions respect the hot spot criterion associated with a temperature less than 250 K in the conductor and taking into account the fast safety discharge designed by ITER after the current breaker opening.

The selected values in particular the holding time are sufficiently high to ensure the reliability of the system and avoid fast safety discharges not induced by a quench which is a classical problem in an industrial environment.

d. Perspectives

In the framework of the thesis it has not been possible to cover all the aspects of the quench detection in ITER. As mentioned, the thesis focused on the plasma reference scenario at 15 MA plasma current. For this study very useful tools have been developed in particular TrapsAV to predict inductive electromotive forces. These tools can be further used and developed to perform other studies. The studies could concern other plasma scenarios, disruptions and Vertical Displacement Events (VDE) to confirm that the designed solutions are sufficient robust for these new cases.

It is also certainly very important to observe the results of voltage compensation in existing superconducting tokamaks such as EAST, KSTAR and Tore Supra. A very preliminary tentative has been made for Tore Supra in the thesis regarding the electromotive forces due to plasma magnetism. Another tentative has been made to explain a fast safety discharge in EAST induced by a transposition imperfection in the co-wound strip. These experimental observations could be very precious especially regarding the TF system where theoretical calculations are hardly possible.

Regarding the quench propagation during early times, it appeared during the thesis that there were very few studies regarding the parameters influencing the quench velocity. It was pointed out that there is a linear dependency between the adiabatic velocity and the quench propagation velocities simulated with Gandalf. However it has not been possible to completely cover the subject within the thesis. It has been proven using Gandalf in the PF studies that the quench propagation velocity is very depending on the temperature margin. However the exact role of the helium in the bundle and central channel must still be explored such that general rules can be drawn.

10. References

[1] KHATIB BARBER H., IEA "World Energy Outlook 2010", Energy Policy, Volume 39, Issue 5, May 2011, Pages 2507-2511

[2] MEHLHORN T.A., CIPITI B.B., OLSON C.L., ROCHAU G.E., "Fusion–fission hybrids for nuclear waste transmutation: A synergistic step between Gen-IV fission and fusion reactors", Fusion Engineering and Design, Volume 83, Issues 7-9, December 2008, Pages 948-953

[3] World Energy Outlook 2010, International Energy Agency

[4] WESSON J., "Tokamaks", Oxford University Press, USA; 4 edition (August 1, 2011)

[5] LECHON Y., CABAL H., VARELA M., SAEZ R., EHERER C., BAUMANN M., DUWEKE J., HAMACHER T., TOSATO G.C., "A global energy model with fusion", Fusion Engineering and Design, Volumes 75-79, November 2005, Pages 1141-1144

[6] RAX J.M., Physique des plasmas, Dunod, August 2005

[7] SPITZER L., "Physics of Fully Ionized Gases", Interscience, New York, 1962

[8] GAMOW G., et al., "The Atomic Nucleus and Nuclear Energy Sources", Oxford University Press, 1949

[9] DARVAS J., et al., Nuclear Fusion supplementary, 1991

[10] WILSON M., "Superconducting Magnets", Oxford University Press, 1987

[11] PEACOCK N. J. et al., Nature, 1969, 224, 488

[12] LAWSON J. D., "Some Criteria for a Power Producing Thermonuclear Reactor", Proceedings of the Physical Society B, Volume 70 (1957), p. 6

[13] Dossier Atout Cadarache, n°6, Dec/Jan 2005

[14] JOHNER J., “HELIOS: A Zero-Dimensional Tool for Next Step and Reactor Studies, Fusion Science and Technology, Volume 59, Number 2, February 2011, Pages 308-349

[15] ITER Design Description Document DDD11-1 ITER_D_2NPLKM v1.8, “Section 1, Design Basis“, 2009

[16] ITER Design Description Document DDD11-3, ITER_D_2NHKHH v1.5, “Section 3: CS Coils and Pre-Compression Structure“, 2009

[17] ITER Design Description Document DDD11-7, ITER_D_2NBKXY v1.2, “Section 7: Conductors“, 2009

[18] ITER Design Description Document DDD11-4, ITER_D_2LGJUP v3.0, “Section 4: PF Coils and Supports“, 2009

[19] ITER Design Description Document DDD11-2, ITER_D_2MVZNX v2.2, “Section 2: TF Coils and Structures“, 2009

[20] MEADE D.M. et al., “TFTR experience with D-T operation“, Fusion Engineering and Design, Volume 27, 1 March 1995, Pages 17-26

[21] ABRIKOSOV A., EKSPERIM Zh. “On the magnetic properties of superconductors of the second group”, Soviet Phys-JETP 5,114 (1957)

[22] GINZBURG V.L., LANDAU L.D., Zh. Eksp. Teor. Fiz. 20, 1064 (1950) .

[23] RENARD Bertrand, “Thermo-hydraulic behaviour of dual channel superconducting cable-in-conduit conductors for ITER”, 164 pages, Thesis: energy mechanics: Château-Gombert: 2006

[24] STEKLY Z. J. J., ZAR J. L., “Stable Superconducting Coils“, IEEE transactions on nuclear science, June 1965

[25] BESSETTE D., CIAZYNSKI D., DECOOL P., DUCHATEAU J.L. & KAZIMIERZAK B.B., “Fabrication and test results of the 40 kA CEA conductors for NET/ITER“, 1992, proceedings of the 17th symposium on fusion technologies, Rome (Italy), pp 788-792

[26] BARDEEN J., COOPER L. N., SCHRIEFFER J. R., “Theory of Superconductivity”, 8 July 1957, Physical Review, 108, 1175–1204

[27] O. TSUKAMOTO et al. “Statistical study on stability and quench protection of pool cooled superconducting magnets”, Cryogenics, Volume 31, Issue 7, July 1991, Pages 585-589, Symposium on Superconductor Stability

[28] WIPF S. L., MARTINELLI A. P. Proc. Applied Superconductivity Conference, Anapolis. IEE, New York, p. 331, 1972

[29] WILSON M., "100 years of superconductivity and 50 years of superconducting magnets", Plenary presentation at the 22th Conference of magnet technology 2011 Marseille France

[30] DUCHATEAU J.L., "New consideration about stability in NbTi Cable-In-Conduit Conductors" IEEE Trans. Appl. Sup. 19 2 2009 55.

[31] ROSSI L., "The large Hadron Collider and the role of Superconductivity in one of the largest scientific enterprises", IEEE Trans. Appl. Sup. 17 2 2007 1005

[32] RODRIGUEZ-MATEOS F., "The protection system for the superconducting elements of the large hadron collider" Proceeding of the 1999 particle Accelerator Conference” New York 1999

[33] DUCHATEAU J.L., JOURNEAUX J.Y., GRAVIL B., "Tore Supra superconducting toroidal field" system Fusion science technology 56 2009 1092

[34] MORROW G. "Progress in MRI Magnets", IEEE Trans. Appl. Sup. 10 1 2000 744

[35] VERWEIJ A., "Thermal runaway of the 13 kA busbar joints in the LHC", IEEE Trans. Appl. Sup. 20 3 2010 2155

[36] FINK S., FIETZ W.H., MIRI A., "High voltage investigations for ITER coils", Fusion Engineering and Design, Volume 82, Issues 5-14, October 2007, Pages 1443-1446

[37] FINK S., BONICELLI T., FIETZ W.H., MIRI A., QUAN X., ULBRICHT A., "Transient electrical behaviour of the ITER TF coils during fast discharge and two fault cases", Fusion Engineering and Design, Volumes 75-79, November 2005, Pages 135-138

[38] WINKLER A., FINK S., FIETZ W.H., NOE M., "Calculation of transient electrical behaviour of ITER PF coils", Fusion Engineering and Design, Volume 84, Issues 7-11, June 2009, Pages 1979-1981

[39] SACKETT S.J., "EFFI, a code for calculating the electromagnetic field, force and inductance in coil systems of arbitrary geometry" Lawrence Livermore National Laboratory, Livermore, California, UCRL 52402 1978

[40] CORDIER J.J., HERTOUT P., GARGIULO L., CANTONE V., SOLER B., "New magnetic measurement of the Tore Supra Toroidal Field profile", Proceedings of the 20 th SOFT Marseille 1998

[41] HERTOUT P., BLEYER A., DUCHATEAU J.L., NICOLLET S., "Heat deposition in the ITER FEAT poloidal field coils during a plasma scenario", IEEE Trans. App. Sup. 2002 562.

[42] ULBRICHT A., CIAZYNSKI D., DUCHATEAU J.L., FIETZ W., FILLUNGER H., FINK S., HELLER R., MAIX R., NICOLLET S., RAFF S., RICCI M., SALPIETRO E., ZAHN G., ZANINO R. et al., "The ITER toroidal field model coil project" Fusion Engineering and Design 73 (2005) 189-327.

[43] TAKAHASHI Y., Memos on "Quench detection method with pick-up coils for CS" 02 and 07 of 2004

[44] TAKAHASHI Y., "Quench detection method with pick-up coils for CS (2) ", Ref. No.: N 13 MD 76 04-07-15 W 0.1, 2004/7/14

[45] NICOLLET S., LACROIX B., DUCHATEAU J.L., COATANEA M., CIAZYNSKI D., "Extension of ITER Contract CT/08/1049 : CS Model for Quench studies of pancake and Module" Internal CEA Note AIM/NTT-2009

[46] RADOWINSKI A.L., QD "Modeling with and w/o Passive Structure for Scenarios w/o and with the Plasma Disruption", ITER MEMORENDUM, ITER-MIT-ALRadovinsky-080306-01, August 3, 2006

[47] ANGHEL A., "Quell experiment; analysis and interpretation of the quench propagation results" Cryogenics 38 (1998) 549.

[48] KATO T., et al. "First test results for the ITER central solenoid model coil" Fusion Engineering and design 56-57 (2001) 59

[49] INAGUCHI T. et al. "Quench analysis of an ITER 13T-40kA Nb_3Sn coil (CS insert)", Cryogenics 44 (2004) 121.

[50] NICOLLET S., LACROIX B., DUCHATEAU J.L., COATANEA M., "ITER CONTRACT CT/08/1049 Deliverable 5.2 Description and model cryogenic environment of the CS ITER coil", Internal CEA Note AIM/NTT-2009.012 December 2009

[51] DUCHATEAU J.L., COATANEA M., NICOLLET S., LACROIX B., « ITER CONTRACT CT/08/1049 Final report. "Selection of a detection for the ITER CS coil" Internal CEA Note AIM/NTT-2009.011 December 2009

[52] E. GAIO et Al., "Conceptual design of the quench protection circuits for the JT-60SA superconducting magnets", Fusion Engineering and Design, Volume 84, Issues 2-6, June 2009, Pages 804-809

[53] BOTTURA L. "Scaling law for NbTi critical current, a practical fit for the critical surface of NbTi" IEEE Transactions on Applied Superconductivity 10, 2000, 1054

[54] BESSETTE D. "Data package for simulating the in-coil operation of the PF and CC conductors during the reference scenario #2 15 MA baseline". (memo 07 May 2011 (revision 04)

[55] "Magnet superconducting and electrical design criteria" ITER-D_22GRQH v1.2 5 Sept 2009

[56] COATANEA M., DUCHATEAU J.L., NICOLLET S., LACROIX B. "ITER CS Quench Detection Detailed study (electromagnetic aspect) ", Internal CEA note AIM/NTT-2010.008

[57] DUCHATEAU J.L., COATANEA M., NICOLLET S., LACROIX B., "ITER CONTRACT ITER/CT/09/4300000014 Deliverable 2.1 Selection of a detection for the ITER TF system" Internal CEA Note AIM/NTT-2010.023

[58] COATANEA M. et al. "Selection of a quench detection system for the ITER CS magnet", Fusion Engineering and Design, 86 2010 1418

[59] CHU Y. et al., "Quench detection based on voltage measurement for the KSTAR superconducting coils", Trans. on Appl. Supercond. 20 2008 1568

[60] HU Y. and quench team "design of quench detection for EAST Tokamak" Internal ASIPP report, 2010

[61] BAREYT B. "Update of the assessment of the TF coil discharge parameters and passive structure electromechanical stresses during a fast discharge" Naka joint Work site March 14, 2001 G40 RI 101-03-14 W0.1

[62] BESSETTE D., "Current decay during ITER TF fast discharge" https://user.iter.org./?uid-2NKRCR

[63] COPETTI R. et al "Quench initiation and propagation in the ITER TF conductor" September 2010 Internal CEA note AIM/NTT-2010.16

[64] BONICELLI T. et al. "The European development of a full scale switching unit for the ITER switching and discharging network" Fusion engineering and design 75-79 (2005) 193.

[65] "Interface specifications TF coils – feeder system" ITER_D_2LFGH

[66] "TF_winding_pack_schematic instrumentation diagram modification sheet", ITER Organization Drawing number 003245

[67] TIXADOR P., "Matériaux Supraconducteurs", Ed. Hermes-Lavoisier, 2003

[68] CIAZYNSKI D. "Contribution to the electromagnetic analysis of the ITER TFMC Phase I experiment" Internal CEA note AIM/NTT-2002.001 (2002)

[69] SHATIL, N., et al., "The First Experimental Observation of the Helium Mass Exchange between Cable Space and Central Channel in CICC Obtained by SHF Method during QUELL," in Proceedings of the 20th SOFT, Fusion Technology 1, pp. 715-718 (1998).

[70] NICOLLET S., LACROIX B., BESSETTE D., COPETTI R., DUCHATEAU J.L., COATANEA M., RODRIGUEZ-MATEOS F., "Thermal-hydraulic behaviour of the ITER TF system during a quench development", Fusion Engineering and Design 86, 2011, pages 1497-1500

[71] COATANEA M., DUCHATEAU J.L., HERTOUT P., BESSETTE D., RODRIGUEZ-MATEOS F., "Quench Detection in the ITER Magnet System", IEEE Transactions on Applied Superconductivity, Volume 20, No. 3, June 2010

[72] COATANEA M. et al. "Investigations about quench detection in the ITER TF system", IEEE Transactions on Applied Superconductivity, Volume 22, No. 3, 2012.

[73] LEHMANN W., ZAHN G., "Safety Aspects for LHe Cryostats and LHe Transport Containers", ICEC7, London, 1978

[74] TAYLOR D.J., "The scaling law for the strain-dependence of the critical current density in Nb_3Sn superconducting wires", Supercond. Sci. Technol. 18, S241-252, 2005.

[75] BOTTURA L., ROSSO C., "Flower, a model for the analysis of hydraulic network and processes", Cryogenics, Volume 43, pages 215-223, 2003

[76] BOTTURA L., "A Numerical Model for the Simulation of Quench in the ITER Magnets", J. Comp. Phys., Volume 125, pp. 26-41, 1996.

[77] COATANEA M. et al., "ITER CONTRACT CT/08/1049 Adaptation of Traps to quench detection in ITER" Internal CEA report AIM/NTT 2009.006. July 2009

[78] COATANEA M. et al., "Analytical Calculation of the voltage induced by a plasma event across a CICC petal or a co-wound tape of ITER TF Coils" Internal CEA report AIM/NTT 2009.001 March 2009

[79] COATANEA M. et al, "ITER CONTRACT ITER/CT/09/4300000014, Deliverable 2.1, Selection of a detection for the ITER PF system", Internal CEA report AIM/NTT 2011.001 January 2011

[80] MITCHELL N. et al, “The ITER magnet system”, IEEE Transactions on applied superconductivity, vol. 18, February 2008, page 435.

[81] LIBEYRE P. et al, “Electrical design requirements on the ITER coils”, Transactions on applied superconductivity, vol. 18, February 2008, page 479

[82] INAGUCHI T. Et al, “Quench analysis of an ITER 13 T-40 kA Nb_3Sn coil (CS insert)”, Cryogenics, vol 44, pages 121-130, 2004

[83] Magnet Superconducting and Electrical Design Criteria, ITER_D_22GRQH_v1.2, 5 Sept 2009

[84] SERIO L., “Challenges for cryogenics at ITER”, Advance in Cryogenic Engineering, 45, 2010, page 651

[85] EDWARDS H. T., “The Tevatron energy doubler: A superconducting accelerator,” Annual Review of Nucl. Part. Sci., vol. 35, pp. 605–660

[86] BUCALOSSI J., “the Gigajoules discharges”, Fusion Science and technology, vol. 56, 2009 page 1366

[87] RENARD B., DUCHATEAU J.L., ROUSSET B., TADRIST L., “Evaluation of thermal gradients and thermosiphon in dual channel cable-in-conduit conductors”, Cryogenics, vol. 46, 2006, page 629

[88] ROSSI L., “The Large Hadron Collider and the Role of Superconductivity in One of the Largest Scientific Enterprises” IEEE Transactions on applied superconductivity 17 2007, page 1005

[89] TAKAHASHI Y., YOSHIDA K., NABARA Y., EDAYA M., BESSETTE D., SHATIL N., and MITCHELL N., “Stability and Quench Analysis of Toroidal Field Coils for ITER” IEEE Transactions on Applied superconductivity 17 2007, page 2426

[90] “High temperature superconductors (HTS) for energy applications”, Woodhead Publishing limited 2012

[91] IWASA Y., “Case studies in superconducting magnets: design and operational issues”, Springer 2009

[92] SHAJII A., FREIDBERG J.P., CHANIOTAKIS A., “Universal scaling laws for quench and thermal hydraulic quenchback in CICC coils” IEEE Transactions on Applied Superconductivity, 5 2 1997 477

[93] LAKRIMI M., et al., “The principles and evolution of magnetic resonance imaging”, Journal of Physics, 286, 2011

[94] LIBEYRE P. et al., “An optimized Central Solenoid for ITER”, IEEE Transactions on Applied Superconductivity, 20 3 2010 398

[95] DEVRED A. et al., “Status of ITER conductor development and production”, IEEE Transactions on Applied Superconductivity, 22 3 2012

Appendix : units and abbreviations

AC	Alternative Current
ASDEX	Axially Symmetric Divertor Experiment
BCC	Bottom Correction Coils
CC	Correction Coils
CDA	Central Difference Averaging
CICC	Cable-In-Conduit Conductor
CS	Central Solenoid
D	Deuterium
DC	Direct Current
DEMO	DEMOnstration Power Plant
D-T	Deuterium-Tritium
EAST	Experimental Advanced Superconducting Tokamak
HTS	High critical Temperature Superconductors
IEA	International Energy Agency
ITER	International Thermonuclear Experimental Reactor
JET	Joint European Torus
KSTAR	Korea Superconducting Tokamak Advanced Research
LTS	Low critical Temperature Superconductors
MRI	Magnetic Resonance Imaging
NBI	Neutral Beam Injection
PF	Poloidal Field coils
PS	Passive Structures
RF	RadioFrequence
SCC	Side Correction Coils
T	Tritium
TCC	Top Correction Coils
TF	Toroidal Field coils
TFTR	Tokamak Fusion Test Reactor
TS	Tore Supra